PONTIFÍCIA UNIVERSIDADE CATÓLICA
DO RIO DE JANEIRO

Vitor Moreira de Alencar Monteiro

Mechanical behavior and damage evolution of fiber reinforced concrete under flexural fatigue loading for structural applications

Tese de Doutorado

Thesis presented to the Programa de Pós-Graduação em Engenharia Civil of PUC-Rio in partial fullfilments of the requirements for the degree of Doutor em Ciência – Engenharia Civil.

Advisor: Prof. Flávio de Andrade Silva
Co-Advisor: Prof. Daniel Carlos Taissum Cardoso

Rio de Janeiro
December 2023

PONTIFÍCIA UNIVERSIDADE CATÓLICA
DO RIO DE JANEIRO

Vitor Moreira de Alencar Monteiro

Mechanical behavior and damage evolution of fiber reinforced concrete under flexural fatigue loading for structural applications

Thesis presented to the Programa de Pós-Graduação em Engenharia Civil of PUC-Rio in partial fullfilments of the requirements for the degree of Doutor em Ciência – Engenharia Civil.

Prof. Flávio de Andrade Silva
Advisor
PUC-Rio

Prof. Daniel Carlos Taissum Cardoso
Co-Advisor
PUC-Rio

Prof. Barzin Mobasher
Arizona State University

Prof. Albert de la Fuente Antequera
Universidad Politecnica de Catalunya

Prof. Elisa Dominguez Sotelino
PUC-Rio

Prof. Pablo Augusto Krahl
Mackenzie Presbyterian University

Rio de Janeiro, 4th December, 2023

Vitor Moreira de Alencar Monteiro

Graduated in Civil Engineering at Pontifícia Universidade Católica do Rio de Janeiro in 2018 and obtained his M.Sc. Degree in Civil Engineering from the Pontifícia Universidade Católica do Rio de Janeiro in 2020.

Bibliographic data

Monteiro, Vitor Moreira de Alencar

Mechanical behavior and damage evolution of fiber reinforced concrete under flexural fatigue loading for structural applications / Vitor Moreira de Alencar Monteiro ; advisor: Flávio de Andrade Silva ; co-advisor: Daniel Carlos Taissum Cardoso. – 2023.
234 f. : il. color. ; 30 cm

Tese (doutorado) – Pontifícia Universidade Católica do Rio de Janeiro, Departamento de Engenharia Civil e Ambiental, 2023.
Inclui bibliografia

1. Engenharia Civil e Ambiental - Teses. 2. Concreto reforçado com fibras. 3. Fadiga. 4. Degradação mecânica. 5. Modelos analíticos. 6. Concreto armado. I. Silva, Flávio de Andrade. II. Cardoso, Daniel Carlos Taissum. III. Pontifícia Universidade Católica do Rio de Janeiro. Departamento de Engenharia Civil e Ambiental. IV. Título.

CDD: 624

Aknowledgements

This doctoral thesis is especially dedicated to my grandfather Lee and to my father José Jorge, who passed away in the last months before the end of my PhD course.

I am immensely grateful to my parents, José Jorge and Mônica, who were my most important pillars throughout this journey. This work would not have been possible without the support and encouragement of my family all this time. A special thanks also to my cousins Érica, Sandra and Gabriel and my godmother for all the love, fun, and friendship all the time.

I would like to thank professors Flávio Silva and Daniel Cardoso for all the encouragement and support throughout my academic journey. More importantly, I would like to acknowledge all the trust and investment in my professional growth over all those past years. A special thanks to professor Barzin Mobasher for welcoming me in the USA and collaborating on the development of my doctoral thesis.

One of the main assets from the Department of Civil and Environmental Engineering's is the Structures and Materials Laboratory. The excellent working environment, effective management and the high level of technology achieved by the laboratory in seven years was impressive. I had the privilege to witness the growth of a dynamic research environment and work with a world-class team. A big thank you to the working colleagues Euclides, Jhansen, Bruno, Anderson, Rogério, Marques, and José Nilson. The knowledge I gained from working with you was key for the development of this work.

I would like to express my gratitude for all the support from the Furnas team for the investment in the research project and their assistance in the development of this work, especially to the technicians Adolfo, Fernando, and Marcelo, and to the engineer Daiane. I also want to acknowledge the crucial support from my research colleagues Felipe, Iranildo, Cássio, Nábila, Rennan, Rebecca, Marcello, Natalia Victoria, Thais and Raylane throughout the entire project.

Finally, I would like to thank my colleagues from Belgo Bekaert Gelmo, Daniel for their constant support.

This work was carried out with the support of the Carlos Chagas Filho Foundation for Research Support of the State of Rio de Janeiro (FAPERJ). This doctoral thesis is part of the research project Aneel PD-0394-1905/2019 (Furnas – PUC-Rio): *Determinação de parâmetros para ensaios mecânicos do concreto reforçado com fibras sob condições extremas de carregamento em empreendimentos de geração hidrelétrica e eólica*. This study was financed in part by the Coordenação de Aperfeiçoamento de Pessoal de Nível Superior – Brasil (CAPES) – Finance Code 001.

Abstract

Moreira de Alencar Monteiro, Vitor; de Andrade Silva, Flávio (Advisor); Carlos Taissum Cardoso, Daniel (Co-Advisor). **Mechanical behavior and damage evolution of fiber reinforced concrete under flexural fatigue loading for structural applications**. Rio de Janeiro, 2023. 234 p. Tese de Doutorado – Departamento de Engenharia Civil e Ambiental, Pontifícia Universidade Católica do Rio de Janeiro.

This doctoral thesis originates from the research project Aneel PD-0394-1905/2019, carried out through a collaboration between Furnas and PUC-Rio. The main objective of this extensive research project is the development of fiber reinforced concrete for distinct structural application which are subjected to continuous flexural fatigue loading along their useful life, such wind tower endeavors, concrete pavements and bridge elements. The addition of fibers in the concrete mix has the potential to mitigate the mechanical deterioration along the continuous load cycles, enhancing, as a consequence, the durability and the fatigue life of the cited concrete structural elements. Throughout this doctoral thesis, the mechanical degradation of fiber reinforced concrete under fatigue is carefully analyzed, starting from the fiber scale with pull-out tests and going up to the structural scale through large-scale fatigue mechanical tests. The first stage of this study involves an analysis of the mechanical behavior of fiber reinforced concrete under fatigue loading. The material fatigue life is examined using different statistical models, which allow evaluating material failure based on a failure probability. Fatigue pull-out tests help explain, at the fiber-matrix interface scale, how the prisms rupture under cyclic loading. A second phase of this work demonstrates the mechanical degradation of reinforced structural beams under fatigue and the impact of fiber addition on key concerned parameters. The addition of fiber reinforcement causes a redistribution of stresses in the tension zone of the structural element, reducing the deformations of the longitudinal rebar and mitigating the mechanical degradation of reinforced concrete in terms of curvature, displacement and stiffness. Furthermore, fiber addition significantly improves the bond between the steel bar and the surrounding concrete matrix, a key factor in explaining the enhanced mechanical response of the structure under fatigue, as studied in this doctoral thesis through rebar pull-out tests. Finally, a new analytical solution was developed to assess the mechanical degradation of fiber reinforced concrete prisms under fatigue loads. The proposed analytical curves successfully fit the experimental results analyzed in this work. The addition of fibers showed great potential in reducing the mechanical degradation of reinforced concrete structures subjected to cyclic loading. The stress redistribution in the tension zone, caused by the fibers, promotes greater stiffness of the structure under fatigue, improves the bond with the reinforcement and enhances the ability to withstand fatigue cycles over time. Therefore, the observed enhancement of mechanical properties through fiber reinforcement can ensure a longer service life for reinforced concrete structures.

Keywords:

Fiber reinforced concrete; Fatigue; Mechanical degradation; Analytical models; Reinforced concrete structures.

Resumo

Moreira de Alencar Monteiro, Vitor; de Andrade Silva, Flávio (Orientador); Carlos Taissum Cardoso, Daniel (Coorientador). **Comportamento Mecânico e Análise da Evolução do Dano em Concreto Reforçado com Fibras sob Fadiga à Flexão para Aplicações Estruturais**. Rio de Janeiro, 2023. 234 p. Tese de Doutorado – Departamento de Engenharia Civil e Ambiental, Pontifícia Universidade Católica do Rio de Janeiro.

A presente tese de doutorado tem como origem o projeto de pesquisa Aneel PD-0394-1905/2019, realizado a partir de uma colaboração entre Furnas e PUC-Rio. A principal meta desse grande projeto de pesquisa está no desenvolvimento do concreto reforçado com fibras visando sua aplicação em elementos estruturais que estão submetidos à fadiga na flexão ao longo de toda sua vida útil, como torres eólicas, pavimentos e elementos de pontes. Dessa maneira, ao longo de todo essa tese doutorado, a degradação mecânica do concreto reforçado com fibras sob fadiga é analisada em detalhe desde a escala da fibra em ensaios de arrancamento até a escala estrutural através de testes mecânicos de fadiga em larga escala. A primeira etapa desse estudo traz uma análise do comportamento à fadiga do concreto reforçado com fibras. A vida à fadiga desse material é estudada através de diferentes modelos estatísticos, que garantem avaliar a falha do material baseada em uma probabilidade falha. Já os ensaios de fadiga no arrancamento ajudam a explicar na escala interface fibra-matriz como ocorre a ruptura dos prismas sob carregamentos cíclicos. Uma segunda fase desse trabalho mostra a degradação mecânica de vigas armadas sob fadiga e o impacto da adição de fibras nos principais parâmetros de interesse. A adição do reforço fibroso é responsável por causar uma redistribuição de tensões na zona tracionada do elemento estrutural, diminuindo as deformações da armadura longitudinal e amenizando a degradação mecânica do concreto armado em termos de curvatura, deslocamento e rigidez. Além disso, a adição de fibras também é responsável por incrementar significativamente a aderência da barra de aço ao redor da matriz de concreto. Fator chave para explicar a melhora da resposta mecânica da estrutura sob fadiga e estudada nessa tese de doutorado através dos ensaios de arrancamento da barra aço. Por fim, uma nova solução analítica foi desenvolvida para avaliar a degradação mecânica dos prismas de concreto reforçado com fibras sob fadiga. As curvas analíticas propostas se adequaram de forma bem sucedida os resultados experimentais analisados nesse trabalho. A adição de fibras apresentou grande potencial visando uma diminuição da degradação mecânica das estruturas de concreto armado submetidas a carregamentos cíclicos. A redistribuição de tensões na zona tracionada devido às fibras promove uma maior rigidez da estrutura sob fadiga, uma melhora da aderência da armadura e uma maior capacidade de resistir aos ciclos de fadiga ao longo do tempo. Esse ganho mecânico com o reforço fibroso, portanto, pode garantir maior vida útil das estruturas em concreto armado.

Palavras-chave

Concreto reforçado com fibras; Fadiga; Degradação mecânica; Modelos analíticos; Concreto armado.

Table of contents

Aknowledgements 4

Abstract 6

Resumo 8

1 Introduction 23

1.1. Motivation 23
1.2. Objectives 25
1.3. Thesis structure 25
1.4. References 27

2 Literature review 28

2.1. Mechanical response of fiber reinforced concrete under cyclic loadings 28
2.1.1. Cyclic behavior in compression 28
2.1.2. Cyclic behavior in bending 30
2.1.3. Cyclic behavior in structural elements 31
2.2. Fatigue response of fiber reinforced concrete 39
2.3. Damage evolution models of fiber reinforced concrete subjected to cyclic loadings 48
2.4. References 54

3 Mechanisms of fiber-matrix interface degradation under fatigue in steel FRC 62

3.1. Introduction 63
3.2. Experimental program 65
3.2.1. Materials 65
3.2.2. Mixing procedure 66

3.3. Test Program 67
3.3.1. Static pullout test 67
3.3.2. Fatigue test 68
3.4. Discussion and analysis 69
3.4.1. Steel fiber pullout behavior 69
3.4.2. Steel fiber-reinforced concrete matrix interface failure under fatigue loading 72
3.4.3. Slip evolution under fatigue 79
3.5. Conclusions 82
3.6. References 84

4 A novel methodology for estimating damage evolution and energy dissipation for steel fiber reinforced concrete under flexural fatigue loading 88

4.1. Introduction 89
4.2. Experimental program 91
4.2.1. Materials 91
4.2.2. Mixing procedure 93
4.3. Test program 93
4.3.1. Monotonic three-point bending tests 93
4.3.2. Fatigue tests 94
4.4. Methodology for estimating SFRC degradation under fatigue 97
4.5. Discussion and analysis 98
4.5.1. Influence of steel fibers on fatigue life (uncracked specimens) 98
4.5.2. Fatigue life analysis (pre-cracked specimens) 101
4.5.3. Evolution of crack mouth opening displacement (CMOD) 109
4.5.4. Mechanical degradation under fatigue loading: stiffness decay and energy release 111
4.5.5. Damage evolution and energy release growth rate models 114
4.6. Conclusions 116
4.7. References 119

5 The influence of steel fibers on the bond-slip behavior between rebars and concrete: experimental and analytical investigation 123

5.1. Introduction 125
5.2. Experimental program 127
5.2.1. Materials 127
5.2.2. Concrete mixing procedure 129
5.2.3. Test program 130
5.3. Analytical model 134
5.3.1. Rebar pull out equations 135
5.3.2. Bond-slip behavior in elastic stage (I) 136
5.3.3. Bond-slip behavior in nonlinear stage (II) 137
5.3.4. Bond-slip behavior in dynamic stage (III) 138
5.3.5. Pull out model application algorithm 139
5.4. Discussion and analysis 140
5.4.1. Bond under quasi-static pull out tests 140
5.4.2. Analytical model 146
5.4.3. Bond under fatigue pull out tests 153
5.5. Conclusions 159
5.6. References 161

6 Closed-form solutions for flexural fatigue mechanical degradation of steel fiber reinforced concrete beams 166

6.1. Introduction 168
6.2. Model development 170
6.2.1. Closed-form solution for moment-curvature response 170
6.2.2. Fracture parameter equations 175
6.2.3. Flexural fatigue degradation 178
6.2.4. Discussion and analysis for the model application 181
6.3. Conclusions 192
6.4. References 194

7 On the mechanical degradation of R/SFRC beams under flexural fatigue loading 199

7.1. Introduction 200
7.2. Experimental program 203
7.2.1. Mix composition and material characterization 203
7.2.2. Mixing procedure 205
7.2.3. Test program 205
7.3. Discussion and analysis 210
7.3.1. Quasi-static mechanical response 210
7.3.2. Fatigue mechanical degradation 212
7.3.3. Crack opening oscillation under fatigue loading 221
7.3.4. Fatigue life of R/SFRC beams 224
7.4. Conclusions 226
7.5. References 228

8 Final conclusions 233

List of figures

Figure 1.1 – Fatigue load spectra categories 24

Figure 2.1 - Ideal schematic of cyclic loading process of concrete specimen. 29

Figure 2.2 – Test setup applied by Huang *et al.* [48]. 33

Figure 2.3 – Test procedure applied by Huang *et al.* [48]. 34

Figure 2.4 – Illustrative lateral load per displacement response [48]. 34

Figure 2.5 – Main phenomenological aspects of cyclic and fatigue behavior of concrete: (a) dissipative mechanism, (b) hysteretic loops, (c) fatigue creep curves, (d) Wöhler curves and (e) loading sequence effect. 41

Figure 2.6 – Fatigue loading history a applied by Carlesso *et al.* [83]. 42

Figure 2.7 – Typical CMOD rate under fatigue loading [87]. 43

Figure 2.8 – Typical cyclic stress-strain curve and the corresponding damage evolution of concrete in compression. 51

Figure 2.9 – Schematic drawing showing the propagation of a crack of fiber reinforced concrete under cyclic compression. 53

Figure 3.1 - Details of the pullout specimen molding: (a) fabrication and (b) specimen dimensions in mm. 67

Figure 3.2 - Pullout test setup: (a) test illustration, (b) pullout test setup overview and (c) LVDT positioning detail. 68

Figure 3.3 – Fatigue test program 69

Figure 3.4 - Pullout test results: (a) pullout behavior of SF1 and SF2 and (b) pre-slip curves before fatigue test initiation. 71

Figure 3.5 - Typical pullout response for straight and hooked-end steel fibers 71

Figure 3.6 - Observed failure modes in terms of load level S ($\%P_{max}$) for applied fatigue tests. 73

Figure 3.7 - Hooked-end steel fiber (SF1) pullout under fatigue loading: (a) pre-slip and (b) hysteresis cycles under fatigue. 74

Figure 3.8 - Fiber failure images after fatigue test with Scanning Electron Microscope: (a) fiber hook straightening after pullout and (b) fiber cross-section after rupture. 74

Figure 3.9 - Stress amplitude in terms of the number of cycles until failure for fiber rupture under pullout fatigue tests. Comparison with 0.15%C, 60Si2Mn and 54SiCr6 steels from distinct authors. 76

Figure 3.10 - Fiber rupture after fatigue test: (a) CT-scan image with the remaining hook inside the pullout specimen, (b) fiber cross-section after rupture and (c) pullout specimen. 77

Figure 3.11 - Straight steel fiber (SF2) pullout under fatigue loading: (a) pre-slip and (b) hysteresis cycles under fatigue. 78

Figure 3.12 - Slip evolution for (a) different failure modes, (b) pullout failure under distinct pre-slips and (c) empirical models 79

Figure 3.13 - Fatigue slip evolution under distinct failure under: (a) pullout failure and (b) fiber rupture. 81

Figure 4.1 - Test setup: (a) specimen dimensions for monotonic and dynamic three-point bending tests (EN 14651 [29]) and (b) setup image. Dimensions in mm 94

Figure 4.2 - Fatigue test program for (a) uncracked and (b) pre-cracked specimens 96

Figure 4.3 - Proposed methodology for estimating FRC mechanical degradation through EN 14651 [29] bending test 98

Figure 4.4 - Number of cycles until failure for uncracked plain and steel fiber reinforced concrete under fatigue. Load level of 70% applied (*S = 70%*). 100

Figure 4.5 - Fatigue lifetime curve S-N for pre-cracked FRC 101

Figure 4.6 - Weibull distribution (pre-cracked FRC) for the studied load levels (70%, 80% and 90%): (a) Representation of the fatigue results in Gumbel distribution including the model parameters and (b) Weibull cdfs of lifetimes for the (a) results 104

Figure 4.7 - Fatigue life of pre-cracked steel fiber reinforced concrete through two parameter Weibull distribution 106

Figure 4.8 - Development of the three parameter Weibull distribution: (a) relation between the variable V as a function of the normalized survivorship function and (b) fatigue life of pre-cracked steel fiber reinforced concrete through three parameter Weibull distribution 108

Figure 4.9 - CMOD evolution of all studied load level (90%, 80% and 70% of the $P_{0.50mm}$) in accordance with (a) number cycles (n) and (b) referred load cycle number (n/N). 110

Figure 4.10 - Comparison between typical (a) cyclic creep curve and (b) CMOD per load curves. 111 111

Figure 4.12 - Fatigue test on the FRC composite C40SF: (a) specimen pre-crack until reaching 0.50 mm of CMOD and (b) material degradation throughout the fatigue loading 112

Figure 4.12 - Mechanical deterioration of steel fiber reinforced self-consolidating concrete under distinct load levels (70%, 80% and 90%): (a) stiffness decay and (b) energy release across n/N. 113

Figure 4.13 - Linear correlation between (a) initial stiffness and (b) initial energy release with residual strength $f_{R,1}$ 113

Figure 4.14 - Damage evolution: (a) experimental results and (b) mean points and damage model in terms of *n/N*. the vertical bars represents the standard deviations. 115

Figure 4.15 - Energy release growth rate along *n/N*: (a) experimental results for distinct load levels (70%, 80% and 90%) and (b) proposed model 116

Figure 5.1 - Pull out specimen details: (a) specimen molding and (b) dimensions. 131

Figure 5.2 - Pull out test setup: (a) test photo and (b) test illustration. 131

Figure 5.3 - Pull out fatigue test experimental procedure: (a) sinusoidal cyclic loading in 6 Hz of frequency and (b) loading variation in relation slip evolution. 131

Figure 5.4 - Bond-slip behavior for rebar pull out from concrete matrix: (a) global load-slip response and (b) local shear strength distribution along the slip. 134

Figure 5.5 - Pull out model geometrical properties. 136

Figure 5.6 - Shear stress and force distribution along the rebar: (a) stage I (elastic behavior), (b) stage II (nonlinear behavior) and (c) dynamic response with incremental sliding. 137

Figure 5.7 - Mean bond slip curves for studied plain and steel fiber reinforced concrete specimens. 140

Figure 5.8 - Proposed regression models for bond strength in accordance with (a) the fiber fraction (λ) and (b) flexural residual strength ($f_{R,1}$). 142

Figure 5.9 - Typical bond stress-slip curve illustrating the studied bond parameters.

Figure 5.10 - Secant stiffness (K_b) in terms of fiber factor (λ). 144

Figure 5.11 - Bond toughness regression models for (a) T_{peak} and (b) T_{4mm}. 145

Figure 5.12 – Observed pull out failure after the mechanical test 146

Figure 5.12 - Model application for the experimental results achieved in present research in terms of the following fiber factors (λ): (a) 0.11, (b) 0.22, (c) 0.33, (d) 0.44 and (e) 0.55. 147

Figure 5.13 - Model application for pull out experimental data carried on by (a-c) Chu *et al.* [25], (d-f) Huang *et al.* [41] and (g-i) Varona *et al.* [6]. 149 149

Figure 5.14 - Model application for pull out experimental data carried on by (a-c) Li *et al.* [42] and (d-f) Liang *et al.* [43]. 150

Figure 5.15 - Comparison between the shear stress used on the analytical model with the shear stress from the empirical formulation. 151

Figure 5.17 - Slip evolution under fatigue pull out loading for plain and steel fiber reinforced concrete specimens: (a) results for plain concrete under distinct load levels (S), (b) slip increase for C0SF and C0.22SF under the same load range (1.50 kN < P < 5.0 kN) and (c) fatigue results for C0SF in accordance to the referred number load cycle (n/N). 154

Figure 5.18 - Overall description of the proposed model for fatigue pull out 155

Figure 5.19 - Application slip evolution model for plain concrete under distinct load levels (*S*): results for slip per cycles and (b) slip per normalized load cycle. 157

Figure 5.20 - Application slip evolution model for plain concrete under distinct load levels (*S*) for (a) and (b) Lindorf *et al.* [39] in (a) and (b) and for Rehm *et al.* [66] in (c) and (d). 158

Figure 6.1 - Constitutive relations for FRC: (a) tensile and (b) compressive responses. 172

Figure 6.2 - Stress-strain distribution along the beam height. 173

Figure 6.3 - Stress distribution based on linearized strain at different stages. 174

Figure 6.4 - Model geometrical parameters: (a) three-point bending test geometrical parameters and (b) application of the characteristic length (L_p) on the closed-form solution model. 178
Figure 6.5 - Model workflow from defining the FRC quasi-static response until its mechanical degradation under flexural fatigue. 180
Figure 6.6 - Constitutive models for the different FRCs from Monteiro et al [23], Carlesso *et al.* [19] and Stephen *et al.* [21]: (a), (b) and (c) tension and (d), (e) and (f) compression models. 181
Figure 6.7 - Moment-curvature response for (a) Monteiro *et al.* [23], (b) Carlesso *et al.* [19] and (c) Stephen *et al.* [21] studied FRCs. 182
Figure 6.8 - Load-CMOD response for (a) Monteiro *et al.* [23], (b) Carlesso *et al.* [19] and (c) Stephen *et al.* [21]. 183
Figure 6.9 - Quasi-static response for the fracture parameters crack length and stress intensity factor for (a) Monteiro *et al.* [23], Carlesso *et al.* [19] and (c) Stephen *et al.* [21]. 184
Figure 6.10 - S-N curves for the distinct studied FRCs under fatigue flexural by Monteiro *et al.* [23], Carlesso *et al.* [19] and (c) Stephen *et al.* [21]. 185
Figure 6.11 - CMOD evolution under flexural fatigue and the application of the proposed empirical model for (a) Monteiro *et al.* [23], (b) Carlesso *et al.* [19] and (c) Stephen *et al.* [21]. 186
Figure 6.12 - Fatigue CMOD evolution after material pre-crack for the FRCs by (a) Monteiro *et al.* [23], Carlesso *et al.* [19] and Stephen *et al.* [21]. 187
Figure 6.13 - FRC mechanical degradation under flexural fatigue in terms of (a) crack length increase, (b) normalized strain parameter (β), (c) tensile strain, (d) curvature and (e) residual flexural stress for Monteiro *et al.* [23]. 189
Figure 6.14 - FRC mechanical degradation under flexural fatigue in terms of (a) crack length increase, (b) normalized strain parameter (β), (c) tensile strain, (d) curvature and (e) residual flexural stress for Carlesso *et al.* [19]. 190
Figure 6.15 - FRC mechanical degradation under flexural fatigue in terms of (a) crack length increase, (b) normalized strain parameter (β), (c) tensile strain, (d) curvature and (e) residual flexural stress for Stephen *et al.* [21]. 191

Figure 7.1 - Structural tests setup illustration: (a) beam reinforcement configuration and strain gauge positions and (b) tests setup with LVDTs disposal. Dimensions in mm. 206
Figure 7.2 – Structural test setup photo. 207
Figure 7.3 - Fatigue test program: (a) test stages (pre-crack and fatigue loading) and (b) loading oscillation based on a sine function. 208
Figure 7.4 - Digital image correlation system: (a) spackle pattern on the beam surface and (b) camera and lights position. 209
Figure 7.5 - Monotonic structural bending tests results: (a) force x deflection, (b) moment x curvature. Cracking response after rebar yielding for (c) C0SF and (d) C40SF. 212
Figure 7.6 - Fatigue longitudinal rebar strain evolution, quasi-static and pre-crack results for (a) C0SF and (b) C40SF under the same fatigue loading range. 214
Figure 7.7 - Fatigue longitudinal rebar strain evolution under fatigue loading for C0SF and C40SF under distinct loading ranges. 214
Figure 7.8 - Beam deflection evolution, quasi-static and pre-crack results for (a) C0SF and (b) C40SF under the same fatigue loading range. 216
Figure 7.9 - Beam deflection evolution under fatigue loading for C0SF and C40SF under distinct loading ranges. 216
Figure 7.10 - Beam curvature evolution, quasi-static and pre-crack results for (a) C0SF and (b) C40SF under the same fatigue loading range. 218
Figure 7.11 - Beam curvature evolution under fatigue loading for C0SF and C40SF under distinct loading ranges. 219
Figure 7.12 - Illustration for beam stiffness calculation for each cycle. 220
Figure 7.13 - Beam stiffness evolution under fatigue loading for C0SF and C40SF under distinct loading ranges. 221
Figure 7.14 - Application of the DIC analysis to verify the crack opening variation along the fatigue cycles during a 5 s time frame: (a) maximum observed crack opening during the load cycles at the cycle number 500,000 and (b) failure surface at the end the fatigue test. 222
Figure 7.15 - Crack opening variation for the cycle number 500,000 C0SF and C40SF under distinct loading ranges. 223

Figure 7.16 - Fatigue life of reinforced concrete beams under fatigue loading as a function of the rebar stress range. 224

List of tables

Table 2.1 – Overview from mechanical response of fiber reinforced concrete under cyclic loadings main results. 37

Table 2.2 – Overview from fatigue response of fiber reinforced concrete main results. 46

Table 3.1 - Mix composition of self-consolidating concrete matrix66 66

Table 3.2 – Steel fiber properties 67

Table 3.3 - Results for fiber-matrix interface degradation under fatigue loading 75

Table 3.4 - Fatigue test results for fiber rupture under pullout fatigue 78

Table 4.1 - Mix composition of matrix and steel fiber reinforced self-consolidating concrete 92

Table 4.2 - Experimental mean results of peak and post-peak parameters for monotonic three-point bending tests in accordance with EN 14651 [29]. Standard deviation values presented in parentheses 99

Table 4.3 - Fatigue tests results on uncracked steel fiber self-consolidating concrete specimens 100

Table 4.4 - Fatigue tests results on pre-cracked steel fiber self-consolidating concrete specimens 102

Table 4.5 - Main parameters evaluated for the applied Weibull distribution 103

Table 5.1 – Mix composition of self-consolidating concrete matrix 128

Table 5.2 – Steel fiber properties 129

Table 5.3 – Post-peak parameters for monotonic three-point bending tests in accordance with EN 14651 [41] standard. Standard deviation values presented in parentheses. 130

Table 5.4 - Mean results of obtained from the pull out tests. Standard deviations are presented in parentheses. 141

Table 5.5 - All used geometrical and material parameters used to fit the proposed model on the experimental results. 152

Table 5.6 - Slip evolution under fatigue pull out loading experimental parameters. Standard deviation presented in parentheses. 154

Table 5.7 – Slip evolution model parameters used for each author in this research 157
Table 6.1 - Description of each stage for the quad-linear model 175
Table 6.2 - The complete solutions in accordance with the proposed constitutive model 176
Table 6.4 - List of used parameters for the analysis of the quasi-static FRC response for each author 177
Table 7.1 – Mix composition of the self-consolidating concrete 203
Table 7.2 – Steel fiber properties 204
Table 7.3 - Post-peak parameters for monotonic three-point bending tests in accordance with EN 14651 [41] standard. Standard deviation values presented in parentheses. 204
Table 7.4 - Overall results for structural beams under quasi-static flexural loading 211
Table 7.5 - Structural beam fatigue test results. 215
Table 7.6 - Collected fatigue life data for plain and steel fiber reinforced concrete structural beams under fatigue loading 225

1 Introduction

1.1. Motivation

Fiber reinforced concrete (FRC) members have been extensively used in applications exposed to cyclic loadings, which include from precast tunnel segments [1-2] and concrete pavements [3] to wind tower rings [4] and offshore structures [5]. In general, FRC structures are subjected to fatigue loadings in the form of wind or wave action, thermal variations, traffic loading and machine vibrations, which are responsible for producing tensile stresses that can lead to crack initiation and propagation [6]. With damage accumulation and crack growth, the material performance eventually reduces in terms of strength, stiffness and toughness [7].

In general, the S-N field is divided in three major regions related to the lifetime: low-cycle, high-cycle and very-high cycles fatigue domains. The type of fatigue is distinguished by its number of cycles, as shown by Göransson et al. [8]. Up to 10^3 cycles, it is categorized as low-cycle fatigue, such as structures subjected to earthquakes or to storm. For a number of cycles between 10^3-10^7, classification as high-cycle fatigue is applied. The last category is super-high-cycle fatigue with more than 10^7 cycles. Figure 1.1 summarizes fatigue load spectra and examples of structures subjected to flexural fatigue loading.

In general, the proposed design guidelines address the fiber contribution on the post-crack strength through flexural data obtained from beam tests such as three point bending tests by EN 14651 [9] and four point bending tests in accordance with ASTM C1609 [10]. The mentioned standards reach the tensile stress-strain relation from the load capacity at certain deflections or crack mouth opening displacements. However, present guidelines and analytical models still do not incorporate the effects of long-term and fatigue degradation along the time. The present equations on the Model Code [11], for instance, only account for empirical equations for deformation evolution under compression. When it comes to flexural fatigue, little can be found in the literature on how to incorporate the mechanical decay on the stress-strain models.

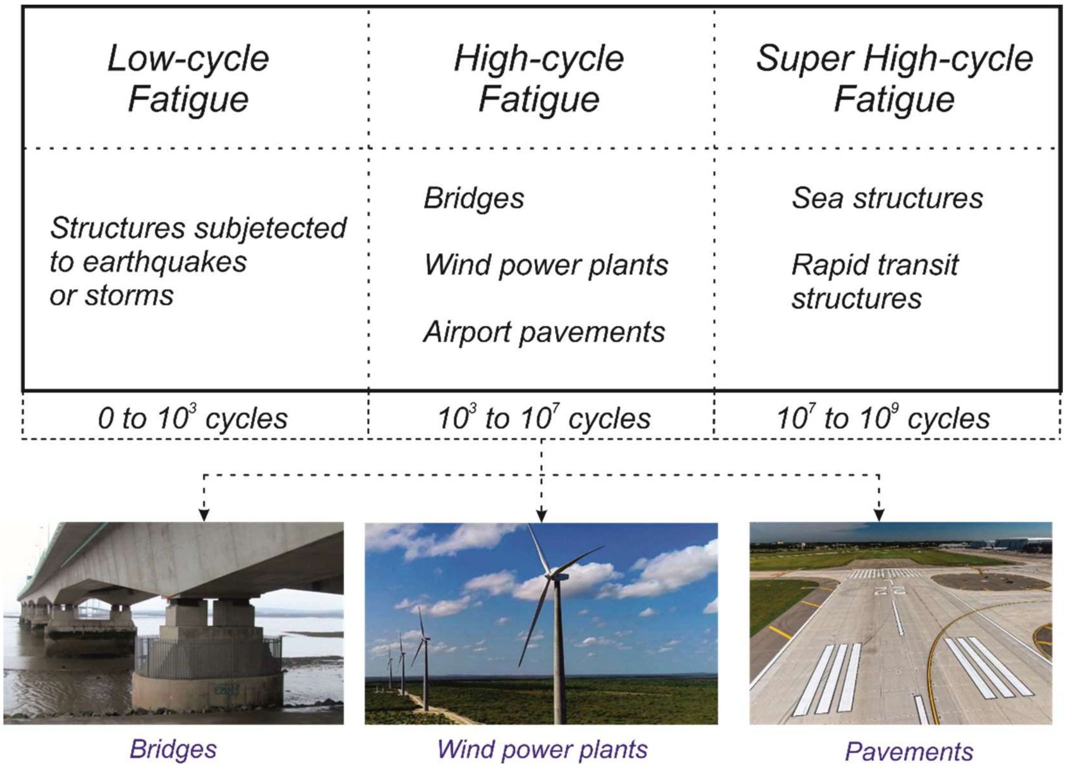

Figure 1.1 – Fatigue load spectra categories

Among the major concerns on reinforced concrete structures under cyclic loading is associated to crack evolution and mechanical deterioration along its useful life. Cracks on concrete provide a pathway for aggressive chemicals to reach the steel reinforcement and accelerate concrete deterioration [12, 13]. Moreover, durability and long-term performance can be compromised due to the mechanical deterioration promoted by flexural fatigue loading, causing expensive maintenance and undesirable downtime. Therefore, most recent studies have trying to address the potential use of fibers in controlling crack increase for beams subjected to repetitive loading. Fiber reinforcement can give not only considerably increased resistance to cracking, but also much greater toughness over plain concrete [14].

This research seeks to evaluate the influence of steel fibers on the flexural fatigue mechanical response and damage evolution of fiber reinforced concrete. This research thesis aims to bring a broad study on the fatigue of FRC, encompassing the analysis on the fiber, material and structural levels. Therefore, the degradation can be analyzed from the fiber-matrix interface until the level of reinforced concrete structures. This study also involves the development of the use of analytical equations to verify mechanical degradation and the experimental analysis of the fatigue degradation of rebar pullout from FRC matrixes.

Present work is part of the cooperation project Aneel PD-0394-1905/2019 (Furnas – PUC-Rio). At the moment, the Furnas engineer staff is prominently working on the technical management of the current wind power plants and is carrying the current research project to verify the inclusion of fibers on the future wind power endeavors. Part of this research was carried on at the Arizona State University under supervision of Barzin Mobasher.

1.2. Objectives

The main objective of this work is to assess the mechanical degradation of fiber reinforced concrete. A 50 MPa steel fiber reinforced concrete (SFRC) selected aiming its use for wind tower applications. The present research brings a complete overview of the fatigue degradation of fiber reinforced concrete, encompassing fiber, material and structural levels. In order to study the mechanical degradation under fatigue of SFRC, secondary goals were drawn as follows:

- Analysis of the mechanisms of fiber-matrix interface degradation under fatigue loading;
- Development of novel methodologies to estimate damage evolution in FRC under flexural fatigue loading;
- The influence of steel fibers on the bond-slip behavior between rebars and concrete;
- Application of closed-form solutions for flexural mechanical degradation of FRC;
- Study of the mechanical degradation of R/SFRC beams under fatigue loading.

1.3. Thesis structure

The thesis is composed of the present introduction, a literature review, followed by five chapters structured as individual full papers and final conclusions, as follows:

- **Chapter 1:** The introduction presents the motivation, objectives and the structure of the study.
- **Chapter 2:** The literature review brings past works on cyclic behavior of fiber reinforced concrete. It encompasses the fatigue analysis in the structural and material levels.
- **Chapter 3:** This chapter brings the results for the analysis of the mechanisms of fiber-matrix interface degradation under fatigue in steel FRC.
- **Chapter 4:** The results for the mechanical degradation of FRC under flexural fatigue loading takes place in chapter 4. It is also possible to verify the proposed novel methodologies for damage evolution under fatigue loading in this section.
- **Chapter 5:** The influence of steel fibers on the bond-slip behavior between rebars and concrete is presented in chapter 5. This section encompasses both the analytical equations of bond tests and the interface degradation under fatigue loading.
- **Chapter 6:** This section focus primarily on the development of closed-form solutions for flexural fatigue mechanical degradation of SFRC specimens. The complete description and applications of the equations is presented in this section.
- **Chapter 7:** Present section applies all studied fatigue parameters to verify the mechanical degradation of R/SFRC beams under flexural fatigue loading. This work verifies the mechanical degradation in terms of the rebar strain evolution, curvature increase and stiffness deterioration along the fatigue cycles.
- **Chapter 8:** Finally, the last section brings the overall conclusions of the present thesis.

1.4. References

1 CONFORTI, A. TIBERTI, G. PLIZZARI, G. CARATELLI, A. MEDA, A. Precast tunnel segments reinforced by macro-synthetic fibers. **Tunnelling and Underground Space Technology**, vol. 63, p. 1-11, 2017.

2 LIAO, L. DE LA FUENTE, A. CAVALARO, S. AGUADO, A. Design procedure and experimental study on fibre reinforced concrete segmental rings for vertical shafts. **Materials and Design**, vol. 92, p. 590-601, 2016.

3 BELLETTI, B. CERIONI, R. MEDA, A. PLIZZARI, G. Design aspects on steel fiber-reinforced concrete pavements. **Journal of Materials in Civil Engineering**, vol. 20, p. 599-607, 2008.

4 SRITHARAN, S. SCHMITZ, G. **Design of tall wind turbine towers utilizing UHPC**. In: RILEM-fib-AFGC International Symposium on Ultra-High Performance Fibre-Reinforced Concrete, 2013.

5 HOLMEN, J. Fatigue design evaluation of offshore concrete structures. **Matériaux et Construction** (1984), vol. 17, p. 39-42, 1984.

6 AGLAN, H. FIGUEROA, J. Damage-evolution approach to fatigue cracking in pavements. **Journal of Engineering Mechanics**, vol. 119, p. 1243-1259, 1993.

7 SUBRAMANIAM, K. GOLDSTEIN, G. POPOVICS, J. SHAH, S. fatigue response of concrete subjected to biaxial fatigue in the compression-tension region. **ACI Materials Journal**, vol. 96, p. 663-669, 1999.

8 GÖRANSSON, F. NORDENMARK, A. **Fatigue assessment of concrete foundations for wind power plants**. MSc dissertation, 142 p. Göteborg, Sweden: Chalmers University of Technology, 2011.

9 EUROPEAN COMMITTEE FOR STANDARDIZATION. **EN 14651**. Test method for metallic fibre concrete – Measuring the flexural tensile strength (limit of proportionality (LOP), residual), 2005.

10 AMERICAN SOCIETY FOR TESTING AND MATERIALS. **ASTM C1609**. Standard Test Method for Flexural Performance of Fiber-Reinforced Concrete (Using Beam With Third-Point Loading), 2019.

11 INTERNATIONAL FEDERATION FOR STRUCTURAL CONCRETE. **CEB-FIB**. International Recommendations for the Design and Construction of Concrete Structures, 2010.

12 SHI, X. XIE, N. FORTUNE, K. GONG, J. Durability of steel reinforced concrete in chloride environments: An overview. **Construction and Building Materials**, vol. 30, p. 125-138, 2012.

13 BERROCAL, C. FERNANDEZ, I. LUNDGREN, K. LÖFGREN, I. Corrosion-induced cracking and bond behaviour of corroded reinforcement bars in SFRC. **Composites Part B**, vol. 113, p. 123-137, 2017.

14 THE CONCRETE CENTER, **Concrete towers for onshore and offshore wind farms: conceptual design studies**, 2005.

2 Literature review

2.1. Mechanical response of fiber reinforced concrete under cyclic loadings

2.1.1. Cyclic behavior in compression

A deep understanding of the cyclic characteristics of structural materials is a key step in developing new materials and structural systems, especially when it comes for the construction of wind towers. To date, considerable efforts have been made to investigate the mechanical behavior of plain and fiber reinforced concretes under compressive cyclic loading conditions [1-26]. Most of the research works involve the mechanical response of the composite with the addition of fibers on the mix and when confined by fiber reinforced polymers systems under cyclic compression.

Macro-strain, strength, elastic stiffness and dissipated energy have been the main used cyclic mechanical parameters for the characterization of the damage index [8, 10, 11]. Those parameters are obtained from cyclic stress-strain curves, which consist of two distinct paths: unloading and reloading paths. As explained by Xu *et al.* [12], the unloading path is curvilinear characterized by a progressively diminishing slope, until it intersects the strain axis. The reloading path is almost linear from the strain axis until reaching the envelope curve. Significant degradation in elastic stiffness and stress with increasing cycles can be observed through cyclic tests curves, caused by crack propagation and damage accumulation [12]. An illustration of the compressive cycle process of concrete is shown in Figure 2.1. A similar procedure is applied to bending and direct tension cyclic test.

External confinement has been generally applied in order to mitigate the concrete deterioration with the cycles of loading and unloading cycles [13-19, 22, 23]. Bai *et al.* [19], for instance, studied the cyclic compressive behavior of confined concrete with large rupture strain (LRS) fiber reinforced polymer (FRP), which enhanced ductility under cyclic compressive loading. Moreover, the energy consumed in each unloading/reloading cycle increases with the plastic axial strain of concrete. Plastic strain is defined as the axial strain on concrete on the unloading path when the stress is unloaded to the zero stress [20, 21].

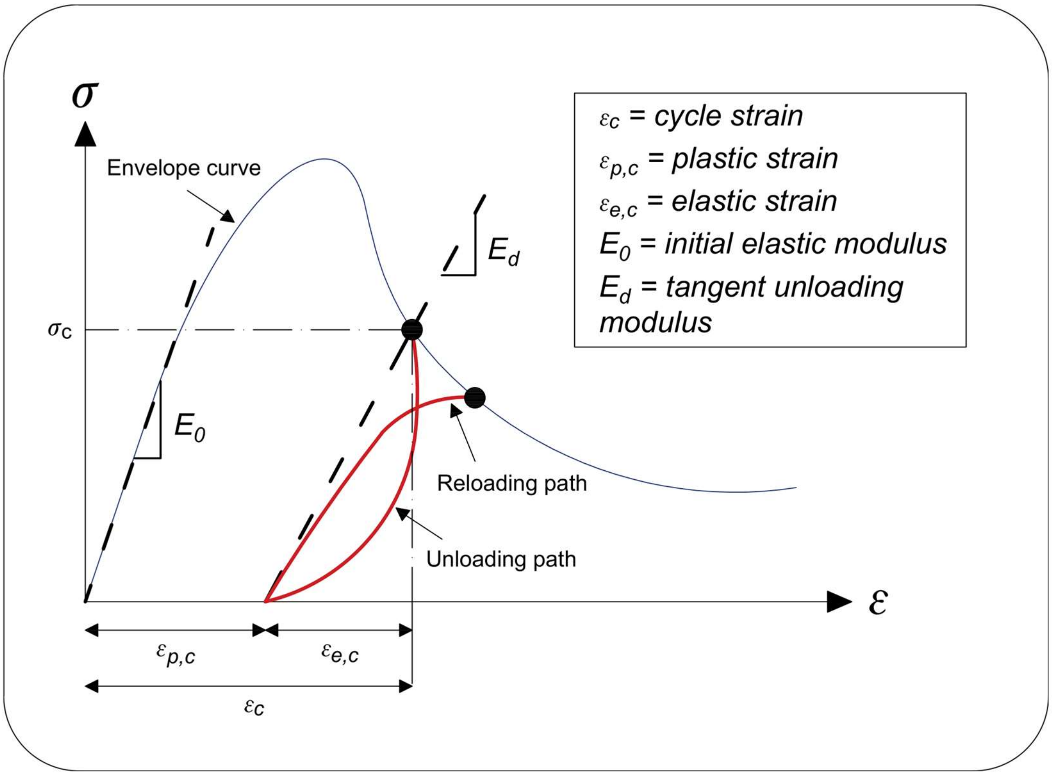

Figure 2.1 - Ideal schematic of cyclic loading process of concrete specimen.

An experimental investigation on the influence of parameters such as confinement level, aspect ratio, unconfined concrete compressive strength and corner radius on the behavior of concrete prisms confined with FRP under cyclic loading was carried out by Abbasnia *et al.* [22]. While authors concluded that the plastic strain decreases with an increase in unconfined strength, the other studied characteristics showed almost no influence on the stress deterioration ratio. Lam *et al.* [23] also adds that the frequency of unloading/reloading cycles have little effect on the envelope curve of stress-strain responses of FRP-confined concrete.

Fibers also play a key role when it comes to the reduction of the concrete mechanical parameters degradation [12, 23-24]. Xu *et al.* [12] studied the influence of different types and volume fractions of polypropylene (PP) fibers on the concrete mix. It was possible to verify that PP fiber has a positive effect on the cyclic compressive stress-strain behavior of concrete due to fiber crack arresting and bridging effect, especially on the post-cracking branch. Although PP and other synthetic [24] fibers has little influence on the plastic strain accumulation, it improves the dissipated capacity and enhance the performance in terms of post-peak stiffness and strength.

Similar results were reported for the addition of different types and volume fractions of steel fibers by different authors [25, 26]. However, compared to the addition of PP fibers and plain concrete, steel fiber reinforced concrete can lead to a significant decrease in plastic strain. The cyclic stress-strain behavior is insensitive to the fiber aspect ratio. The high quantities of fibers improve the distribution of the carrying stresses retaining the frictional slip.

2.1.2. Cyclic behavior in bending

Similar research to assess the cyclic behavior of plain and fiber reinforced concrete in compression has also been carried up for cyclic bending tests [27-31]. The process of cyclic loading and unloading was already explained in section 1.3.1 and Figure 2.1 shows an ideal schematic of the test process.

Smedt *et al.* [27], in turn, studied the effect of cycles of loading and unloading in bending for steel fiber reinforced concrete and obtained damage indicators through acoustic emission activity. It was possible to verify that the largest damage occurs during the peak phase at load cycles before crack mouth opening displacements (CMOD) before 0.50 mm. A higher amount of fibers leads to a slower damage increase whereas a faster damage evolution was verified for the use of double end-hook and larger diameter fibers. The presence of the double hook causes more concrete matrix damage during straightening. After CMOD of 0.50 mm, the plastic CMOD evolution displays a quasi-linear behavior.

As seen through cyclic compression tests, Gonzalez *et al.* [28] observed a progressive reduction of stiffness in bending for FRC. Based on these results, the authors reported that cyclic loads provoke cracking in the fiber-cement paste interface, causing a reduction of fiber-concrete bond, resulting in a reduction of the residual strength. Synthetic fiber reinforced concrete suffered from excessive pullout, preventing crack recovery [29]. The application of hybrid fibers displayed the least residual mid-span displacement, better crack-closure capabilities and a slightly higher flexural strength [29].

The study of improving crack control in wind tower plays a key role when durability and long-term performance of reinforced concrete structures are concerned. Crack growth are directly associated to repetitive cycles of flexural loading and unloading due wind action, thermal variations and traffic loads, for instance. Due to the higher modulus and the stronger bond inside the concrete matrix, steel fibers can better promote crack growth control [32-34] when compared to PP fibers and are more suitable for high tower applications.

However, to address this durability concern, engineered cementitious composites (ECC) – a class of high-performance fiber reinforced cementitious composite (also known as strain hardening cement composites – SHCC) – have been developed based on performance driven design approach (PDDA) [35]. In this study, ECC is proposed to be used as a protective coating on the exterior of concrete wind turbine towers. While reinforced concrete is responsible for providing the required stiffness of the tall structure, ECC is applied in order to ensure crack control and durability performance. Therefore, it requires fewer repairs during its fatigue life since it maintains a constant crack width substantially less than 300 μm.

2.1.3. Cyclic behavior in structural elements

One the most critical drawbacks in currently used steel reinforcement in reinforce concrete structures is its tendency to accumulate plastic deformation under cyclic loads [36]. When it comes to cyclic loadings, structural ductility and energy dissipation capability are two main important features that are sought in dynamic resistant structures. Excessive steel deformation (beyond yielding) in RC moment resisting frames often result in permanent residual drifts, which cause overall capacity degradation.

To tackle this problem, the traditional method is to set closely spaced transverse stirrups, which is able to improve the confinement of concrete at those regions where plastic hinges may possibly develop [36-41]. Well-confined concrete can significantly restrain the opening and propagation of cracks, reducing the strength degradation that consequently improve cyclic performance of RC structures [37-41]. However, relatively large amount of transverse stirrups may result in congestion of reinforcement, as well as increase the difficulties in construction/manufacturing. As FRC demonstrates excellent toughness, energy dissipation capacity and resistance to cracking, more recent research works have sought to verify the effect of the addition of fibers on the cyclic performance of RC structures [42-56].

Huang *et al.* [48] studied the effect of the addition of steel, polypropylene and hybrid fibers on the seismic performance of reinforced concrete columns. Concrete columns specimens attached to the reaction frame through steel bolts, while a servo-hydraulic actuator applies a cyclic lateral force on the top of the column. Figure 2.2 shows an illustrative scheme of the applied test setup by Huang *et al.* [48]. The test procedure consisted, firstly, by applying a predetermined axial compressive load. Thereafter, controlled periodical displacements with increasing magnitude were applied to the specimen, as displayed in Figure 2.3. An illustrative load per displacement showing the characteristics hysteresis loops is shown in Figure 2.4. Similar test procedures were also adopted by other researchers [48-53].

It was possible to verify that the introduction of fibers into RC columns has a positive influence on improving the seismic load capacity. Compared to RC columns, the use of fiber could significantly delay and reduce the spalling of concrete. Therefore, the amount of stirrups required by design codes to prevent buckling can be reduced. Moreover, hybrid fiber reinforced concrete columns exhibit a more favorable behavior in terms of ductility, energy dissipation as well as degradation in strength and stiffness. This behavior is attributed to the positive synergetic effect of hybrid fibers in cementitious composites.

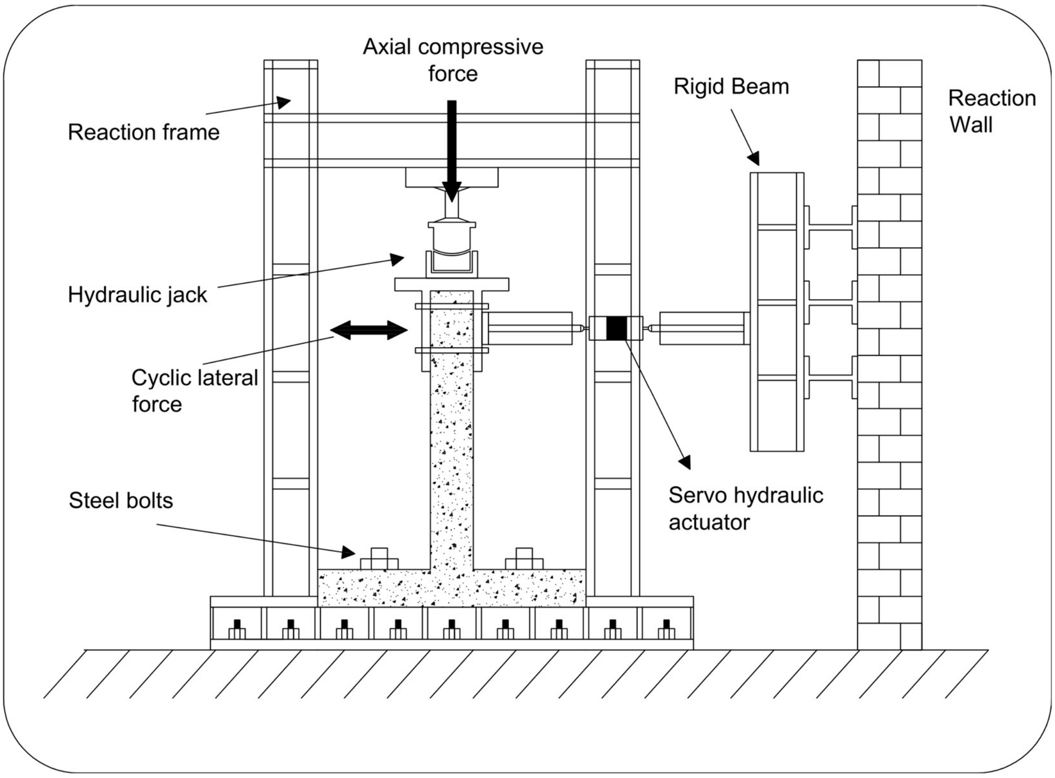

Figure 2.2 – Test setup applied by Huang *et al.* [48].

Similar study was also carried on by Xu *et al.* [49], who compared the cyclic behavior of normal strength (NSSFRC), high strength (HSSFRC) and ultra-high performance reinforced concrete (UHPSFRC). Steel fibers were added to all analyzed concrete mixes in three different volume fractions. The authors verified that normal and high strength concretes presented a more rapidly lateral stiffness degradation in relation to UHPSFRC. Similar failure modes were verified for all analyzed concrete mixes, with crushing and spalling of concrete observed on the compression region. Moreover, by increasing the volume ratio of steel fiber, the narrow hysteretic loops can be converted to plump hysteretic loops with a marginal improvement on lateral strength. A more pronounced effect is evident with the delay of the lateral stiffness decrease and an improvement of the ductile performance and of the overall energy absorption capacity of the steel fiber reinforced columns.

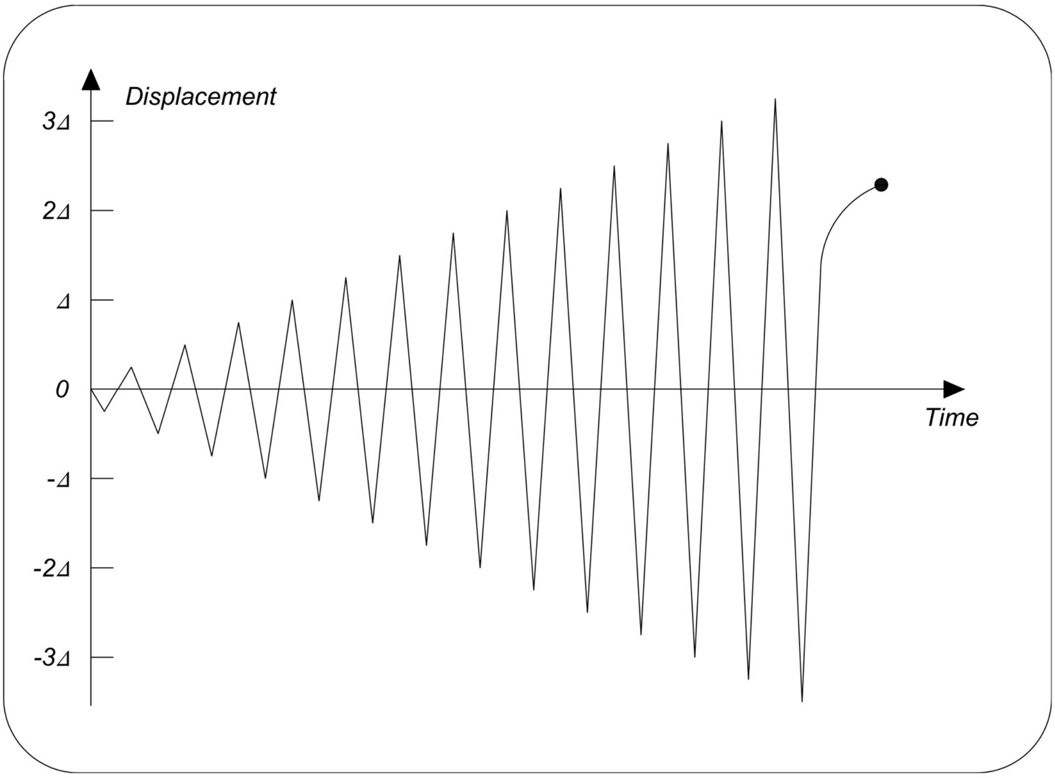

Figure 2.3 – Test procedure applied by Huang *et al.* [48].

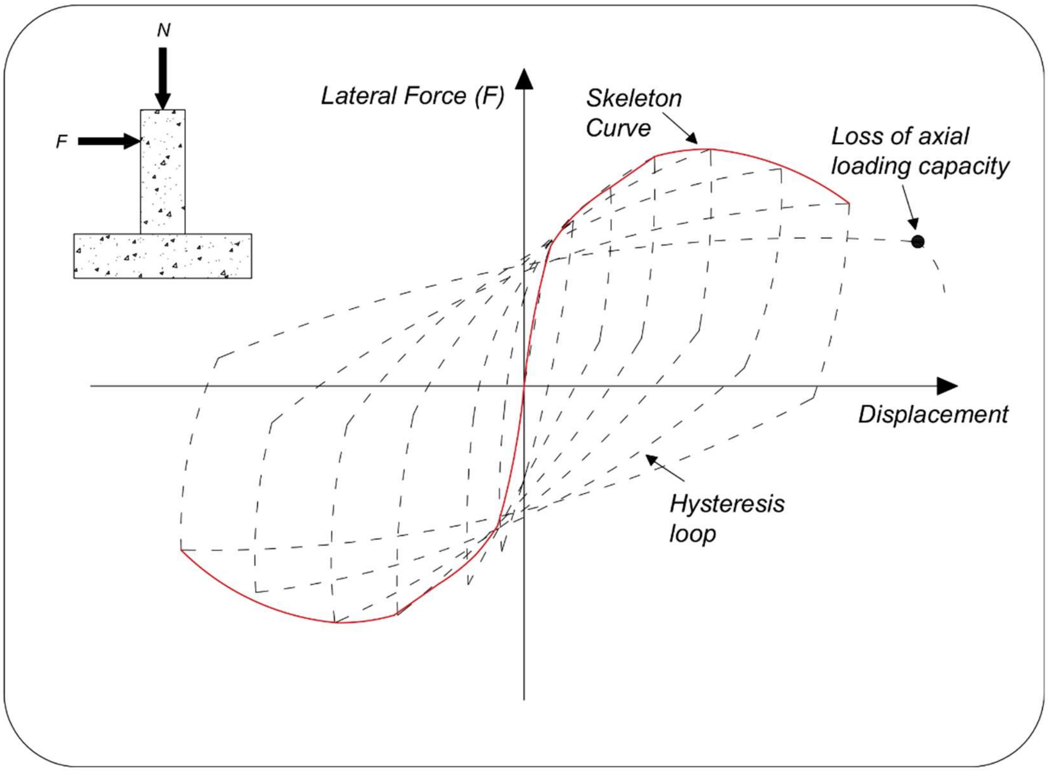

Figure 2.4 – Illustrative lateral load per displacement response [48].

Zhang *et al.* [50], in turn, studied the mechanical behavior of precast steel fiber reinforced concrete beam-column connections when subjected to cyclic loading. Based on the authors' results, the addition of fibers effectively controlled cracks presenting an increase on cracking load and a decrease on the crack width. Although all connections exhibited shear failure in the core region, the shear deformation was reduced with the addition of fibers. As a result, the precast connections with steel fiber reinforced concrete exhibited better joint shear capacity and less stiffness degradation.

Haraji *et al.* [54] verified the effect of steel fibers on normal and high strength concrete reinforced beams under load reversals. The cyclic response of reinforced beams encountered sudden and brittle bond splitting failure with almost total loss in load resistance and considerable strength and stiffness degradation on the first cycle following splitting failure. The addition of fibers on the concrete mix delayed the formation and propagation of the splitting cracks, increased rebar stress and, consequently, enhanced peak bond strength and reduced concrete damage. Therefore, the use of steel fibers substantially increased the energy absorption capacity under cyclic loading.

Chalioris *et al.* [55] investigated the influence of steel fibers on the cyclic hysteretic response of SFRC slender beams and studied its different failure modes. While non-fibrous reference specimen demonstrated shear diagonal cracking in a brittle manner, the RC beam with 1% of steel fibers failed after concrete spalling with satisfactory ductility. Steel fiber reinforced concrete with 3% of fibers, in turn, exhibited an improved cyclic response, since no inclined crack of shear nature or concrete spalling were observed on the beam that failed due to flexure. According to the values of damage indices, fiber reinforced concrete beams presented lower damage index factors than the corresponding non-fibrous reference specimen, especially when 3% of steel fibers were added to the concrete mix.

Further research on slender beams was carried on by Chalioris [56] aiming to study the structural enhancement by the incorporation of steel fibers into shear-critical RC beams subjected to reversal loading. The contribution of steel fibers on the shear behavior is observed at the onset of concrete cracking and at the post-cracking response. Cyclic tests indicated that steel fibers inhibit not only crack propagation and crack width grow but they also prevent cracks from closing during the reversal loading. Moreover, the steel fibrous concrete beams without stirrups exhibited increased shear capacity with respect to the reference plain concrete beam. However, the addition of up to 0.75% of steel fibers was not sufficient to modify shear failure on beams.

Xargay *et al.* [57] evaluated the damage evolution of steel fiber reinforced concrete beams under cyclic loading. For this experimental program, two reinforced beams were designed without stirrups expecting shear failure throughout the loading and unloading cycles. While the first beam was produced with normal strength concrete, the second one was casted with 0.50% steel fiber reinforced concrete. The authors could verify that the addition of steel fibers modified the structural behavior of RC beam without stirrups by improving shear strength. Its failure shifted from a premature shear mode to bending-like one by arresting inclined crack growth. Moreover, it was possible to verify that the fiber effect on bridging cracks opening. The reinforced beams of fiber reinforced concrete exhibited the addition of fibers were responsible for thinner crack widths in relation to normal concrete structures.

The latest study on the seismic response of RC structures strongly focused on beam-column joints and on laterally loaded columns [42-53]. An overview of the main results can be verified in Table 1. More recent work also verified the effect of addition of steel fibers on the mechanical behavior of reinforced beams under flexure. The addition of fibers positively influenced the overall strength, delayed stiffness degradation and significantly increased the global energy absorption capacity and the ductile performance of the fiber reinforced concrete structural element. Therefore, the addition of fibers plays a key role when seeking an improvement on seismic response of RC structures. Further studies are still required to assess the influence of other concrete mix compositions and fiber types on the mechanical behavior under cyclic loadings and for a better understanding of other fiber RC structures under seismic tests.

Table 2.1 – Overview from mechanical response of fiber reinforced concrete under cyclic loadings main results.

References	Analysis	Conclusions
[2, 10-12]	Damage evolution of FRC in cyclic compression	Significant degradation in elastic stiffness and stress with increasing cycles can be observed through cyclic tests curves, caused by crack propagation and damage accumulation
[13-22]	Cyclic compressive behavior of confined concrete	Confined concrete exhibits excellent ductility under cyclic compressive loading; the energy consumed in each unloading/reloading cycle increases with the plastic axial strain of concrete
[23-26]	Cyclic compressive behavior of FRC	Fiber has a positive effect on the cyclic compressive stress-strain behavior of concrete due to fiber crack arresting and bridging effect, especially on the post-cracking branch. Fiber improves the dissipated capacity, enhance the performance in terms of post-peak stiffness and strength and may decrease plastic strain
[27-31]	Cyclic behavior of FRC in bending	A higher amount of fibers leads to a slower damage increase. Cyclic loads provoke cracking in the fiber-cement paste interface, causing a reduction of fiber-concrete bond, resulting in a reduction of the residual strength
[37-41]	Cyclic behavior in RC structures	Well-confined concrete can significantly restrain the opening and propagation of cracks, reducing the strength degradation that consequently improve cyclic performance of RC structures

[48-53]	Cyclic behavior in FRC structures	The introduction of fibers into RC columns has a positive influence on improving the seismic load capacity. Compared to RC columns, the use of fiber could significantly delay and reduce the spalling of concrete.
[50]	Precast FRC beam-column connections	The addition of fibers effectively controlled cracks presenting an increase on cracking load and a decrease on the crack width. Although all connections exhibited shear failure in the core region, the shear deformation was reduced with the addition of fibers.
[54]	Cyclic response of FRC structural beams	The addition of fibers on the concrete mix delayed the formation and propagation of the splitting cracks, increased rebar stress and, consequently, enhanced peak bond strength and reduced concrete damage
[55-57]	Incorporation of fibers into shear-critical RC beams subjected to reversal loading.	Cyclic tests indicated that steel fibers inhibit not only crack propagation and crack width grow but they also prevent cracks from closing during the reversal loading.

2.2. Fatigue response of fiber reinforced concrete

Traditionally, the fatigue of FRC has been analyzed through S-N curves, which correlate the applied nominal load and the fatigue life. The main phenomenological aspects of the cyclic and fatigue behavior of plain and fiber reinforced concrete are displayed in Figure 2.5 and are briefly characterized as follows:

- *Dissipative mechanisms:* inelastic processes occur within the material structure, which are responsible for the energy dissipation during the loading history such as stiffness degradation and the development of irreversible strains;
- *Hysteric loops:* representing the history dependence of the stress-strain relationship upon loading and reloading and the relation to energy dissipation [58-60];
- *Fatigue creep curves*: show the nonlinear strain evolution during the fatigue life with rapid strain growth in the first and the last stages and moderate, nearly linear strain growth in the middle stage [61-63];
- *Wöhler curves*: defining the fatigue life under constant cyclic loading range [64, 65]
- *Loading sequence effect*: representing the dependence of the concrete fatigue behavior on the loading sequence [66-69].

The mechanism of fatigue failure in concrete or mortar can be divided into three distinct stages [63]. The first involve the weak regions within the concrete and is termed flaw initiation. The second stage is characterized by slow and progressive growth of the inherent flaws to a critical size and is generally known as microcracking. In the final stage, macrocracks will develop and eventually lead to failure.

As explained by Cavalaro *et al.* [70], both plain and fiber reinforced concrete are known by its in scatter among their mechanical parameters. The main sources of scatter are the intrinsic material flaws, the process of sample production and variations associated to the equipment precision [70]. This variation becomes more pronounced when verifying fatigue results as the fatigue mechanical response itself is known for also having considerable scatter [71]. This characteristic leads to either the formulation of models that take into account logical basis for analyzing design uncertainties to ensure the adequate evaluation of failure probability.

Lee *et al.* [72] presented a general overview of the fatigue behavior of plain and fiber reinforced concrete. It was verified that the addition of fiber reinforcement has a dual effect on the fatigue behavior of concrete in compression. Lee *et al.* [72] verified that there appears to be a slight degradation in the fatigue life of steel fiber reinforced concrete relative to plain concrete due to the introduction of additional flaws within the concrete matrix [73]. The presence of fibers increases the pore and initial microcracks density, resulting in strength decrease.

However, fiber addition benefits the fatigue performance in bending, as fibers are able to bridge cracks and, therefore, prolong fatigue life. Fibers are able to bridge microcracks and retard their growth, enhancing the composite mechanical performance. The overall outcome of these two competing effects depends significantly on the fiber volume fraction [73]. Cachim *et al.* [74] verified that while 30 mm fibers increased fatigue life, 60 mm fibers actually reduced it in compression fatigue tests. It was concluded that the additional flaws introduced by fiber addition outweighed the benefits for some of the carried out tests.

Poveda *et al.* [75], in turn, studied the compressive fatigue life of steel fiber reinforced concrete in four volume fractions: 15, 30, 45, 60 kg/m^3. The authors observed that concrete with smaller amount of fibers presented very close fatigue life in relation to plain concrete. Intermediate fractions around 45 kg/m^3 were responsible for increasing up to five times the fatigue life of the cement based composites in relation to plain concrete. On the other hand, when 60 kg/m^3 was added to mix, the fiber reinforced concrete presented a significant decrease on the fatigue parameters.

Banjara *et al.* [76] carried on an experimental investigation to investigate the flexural fatigue behavior of plain and fiber reinforced concretes. Flexural fatigue lives of fiber reinforced concrete prisms with 0.50%, 1.00% and 2.00% of steel fibers were evaluated. Significant improvement was observed when 0.50% and 1.00% of steel fibers were used. On the other hand, when 2.00% of fibers were added, a slight decrease on the fatigue life was observed. A similar phenomenon was previously reported in the literature [77, 78], which verified that the best design for fatigue life is given by the addition of 1% of volume fraction.

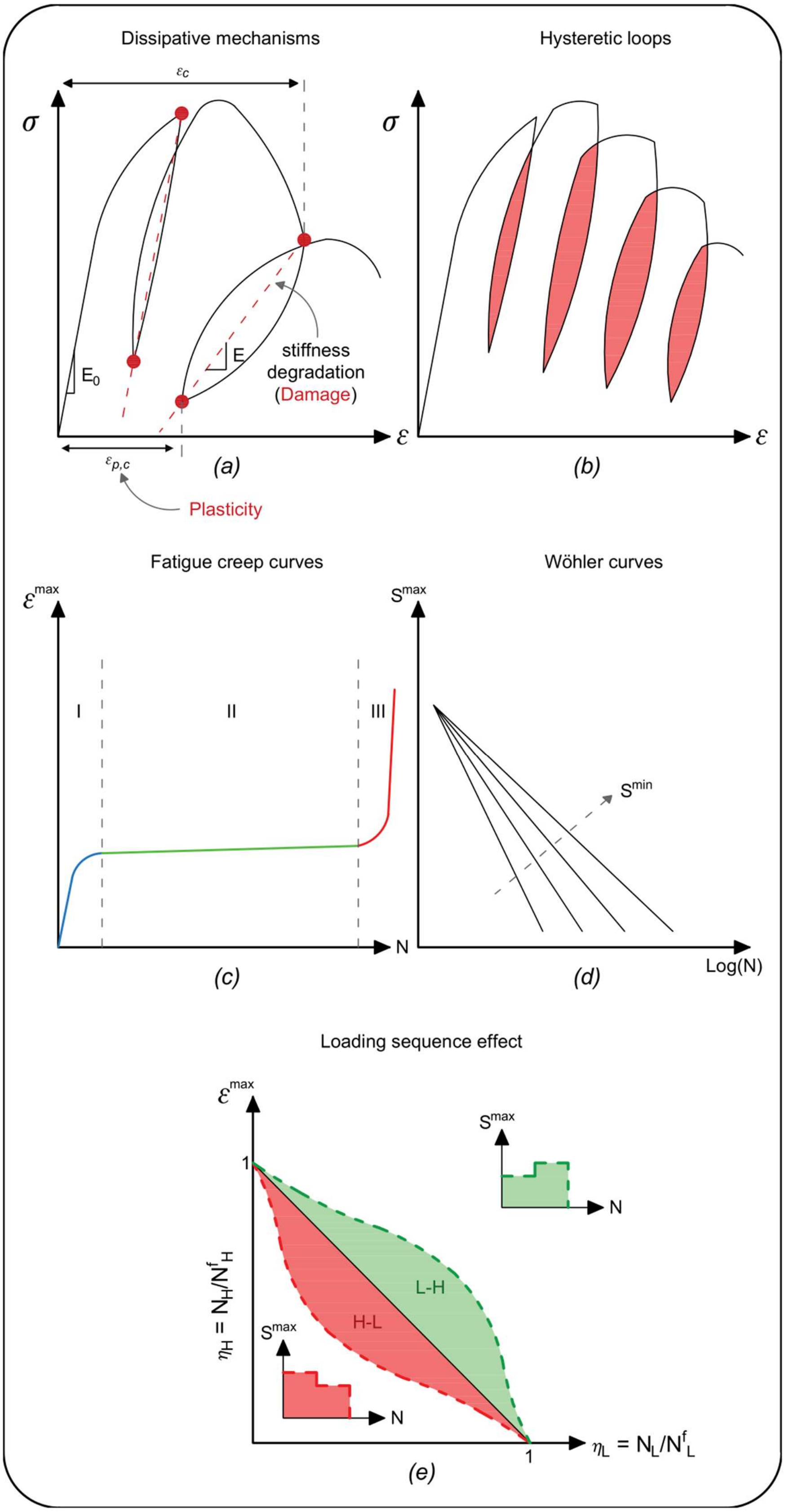

Figure 2.5 – Main phenomenological aspects of cyclic and fatigue behavior of concrete: (a) dissipative mechanism, (b) hysteretic loops, (c) fatigue creep curves, (d) Wöhler curves and (e) loading sequence effect.

Medeiros *et al.* [79] studied the effect of the loading frequency on the compressive fatigue behavior of plain and fiber reinforced concrete. Compressive fatigue tests were performed for three types of concrete and four loading frequencies (4 Hz, 1 Hz, ¼ Hz, 1/16 Hz). The authors observed that the number of cycles to failure decreased as the loading frequency decreased and this reduction is more pronounced for plain concrete. Moreover, the addition of fibers improves the fatigue life for lower frequencies (1 Hz, ¼ Hz and 1/16 Hz), while no significant gain is observed at the highest frequency (4 Hz). Among different probability of failure models set by other authors [80, 81], the model of Saucedo *et al.* [80] showed better agreement with the experimental results.

Most technical reports and guidelines [71, 82] report the fatigue behavior of concrete under compression and just a few take into consideration the flexural tensile response. Nevertheless, those reports dealing with flexural tensile fatigue are valid for uncracked sections with few recommendations for post-cracking fatigue response. Carlesso *et al.* [83, 84], therefore, studied the fatigue of cracked high performance fiber reinforced concrete subjected to bending. The fatigue assessment was carried on after a constant deformation rate was imposed up to a CMOD of 0.50 mm. Specimens that reached the endurance limit [85, 86] of 2,000,000 cycles were then tested monotonically until its complete failure (CMOD > 4.0 mm). Figure 2.6 illustrates the experimental procedure.

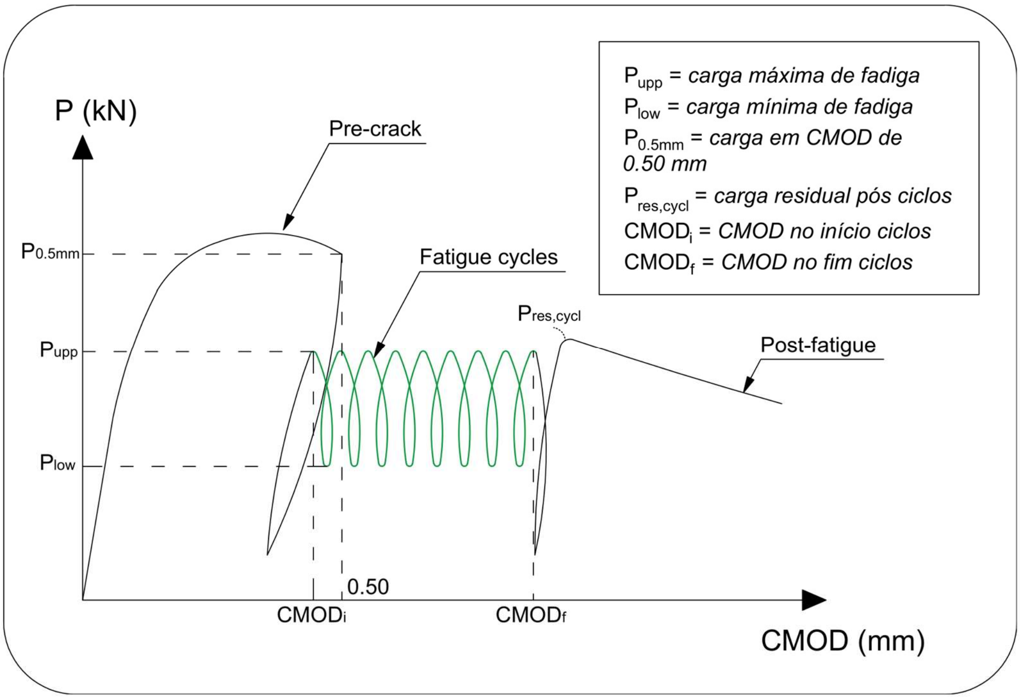

Figure 2.6 – Fatigue loading history a applied by Carlesso *et al.* [83].

Carlesso *et al.* [83] verified that the applied load level plays an important role on CMOD development through cycles. As the load level increases, the slope of the crack increment per cycle becomes steeper and the CMOD grows as well. This suggests that lower load levels can cause a reduction of the ductility. Higher load levels lead to failure through a continuous pullout of the fibers, generating a more ductile response, while smaller load levels can be responsible for the progressive weakening of the fiber-matrix interface through micro-cracks.

Stephen *et al.* [87] also discuss the fatigue fracture of pre-cracked fiber reinforced concrete in flexure. The authors defined the rate of increase in the upper CMOD with cyclic loading has been computed as dCMOD/dN = $(CMOD_n - CMOD_m)/(n - m)$, with CMOD*n* and CMOD*m* being the maximum CMOD at the end of the *nth* and *mth* cycle, respectively. It is seen that the CMOD rate per cycle generally decreases and then increases, similar to what was observed by Subramaniam *et al.* [88] for plain concrete (Figure 2.7). There is always a critical point, denoted here as $CMOD_{cr}$, when transition from the second to the third stage of cracking occurs. The $CMOD_{cr}$ increases with an increases in the fatigue load, implicating the higher cumulative energy for the failure, as proposed by Germano *et al.* [89].

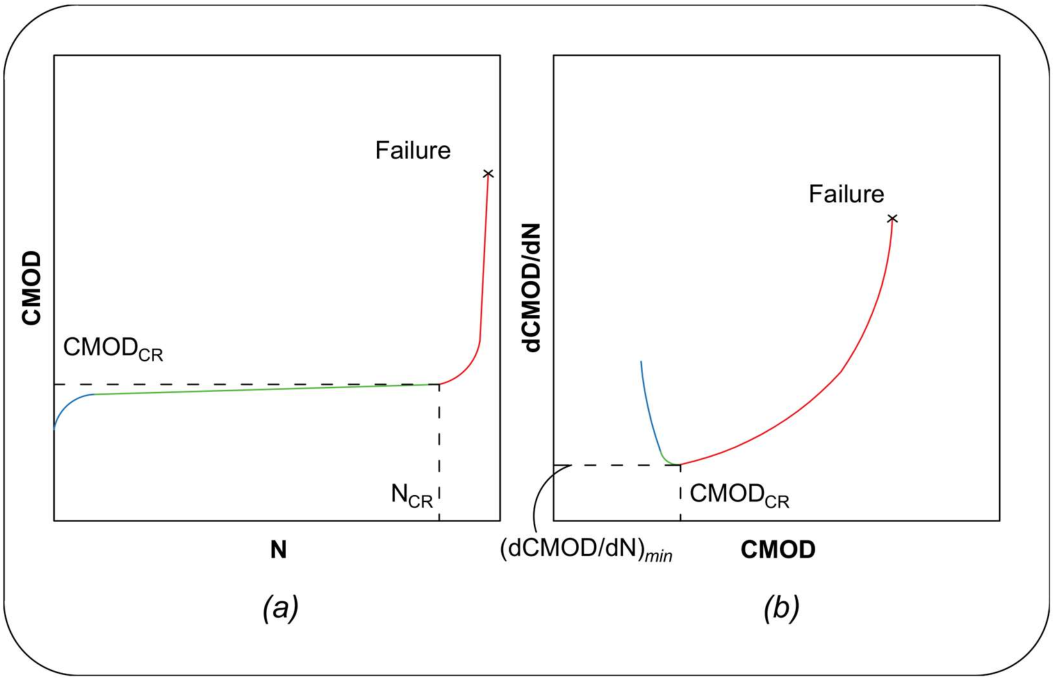

Figure 2.7 – Typical CMOD rate under fatigue loading [87].

Past research works also proposed unified S-N expressions for fiber-reinforced concrete under flexural fatigue. Equations (2.1-2.3) present S-N relations developed by Naaman *et al.* [90], Chacim *et al.* [74] and Singh *et al.* [77]. In general, the proposed equations involve the target fatigue load range (S_{max}), the number of cycles to failure (N), the flexural strength (f_s). and the stress ratio (R). More recently, Stephen *et al.* [87] and Banjara *et al.* [76] proposed a generalized model including a percentage of the residual strength at CMOD of 0.50 mm($f_{R,1}$), calculated according to EN 14651 [91] standard (Equations 2.4 and 2.5). From the S-N models, it can be inferred that the incorporation of even low fiber dosages can significantly improve the fatigue performance of concrete due to crack bridging and mitigation of fracture propagation.

$$\frac{S_{\max}}{f_s} = 93 - 3.68\log(N) \tag{2.1}$$

$$\frac{S_{\max}}{f_s} = \left(\frac{20.156\log(N)}{18.708}\right) \tag{2.2}$$

$$\frac{S_{\max}}{f_s} = c_1 N^{-c_2(1-R)} \tag{2.3}$$

$$\log(N) = A + B\log(\% f_{R,1}) \tag{2.4}$$

$$\ln(N) = 244.1\left(\frac{S_{\max}}{f_s}\right) - 179.4\left(\frac{S_{\max}}{f_s}\right)^2 + 3.106V_f - 1.2V_f^2 - 70.29 \tag{2.5}$$

When it comes to the structural level, Parvez *et al.* [92] analyzed the fatigue behavior of steel fiber reinforced concrete beams. The authors stated that steel fibers played a key role in increasing the fatigue life. However, mixed results were observed when it comes to influence of the aspect ratio and of the fiber volume fraction on the fatigue behavior. Similar results were observed by Johnston *et al.* [93], Zhang *et al.* [94] and Gao *et al.* [95]: the fatigue life decreased with the increase in stress level and increased with the increase in fiber volume fraction. The strength of steel reinforcement does not show significant effect from the experimental data and observations.

Huang *et al.* [96] verified the fatigue performance of reinforced concrete beam strengthened with strain-hardening fiber reinforced cementitious composites.

The authors showed that the application of a SHCC layer can reduce the strain in the longitudinal reinforcement of a reinforced concrete beam. The fatigue degradation of the SHCC layer and the yield of the steel bars are responsible for the increase in the fatigue deflection of the reinforced structure. The SHCC layer physically contributes by taking part of the stress in the tension zone and can lower the strain localization and stress concentration of the longitudinal reinforcement.

So far, an extensive research has already evaluated the main plain and fiber reinforced concrete fatigue parameters, such as the influence of fibers on the number of cycles to failure, the development of new S-N curves for fiber cementitious composites and the analysis of the essential mechanisms of fatigue failure in concrete and mortar (Overview in Table 2). However, most past papers still give a significant focus on compressive fatigue tests and, in most cases, evaluate the cementitious composite in uncracked form. Only now, last studies have been giving more attention to the flexure fatigue parameters and trying to evaluate damage on pre-cracked fiber reinforced concrete specimens. Therefore, new surveys still need to be carried on to assess fatigue and damage evolution of cracked and uncracked FRC when under shear or torsion loadings, as well verifying this phenomenon in structural level.

Table 2.2 – Overview from fatigue response of fiber reinforced concrete main results.

References	Analysis	Conclusions
[58-69]	Main phenomenological aspects of the cyclic and fatigue behavior of plain and fiber reinforced concrete	Dissipative mechanisms, Hysteretic loops Fatigue creep curves Wöhler curves Loading sequence effects.
[72, 73]	Fatigue behavior of plain and fiber reinforced concrete in compression	Slight degradation in the fatigue life of steel fiber reinforced concrete relative to plain concrete due to the introduction of additional flaws within the concrete matrix
[73, 74]	Fatigue behavior of plain and fiber reinforced concrete in bending	Fiber addition benefits the fatigue performance in bending, as fibers are able to bridge cracks and, therefore, prolong fatigue life
[76-78]	Fatigue behavior of SFRC in bending	In terms of fatigue life, the addition of 1.00% of steel fibers presented optimum results
[79-82]	Effect of the loading frequency on the compressive fatigue behavior of plain and fiber reinforced concrete	The number of cycles to failure decreased as the loading frequency decreased and this reduction is more pronounced for plain concrete
[83, 84]	Fatigue behavior of pre-cracked SFRC in bending	Lower load levels can cause a reduction of the ductility. Higher load levels lead to failure through a continuous pullout of the fibers, generating a more ductile response, while smaller load levels can be responsible for the progressive weakening of the fiber-matrix interface through micro-cracks

[87, 88]	Fatigue behavior of pre-cracked FRC in bending	CMOD rate per cycle generally decreases and begin to increase after reaching the critical CMOD point. There is always a critical point, when transition from the second to the third stage of cracking occurs
[74, 76, 77, 87, 89]	Development of unified S-N expressions FRC under flexural fatigue	From the S-N models, it can be inferred that the incorporation of even low fiber dosages can significantly improve the fatigue performance of concrete due to crack bridging and mitigation of fracture propagation
[92-95]	Fatigue behavior of steel fiber reinforced concrete beams	Steel fibers played a key role in increasing the fatigue life. However, mixed results were observed when it comes to influence of the aspect ratio and of the fiber volume fraction on the fatigue behavior.
[99]	Fatigue performance of reinforced concrete beam strengthened with SHCC	The application of a SHCC layer can reduce the strain in the longitudinal reinforcement of a reinforced concrete beam. The SHCC layer physically contributes by taking part of the stress in the tension zone and can lower the strain localization and stress concentration of the longitudinal reinforcement

2.3. Damage evolution models of fiber reinforced concrete subjected to cyclic loadings

Past constitutive stress-strain models have been developed to describe the behavior of plain concrete under cyclic loadings [8, 14, 25, 97-103], which served as a basis for the development of models for fiber reinforced concrete. In the framework of damage mechanics, damage evolution laws are fundamental in order to predict the behavior FRC composites. The damage evolution equations must account for different factors such as fiber content, fiber material and geometrical properties, as well as the concrete matrix properties [104-107]. Also, concrete presents permanent strains and stiffness degradation that can be observed during cyclic tests, which are also represented through constitutive models [108].

Li *et al.* [25] carried on an experimental investigation on the stress-strain behavior of steel fiber reinforced concrete subjected to uniaxial compression. The authors evaluated the damage through acoustic emission (AE) signals and verified that the total AE activity of SFRC is higher than that of plain concrete due to fiber pull-out and fiber sliding events and the AE hits increase with increasing fiber volume fraction. The stiffness degradation process induced by progressive damage accumulation, as shown by AE activity, was characterized by a damage evolution law. A scalar damage d is equal to zero in the absence of damage and equal to one in the case of complete damage. According to this concept, the tangent unloading modulus can be calculated by means of Equation 2.6. The plastic strain in the loading direction for each point of the stress-strain curve can be obtained by Equation 2.7. Finally, Li *et al.* [25] proposed a damage law evolution for different fiber reinforcing parameters and is described in Equation 2.8.

$$E_d = (1-d)E_0 \tag{2.6}$$

$$\varepsilon_c^p = \varepsilon_c - \frac{\sigma}{E_d} \tag{2.7}$$

$$d = 1 - ax^{-b} \tag{2.8}$$

In this case, d is the scalar damage variable, E_0 is the tangent initial unloading elastic modulus, E_d is the simplified calculated tangent unloading modulus at any point, ε_c^p is the plastic strain when the cycle terminates, a and b are determined through regression analysis. Close estimation for plain concrete and SFRC was observed for the developed model.

A similar model was proposed by Krahl *et al.* [107] which evaluated the damage index of the ultra-high performance fiber reinforced concrete under cyclic compression through ultrasonic technique. Therefore, it was expected that the velocity of the wave propagation in the solid varies with cracking development. After mechanical damage and at the end of each cycle, the ultrasound was used to estimate the damage index *d*, relating the velocity that the wave takes to pass through the cracked sample v_{Lo} and undamaged sample v_L (Equation 2.9). It was found by ultrasonic tests that damage growth at small rates since the beginning of the load and, after peak, damage increased at high rates due to the appearance of macrocracks. The magnitude of the decay was associated with fiber volume fractions.

$$d = 1 - \frac{v_L^2}{v_{L0}^2} \tag{2.9}$$

Xu *et al.* [12, 26, 109] studied the damage evolution of steel-polypropylene hybrid fiber reinforced concrete under cyclic compression. The authors added the factor η in order to verify the contribution of blended fibers numerically on the stress-strain model. Equation 2.10 brings the definition of the factor η. The format of the fiber characteristic parameter λ is given in Equation 2.11. The parameters α and β were obtained through least-squares analysis.

$$\eta = 1 + \alpha\lambda_1 + \beta\lambda_2 \tag{2.10}$$

$$\lambda_f = \frac{V_f l_f}{d_f} \tag{2.11}$$

Based on the previous research on the mechanical damage evolution, Xu *et al.* [12] divided the damage process of concrete into the following three stages (Figure 2.8):

1. *Initial undamaged stage*: at this stage, the damage index is set to zero. The concrete is still elastic and the elastic stiffness ratio increases with increasing envelope strain. Before reaching the maximum axial stress, the increasing axial compressive load make concrete denser with the initial micro-voids collapsed and the cracks closed. The propagation of cracks has still not induced the degradation in macro elastic stiffness of concrete;

2. *Sharp damage increasing stage*: the concrete specimen reaches the maximum density, the micro cracks start to propagate and the damage index initially increases, which induces a decrease in the elastic stiffness. After the peak stress, the damage evolves quickly in the form of a power function with unstable propagation of the cracks;
3. *Stable damage stage*: the main damage has already been evolved completely. The cyclic stress-strain curve is stable, with axial stress decreasing at a slow speed. The stiffness ratio remains at a constant tendency.

Similar studies and other damage laws models have been suggested for direct tension and bending tests. Li *et al.* [105] suggested an exponential equation to model the damage evolution on fiber reinforced concrete under direct tension (equation 7), which could well estimate stiffness degradation with increasing strain. Krahl *et al.* [106] also proposed a new model to estimate the stress-strain relation of steel fiber reinforced concrete under cyclic direct tension. The proposed analytical equations were incorporated to its constitutive model and implemented in the commercial finite element code Abaqus to capture the mechanical response of the ultra-high performance fiber reinforced concrete. The numerical model was capable of predicting the damage evolution and cyclic envelopes during all phases of the tension tests.

$$d = a + be^{-c\varepsilon} \tag{2.12}$$

In this case, d is the scalar damage variable, ε is the strain and a, b and c are determined through regression analysis.

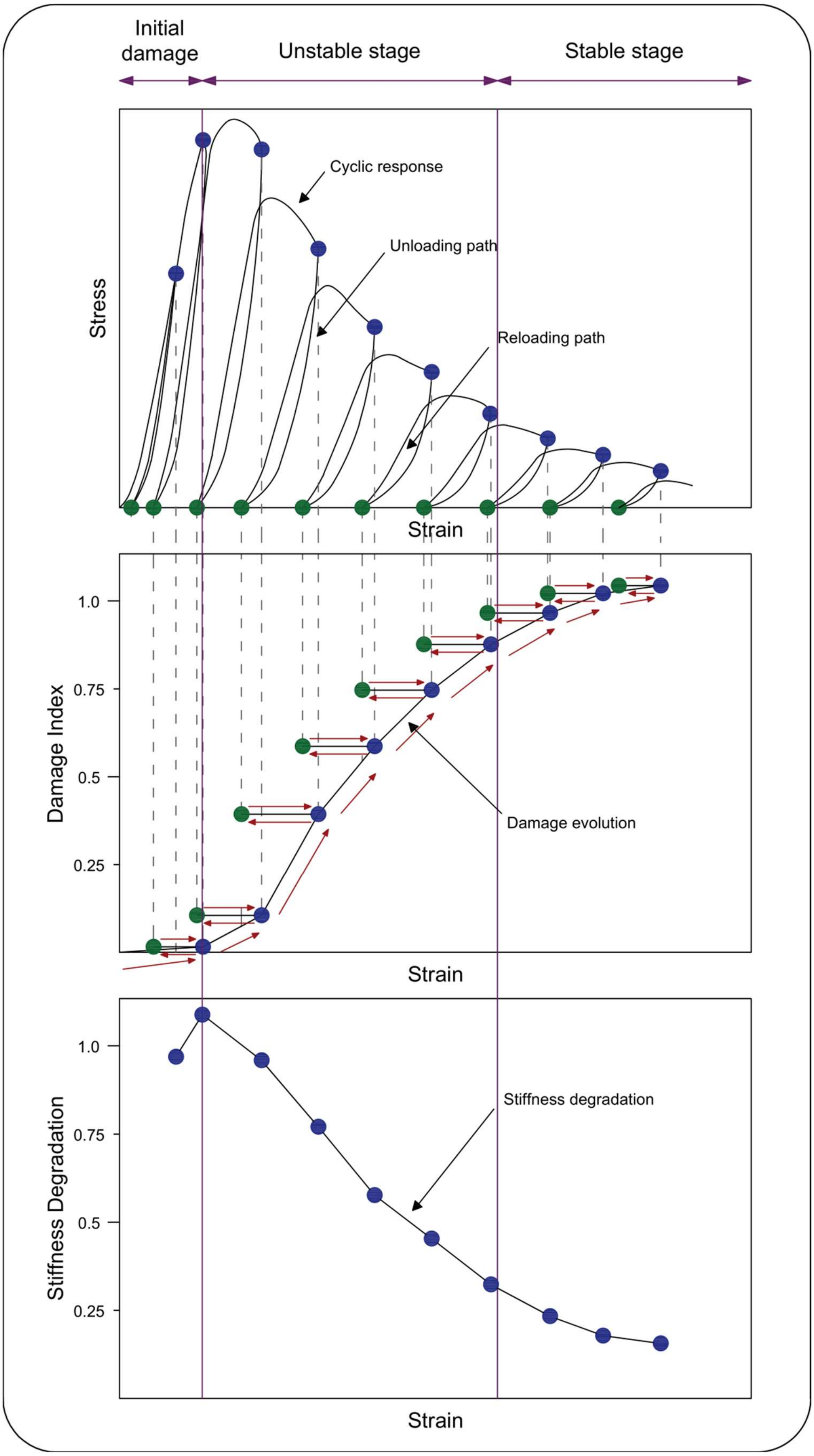

Figure 2.8 – Typical cyclic stress-strain curve and the corresponding damage evolution of concrete in compression.

Xu *et al.* [26] explains the different stages of crack propagation along a cyclic compression test. A schematic drawing showing the propagation of a crack of fiber reinforced concrete under cyclic compression is displayed in Figure 2.9. The authors observed from previous test results that the cyclic compressive process can be divided into six stages:

1. Elastic stage (Path OA): the initial microcracks are restrained by the randomly distributed fibers;
2. Initial crack propagation stage (Path AB): visible fine cracks can be observed on the specimens at this stage;
3. Stable crack propagating can be seen when the load reaches the ultimate strength, a sudden increase in the width of cracks can be observed, which is induced by events of steel fiber pull-out and matrix cracking;
4. Fracture occurring stage (Path CD): the cracks in the specimens propagate and coalesce into a main crack. Steel fiber debonding occurs continuously with increasing loads and loading cycles;
5. Unloading stage (path DH): during unloading stage, cracks begin to close and plastic strain is present;
6. Reloading stage (path HE): the width of the main cracks becomes larger promoting stiffness degradation and complete pullout of steel fibers;
7. Convergence path (EF): the tensile stress between the two sides of a crack is undertaken by steel fibers until complete failure is reached.

Past works have already developed stress-strain relations of plain and fiber reinforced concretes under uniaxial monotonic and cyclic compression. However, there still a lack of research when it comes to stress-strain relations in bending, shear and torsion. Further analysis still need to be carried on in order to establish new damage evolution laws and constitutive models for FRC in different loading types. This analysis also needs to reach the structural level.

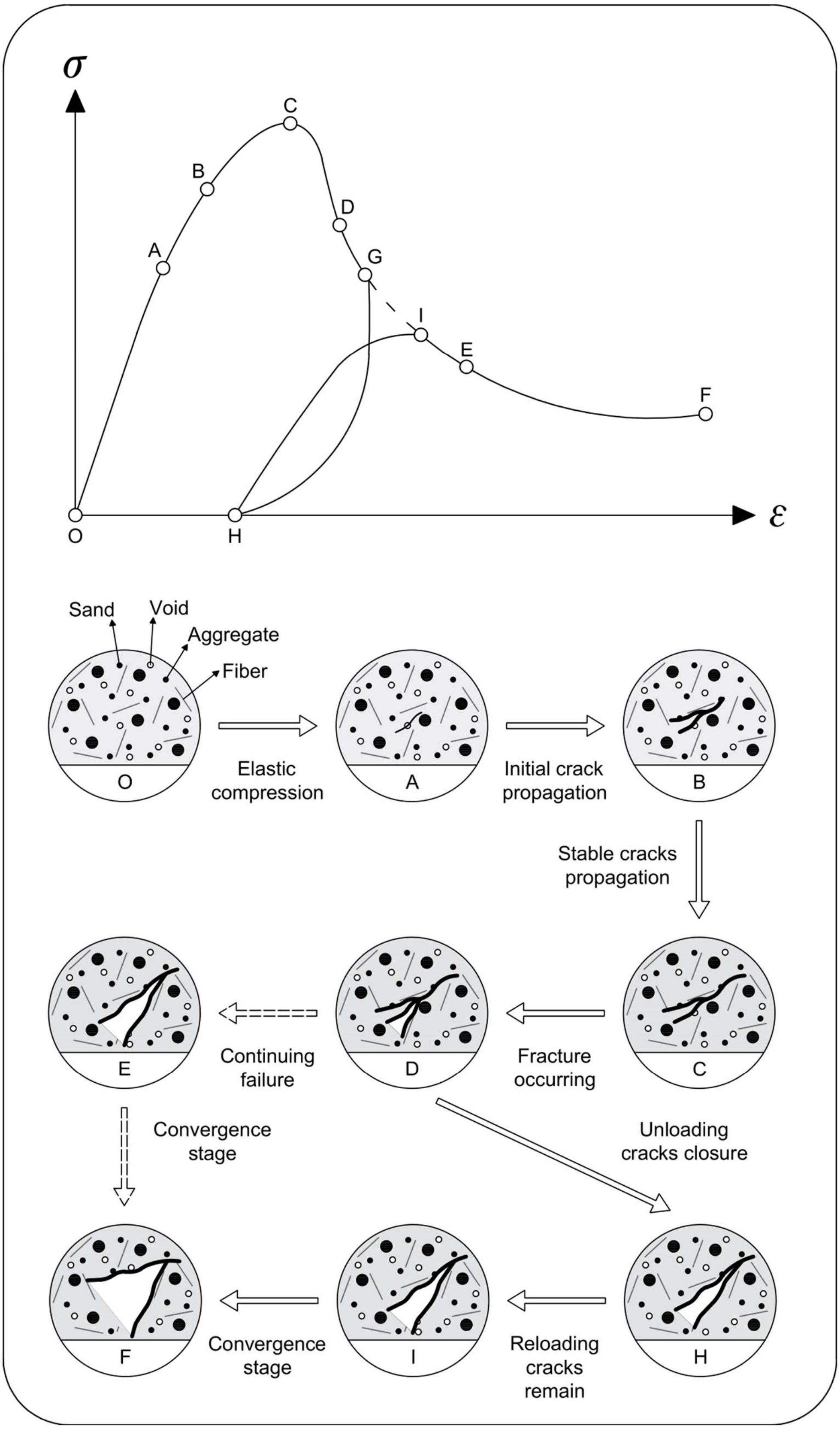

Figure 2.9 – Schematic drawing showing the propagation of a crack of fiber reinforced concrete under cyclic compression.

2.4. References

1 BAHN, B. HSU, C. Stress-strain behavior of concrete under cyclic loading. **ACI Materials Journals**, vol. 95, 1998.

2 MAEKAWA, K. KASHIF, EI. Cyclic cumulative damaging of reinforced concrete in post-peak regions. **Journal of Advanced Concrete Technology**, vol. 2, p. 257-271, 2004.

3 OSORIO, E. BAIRAN, J. MARI, A. Lateral behavior of concrete under uniaxial compressive cyclic loading. **Materials Structures**, vol. 46, p. 709-724, 2013.

4 SINAIE, S. HEIDARPOUR, A. ZHAO, X. SANJAYAN, J. Effect of size on the response of cylindrical concrete samples under cyclic loading**. Construction and Building Materials**, vol. 84, p. 399-408, 2015.

5 LEE, H. AWANG, A. OMAR, W. Steel strap confined high strength concrete under uniaxial cyclic compression. **Construction and Building Materials**, vol. 72, p. 48-55, 2014.

6 YU, T. HU, Y. TENG, J. FRP-confined circular concrete-filled steel tubular columns under cyclic axial compression. **Journal of Constructional Steel Research**, vol. 94, p. 33-48, 2014.

7 LI, P. WU, Y. GRAVINA, R. Cyclic response of FRP-confined concrete with post-peak strain softening behavior. **Construction and Building Materials**, vol. 123, p. 814-828, 2016.

8 YANKELEVSKY, D. REINHARDT, H. Uniaxial behavior of concrete in cyclic tension. **Journal of Structural Engineering**, vol. 115, p. 166-182, 1989.

9 CAMPIONE, G. MENDOLA, L. stress-strain behavior in compression of lightweight fiber reinforced concrete under monotonic and cyclic loads. **Earthquake Resistant Engineering Structures III**, vol. 57, 387-396.

10 NEUENSCHWANDER, M. KNOBLOCH, M. FONTANA, M. Suitability of the damage-plasticity modelling concept for concrete at elevated temperatures: experimental validation with uniaxial cyclic compression tests. **Cement and Concrete Research**, vol. 79, p. 57-75, 2016.

11 SUARIS, W. OUYANG, C. FERNANDO, V. Damage model for cyclic loading of concrete. **Journal of Engineering Mechanics**, vol. 116, 1020-1035, 1990.

12 XU, L. DING, X. CHI, Y. LI, C. HUANG, B. SHI, Y. Experimental investigation on damage behavior of polypropylene fiber reinforced concrete under compression. **International Journal of Concrete Structures and Materials**, vol. 12, 2018.

13 LI, P. LILI, S. XING, F. ZHOU, Y. Static and cyclic response of low-strength recycled aggregate concrete strengthened using fiber-reinforced polymer. **Composites: Part B**, vol. 160, p. 37-49, 2019.

14 ABBASNIA, R. ZIAADINY, H. Behavior of concrete confined with FRP composites under axial cyclic compression. **Engineering Structures**, vol. 32, p. 648-655, 2010.

15 CAO, Q. LV, X. LI, X. ZHOU, C. SONG, S. High strength expansive concrete-encased-steel filled carbono fiber reinforced polymer tubes under axial monotonic and cyclic load. **Journal of Composite Materials**, vol. 54, p. 4557-4573, 2020

16 HANY, N. HANTOUCHE, E. HARAJI, M. Axial stress-strain model of CFRP-Confined concrete under monotonic and cyclic loading. **Journal of Composite Construction**, vol. 19, 2015.

17 YU, T. HU, Y. TENG, J. FRP-confined circular concrete-filled steel tubular columns under cyclic axial compression. **Journal of Constructional Research Steel Research**, vol. 94, p. 33-48, 2014.

18 DALGIC, K. ISPIR, M. ILKI, A. Cyclic and monotonic compression behavior of CFRP-jacketed damaged noncircular concrete prisms. **Journal of Composites for Construction,** vol. 20, 2016.

19 BAI, Y. DAI, J. TENG, J. Cyclic compressive behavior of concrete confined with large rupture strain FRP composites. **Journal of Composites for Construction**, vol. 18, 2014.

20 BAHN B. HSU, C. Stress-strain behavior of concrete under cyclic loading. **ACI Materials Journal**, vol. 95, p. 178-193, 1988.

21 SINAIE, S. HEIDARPOUR, A. ZHAO, X. SANJAYAN, J. Effect of size on the response of cylindrical concrete samples under cyclic loading. **Construction and Building Materials**, vol. 84, p. 399-408, 2015.

22 ABBASNIA, R. AHMADI, R. ZIAADINY, H. Effect of confinement level, aspect ratio and concrete strength on the cyclic stress-strain behavior of FRP-confined concrete prisms. **Composites: Part B**, vol. 43, p. 825-831, 2012.

23 LAM, L. TENG, J. CHEUNG, C. XIAO, Y. FRP-confined concrete under axial cyclic compression. **Cement & Concrete Composites**, vol. 28, p. 949-958, 2006.

24 KESNER, K. BILINGTON, S. DOUGLAS, K. Cyclic response of highly ductile fiber-reinforced cement-based composites. **ACI Materials Journal**, vol. 100, p. 381-390, 2003.

25 LI, B. XU, L. CHI, Y. HUANG, B. LI, C. Experimental investigation on the stress-strain behavior of steel fiber reinforced concrete subjected to uniaxial cyclic compression. **Construction and Building Materials**, vol. 140, p. 109-118, 2017.

26 XU, L. LI, B. CHI, Y. LI, C. HUANG, B. SHI, Y. Stress-strain relation of steel-polypropylene-blended fiber-reinforced concrete under uniaxial cyclic compression**. Advances in Materials Science and Engineering**, vol. 2018, 2018.

27 SMEDT, M. VRIDAGHS, R. STEEN, C. VERSTRYNGE, E. VANDEWALLE, L. Damage analysis in steel fibre reinforced concrete under monotonic and cyclic bending by means of acoustic emission monitoring. **Cement and Concrete Composites**, vol. 114, 2020.

28 GONZALEZ, D. MORADILLO, R. MINGUEZ, J. MARTINEZ, J. VICENTE, M. Post-cracking residual strength of fibre-reinforced high-performance concrete after cyclic loading. **Structural Concrete**, vol. 19, p. 340-351, 2018.

29 SHERIF, M. KAKHIMOVA, E. TANKS, J. OZBULUT, O. Cyclic flexural behavior of hybrid SMA/steel fiber reinforced concrete analyzed by optical and acoustic techniques. **Composite Structures**, vol. 201, p. 248-260, 2018.

30 BOULEKBACHE, B. HAMRAT, M. CHEMROUK, M. AMZIANE, S. Flexural behavior of steel fibre-reinforced concrete under cyclic loading. **Construction and Building Materials**, vol. 126, p. 253-262, 2016.

31 MONTEIRO, V. LIMA, L. SILVA, F. On the mechanical behavior of polypropylene, steel and hybrid fiber reinforced self-consolidating concrete. **Construction and Building Materials**, vol. 188, 280-291, 2018.

32 KIM, D. KIM, H. CHUNG, Y. CHOI, E. Pullout resistance of straight NiTi shape memory alloy fibers in cement mortar after cold drawing and heat treatment. **Composites Part B: Engineering**, vol. 67, p. 588-594, 2014.

33 CHOI, E. KIM, D. CHUNG, Y. NAM, T. Bond-slip characteristics of SMA reinforcing fibers obtained by pull-out tests. **Materials Research Bulletin**, vol. 1, p. 28-31.

34 CHOI, E. Choi E, MOHAMMADZADEH, B. HWANG, J. KIM, W. Pullout behavior of superelastic SMA fibers with various end-shapes embedded in cement mortar. **Construction and Building Materials,** vol. 10, p. 605-616, 2018.

35 LI, V. Integrated structures and materials design. **Materials and Structures**, vol. 40, p. 387-396, 2007.

36 ZFAR, A. ANDRAWES, B. Experimental flexural behavior of SMA-FRP reinforced concrete beam. **Frontiers of Structural and Civil Engineering**, vol. 7, 341-355, 2013.

37 MOSTAFA, M. LIU, T. LIU, X. FU, B. The composite steel reinforced concrete column under axial and seismic loads: A Review. **International Journal of Steel Structures**, vol. 19, p. 1969-1987, 2019.

38 SALJOUGHIAN, A. MOSTOFINEJAD, D. Using grooving and corner strip-batten techniques for seismic strengthening of square reinforced concrete column with fiber-reinforced polymer composites. **Structural Concrete**, p. 1-17, 2020.

39 NIU, J. BIAN, Y. ZUO, F. Study on the seismic performance of high-performance polypropylene fiber-reinforced lightweight aggregate concrete columns. **European Journal of Environmental and Civil Engineering**, 2020.

40 ASHA, P. SUNDARARAJAN, R. Effect of confinement on the seismic performance of reinforced concrete exterior beam-column joints. **Australian of Structural Engineering Journal**, vol. 19, p. 59-66, 2018.

41 MO, Y. WONG, D. MAEKAWA, K. Seismic performance of hollow bridge columns. **ACI Structural Journal**, vol. 100, p. 337-348, 2003.

42 OZBAKKALOGLU, T. SAATCIOGLU, M. Seismic behavior of high strength concrete columns confined by fiber-reinforced polymer tubes. **Journal of Composites for Construction**, vol. 10, p. 538-549, 2006.

43 ELADAWY, M. HASSAN, M. BENMOKRANE, B. FERRIER, E. Lateral cyclic behavior of interior two-way concrete slab-column connections reinforced with GFRP bars. **Engineering Structures**, vol. 209, 2020.

44 ZOHREVAND, P. MIRMIRAN, A. Cyclic behavior of hybrid columns made of ultra high performance concrete and fiber reinforced polymers. **Journal of Composites for Construction**, vol. 16, p. 91-99, 2012.

45 WU, B. ZHAO, X. ZHANG, J. Cyclic behavior of thin-walled square steel tubular columns filled with demolished concrete lumps and fresh concrete. **Journal of Constructional Steel Research**, vol. 77, p. 69-81, 2012.

46 SHIM, C. KOEM, C. SONG, H. Seismic performance of repaired severely damaged precast columns with high-fiber reinforced cementitious composites. **KSCE Journal of Civil Engineering**, vol. 22, p. 736-746, 2018.

47 ABOUHUSSIEN, A. HASSAN, A. ISMAIL, M. ALEEM, B. Evaluating the cracking of ECC beam-column connections under cyclic loading by acoustic emission analysis. **Construction and Building Materials**, vol. 215, p. 958-968, 2019.

48 HUANG, L. XU, L. CHI, Y. XU, H. Experimental investigation on the seismic performance of steel-polypropylene hybrid fiber reinforced concrete columns. **Construction and Building Materials**, vol. 87, p. 16-27, 2015.

49 XU, S. WU, C. LIU, Z. SHAO, R. Experimental investigation on the cyclic behavior of ultra-high performance steel fiber reinforced concrete filled thin-walled steel tubular columns. **Thin-Walled Structures**, vol. 140, p. 1-20, 2019.

50 ZHANG, J. DING, C. RONG, X. YANG, H. WANG, K. ZHANG, B. Experimental seismic study of precast hybrid SFC/RC beam-column connections with different connections details. **Engineering Structures**, vol. 208, 2020.

51 SHARMA, R. BANSAL, P. Behavior of RC exterior beam column joint retrofitted using UHP-HFRC. **Construction and Building Materials**, vol. 195, p. 376-389, 2019.

52 BARCELO, J. BONET, J. ESCUDERO, B. JAEN, B. Cyclic behavior of hybrid RC columns using high performance fiber reinforced concrete and Ni-Ti SMA bars in critical regions. **Composite Structures**, vol. 212, p. 207-2019, 2019.

53 KHAN. M. AL-OSTA, M. AHMAD, S. RAHMAN, M. Seismic behavior of beam-column joints strengthened with ultra-high performance fiber reinforced concrete. **Composite Structures**, vol. 200, p. 103-119, 2018.

54 HARAJI, M. GHARZEDDINE, O. Effect of the steel fibers on bond performance of steel bars in NSC and HSC under load reversals. **Journal of Materials in Civil Engineering**, vol. 19, p. 864-873, 2007.

55 CHALIORIS, C. KOSMIDOU, P. KARAYANNIS, C. Cyclic response of steel fiber reinforced concrete slender beams: An experimental study. **Materials**, vol. 12, 2019.

56 CHALIORIS, C. Steel fibrous RC beams subjected to cyclic deformations under predominant shear. **Engineering Structures**, vol. 49, p. 104-118, 2013.

57 XARGAY, H. RIPANI, M. FOLINO, P. NUNEZ, N. CAGGIANO, A. Acoustic emission and damage evolution in steel fiber-reinforced concrete beams under cyclic loading. **Construction and Building Materials**, in press.

58 DO, M. CHAALLAL, O. AITCIN, P. Fatigue behavior of high-performance concrete. **Journal of Materials in Civil Engineering**, vol. 5, p. 96-111, 1993.

59 DEUSTSCHER, M. TRAN, N. SCHEERER, S. Experimental investigations on temperature generation and release of ultra-high performance concrete during fatigue tests. **Applied Sciences**, vol. 10, 2020.

60 THIELE, M. PETRYNA, Y. ROGGE, A. Experimental investigation of damage evolution in concrete under high-cycle fatigue. In: **9th International Conference on Fracture Mechanics of Concrete and Concrete Structures**, 2016.

61 ROSSI, P. PARANT, E. Damage mechanism analysis of a multi-scale fibre reinforced cement-based composite subjected to impact and fatigue loading conditions. **Cement and Concrete Research**, vol. 38, p. 413-421, 2008.

62 KIM, J. KIM, Y. Experimental study on the fatigue behavior of high strength concrete. **Cement and Concrete Research**, vol. 26, p. 1513-1523, 1996.

63 GAO, L. HSU, T. Fatigue of concrete under uniaxial compression cyclic loading. **ACI Material Journal**, vol. 95, p. 575-581, 1998.

64 HÜMME, J. HAAR, C. LOHAUS, L. MARX, S. Fatigue behavior of a normal-strength concrete – number of cycles to failure and strain development. **Structural Concrete**, vol. 4, 2016.

65 SONG, H. SONG, Y. Fatigue capacity of plain concrete under fatigue loading with constant confined stress. **Materials and Structures**, vol. 44, p. 253-262, 2011.

66 HOLMEN, J. Fatigue of concrete by constant and variable amplitude loading. **ACI Journal Special Publication**, vol. 75, p. 71-110, 1982.

67 PETKOVIC, G. LENSCHOW, R. STEMLAND, H. ROSSELAND, S. Fatigue of high-strength concrete. **ACI Journal Special Publication**, vol. 121, p. 505.

68 BAKTHEER, A. HEGGER, J. CHUDOBA, R. Enhanced assessment rule for concrete fatigue under compression considering the nonlinear effect of loading sequence. **International Journal of Fatigue**, vol. 126, p. 130-142, 2019.

69 BAKTHEER, A. CHUDOBA, R. Experimental and theoretical evidence for the load sequence effect in the compressive fatigue behavior of concrete. **Materials and Structures**, vol. 54, 2021.

70 CAVALARO, S. AGUADO, A. Intrinsic scatter of FRC: an alternative philosophy to estimate characteristic values. **Materials and Structures**, vol. 48, p. 3537-3555, 2015.

71 INTERNATIONAL FEDERATION FOR STRUCTURAL CONCRETE. **CEB-FIB**. International Recommendations for the Design and Construction of Concrete Structures, 2010.

72 LEE, M. BARR, B. An overview of the fatigue behavior of plain and fiber reinforced concrete. **Cement & concrete Composites,** vol. 26, p. 299-305, 2004.

73 GRZYBOWSKI, M. MEYER, C. Damage accumulation in concrete with and without fiber reinforcement. **ACI Materials Journal**, vol. 90, p. 594-604, 1993.

74 CACHIM, P. FIGUEIRAS, J. PEREIRA, P. Fatigue behavior of fiber-reinforced concrete in compression. **Cement & Concrete Composites**, vol. 24, p. 211-217, 2002.

75 POVEDA, E. RUIZ, G. CIFUENTES, H. YU, R. ZHANG, X. Influence of the fiber content on the compressive low-cycle fatigue behavior of the self-compacting SFRC. **International Journal Fatigue**, vol. 101, p. 9-17, 2017.

76 BANJARA, N. RAMANJANEYULU, K. Experimental investigations and numerical simulations on the flexure fatigue behavior of plain and fiber-reinforced concrete. **Journal of Materials in Civil Engineering**, vol. 30, 2018.

77 SINGH, S. SHARMA, U. Flexure fatigue strength of fibrous concrete beams. **Advances in Structural Engineering**, vol. 10, p. 197-207, 2007.

78 GOEL, S. SINGH, P. Fatigue performance of plain and steel fibre reinforced self-compacting concrete using S-N relationship**. Engineering Structures**, vol. 74, p. 65-73, 2014.

79 MEDEIROS, A. ZHANG, X. RUIZ, G. YU, R. VELASCO, M. Effect of the loading frequency on the compressive fatigue behavior of plain and fiber reinforced concrete. **International Journal of Fatigue**, vol. 70, p. 342-350. 2015.

80 SAUCEDO, L. YU, R. MEDEIROS, A. ZHANG, X. RUIZ, G. A probabilistic fatigue model based on the initial distribution to consider frequency effect in plain and fiber reinforced concrete. **International Journal of Fatigue**, vol. 48, p. 308-318, 2013.

81 HSU, T. Fatigue of plain concrete. **Journal of American Concrete Institute**, vol. 76, p. 292-305, 1981.

82 STANDARD DNVGL-ST-0126. **DNV GL AS:** Support structures for wind turbines, 2016.

83 CARLESSO, D. DE LA FUENTE, A. CAVALARO, S. Fatigue of cracked high performance fiber reinforced concrete subjected to bending. **Construction and Building Materials**, vol. 220, p. 444-455, 2019.

84 CARLESSO, D. CAVALARO, S. DE LA FUENTE, A. Flexural fatigue of pre-cracked plastic fibre reinforced concrete: Experimental study and numerical modeling. **Cement and Concrete Composites**, vol. 115, 2021.

85 RAMAKRISHNAN, V. WU, Y. HOSALLI, G. Flexural fatigue strength, endurance limit, and impact strength of fiber reinforced concretes. **Transportation Research Record**, vol. 1226, p. 17-24 1990.

86 PARANT, E. ROSSI, P. BOULAY, C. Fatigue behavior of a multi-scale cement composite. **Cement and Concrete Research**, vol. 37, p. 264-269, 2007.

87 STEPHEN, G. GETTU, R. Fatigue fracture of fibre reinforced concrete in flexure. **Materials and Structures**, p. 53-56, 2020.

88 SUBRAMANIAM, KV. O'NEIL, E. POPOVICS, J. SHAH, S. Crack propagation in flexure fatigue of concrete. **Journal of Engineering Mechanics**, vol. 126, p. 891-898, 2000.

89 GERMANO, F. TIBERTI, G. PLIZZARI, G. Post-peak fatigue performance of steel fiber reinforced concrete under flexure. **Materials and Structures**, vol. 49, p. 4229-4245, 2015.

90 NAAMAN, A. HAMMOUD, H. Fatigue characteristics of high performance fiber-reinforced concrete. **Cement and Concrete Composites**, vol. 20, p. 353-363, 1998.

91 EUROPEAN STANDARD. **EN 14651**: Test method for metallic concrete - Measuring the flexural tensile strength (limit of proportionality (LOP), residual), 2005.

92 PARVEZ, A. FOSTER, S. Fatigue behavior of steel fiber reinforced concrete beams. **Journal of Structural Engineering**, vol. 141, 2014.

93 JOHNSTON, C. ZEMP, R. Flexural fatigue performance of steel fiber reinforced concrete – influence of fiber content, aspect ratio and type. **ACI Materials Journal**, vol. 88, p. 374-383, 1991.

94 ZHANG, J. STANG, H. Fatigue performance in flexure of fiber reinforced concrete. **ACI Materials Journal**, vol. 95, 58-67, 1998.

95 GAO, D. GU, Z. WU, C. Bending behavior and deflection prediction of high-strength SFRC beams under fatigue loading. **Journal of Materials Research and Technology**, vol. 9, p. 6143-6159, 2020.

96 HUANG, B. LI, Q. XU, S. ZHANG, L. Static and fatigue performance of reinforced concrete beam strengthened with strain-hardening fiber-reinforced cementitious composite. **Engineering Structures**, vol. 199, 2019.

97 LEE, Y. WILLAN, K. Mechanical properties of concrete under cyclic compression. **ACI Materials Journal**, vol. 94, p. 457-467, 1997.

98 OTTER, D. NAAMAN, A. Properties of steel fiber reinforced concrete under cyclic load. **ACI Materials Journal**, vol. 85, 254-261, 1988.

99 TANGAWA, S. HATANAKA, S. Stress-strain relations of steel fiber reinforced concrete under repeated compressive load. **Cement and Concrete Research**, vol. 19, p. 801-808, 1983.

100 SAKAI, J. KAWASHIMA, K. Unloading and reloading stress-strain model for confined concrete. **Journal of Structural Engineering**, vol. 132, p. 112-122, 2006.

101 ANDRIOTIS, C. GKIMOUSIS, I. KOUMOUSIS, V. Modeling reinforced concrete structures using smooth plasticity and damage models. **Journal of Structural Engineering**, vol. 142, 2016.

102 BRECCOLOTTI, M. BONFIGLI, M. D'ALESSANDRO, A. MATERAZZI, A. Constitutive modeling of plain concrete subjected to cyclic uniaxial compressive loading. **Construction and Building Materials**, vol. 94, p. 172-180, 2015.

103 ASLANI, F. JOWKARMEIMANDI, R. Stress-strain model for concrete under cyclic loading. **Magazine of Concrete Research**, vol. 64, p. 673-685, 2012.

104 SIMA, J. ROCA, P. MOLINS, C. Cyclic constitutive model for concrete, **Engineering Structures**, vol. 30, p. 695-706, 2008.

105 LI, B. XU, L. CHI, Y. LI, C. Cyclic tensile behavior of SFRC: experimental research and analytical model. **Construction and Building Materials**, vol. 190, p. 1236-1250, 2018.

106 KRAHL, P. CARRAZEDO, R. DEBS, M. Mechanical damage evolution in UHPFRC: experimental and numerical investigation. **Engineering Structures**, vol. 170, p. 63-77, 2018.

107 KRAHL, P. GIDRÃO, G. CARRAZEDO, R. Cyclic behavior of UHPFRC under compression. **Cement and Concrete Composites**, vol. 104, 2019.

108 GRASSL, P. JIRASEK, M. Damage-plastic model for concrete failure. **International Journal of Solids and Structures**, vol. 43, p. 7166-7196, 2006.

109 XU, L. WEI, C. LI, B. Damage evolution of steel-polypropylene hybrid fiber reinforced concrete: experimental and numerical investigation. **Advances in Materials Science and Engineering**, vol. 2018, 2018.

3 Mechanisms of fiber-matrix interface degradation under fatigue in steel FRC

The present work reports the outcomes of an experimental research on the steel fiber-cement based matrix interface degradation under fatigue loading. The bond degradation was assessed for two distinct fiber types: hooked and straight steel fibers. First, the fiber bond inside the concrete matrix was analyzed through quasi-static pullout tests in accordance with the stablished literature of the topic. Thereafter, fatigue tests were carried on at different load levels (95%, 85%, 70% and 50%) up to 1,000,000 cycles or up to failure. Through the experimental campaign, it was possible to investigate two distinct failure modes: fiber pullout and fiber rupture under fatigue. While the hook is progressively straightened along the fatigue life when the fiber is pulled out under fatigue, no slip takes place when fiber rupture is concerned. Novel models were proposed to estimate slip evolution of steel fibers during the fatigue pullout tests. Although slip is almost constant when fiber rupture takes place, an exponential curve was adopted in terms of the pre-slip level for the fiber pullout failure mode.

Published article: February 23rd, 2023 – *Journal of Building Engineering, https://doi.org/10.1016/j.jobe.2023.106168*

3.1. Introduction

The number of applications of fiber reinforced concrete (FRC) members exposed to fatigue loading has sharply increased in the last years, including concrete railway bridges [1] and pavements [2] until wind tower rings [3] and offshore structures [4]. Generally, FRC structures are subjected to cyclic and repetitive loading due to thermal variations, traffic loadings, external vibrations and wind/wave actions, which are responsible for crack initiation and propagation throughout the structure life [5-7]. The types of fatigue loading can occur independently or simultaneously, which can result in a drastic lifespan reduction of the structure and an unexpected failure [8].

When it comes to the study of fiber reinforced concrete under fatigue loading, the stiffness progressive decrease is key when it comes to the evaluation of the degradation throughout the lifespan [9, 10]. Past research has successfully described how damage evolves in FRC under cyclic loading, bringing new empirical equations to model stiffness decay [11-15]. Carlesso *et al.* [11], for instance, verified that, after reaching 30% of damage index, a sharp increase in damage takes place until reaching the material failure. Similar study was also carried on by Stephen *et al.* [12], who observed a major change on the crack mouth opening displacement (CMOD) rate per cycle. The CMOD evolution rate presents a decrease tendency at the beginning and then becomes almost constant along the material life span. This behavior dramatically changes when the specimen reaches a critical point (CMODCR) situated between the transition between the second and the third stages of cracking under fatigue. After the critical point, cracking sharply increases and leads to the complete collapse of the FRC.

The mechanical behavior and fatigue response of fiber reinforced composites are directly controlled by the fiber-matrix characteristics [16-18], which are responsible for affecting the adherence strength [19]. The post-peak response of FRC is attributed to some general fiber material and geometrical properties, such as elasticity modulus, diameter and length [20]. The most common method to properly assess the bond strength is through pullout tests [21, 22], in which fiber slip is monitored as a function of the pullout load applied to the fiber. The bond between fiber and the surrounding cementitious matrix has already been vastly studied in the literature [23-26] and is divided in two main phases: debonding and frictional pullout. While debonding can be understood as a cracking process inside the fiber-matrix zone, the frictional process developed along the interface after the adhesion bond is fully ruined [27, 28]. When hooks are added on the fiber ends, they provide mechanical interlock through matrix, significantly increasing the peak bond strength [29, 30].

However, there is still a gap of research when it comes to the evaluation of fiber-matrix degradation under fatigue loading. More recently, Fataar *et al.* [31] brought an experimental study on the fatigue failure of steel fiber reinforced concrete at a single fiber level. The authors performed a series of fatigue tests on pre-slipped, steel fiber reinforced concrete at different fatigue load levels (50%, 70% and 85%). According to the results, the failure mechanisms observed were fiber rupture and fiber pullout. At high pre-slip and high-load levels, pullout was the dominant failure mechanism. On the other hand, fiber rupture was dominant at low pre-slip values. Once the hook was completely straightened out, the fatigue resistance was significantly reduced. However, the worked of Fataar *et al.* [31] still did not bring an appropriate and comprehensive analysis on the mechanisms that lead to the distinct interface failure types under fatigue loading. Moreover, novel equations to verify fatigue slip evolution along interface were also not proposed in the literature. Present research aims to partially fill some of the gaps left by the last works of Fataar *et al.* [31].

Aiming to better understand the damage evolution in the fracture process zone (FPZ), Vicente *et al.* [32] studied the internal microstructure of FRC after carrying cyclic tests on pre-cracked beams through computed tomography scanning [33, 34]. According to the captured tomography images of the areas surrounding the crack, fiber rupture and debonding were the two main observed failure modes. Overall, over 80% of failure are due to debonding, while 20% is associated due to fiber breakage. Failure due to debonding showed a more ductile behavior.

The present work brings an experimental research on the steel fiber-cement based matrix interface degradation when under fatigue loading. Both hooked-end and straight steel fibers are analyzed. The steel fibers were, first, pre-slipped in distinct levels after peak before beginning the fatigue load. Tests were carried on at different load levels (95%, 85%, 70% and 50%) up to 1,000,000 cycles or up to failure. Since fibers are activated after crack has taken place, the process of pre-slipping simulates the behavior of a fiber in a cementitious matrix once a crack has evolved. The process of pre-slipping misses initial phase of the process, which is would be mainly governed by the physicochemical adherence of the matrix onto the fiber surface. Therefore, the analysis of the fatigue pullout after pre-slipping focuses primarily on the mechanical friction on the fiber-matrix interface. Present work considers, therefore, only the fiber bridging along a perpendicular crack propagation in a fiber reinforced concrete structure. Fiber failure modes and slip evolution were subsequently studied for analyzed fatigue loading conditions.

Finally, novel models for evaluating slip evolution and fiber rupture are proposed in accordance to the achieved experimental results. The main contribution of the present experimental analysis is by bringing a clear comprehension on the interface degradation under fatigue loading, which has not still properly studied in the literature.

3.2. Experimental program

3.2.1.Materials

A self-consolidating concrete matrix was used to evaluate the interface degradation under fatigue loading. The matrix composition consisted of two classes of particle size of river sand: the first one ranged from 0.15 mm to 4.8 mm (S1) and the second from 0.15 to 0.85 mm (S2). Brazilian CPII-F 32 (ASTM Cement type IL - Portland-Limestone Cement [35]) was the applied cement. Fly ash, silica fume and silica mesh 325 (ground quartz) were the three mineral additions for the present mix composition. The original concrete formulation also included coarse aggregate (maximum diameter of 9.5 mm) but it was not used for the pullout tests. Two admixture were used: the superplasticizer MasterFlenium 51 and the viscosity modifying admixture MasterMatrix VMA 358. After 28 days, the concrete matrix reached 50 ± 2 MPa for a water/cement ratio of 0.50. The matrix composition was designed with the compressible packing model (CPM) as proposed by de Larrard [36]. More information on the material development can assessed by Rambo *et al.* [37, 38]. Fresh concrete mixture was characterized according to their flow ability based on ASTM C1611 [39]. A value of 710 mm of concrete spread was reached for the present concrete matrix. For the purpose of molding pullout specimens, the coarse aggregate was not added to the mixture. Table 3.1 shows the studied mix composition.

Two distinct steel fibers (SF1 and SF2) were studied in this research. SF1 refers to a hooked-end steel fiber with 35 mm length, 45 of aspect ratio and 1225 MPa of wire direct tension strength. SF2 is associated to a plain steel fiber with 50 mm length, 67 of aspect ratio and 1225 MPa of direct tension strength. Straight steel fibers were obtained cutting the hooks out from hooked-end steel fibers with 60 mm length. Table 3.2 summarizes the properties for the two studied steel fibers.

Table 3.1 - Mix composition of self-consolidating concrete matrix

Constituent	Matrix
Sand (S1) (kg/m^3)	827
Sand (S2) (kg/m^3)	100
Silica Mesh 325 (kg/m^3)	70
Cement (kg/m^3)	360
Fly Ash (kg/m^3)	168
Silica Fume (kg/m^3)	45
Water (kg/m^3)	164
Superplasticizer (%)	5.50
Viscosity modifying admixture (%)	0.75

**Sand (S2): Sand (S1) with diameter less than 0.85 mm*

3.2.2. Mixing procedure

Figure 3.1(a) shows the details of the molding process. A special designed two-part mold was produced using a 3D-printer. A single fiber was positioned in the center part of the mold before pouring the fresh cement based matrix. The fiber embedded length was set to 15 mm for SF1 and 22.5 mm for SF2. Since the embedded lengths are the same on both sides, the pullout may occur from either side without any detrimental effects on the results. The second half of the mold was poured 24 hours after the first one. The specimens were cured in humid chamber for 28 days at controlled temperature of 22ºC and humidity (55%). Figure 3.1(b) shows the specimen dimensions.

The mortar was produced with a 5L mixer. First, the river sands S1 and S2 were added with 70% of the water and blended together for 1 minute. The second step consisted on applying the mineral and cementitious materials (silica fume, silica flour and fly ash) and mixing with the sand for another minute. Thereafter, the cement is added and blended for 1 minute. The 30% remaining water, the viscosity modifying admixture and superplasticizer are, finally, added to the mixer and blended with the rest of the materials for 10 minutes. For the cast of each side of the pull-out specimens, 1 L of mortar was prepared.

Table 3.2 – Steel fiber properties

Properties	SF1 	SF2 
Type	Hooked-end	Straight
Length (mm)	35	50
Diameter (mm)	0.75	0.75
Aspect Ratio	45	67
Tension strength (MPa)	1225	1225

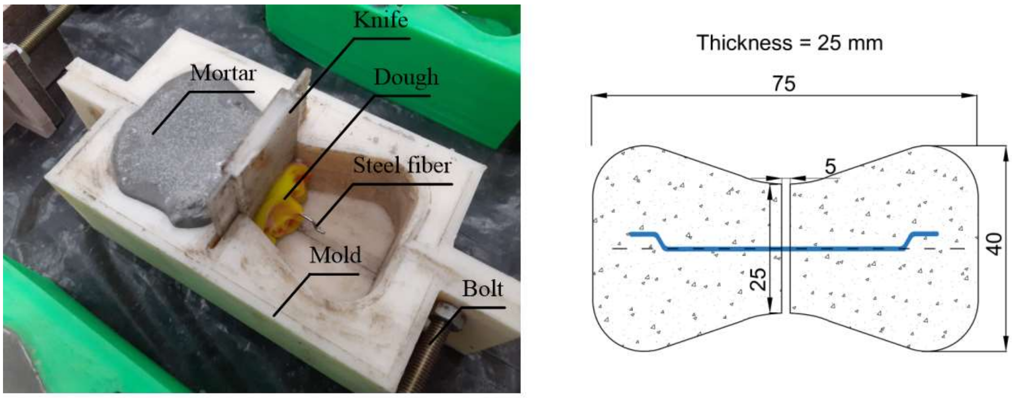

(a) (b)

Figure 3.1 - Details of the pullout specimen molding: (a) fabrication and (b) specimen dimensions in mm.

3.3. Test Program

3.3.1. Static pullout test

All static and fatigue pullout tests were carried on using a MTS 809 servo-hydraulic machine, with 5 kN capacity external load cell. An additional external linear variable differential transducer (LVDT) of 10 mm length limit was also applied to ensure the pullout reading accuracy during both static and fatigue tests. Two aluminum claws were fabricated in order to clamp the specimens prior to the beginning of the tests. Figure 3.2 brings an overview of the test setup used in this research.

The static tests were carried on at a displacement-controlled rate of 0.50 mm/min until reaching the complete fiber pullout of the specimen. The initial accommodation was minimized by applying a 15 N pre-load on the specimen.

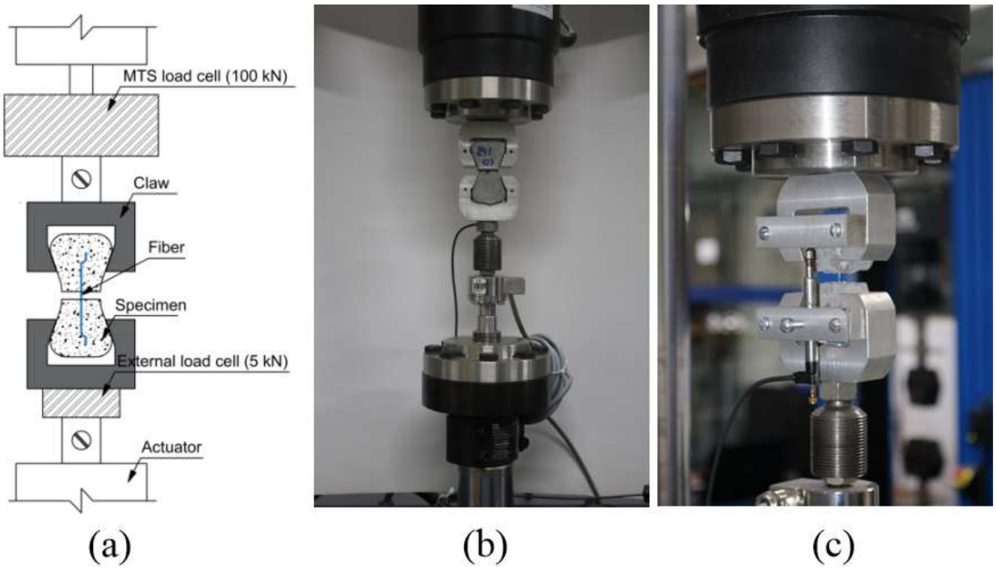

Figure 3.2 - Pullout test setup: (a) test illustration, (b) pullout test setup overview and (c) LVDT positioning detail.

3.3.2. Fatigue test

The fatigue tests were divided in two steps. First a static pullout test was carried on until reaching the determined pre-slips. Pre-slip is defined as a process of displacing a fiber to a certain extent before carrying the test. The processes of pre-slipping the fibers aims to simulate the behavior of the fiber in a cementitious matrix once a crack has formed. Distinct pre-slips were applied in accordance with the static pullout behavior of the steel fiber. The pre-slips were carried on after reaching the maximum bond strength, situated in the region after the fiber has been fully debonded (pre-slip range between 1.4 and 1.8 mm and above 3.0 mm) for hooked end steel fibers and for straight steel fiber (from 1.0 mm to 1.5 mm of pre-slip). The static pre-slip tests were displacement-controlled at a rate of 0.50 mm/min. The maximum bond pullout load was recorded as a reference for the fatigue tests. Figure 3.3 summarizes the fatigue test routine.

Thereafter, the fatigue tests were loaded up to 1 million cycles with a sinus load application having a frequency of 6 Hz. The fatigue tests were carried on in accordance with the load level (S). The fatigue cycle's upper load (P_{upp}) was evaluated by multiplying the load level (*S*) by of the maximum pullout load previously recorded during the pre-slip (P_{max}), $P_{upp} = SxP_{max}$. The lower load (P_{low}) was estimated based on the load amplitude, which was kept constant for all tests ($R = P_{low}/P_{upp} = 0.05$). A total of 33 specimens were tested for the following percentages of P_{max} (load level *S*): 95%, 85%, 70% and 50%.

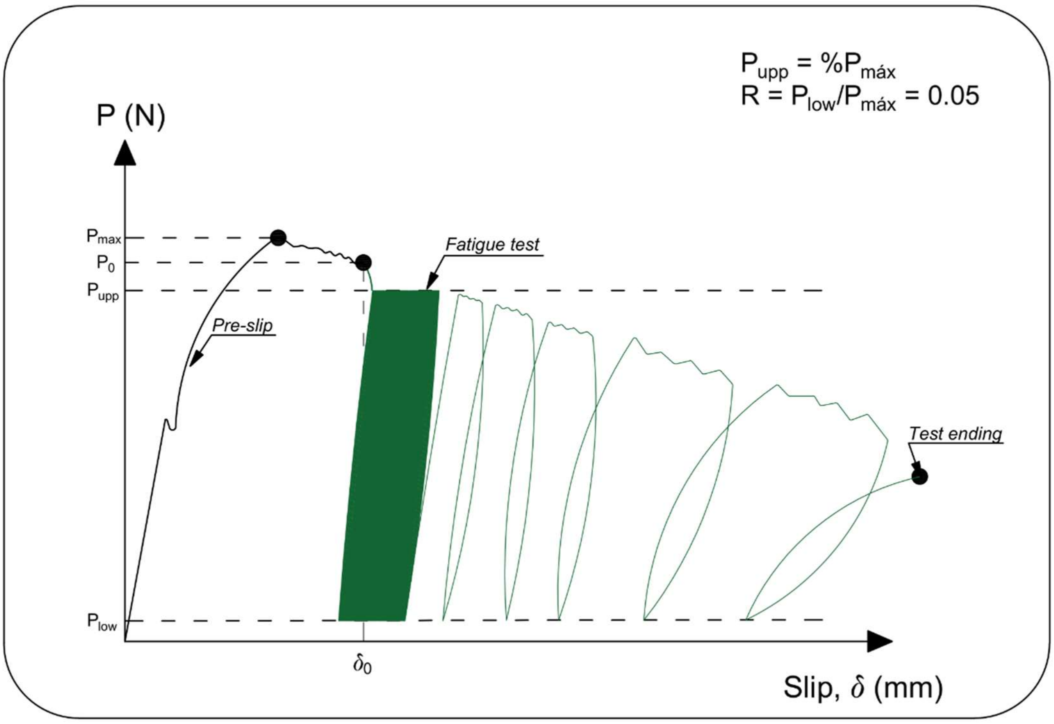

Figure 3.3 – Fatigue test program

3.4. Discussion and analysis

3.4.1. Steel fiber pullout behavior

Figure 3.4(a) shows the pullout behavior for both SF1 and SF2. A total of 10 specimens were tested for each fiber in order to characterize the pullout response inside the cementitious matrix. The mean curve is displayed by a prominent line with the standard deviation presented through a grey transparent cloud around it. While SF1 reports 7.8 MPa of peak adherence strength, SF2 presents a mean maximum value of pullout stress of around 1.3 MPa. Interfacial pullout stress was calculated according to equation 3.1.

$$\tau = \frac{P}{\pi d l_f} \tag{3.1}$$

Where *d* is the fiber diameter and l_f the embedded length.

The steel fiber pullout response has already been vastly studied in the literature [21-30] for both hooked and straight steel fibers. Figure 3.5 presents a global overview of the fiber pullout phases from a cementitious matrix. Generally, the pullout response consists of two basic stages: debonding and frictional pullout [40, 41]. While the debonding process has generally the same characteristics for both fiber types, large differences take place in the frictional stage as a cracking process along the interface between fiber and matrix occurs. During debonding (phase *a* in Figure 3.5), the pullout force increases until the adhesion is completely lost [40]. For straight fibers, after complete debonding (phase *b*), frictional stresses develop along the interface zone during fiber slip across the interface with progressive decrease of the pullout force.

Basically, the same phenomena reported for straight fibers are valid for hooked-end fibers as well [42]. However, fiber hook provides a mechanical interlock and its plastic deformation in the first phases is responsible for enriching the peak pullout force of the fiber from the matrix. After the fiber is fully debonded (phase *b*), bending of both curved parts of the hook begins (phases *b* to *c*) [43]. As pullout continues and reaches its peak stress, the pullout force begins to decrease (phase *c* to *d*). After the second curvature of the hook has also been completely straightened, the fiber keeps on slipping through the channel (phase *e*). Since the fiber hook is usually not completely straightened during phase e, this generates an additional effect on the pullout resistance in relation to straight fiber [44]. Figure 3.4(a) reports significantly higher results of frictional pullout stress for SF1 with a mean value of 3 MPa. SF2, in turn, presents an almost constant pullout stress of around 0.8 MPa after 4 mm slip.

The pullout characteristic response is key for evaluating the fatigue behavior in the next section. Figure 3.4(b) brings the pre-slip of nine distinct pullout specimens before beginning the fatigue test. When it comes to SF1, the pre-slip is interrupted right after reaching peak (phases *c* to *d*) and the hooked-end has not been completely straightened (pre-slip range between 1.4 and 1.8 mm). On the other hand, three specimens on figure 3.4(b) show higher levels (above 3 mm) of pre-slip, which a major decay on the pullout force has already taken place (phase *e*). Hence, the pullout fatigue response can be analyzed before and after the hook has already been straightened. The same procedure was applied for SF2, where the pre-slip was carried on right after reaching peak (phase *e*). The process of pre-slipping aims to simulate the fiber behavior in a cementitious matrix right after the crack has evolved.

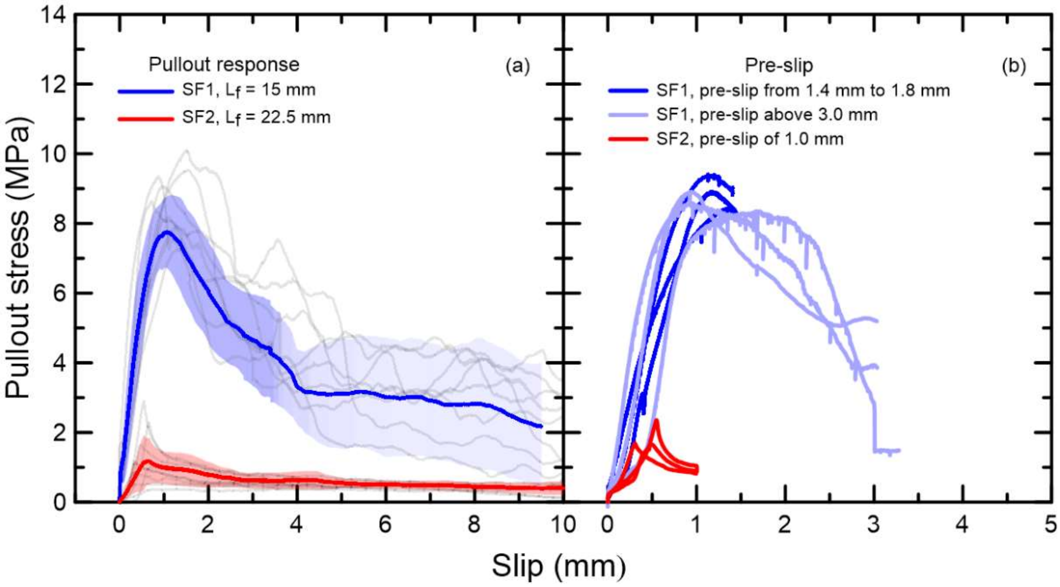

Figure 3.4 - Pullout test results: (a) pullout behavior of SF1 and SF2 and (b) pre-slip curves before fatigue test initiation.

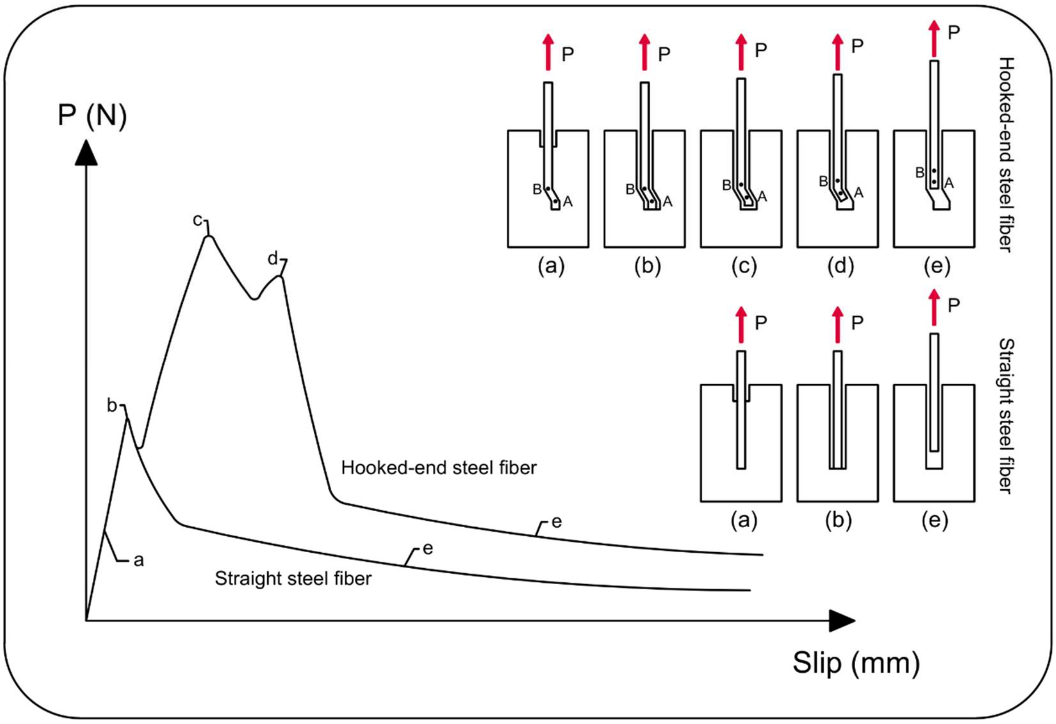

Figure 3.5 - Typical pullout response for straight and hooked-end steel fibers

3.4.2. Steel fiber-reinforced concrete matrix interface failure under fatigue loading

3.4.2.1. Hooked-end steel fiber failure modes

Table 3.3 summarizes the number of cycles until failure in terms of distinct applied load levels ($S = \%P_{max}$) for hooked-end steel fibers under two levels of pre-slip (δ_0 range between 1.4 and 1.8 mm and above 3.0 mm). For all studied specimens, Table 3.3 also indicates the maximum adherence force (*Pmax*) and the maximum interfacial pullout stress (τ_{max}). *P0* and τ_0 are associated to pullout load and interfacial strength at the referenced pre-slip, respectively. The observed failure modes are also indicated.

Two distinct failure modes were observed for the pullout fatigue tests: fiber failure and fiber pullout. The specimens assigned as run-out did not present any of the failure modes before reaching 1,000,000 or 500,000 cycles. Figure 3.6 brings an overall analysis of the number of cycles before failure for all carried on fatigue tests. There is a clear distinct division in terms of number of cycles for each observed failure mode. While any specimen exceeded 10^3 cycles for pullout failure, this limit was around $2x10^5$ for fiber rupture. The failure modes also modify depending on the applied load level and the pre-slip level. For pre-slips between 1.4 and 1.8 mm, the pullout failure was only observed when 95% of load level was carried on the mechanical tests. For over 3 mm of pre-slip, the fiber pullout was verified for $S = 70\%$ and $S = 50\%$.

The pullout fatigue response is directly influenced by the interfacial bond strength and the pre-slip level. For pre-slips between 1.4 and 1.8 mm, the recorded interfacial stress (τ_0) is almost identical to the peak pullout load (P_{max}), which guaranteed higher number of cycles before reaching failure for all studied load levels (*S*). When higher pre-slips take place, the reference interfacial stress (τ_0) becomes significantly lower in relation to the peak. Consequently, the fatigue life of the specimen also decreases. Overall, the higher pre-slip levels promote a significant decay on the pullout resistance in relation to the peak bond strength, which also results in major decay on the fatigue life of the specimens.

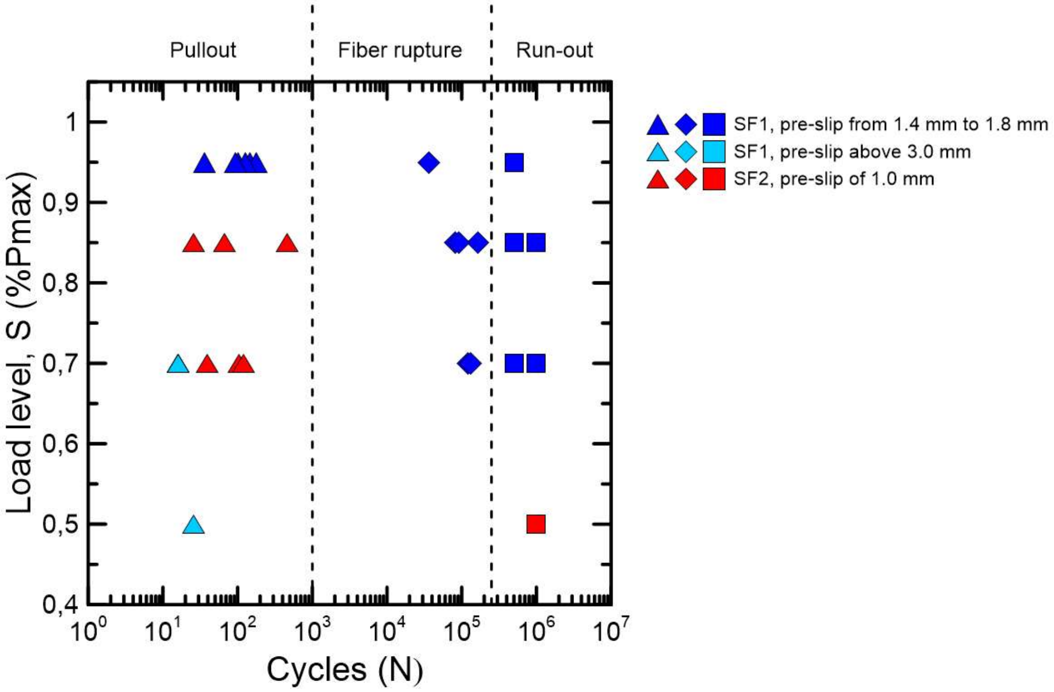

Figure 3.6 - Observed failure modes in terms of load level *S* (*%P_{max}*) for applied fatigue tests.

3.4.2.1.1. Fiber pullout failure

The fiber pullout is directly linked to upper load of the fatigue tests (P_{upp}). When P_{upp} is above the pre-slip pullout force (P_0), the fiber is continuously pulled out along the fatigue test. Since P_0 is the pullout force at the moment the pre-slip is suspended, P_0 is the maximum pullout force capable to maintain the fiber inside the concrete matrix. Figure 3.7 presents a pullout fatigue test result for a hooked-end steel fiber (SF1) pullout failure mode. It is possible to verify the continuous pullout of the fiber during the fatigue test. The slip carries on until reaching the embedded length.

During the process of pullout, the hook is progressively straightened under the fatigue cycles. For the first pre-slip range (from 1.4 mm until 1.8 mm), the hook is still playing a major role on the pullout strength of the steel fiber inside the matrix [41], as shown in Figures 3.4 and 3.5, and is able to promote higher values of cycles before the test end. When the pre-slip is over 3 mm, the hook has already undergone considerable plastic deformation and is not able to resist the uninterrupted pullout cycles. Hence, the number of cycles before completing pullout is slightly higher for lower pre-slips.

Figure 3.8(a) shows the region of the hook after it has been completely straightened during the pullout fatigue test. The image was obtained through a

Scanning Electron Microscope and it is possible to observe a small crack at the original region of the hook. Moreover, a corrugated shape at the region of the hook also takes place due to the partial straightening during pullout. The process of hook straightening under fatigue seems to be similar to that already observed in quasi-static pullout tests and reported in the literature [40, 41, 44].

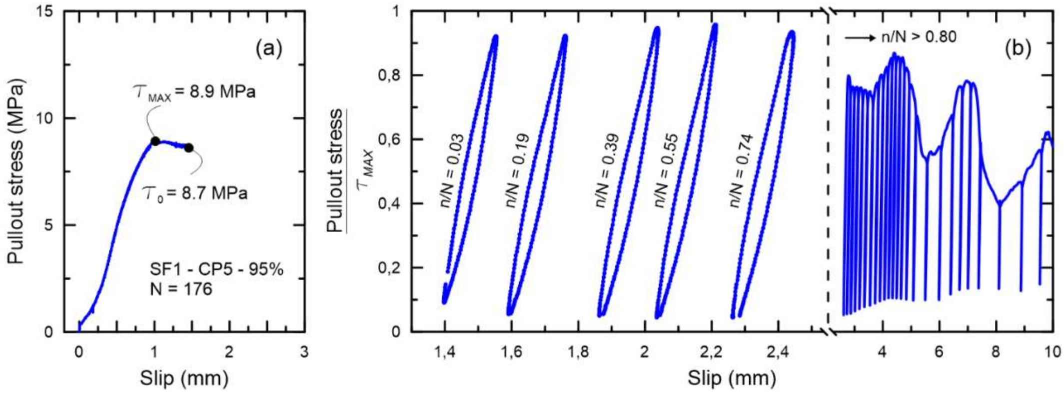

Figure 3.7 - Hooked-end steel fiber (SF1) pullout under fatigue loading: (a) pre-slip and (b) hysteresis cycles under fatigue.

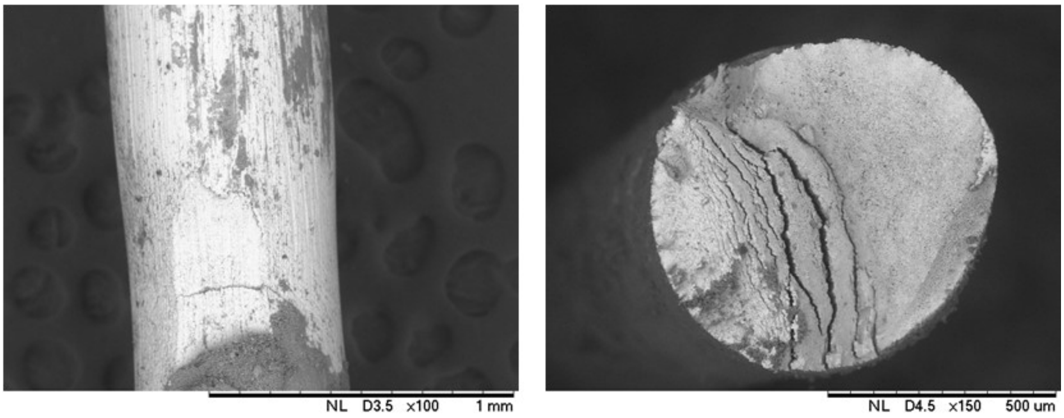

(a)

(b)

Figure 3.8 - Fiber failure images after fatigue test with Scanning Electron Microscope: (a) fiber hook straightening after pullout and (b) fiber cross-section after rupture.

3.4.2.1.2. Fiber rupture

A second failure mode takes place when the fiber is submitted to pullout fatigue loading. Fiber rupture occurs when the maximum fatigue load (P_{upp}) is not sufficient for pulling the fiber out from the cementitious matrix during loading cycles. Since the fiber-matrix interface is able to restrain fiber slip, the fatigue of the steel fiber becomes the predominant study concern. Table 3.4 brings only the results for the specimens, which presented fiber rupture as failure mode.

Table 3.3 - Results for fiber-matrix interface degradation under fatigue loading

Specimen	Fiber	$S = \%P_{max}$	δ_0	P_{max}	τ_{max}	P_0	τ_0	P_{upp}	Cycles (N)	Failure mode
			mm	N	MPa	N	MPa	N		
HE95%δ1 - 1	SF1	95%	1.72	487	13.8	441	12.5	462	144	Pullout
HE95%δ1 – 2	SF1	95%	1.42	315	8.9	290	8.2	300	36852	Rupture
HE95%δ1 – 3	SF1	95%	1.82	471	13.3	446	12.6	447	101	Pullout
HE95%δ1 – 4	SF1	95%	1.63	389	11.0	368	10.4	369	500000	Run-out
HE95%δ1 – 5	SF1	95%	1.73	483	13.7	459	13.0	458	176	Pullout
HE95%δ1 – 6	SF1	95%	1.41	315	8.9	307	8.7	299	128	Pullout
HE95%δ1 – 7	SF1	95%	1.60	316	9.0	311	8.8	300	94	Pullout
HE95%δ1 – 8	SF1	95%	1.62	406	11.5	379	10.7	386	36	Pullout
HE85%δ1 – 1	SF1	85%	1.64	307	8.7	287	8.1	261	82807	Rupture
HE85%δ1 – 2	SF1	85%	1.85	396	11.2	375	10.6	337	1000000	Run-out
HE85%δ1 – 3	SF1	85%	1.46	331	9.4	318	9.0	281	163771	Rupture
HE85%δ1 – 4	SF1	85%	1.55	311	8.8	302	8.5	264	90358	Rupture
HE85%δ1 – 5	SF1	85%	1.49	346	9.8	335	9.5	294	500000	Run-out
HE85%δ1 – 6	SF1	85%	1.44	425	9.8	410	9.5	361	33807	Rupture
HE70%δ1 – 1	SF1	70%	1.45	332	9.4	312	8.8	232	500000	Run-out
HE70%δ1 – 2	SF1	70%	1.47	298	8.4	291	8.2	209	500000	Run-out
HE70%δ1 – 3	SF1	70%	1.69	413	11.7	390	11.0	289	120195	Rupture
HE70%δ1 – 4	SF1	70%	1.32	301	8.5	277	7.83	211	130635	Rupture
HE70%δ1 – 5	SF1	70%	1.45	288	8.149	208	5.89	202	1000000	Run-out
HE70%δ1 – 6	SF1	70%	1.62	346	9.79	325	9.2	242	274447	Rupture
HE70%δ3 – 1	SF1	70%	3	303	8.573	136	3.85	212	16	Pullout
HE70%δ3 – 2	SF1	70%	3	294	8.318	52	1.47	206	16	Pullout
HE70%δ3 – 3	SF1	70%	3	341	9.648	179	5.06	239	16	Pullout
HE50%δ3 – 1	SF1	50%	3	406	11.49	192	5.43	203	26	Pullout
HE50%δ3 – 2	SF1	50%	3	315	8.913	183	5.18	158	1000000	Run-out
HE50%δ3 – 3	SF1	50%	3.3	378	10.7	193	5.46	189	1000000	Run-out
S85%δ1 – 1	SF2	85%	1.1	91	1.717	54	1.02	77	67	Pullout
S85%δ1 – 2	SF2	85%	1	116	2.188	86	1.62	99	463	Pullout
S85%δ1 – 3	SF2	85%	1	125	2.358	49	0.92	106	26	Pullout
S70%δ1 – 1	SF2	70%	1	90	1.698	43	0.81	63	103	Pullout
S70%δ1 – 2	SF2	70%	1	88	1.66	47	0.89	62	120	Pullout
S70%δ1 – 3	SF2	70%	1.1	142	2.679	82	1.55	99	39	Pullout

Identification: Fiber – Load level (S) – Pre-slip – Specimen n°
HE50% δ3 – 2 = Hooked end steel fiber (SF1) - Load level (S) = 50% - around 3 mm of pre-slip – specimen n°2

Figure 3.9 shows a $\Delta\sigma$ x Cycles until failure (N) graph presenting the obtained results of the fiber rupture fatigue pullout tests. $\Delta\sigma$ represents the stress variation during the fatigue test. Similar research was carried on by Fataar *et al.* [31] and the results are also reported in Figure 3.9. The work in hand is also compared with the fatigue curves achieved for a 0.15% C steel with 418 MPa of ultimate tensile stress, studied by Meyer [45]. Another relation is also made with a high strength steel studied by Liu *et al.* [46], where ultimate stresses of 1732 MPa and 1900 MPa are reported for ‘steel 1’ (60Si2Mn) and ‘steel 2’ (54SiCr6), respectively. Both steel types present similar tensile strength in relation to the hooked-end steel fiber, SF1 (1225 MPa).

As shown in Figure 3.9, the number of cycles before failure of the steel fiber under fatigue pullout is significantly lower in relation to other studied steels. For a $\Delta\sigma$ of around 600 MPa, the steel fiber reaches the rupture around 10^5 cycles and the steel 2 (54SiCr6), around 10^7 cycles. Since Fataar *et al.* [31] also reported fiber rupture under pullout fatigue, the author results were integrated to the present research and a novel $\Delta\sigma$ in terms of the number of cycles until failure (N) is proposed in Figure 3.9. Equation 3.2 brings the developed equation for fiber rupture under pullout fatigue.

$$\Delta\sigma = -133.6log_{10}(N) + 2116 \tag{3.2}$$

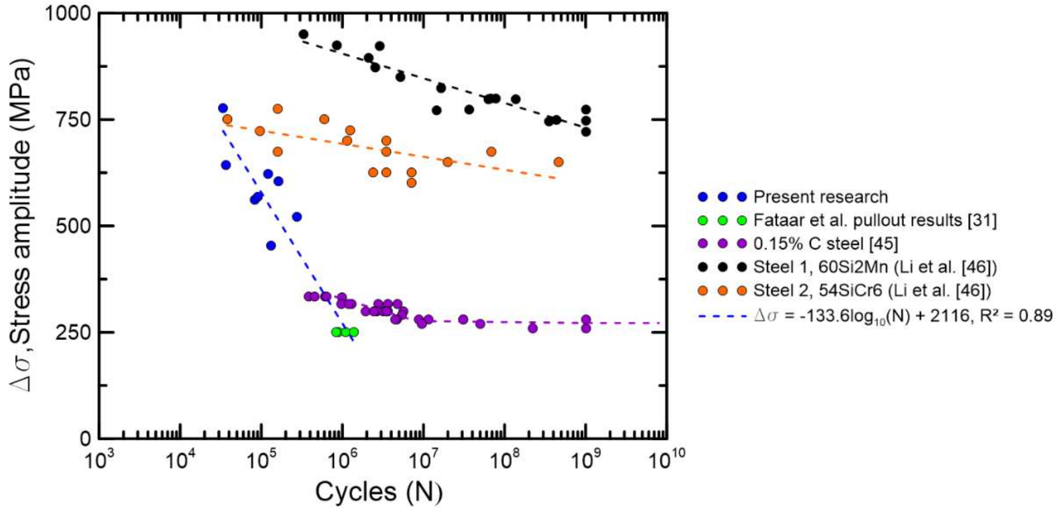

Figure 3.9 - Stress amplitude in terms of the number of cycles until failure for fiber rupture under pullout fatigue tests. Comparison with 0.15%C, 60Si2Mn and 54SiCr6 steels from distinct authors.

The lower fatigue life in relation to the traditional tensile fatigue tests on steel can be associated to the eccentricity of the applied force in relation to the hook position inside the concrete matrix. The eccentricity can be verified through the distance between the fiber central axis and hook axis, which is around the 1.20 mm, in accordance to the manufacturer. Therefore, the region of the curve of the hook ends up becoming the main weakness area. A CT-scan tomography was applied to the concrete specimen after the pullout test and the image of the hook inside the matrix can be analyzed in figure 3.10. Differently to what is observed on traditional fatigue tests, the central region of fiber is not the main area of analysis and the presence of the hook modifies the fatigue rupture failure of the steel fibers. Figure 3.10(b) shows the cracked cross section of the fiber after rupture, which was visualized with the help of a Scanning Electron Microscope.

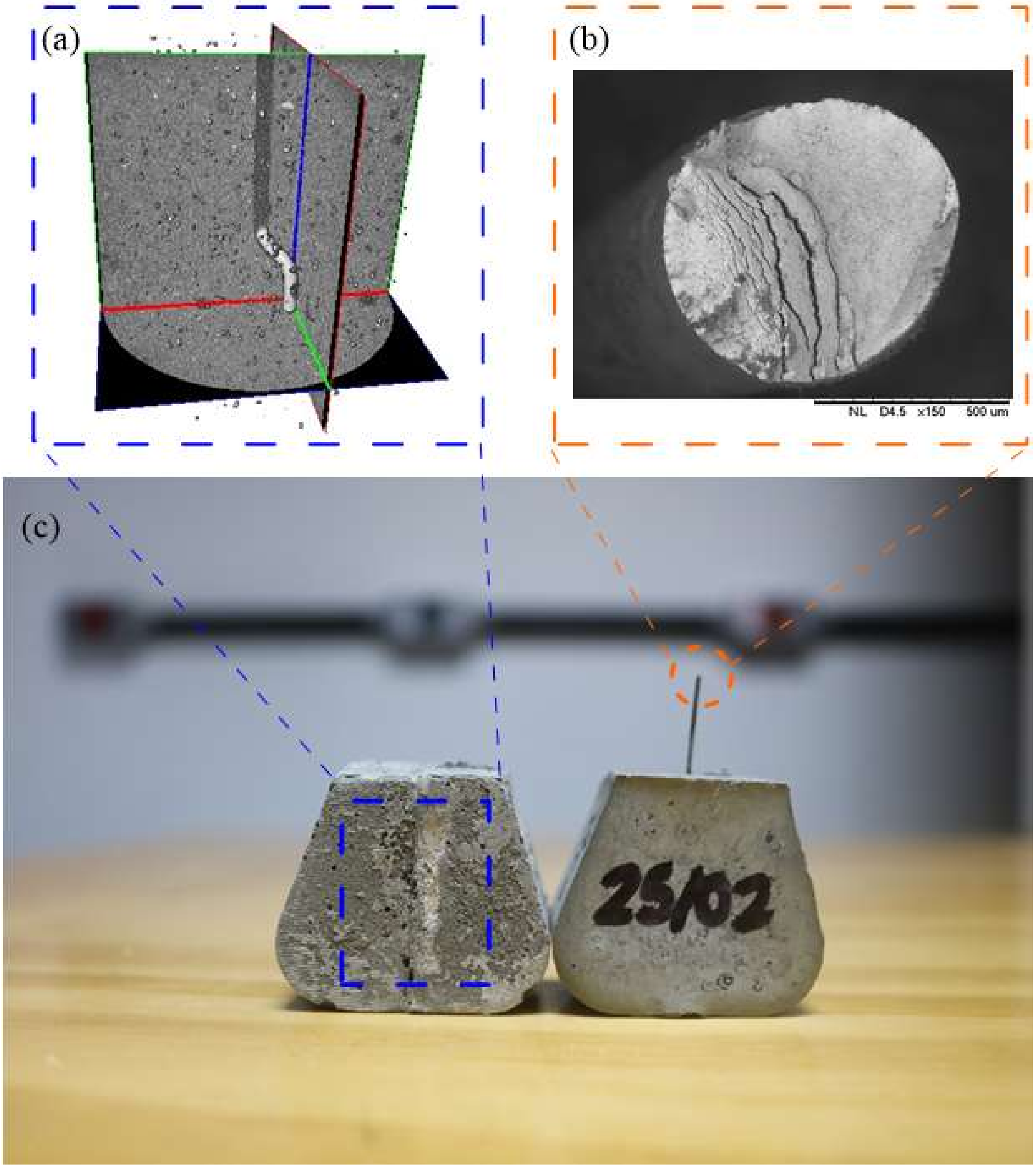

Figure 3.10 - Fiber rupture after fatigue test: (a) CT-scan image with the remaining hook inside the pullout specimen, (b) fiber cross-section after rupture and (c) pullout specimen.

The fiber rupture under fatigue loading only takes place for the pre-slip range between 1.4 and 1.8 mm and the hook has not completely straightened before initiating the loading cycles. After a pre-slip of 3 mm the hook has significantly deformed during pullout and is no longer capable to retain the fiber at higher levels of pullout stresses. As shown in Figure 3.6, for a pre-slip above 3 mm, only pullout failure mode occurs for load levels S = 70% and 85%.

Table 3.4 - Fatigue test results for fiber rupture under pullout fatigue

Specimen	Fiber	$S = \%P_{max}$	δ_0	P_{max}	P_{upp}	P_{low}	$\Delta\sigma$	Cycles until failure (*N*)
			mm	N	N	N	MPa	
CP2	SF1	95%	1.42	315	299	15	643	36852
CP1	SF1	85%	1.64	307	261	13	561	82807
CP3	SF1	85%	1.46	331	281	14	605	163771
CP4	SF1	85%	1.55	311	264	13	568	90358
CP6	SF1	85%	1.44	425	361	18	777	33807
CP3	SF1	70%	1.69	413	289	14	622	120195
CP4	SF1	70%	1.32	301	211	11	453	130635
CP6	SF1	70%	1.62	346	242	12	521	274447

3.4.2.2. Straight steel fiber failure mode

Figure 3.11 presents a pullout fatigue test result for a straight steel fiber (SF2) pullout failure mode. It is possible to verify the continuous pullout of the fiber during the fatigue test. The pullout fatigue behavior of straight fibers is greatly similar when compared to hooked-end fibers after high pre-slip levels. Since there is a major decrease in pullout strength after debonding, the concrete matrix is not capable to resist to high load levels (70% and 85%) in relation to the peak strength. Hence, the straight fiber is steadily pulled out of the specimen along the fatigue test.

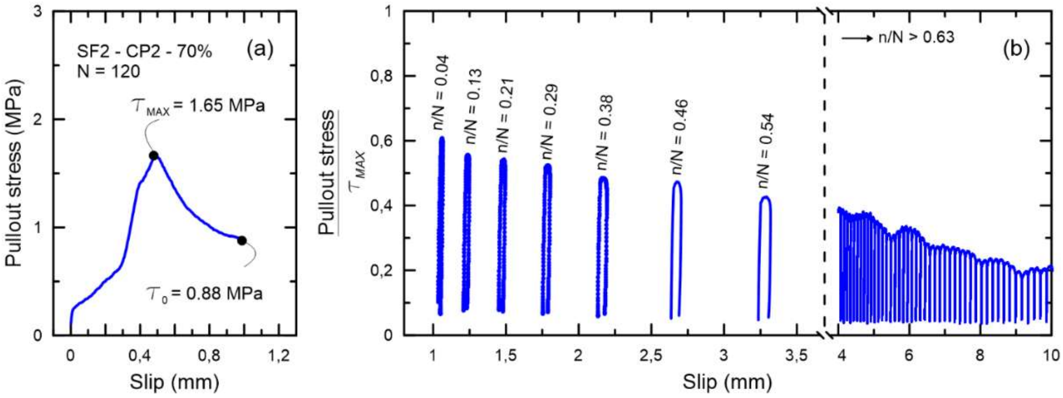

Figure 3.11 - Straight steel fiber (SF2) pullout under fatigue loading: (a) pre-slip and (b) hysteresis cycles under fatigue.

3.4.3. Slip evolution under fatigue

The next in the analysis of the pullout fatigue behavior of steel fibers is on the slip evolution along their relative fatigue life (n/N). Figure 3.12(a) shows the slip increase for the three observed failure modes under pullout fatigue tests in hooked-end steel fibers (SF1): fiber pullout, fiber rupture and run-out. When the fiber is pulled out of the cementitious matrix, the slip presents an almost linear increase until reaching around 80% of the relative fatigue life. Subsequently, the slip increase sharply until reaching the end of the fatigue test. On the other hand, no increase in slip is observed when analyzing the fiber rupture under fatigue. The slip is almost constant until the fiber suddenly breaks and the fatigue test reaches its end. Similar results were also found by Fataar *et al.* [31]. When no failure is observed and the test runs-out, there is also no increment in slip along the cycles.

Figure 3.13 shows the mechanisms that explain how the fiber slips inside the cementitious specimen. When the pullout failure takes place, the fiber is slowly pulled from the specimen until reaching 80% of the relative fatigue life. Up to n/N = 0.80, the hook still plays a key role in trying to retain the fiber inside the matrix. Subsequently, the hook is straightened and the fiber is pulled at a higher rate until reaching the end of the test (figure 3.8(a)). For the fiber rupture event, the fiber is responsible for resisting the load cycles and no slip is observed along the time. Therefore, the fatigue mechanical resistance of the steel fiber becomes the major element of the fatigue test. Occasionally, a region of weakness near the hook arises and the fiber hook reaches rupture at the end of the test (figure 3.13(b)).

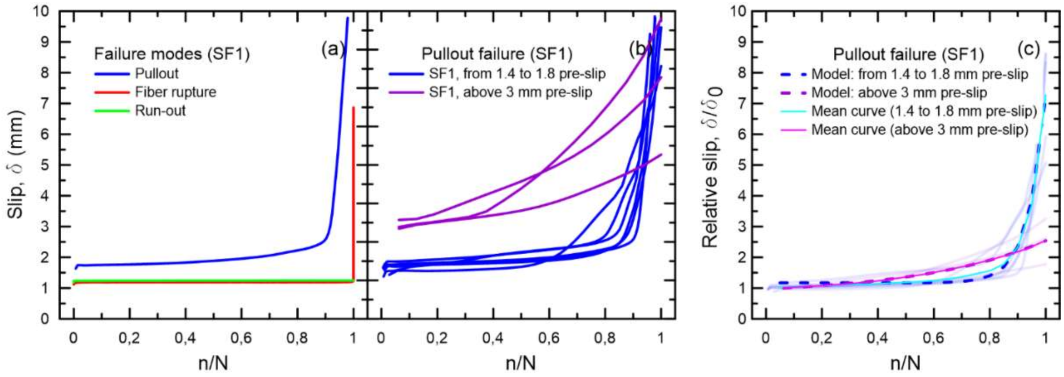

Figure 3.12 - Slip evolution for (a) different failure modes, (b) pullout failure under distinct pre-slips and (c) empirical models

A second step on the slip analysis under fatigue is evaluating the pullout slip after different pre-slip levels. Figure 3.12(b) shows the slip evolution for hooked-end steel fibers (SF1) after a smaller pre-slip level (from 1.40 mm to 1.80 mm) and after the hook has almost completely straightened (above 3 mm). For smaller pre-slip levels, the hook tries to contain the slip before the sharp increase takes place, as explained in Figure 3.13. Above 3 mm of pre-slip, the hook is not able to promote any kind of pullout resistance under fatigue and the exponential slip increase takes place immediately.

Based on the obtained experimental results, it is possible to describe the slip evolution through empirical equations. Figure 3.12(c) presents the experimental results in terms the relative slip δ/δ_0, where δ_0 is the applied pre-slip for each carried experimental test. Thereafter, a mean curve was applied for both pre-slip levels and the model is applied in terms of the mean curve. An exponential model is applied to describe each of the mean curves, as shown in Equation 3.3. Equations 3.4 and 3.5 brings the obtained models for smaller pre-slip levels (from 1.40 mm to 1.80 mm) and pre-slip above 3.0 mm, respectively. The fitting curves were implemented using the OriginPro software and a Levenberg Marquardt iteration algorithm [47].

$$\frac{\delta}{\delta_0} = a \exp\left(\frac{\frac{n}{N}}{b}\right) + c, \textit{ exponential model for slip evolution under fatigue} \tag{3.3}$$

$$\frac{\delta}{\delta_0} = 4.7 \times 10^{-7} \exp\left(\frac{\frac{n}{N}}{0.061}\right) + 1.17, \ 1.40\ mm < \delta_0 < 1.80\ mm, R^2 = 0.99 \tag{3.4}$$

$$\frac{\delta}{\delta_0} = 0.18 \exp\left(\frac{\frac{n}{N}}{0.44}\right) + 0.79, \ \delta_0 > 3.0\ mm, R^2 = 0.99 \tag{3.5}$$

Where δ is the observed slip, δ_0 is the pre-slip of the specimen and n/N is the relative fatigue life.

Both equations can successfully map the slip evolution along the fatigue life. Moreover, the slip evolution curves present similar behavior, which helps to obtain more accurate slip models. Similar models were proposed by Wen *et al.* [48], who described the slip evolution in fiber reinforced polymer through grid-concrete interface under fatigue loading. Differently to what is proposed in this research, Wen *et al.* [48] could evaluate the damage evolution under fatigue pullout test, since the grid-concrete interface damage can be easily mapped in relation to the steel fiber-concrete interface degradation.

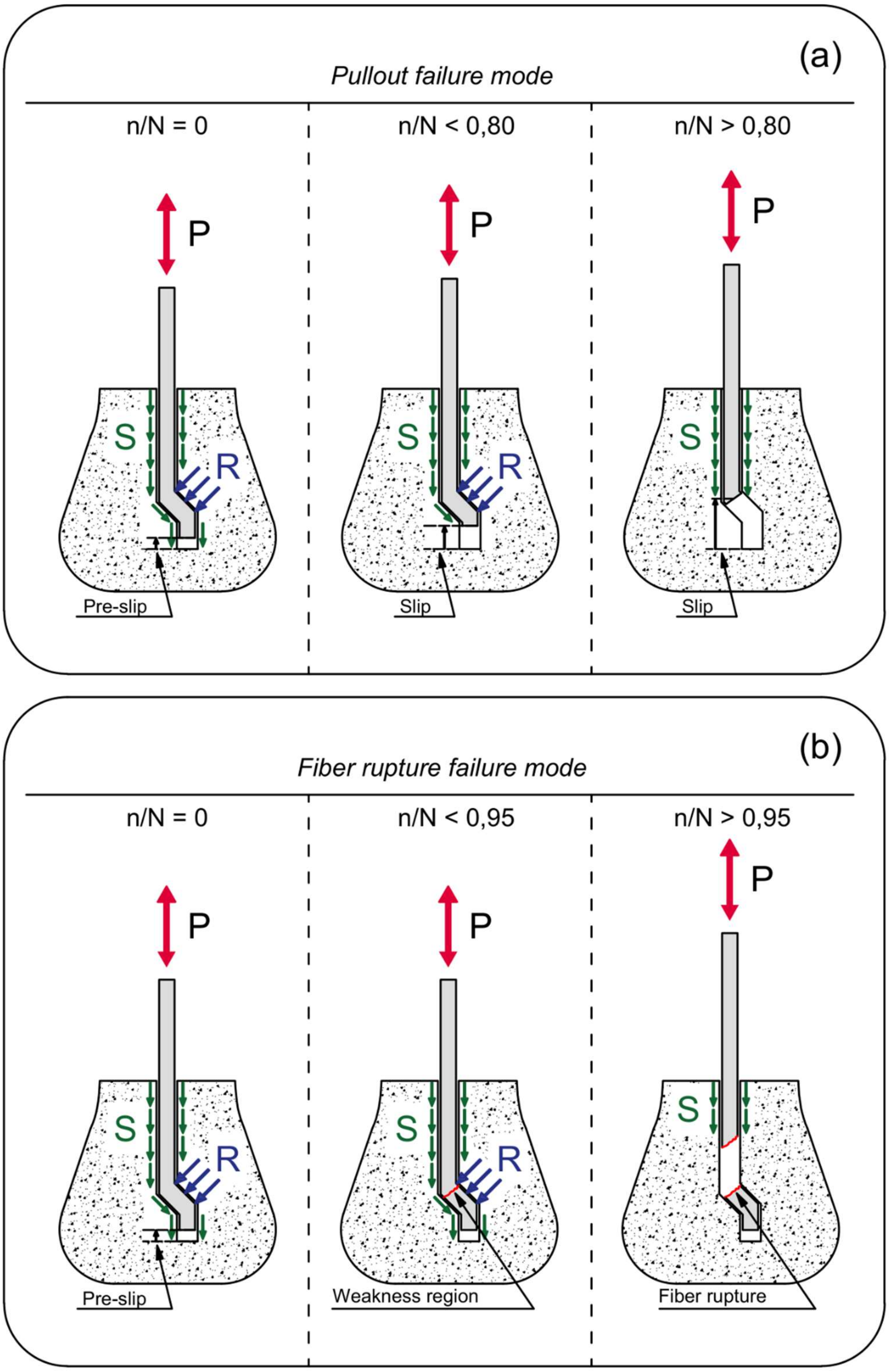

Figure 3.13 - Fatigue slip evolution under distinct failure under: (a) pullout failure and (b) fiber rupture.

The present models proposed a better understanding of the slip evolution in the fiber-concrete interface under fatigue. Past research on fatigue in fiber reinforced concrete have already discussed the crack mouth opening displacement evolution under fatigue [7, 9, 10, 11]. The crack evolution is directly linked to the matrix interface degradation under fatigue and on the slip evolution of the fibers during the loading cycles. The proposed equations may be used for future works, which try to evaluate FRC crack evolution under fatigue through pullout slip equations.

3.5. Conclusions

The present research brings a novel study on the mechanisms of fiber-matrix interface degradation under fatigue loading in steel FRC. The bond degradation was assessed for two distinct fiber types: hooked and straight steel fibers. First, the fiber bond inside the concrete matrix was analyzed through quasi-static pullout tests in accordance with the stablished literature of the topic. Thereafter, fatigue tests were carried on at different load levels (95%, 85%, 70% and 50%) up to 1,000,000 cycles or up to failure. Fiber failure modes, slip evolution and new models were analyzed after the experimental campaign. The following conclusions were derived from the present research:

- The presence of the hook provides a mechanical interlock and its plastic deformation is responsible for enriching the peak pullout force of the fiber from the matrix. As pullout continues and reaches peak stress, the pullout force begins to decrease and the fiber keeps on slipping through the channel until reaching its embedded length. Since the fiber hook is usually not completely straightened after hook deformation, this generates an additional effect on the pullout resistance in relation to straight fiber. When it comes to straight fibers, after complete debonding, frictional stresses develop along the interface zone during fiber slip across interface with progressive decrease of the pullout force.
- Two distinct failure modes were observed for the pullout fatigue tests: fiber failure and fiber pullout. There is a clear division in terms of number of cycles for each failure mode: while any specimen exceeded 10^3 cycles for pullout failure, this limit was around $2x10^5$ for fiber rupture. Moreover, the failure mode modifies depending on the applied load and pre-slip levels. For pre-slip between 1.4 and 1.8 mm, the pullout was only observed when 95%

of load level was carried on the mechanical tests. For over 3 mm, the fiber pullout became more prominent.

- When fiber is pulled out under fatigue loading, the hook is progressively straightened along the fatigue life. For the pre-slip range (from 1.4 mm until 1.8 mm), the hook is still playing a major role on the pullout strength of the steel fiber inside the matrix. When pre-slip is over 3 mm, the hook has already undergone considerable plastic deformation and is not able to resist uninterrupted pullout cycles. Therefore, the number of cycles before complete pullout is slightly higher for lower pre-slips. The pullout fatigue behavior of straight fibers is greatly similar when compared to hooked-end fibers after high pre-slip levels.
- Fiber rupture occurs when the maximum fatigue load is not capable to pull the fiber out from the cementitious matrix during the fatigue cycles. Since the fiber-matrix is able to restrain fiber slip, the fatigue of the steel fiber becomes the major study component. The lower fatigue life in relation to other steel types can be associated to the eccentricity of the applied force in relation to the hook position inside the concrete matrix. The region of the curve of the hook curve ends up becoming the main weakness area due to the described eccentricity. A novel $\Delta\sigma$ x Cycles to estimate the number of cycles before fatigue fiber failure is proposed.
- Novel models were proposed to estimate slip evolution of steel fibers during the fatigue pullout tests. Although slip is almost constant when fiber rupture takes place, an exponential curve was adopted in terms of the pre-slip level for the fiber pullout failure mode. The proposed equations may be used for future works, which try to evaluate FRC crack evolution under fatigue loading.

3.6.References

1 ZHANG, C. GAO, D. GU, Z. Fatigue behavior of steel fiber reinforced high-strength concrete under different stress levels. In: **IOP Conference Series: Materials Science and Engineering**, vol. 274, 2017.

2 BELLETTI, B. CERIONI, R. MEDA, A. PLIZZARI, G. Design aspects on steel fiber-reinforced concrete pavements. **Journal of Materials in Civil Engineering**, vol. 20, p. 599-607, 2008.

3 SRITHARAN, S. SCHMITZ, G. Design of tall wind turbine towers utilizing UHPC. In: **RILEM-fib-AFGC International Symposium on Ultra-High Performance Fibre-Reinforced Concrete**, 2013.

4 HOLMEN, J. Fatigue design evaluation of offshore concrete structures. **Matériaux et Construction**, vol. 17, p. 39-42, 1984.

5 GAO, L. HSU, T. Fatigue of concrete under uniaxial compression cyclic loading. **ACI Materials**, vol. 95, p. 575-581, 1998.

6 SUBRAMANIAM, K. O'NEIL, E. POPOVICS, J. SHAH, S. Crack propagaton in flexural fatigue of concrete. **Journal of Engineering Mechanics**, vol. 126, p. 891-898, 2000.

7 GAEDICKE, C. ROESLER, J. SHAH, S. Fatigue crack growth prediction in concrete slabs. **International Journal of Fatigue**, vol. 31, p. 1309-1317, 2009.

8 ANDERSON, T. **Fracture Mechanics: Fundamentals and Applications**, CRC Press, 2017.

9 CARLESSO, D. CAVALARO, S. DE LA FUENTE, A. Flexural fatigue of pre-cracked plastic fibre reinforced concrete: experimental study and numerical modeling. **Cement and Concrete Composites**, vol. 115, 2021.

10 GERMANO, F. TIBERTI, G. PLIZZARI, G. Post-peak fatigue performance of steel fiber reinforced concrete under flexure. **Materials and Structures**, vol. 49, p. 4229-4245, 2016.

11 CARLESSO, D. DE LA FUENTE, A. CAVALARO, S. Fatigue of cracked high performance fiber reinforced concrete subjected to bending. **Construction and Building Materials**, vol. 220, p. 444-455, 2019.

12 STEPHEN, S. GETTU, R. Fatigue fracture of fibre reinforced concrete in flexure. **Materials and Structures**, vol. 53, 2020.

13 LEI, L. XINGANG, S. YUNHUA, C. LEFAN, W. XIANGCHENG, Y. A new fatigue damage model for pavement concrete beams bearing multi-level bending loads. **Journal Pone,** 2021.

14 GRZYBOWSKI, M. MEYER, C. Damage accumulation in concrete with and without fiber reinforcement. **ACI Materials Journal**, vol. 90, p. 594-604, 1993.

15 SHAH, S. Predictions of cumulative damage for concrete and reinforced concrete. **Matériaux et Construction Journal**, vol. 17, p. 65-68, 1984.

16 LEE, M. BARR, B. An overview of the fatigue behavior of plain and fibre reinforced concrete. **Cement Concrete Composites**, vol. 26, p. 299-305, 2004.

17 PAJAK M, PONIKIEWSKI T. Flexural behavior of self-compacting concrete reinforced with different types of steel fibers. **Construction and Building Materials,** vol. 47, p. 397–408, 2013.

18 MONTEIRO, V. LIMA, L. SILVA, F. On the mechanical behavior of polypropylene, steel and hybrid fiber reinforced self-consolidating concrete. **Construction and Building Materials**, vol. 188, p. 280-291, 2018.

19 MOBASHER, B. M**echanics of Fiber and Textile Reinforced Cement Composites**. First ed., CRC Press, 2019

20 BENTUR A, MINDESS S. **Fiber reinforced cementitious composites**. Second Ed: Taylor & Francis, London, 2007.

21 NAAMAN, A. NAJM, H. Bond-slip mechanisms of steel fibers in concrete. **ACI Materials Journal**, vol. 88, p. 135-145, 1991.

22 ALWAN, J. NAAMAN, A. HANSEN, W. Pull-out work of steel fibers from cementitious composites: analytical investigation. **Cement & Concrete Composites**, vol. 13, p. 247-255, 1991.

23 NIEUWOUDT, P. BABAFEMI, A. BOSHOFF, W. The response of cracked steel fibre reinforced concrete under various sustained stress levels on both macro and single fibre level. **Construction and Building Materials**, vol. 156, p. 828-843, 2017.

24 NAAMAN, A. Engineered steel fibers with optimal properties for reinforcement of cement composites. **Journal of Advanced Concrete Technology**, vol. 1, p. 241-252, 2003.

25 NAAMAN, A. NAMUR, G. ALWAN, J. NAJM, H. Fiber pullout and bond slip I: Analytical study. **Journal of Structural Engineering**, vol. 117, p. 2769-2790, 1991.

26 NAAMAN, A. NAMUR, G. ALWAN, J. NAJM, H. Fiber pullout and bond slip II: Experimental validation. **Journal of Structural Engineering**, vol. 117, p. 2791-2800.

27 CUNHA, V. BARROS, J. SENA-CRUZ, J. Pullout behavior of steel fibers in self-compacting concrete. **Journal of Materials in Civil Engineering**, vol. 22, p. 1-9.

28 ABDALLAH, S. FAN, M. ZHOU, X. Pull-out behavior of hooked end steel fibres embedded in ultra-high performance mortar with various W/B ratios. **International Journal of Concrete Structures and Materials**, vol. 11, p. 301-313, 2017.

29 GHODDOUSI, P. AHMADI, R. SHARIFI, M. Fiber pullout model for aligned hooked-end steel fiber. **Canadian Journal of Civil Engineering**, vol. 37, p. 1179-1188.

30 MARKOVIC, I. **High-performance hybrid-fibre concrete – development and utilization**. Ph.D thesis, Delft University, the Netherlands, 2006

31 FATAAR, H. COMBRINCK, R. BOSHOFF, W. An experimental study on the fatigue failure of steel fibre reinforced concrete at a single fibre level. **Construction and Building Materials**, vol. 299, 2021.

32 VICENTE, M. MÍNGUEZ, J. GONZÁLEZ, D. Computed tomography scanning of the internal microstructure, crack mechanisms, and structural behavior of fiber-reinforced concrete under static and cyclic bending tests. **International Journal of Fatigue**, vol. 121, p. 9-19, 2019.

33 VICENTE, M. RUIZ, G. GONZÁLEZ, D. MÍNGUEZ, J. TARIFA, M. ZHANG, X. CT-scan study of crack patterns of fiber-reinforced concrete loaded monotonically and under low-cycle fatigue. **International Journal of Fatigue**, vol. 114, p. 138-147, 2018.

34 BALAZS, G. CZOBOLY, O. LUBLOY, E. KAPITANY, K. BARSI, A. Observation of steel fibers in concrete with computed tomography. **Construction and Building Materials**, vol. 140, p. 534-541, 2017.

35 AMERICAN SOCIETY FOR TESTING AND MATERIALS. **ASTM C595:** Standard specification for blended hydraulic cements, 2008.

36 DE LARRARD, F. **Concrete mixture proportioning: a scientific approach**. E&FN SPON, 1999.

37 RAMBO, D. SILVA, F. FILHO, R. Effect of steel fiber hybridization on the fracture behavior of self-consolidating concretes. **Cement & Concrete Composites**, vol. 54, p. 100-109, 2014.

38 RAMBO, D. SILVA, F. TOLEDO, R. Mechanical behavior of hybrid steel-fiber self-consolidating concrete: Materials and structural aspects. **Materials and Design**, vol. 54, p. 32-42, 2014.

39 AMERICAN SOCIETY FOR TESTING AND MATERIALS. **ASTM C1611**: Standard test method for slump flow of self-consolidating concrete, 2005.

40 ABDALLAH, S. FAN, M. CASHELL, K. Pull-out behavior of straight and hooked-end steel fibres under elevated temperatures. **Cement and Concrete Composites**, vol. 95, p. 132-140, 2017.

41 ABDALLAH, S. FAN, M. REES, D. Bonding mechanisms and strength steel fiber-reinforced cementitious composites: overview. **Journal of Civil Engineering**, vol. 30, 2018.

42 MARKOVICH, I. VAN MIER, J. WALRAVEN, J. Single pullout from hybrid fiber reinforced concrete. **Heron**, vol. 46, p. 191-200, 2001.

43 ALWAN, J. NAAMAN, A. GUERRERO, P. Effect of mechanical clamping on the pull-out response of hooked steel fibers embedded in cementitious matrices. **Concrete Science Engineering**, vol. 1, p. 15-25, 1999.

44 ISLA, F. RUANO, G. LUCCIONI, B. Analysis of steel fibers pull-out. Experimental study. **Construction and Building Materials**, vol. 100, p. 183-193, 2015.

45 MEYER, H. Fatigue damage of low amplitude cycles in low carbon steel. **Journal Materials Science**, vol. 44, p. 4919-4929, 2009

46 LIU, Y. LI, Y. LI, S. YANG, Z. CHEN, S. HUI, W. WENG, Y. Prediction of the S-N curves of high-strength steels in the very high cycle fatigue regime. **International Journal of Fatigue**, vol. 32, p. 1351-1357, 2010.

47 BARD, Y. **Nonlinear parameter estimation**. Academic Press, 1973.

48 WEN, B. WAN, C. Experimental study on the bond degradation of basalt fiber reinforced polymer grid-concrete interface under fatigue loading. **Construction and building Materials**, vol. 270, 2021.

4 A novel methodology for estimating damage evolution and energy dissipation for steel fiber reinforced concrete under flexural fatigue loading

The present chapter proposes a novel methodology for estimating mechanical degradation for steel fiber reinforced concrete. An experimental campaign was carried out in order to characterize the fatigue response of the cementitious composite and to determine fatigue life using S-N curves based on Weibull distribution. Using the experimental results, two empirical correlations were proposed to estimate damage evolution and energy release growth rate as a function of the number of cycles. Both use the initial stiffness and the energy release of the studied material as an input, which are both evaluated as the flexural strength at 0.50 mm of crack mouth opening displacement.

Published article: January 8th, 2022 – *International Journal of Fatigue, https://doi.org/10.1016/j.ijfatigue.2022.107244*

4.1. Introduction

Fiber reinforced concrete (FRC) members have been extensively used in applications exposed to cyclic loadings, which include from precast tunnel segments [1-2] and concrete pavements [3] to wind tower rings [4] and offshore structures [5]. In general, FRC structures are subjected to fatigue loadings in the form of wind or wave action, thermal variations, traffic loading and machine vibrations, which are responsible for producing tensile stresses that can lead to crack initiation and propagation [6]. With damage accumulation and crack growth, the material performance eventually reduces in terms of strength, stiffness and toughness [7].

In general, the S-N field is divided in three major regions related to the lifetime: Low-cycle, high-cycle and very-high cycles fatigue domains. The type of fatigue is distinguished by its number of cycles, as shown by Göransson *et al.* [8]. Up to 10^3 cycles, it is categorized as low-cycle fatigue, such as structures subjected to earthquakes or to storm. For a number of cycles between 10^3-10^7, classification as high-cycle fatigue is applied. The last category is super-high-cycle fatigue with more than 10^7 cycles.

Gao *et al.* [9] divide the fatigue behavior to failure into three distinct stages: (1) flaw initiation due to the weak regions within concrete, (2) slow and progressive growth of the inherent flaws (microcracking) until a critical crack size is reached and (3) development of unstable macrocracks, leading to failure. The resistance to crack growth increases up to the critical crack length at the peak load of the quasi-static response, as shown by Subramaniam *et al.* [10] and Gaedicke *et al.* [11]. Thereafter, the resistance to crack growth assumes a constant value.

When it comes to the flexural fatigue of FRC, past research has been carried out in the pre-peak regime based on unnotched [12, 13] or notched [14] specimens aiming to better understand the mechanical failure response. Fatigue life generally increases with higher fiber aspect ratio and content [15]. The review of Lee *et al.* [16] summarizes the first results of flexural fatigue in the literature.

Overall, the fatigue of FRC is analyzed through S-N curves, which are developed to correlate fatigue life with load amplitude, allowing to predict the material performance. Several parameters are responsible for modifying fatigue life such as stress level [13], stress ratio [17], loading frequency [18], loading sequence

[19, 20] and material properties. Consequently, different S-N models [21] were proposed trying to include the maximum number of fatigue variables, as shown, for instance, in equations 4.1-4.3. More recently, new regression models have already been developed to describe both fatigue life and cumulative damage evolution, majorly based on probabilistic and Bayesian approaches. Recent research works by Castillo *et al.* [22], Canteli *et al.* [23] and de la Rosa. [24] presents new mathematical methods for fatigue analysis.

$$S = a - b\log(N) \tag{4.1}$$

$$S = 1 - b(1 - R)\log(N) \tag{4.2}$$

$$S = c_1 N^{-c_2(1-R)} \tag{4.3}$$

where S is the stress level, N is the number of cycles until failure, R is the stress ratio, c_1, c_2, a and b are experimental coefficients. More recently, the fatigue performance of FRC began to be studied in the post-peak regime in order to better evaluate the crack bridging of fibers after the formation of the fracture process zone (FPZ) [25-28]. Moreover, considering that FRC structures are designed according to post-cracking mechanical parameters, the need for more fatigue research considering these properties are of great importance. In general, fatigue on pre-cracked FRC is assessed through notched specimens, which are, first, monotonically loaded until reaching 0.50 mm of crack mouth opening displacement (CMOD) and, then, subjected to cyclic loading up to rupture or the fatigue limit [20].

Carlesso *et al.* [25], for instance, studied the post-cracking fatigue flexural strength of high performance fiber reinforced concrete (HPFRC) under different load levels (*S = 0.65, 0.70, 0.75, 0.80, 0.85, 0.90, 1.00*) aiming to develop S-N curves considering Wöhler and Weibull models. The S-N models allowed affirming that HPFRC pre-cracked specimens have a fatigue limit of 2,000,000 cycles at the order of 66% of the flexural residual strength at 0.50 mm of CMOD (fR,1), approximately. Based on the cross section of specimens after rupture, it is suggested that fatigue failure occurs due to damage at the fiber-matrix interface with progressive reduction of the anchorage capacity, as observed elsewhere [29-31].

Stephen *et al.* [26], in turn, bring a deep analysis on fatigue fracture of pre-cracked fiber reinforced concrete in flexure. The authors observed a major change on the CMOD rate per cycle, which decreases and then increases, with a critical point ($CMOD_{CR}$) situated when the transition from the second to third stage of cracking occurs. At lower fatigue load percentages, lower values of critical CMOD is observed, which is attributed to the relaxation of stresses and the reduction of residual strength on account of fiber-matrix interface progressive degradation and damage evolution.

After developing S-N curves for pre-cracked FRC, the next step in terms of design guidelines is providing damage and crack evolution models in order to estimate the main mechanical properties throughout the material lifespan. Carlesso *et al.* [27] carried out an experimental program to develop a numerical model aiming to predict the CMOD variation over the load cycles. This model depends on parameters related to initial damage due to pre-cracking and damage evolution per cycle. Supposing that Carlesso *et al.* [27] model can be applied to reinforced elements at structural level, the resistant capacity of a structure subjected to fatigue loading could be estimated based on the quasi-static flexural response.

Therefore, the present study aims to bring a new step further on the fatigue studies for fiber reinforced concrete subjected to flexural loading by proposing a new methodology to estimate the mechanical degradation with the number of cycles. First, an extensive experimental program was carried out to evaluate the mechanical deterioration on steel fiber reinforced concrete. The flexural fatigue tests were performed on notched uncracked and pre-cracked prisms in accordance with EN 14651 standard [32]. A self-consolidating 50 MPa concrete with hooked-end steel fibers (20, 40 and 60 kg/m^3 fiber volume fractions) was developed for this study. The fatigue tests were performed under distinct load fatigue strength levels (70%, 80% and 90% of $f_{R,1}$ or f_{lop}) considering the same amplitude ratio of 0.30. Moreover, a novel methodology to predict the stiffness decay and energy dissipation along the fatigue life of fiber reinforced concretes is proposed, using probabilistic Weibull curves.

4.2. Experimental program

4.2.1. Materials

Two distinct classes of particle size of river sand were used to the concrete mix design: the first ranging from 0.15 mm to 4.8 mm (S1) and the second ranging from 0.15 mm to 0.85 mm (S2). The following cementitious materials were used in the production of the concrete specimens: Brazilian cement type CPV (ASTM

Cement type III), fly ash and silica fume. Silica flour, coarse aggregate (maximum diameter of 9.5 mm), superplasticizer (MasterGlenium 51) and viscosity modifying admixture (MasterMatrix VMA 358) also compose the concrete formulation. With a water/cement ratio of 0.50, a compressive strength of 50 ± 2 MPa was reached after 28 days. More information on the development of the applied self-consolidating concrete (SCC) is available at Pereira *et al.* [33] and Rambo *et al.* [34]. Steel fibers with hooked-end were used as reinforcement. The steel fiber presents a length (*L*) of 35 mm, diameter (*d*) of 0.75 mm, aspect ratio of 45 (*L/d*) and tensile strength of 1225 MPa.

In order to evaluate the fatigue behavior and damage evolution of steel fiber reinforced concrete, three distinct fiber volume fractions were analyzed: 20, 40 and 60 kg/m³. The cementitious composites were named accordingly with their fiber fractions: C20SF, C40SF and C60SF. The complete mix composition for the present research can be verified in table 4.1.

The following values of concrete spread were obtained for the concrete matrix, C20SF, C40SF and C60SF, respectively: 710, 660, 690 and 650 mm. No evidence of bleeding or segregation was observed for all mixtures. The fresh concrete mixtures were characterized according to their flow ability in accordance with ASTM C1611 standard [35]. The assessment of the self-consolidating concrete spread was performed by the average of two perpendicular measurements SCC mass diameters [36].

Table 4.1 - Mix composition of matrix and steel fiber reinforced self-consolidating concrete

Constituent	Mixtures			
	Matrix	C20SF	C40SF	C60SF
Coarse aggregate (kg/m³)	492	478.54	465.04	438.04
Sand (S1) (kg/m³)	827	826.71	826.71	826.71
Sand (S2) (kg/m³)	100	99.60	99.60	99.60
Silica Mesh 325 (kg/m³)	70	70	70	70
Cement (kg/m³)	360	360	360	360
Fly Ash (kg/m³)	168	168	168	168
Silica Fume (kg/m³)	45	45	45	45
Water (kg/m³)	164	6.0%	6.0%	6.0%
Superplasticizer (%)	5.50	5.50	5.50	5.50
Viscosity modifying admixture (%)	0.75	0.75	0.75	0.75
Hooked end fiber (kg/m³)	0	20	40	60

**Sand (S2): Sand (S1) with diameter less than 0.85 mm*

4.2.2. Mixing procedure

The complete mixing procedure can be divided in five main stages. The aggregates (river sands S1 and S2, coarse aggregate) are first added inside the mixer with 70% of the water and blended together for 1 minute. Thereafter, the mineral and cementitious materials (fly ash, silica fume and silica flour) are mixed with the aggregates for 1 minute. Afterwards, the cement is added and blended for another minute. The remaining water, the superplasticizer and the viscosity modifying admixture is blended with the rest of the materials for at least 10 minutes. At last, the steel fibers are added to the concrete matrix and blended for more 5 minutes. All specimens were cured at saturated conditions and at room temperature of 25 ºC before testing.

4.3. Test program

4.3.1. Monotonic three-point bending tests

The steel fiber reinforced self-consolidating concrete was characterized through three-point bending tests in accordance with EN 14651 [32] standard. Three specimens were produced for each fiber volume fraction. The prims had a cross section of 150 mm x 150 mm and a length of 550 mm, as recommended by EN 14651 [32], and pre-notched at mid-span with a 25-mm deep groove using a 3 mm diamond saw. The loading device was positioned in the middle of the specimens and the span between supports was 500 mm. Figure 4.1 brings a schematic illustration of the applied test setup and the specimen dimensions. The tests were carried after 28 days of curing.

All three-point bending tests were carried on with a closed loop type of control using a MTS servo-controlled hydraulic testing machine. A load cell of 500 kN was attached to the piston. All tests were controlled by the crack mouth opening displacement at a 0.05 mm/min rate until reaching 0.10 mm of CMOD. Thereafter, the test was controlled at 0.20 mm/min rate of CMOD until reaching 4 mm.

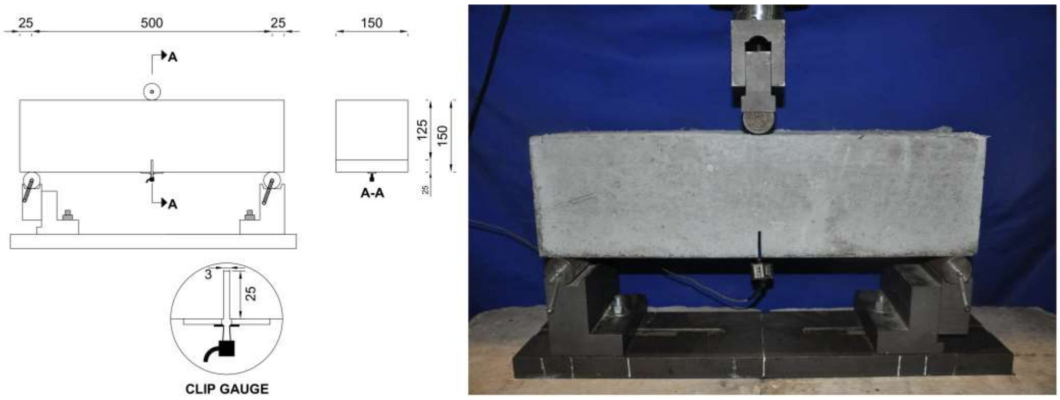

(a) (b)

Figure 4.1 - Test setup: (a) specimen dimensions for monotonic and dynamic three-point bending tests (EN 14651 [29]) and (b) setup image. Dimensions in mm

4.3.2. Fatigue tests

In order to evaluate the fatigue behavior and damage evolution of steel fiber reinforced self-consolidating concretes, 36 prisms were tested under fatigue bending load. The same test setup and specimen dimensions from EN 14651 [32] were adopted for the fatigue tests. With the purpose of monitoring crack opening and fatigue life, fatigue tests were load-controlled and a sinusoidal wave of frequency of 6 Hz was applied for the fatigue test routine on uncracked and pre-cracked test specimens, similar to Carlesso *et al.* [25, 27] work. The fatigue limit of the teste was defined as the fatigue cycles until failure (CMOD > 4 mm) or 1,000,000 cycles (test end). Figure 4.2 illustrates the loading pattern for both uncracked and pre-cracked conditions. The fatigue tests were carried out after at least 28 days of curing of the specimens.

- **Uncracked FRC**

The fatigue experimental campaign on uncracked specimens was based on the results obtained for monotonic tests described previously. The fatigue tests were carried on in accordance with cycle's upper load (P_{upp}), which was set as 70% of the limit of proportionality (P_{lop}) for each studied FRC composition displayed in Table 4.2. For plain concrete, P_{upp} was verified according to a mean value of *Plop* among the EN 14651 results for steel fiber reinforced concrete, as the first crack strength is linked to the matrix compressive strength. The lower load (P_{low}) was estimated based on the load amplitude, which was kept constant for all applied tests ($R = P_{low}/P_{upp} = 0.30$). Twelve specimens were tested.

Last articles by Carlesso [25] *et al.* and Stephen *et al.* [26] applied similar stress ratios ranging between 0.10 and 0.30 for similar types of analysis. However, lower values of R promote a higher stress amplitude on the specimens, which can highly demand on the servo-hydraulic system to maintain force amplitudes until 1,000,000 cycles. Therefore, $R = 0.30$ was adopted as a more conservative strategy to guarantee the execution experimental program.

- **Pre-cracked FRC**

First, the specimen is subjected to a constant deformation rate (0.05 mm/min) controlled by CMOD until reaching 0.50 mm of crack opening, which is considered as the service limit value (fib Model Code 2010 [37]). Thereafter, for each specimen, the corresponding strength to a crack opening of 0.50 mm ($f_{R,1}$) was reached in the first stage and set as reference load ($P_{0.50mm}$). The fatigue tests were carried on in accordance with the cycle's upper load (P_{upp}), which is determined as a percentage of $P_{0.50mm}$. The lower load (P_{low}) was estimated based on the load amplitude, which was kept constant for all applied tests ($R = P_{low}/P_{upp} = 0.30$). A total of 24 specimens were tested for the following studied percentages of $P_{0.50mm}$ (load level S): 70% (7 specimens), 80% (8 specimens) and 90% (9 specimens). A minimum of six specimens was tested for each load level in order to develop the statistical analysis fatigue failure for the present experimental research.

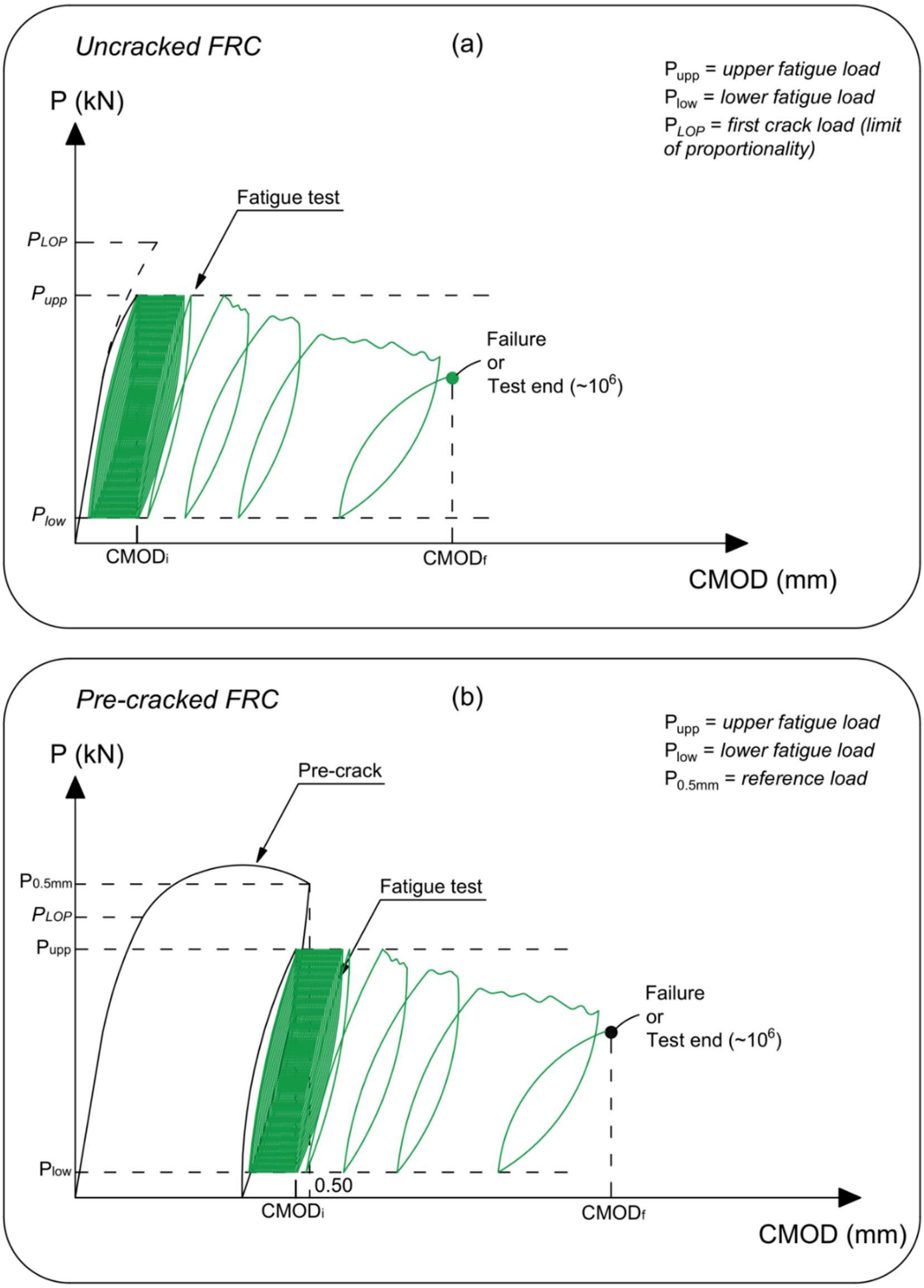

Figure 4.2 - Fatigue test program for (a) uncracked and (b) pre-cracked specimens

4.4. Methodology for estimating SFRC degradation under fatigue

The present research proposes a novel methodology to estimate steel fiber reinforced concrete degradation in terms of stiffness decay and energy dissipation. Figure 4.3 brings an overview of the proposed methodology. The present method can be divided in four main steps, as follows:

1. Residual strength from quasi-static bending test (EN 14651 [32]): the flexural residual strength is obtained through the bending test in accordance with the European standard EN 14651 [29]. The input parameter for degradation estimation is the residual strength at CMOD = 0.50 mm ($f_{R,1}$);
2. Fatigue life estimation: the fatigue life (N) can be estimated through the application of different methods. For the present research, fatigue life was predicted by the use of the Weibull distribution. For a probability of failure (P_f) of 0.05, it is possible to predict fatigue life for a given load level S;
3. Initial stiffness (k_0) and energy release (ER_0) estimations: the initial mechanical parameters can be estimated through the application of the residual strength $f_{R,1}$, obtained from the bending test. As there is an almost linear relation between stiffness and energy release with $f_{R,1}$, the values of k_0 and ER_0 can be predicted with the use of linear regression;
4. Mechanical degradation estimation: based on the previously developed model for damage evolution and energy release growth rate in terms of the cycle ratio n/N, it is possible to obtain the curves of stiffness decay and energy release along the fatigue life of the studied cementitious composite. The proposed model has as input parameters both initial stiffness (k_0) and energy release (ER_0).

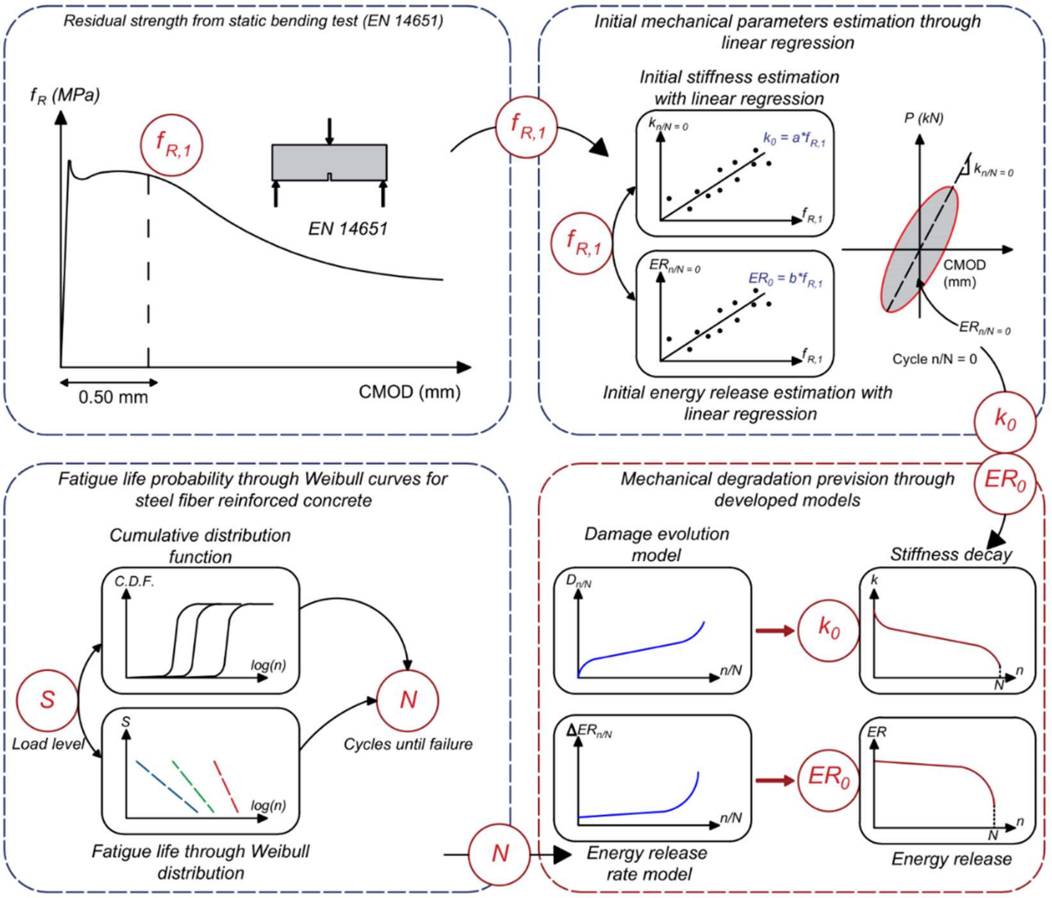

Figure 4.3 - Proposed methodology for estimating FRC mechanical degradation through EN 14651 [29] bending test

4.5. Discussion and analysis

4.5.1. Influence of steel fibers on fatigue life (uncracked specimens)

Table 4.2 brings the post-peak mechanical characterization of the studied steel fiber reinforced self-consolidating concrete in accordance with EN 14651 [32]. The flexural stress at the limit of proportionality (LOP) is assessed by taking P_{lop} as the highest load value in the interval of 0.05 mm of CMOD. According to CEB-FIB [34], $f_{R,i}$ is the flexural residual strength obtained from the pre-notched bending tests with i = 1,2,3 and 4, respectively for CMOD values of 0.50, 1.50, 2.50 and 3.50 mm. The monotonic test results for SFRC presents a significant increase on the residual stress with increasing fiber volume fractions. In terms of mean value of fR,1 residual strength, the concrete with the use of 60 kg/m^3 reached a mean value of 7.88 MPa, while the addition of 20 kg/m^3 led to a mean of 3.31 MPa.

Table 4.2 - Experimental mean results of peak and post-peak parameters for monotonic three-point bending tests in accordance with EN 14651 [29]. Standard deviation values presented in parentheses

Mix	f_{lop} MPa	$f_{R,1}$ MPa	$f_{R,2}$ MPa	$f_{R,3}$ MPa	$f_{R,4}$ MPa
C20SF	5.59	3.31	2.76	1.66	1.23
	(0.21)	(3.31)	(2.76)	(1.66)	(1.23)
C40SF	6.38	7.07	6.01	3.78	2.75
	(0.56)	(1.00)	(0.82)	(0.33)	(0.22)
C60SF	6.37	7.88	6.95	4.87	3.82
	(0.75)	(2.09)	(1.89)	(1.80)	(1.26)

Table 4.3, in turn, brings the fatigue tests results on uncracked plain and steel fiber self-consolidating concrete specimens and Figure 4.4 displays the number of cycles until failure (N) for each studied mix composition (Matrix, C20SF, C40SF and C60SF). There is a clear positive influence of the fiber addition on the fatigue life, in relation to the plain composition. While uncracked plain concrete presented a maximum of N of 192,757, the addition of 40 kg/m³ enhanced the material fatigue life reaching up to 923,063 cycles. For the use of 60kg/m³, all three analyzed specimens reached the applied fatigue limit of 1,000,000 cycles [16]. Figure 4.4 displays the number of cycles to failure for each specimen studied. The results are in accordance with past research on the analysis of fatigue life in uncracked FRC specimens [15, 16]

The residual flexural strength plays a key role when evaluating the fatigue life. Along the loading and unloading cycles, crack keeps on growing up the specimen notch until reaching a critical failure size [10]. When it comes to plain concrete, residual flexural strength is essentially controlled by aggregate bridging effect and is usually assumed negligible. Hence, after cracking evolves upon the first crack strength (around 0.05 mm for EN 14651 [32]), the specimen collapses. If fibers are added to the mix, the reinforcement is able to bridge crack opening after matrix disruption, increasing the number of cycles until failure. For higher values of the relation of $f_{lop}/f_{R,1}$, greater is the capacity of the flexural residual strength of composite to control crack evolution throughout the fatigue loading [16]. Due to the intrinsic scatter presented on the study of fatigue degradation on uncracked specimens, the following models and analysis were carried out on pre-cracked FRC.

Table 4.3 - Fatigue tests results on uncracked steel fiber self-consolidating concrete specimens

S	Mix	P_{lop}	f_{lop}	$f_{R,1}$	$f_{lop}/f_{R,1}$	Cycles until failure, N	$CMOD_{0.90}$
(%P_{lop})	-	(kN)	(MPa)	(MPa)	-	-	(mm)
0.7	Matrix	19.1	6.11	-	-	21500	0.027
0.7	Matrix	19.1	6.11	-	-	192757	0.036
0.7	Matrix	19.1	6.11	-	-	1876	0.033
0.7	C20SF	17.54	5.59	3.31	59%	65550	0.081
0.7	C20SF	17.54	5.59	3.31	59%	16302	0.067
0.7	C20SF	17.54	5.59	3.31	59%	629400	0.096
0.7	C40SF	19.35	6.38	7.07	111%	923063	0.321
0.7	C40SF	19.35	6.38	7.07	111%	276191	0.282
0.7	C40SF	19.35	6.38	7.07	111%	22736	0.053
0.7	C60SF	19.31	6.37	7.88	124%	1000000	0.028
0.7	C60SF	19.31	6.37	7.88	124%	1000000	0.025
0.7	C60SF	19.31	6.37	7.88	124%	1000000	0.020

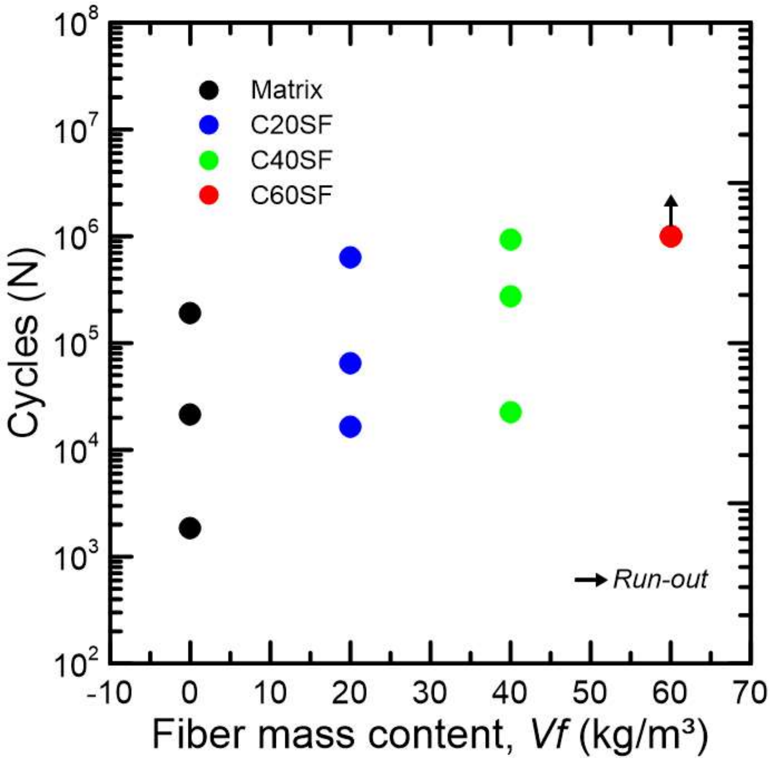

Figure 4.4 - Number of cycles until failure for uncracked plain and steel fiber reinforced concrete under fatigue. Load level of 70% applied (*S = 70%*).

4.5.2. Fatigue life analysis (pre-cracked specimens)

4.5.2.1. S-N Curve

The most traditional method to study fatigue life is based on S-N curves, also called Wöhler curves, obtained as a result of series of fatigue tests at several stress levels [38, 39]. The fatigue life (N) is plotted on a logarithmic scale as a function of the load level (S). When it comes to the analysis of fatigue life of pre-cracked of fiber reinforced concrete, the load level is outlined according to the percentage of the obtained load at 0.50 mm of CMOD ($\%P_{0.50mm}$). Figure 4.5 brings the achieved Wöhler curve and Equation 4.4 presents the achieved S-N equation, based on the fatigue tests results. In general, high number of cycles are achieved in fatigue experiments for fiber reinforced concrete, reaching 1,000,000 cycles depending on the load level (S). Therefore, the logarithmic form log(N) aims to simplify the S-N models and graphs.

$$S = -0.087 \log(N) + 1.15 \tag{4.4}$$

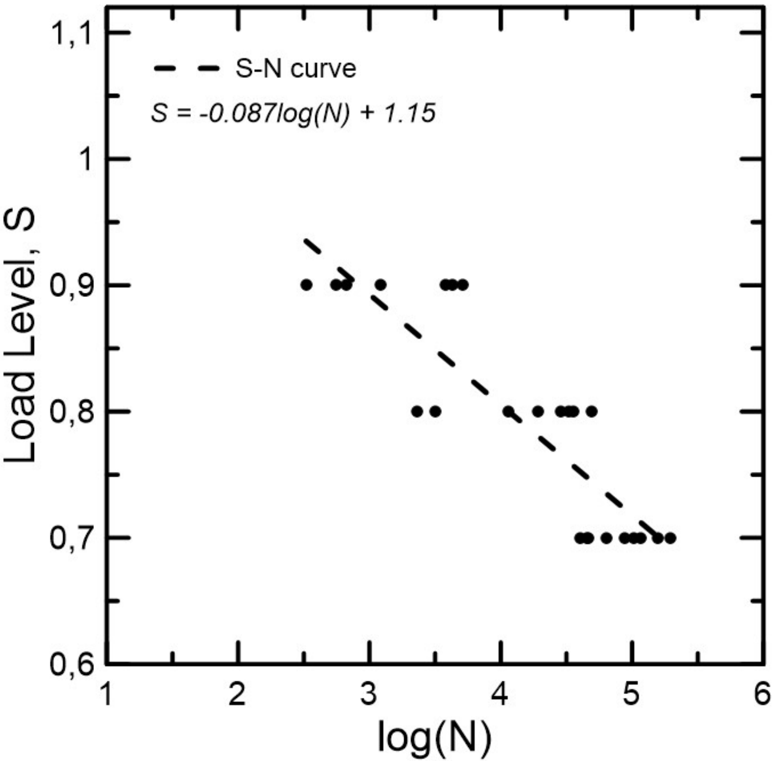

Figure 4.5 - Fatigue lifetime curve S-N for pre-cracked FRC

According to the achieved results, the S-N curve does not permit to accurately establish the fatigue limit. Although it is still not clear if concrete presents a fatigue limit, it is generally accepted that FRC beams can reach up to 2,000,000 cycles [13, 22, 37]. Past results of Stephen *et al.* [26] on SFRC have shown that this material could withstand 2,000,000 cycles for load levels below 50% of $P_{0.50mm}$. Moreover, S-N curves are very limited when it comes to the design of concrete structures under fatigue loading, due to the great scatter present in this type of analysis. More recently, new models based on probabilistic models are more appropriate when it comes to fatigue study, such as the Weibull distribution [22, 23, 38, 39].

Table 4.4 - Fatigue tests results on pre-cracked steel fiber self-consolidating concrete specimens

S	Mix	$P_{0.50mm}$	$f_{R,1}$	Cycles until Failure, N	$CMOD_{0.10}$	$CMOD_{0.90}$	dCMOD/dn
(%$P_{0.50mm}$)	-	(kN)	(MPa)	-	(mm)	(mm)	(mm/cycle)
0.7	C20SF	10.1	3.25	116114	0.44	0.58	1.48E-06
0.7	C20SF	6.6	2.1	104000	0.48	0.70	2.57E-06
0.7	C20SF	8.3	2.66	87300	0.45	0.73	3.93E-06
0.7	C40SF	17.2	5.5	194483	0.46	0.61	9.80E-07
0.7	C40SF	20.12	6.4	157934	0.47	0.55	6.30E-07
0.7	C40SF	14.9	4.85	40025	0.45	0.74	9.06E-06
0.7	C60SF	26.4	8.86	45739	0.46	0.63	4.49E-06
0.7	C60SF	16	5.23	63200	0.46	0.72	5.10E-06
0.7	C60SF	26.5	8.48	46200	0.46	0.62	4.51E-06
0.8	C20SF	6.7	2.14	2305	0.49	0.73	1.32E-04
0.8	C20SF	6.4	2.08	3195	0.48	0.87	1.53E-04
0.8	C40SF	21.5	6.88	11491	0.50	0.77	3.00E-05
0.8	C40SF	22.1	7	28459	0.50	0.59	3.99E-06
0.8	C40SF	16	5.12	35584	0.51	0.59	2.72E-06
0.8	C60SF	22.9	7.3	48712	0.51	0.75	6.18E-06
0.8	C60SF	29.8	9.5	19301	0.51	0.71	1.28E-05
0.8	C60SF	26.8	8.6	32925	0.51	0.81	1.14E-05
0.9	C20SF	5.4	1.7	557	0.47	0.84	8.26E-04
0.9	C20SF	5.5	1.76	1222	0.48	0.86	3.81E-04
0.9	C40SF	14.5	4.6	663	0.50	0.76	4.88E-04
0.9	C40SF	16.8	5.4	5104	0.58	0.77	4.50E-05
0.9	C40SF	16.2	5.2	4248	0.60	0.80	5.91E-05
0.9	C60SF	30.5	9.6	3778	0.59	0.83	7.69E-05
0.9	C60SF	24.4	7.8	329	0.48	0.97	1.83E-03

Table 4.5 - Main parameters evaluated for the applied Weibull distribution

Parameters	Load level, S		
	70%	80%	90%
$\alpha_{calculated}$	1.66	0.81	0.81
α_{final}	1.66	1.0	1.0
$u_{calculated}$	110601	27320	2568
u_{final}	110601	4081	598
D_n	0.22	0.17	0.29
D_c	0.43	0.45	0.48

Weibull distribution: $F_n(n) = 1 - e^{\left(\frac{n}{u}\right)^{\alpha}}$

D_n = critical value of the hypothesized distribution

D_c = critical value taken from the Komogorov-Smirnov table for a 5% significance level

4.5.2.2. Two parameter Weibull distribution

A two parameter Weibull distribution is used in this section in order to ensure a more consistent prediction of fatigue life [40-43]. According to the European Committee for Standardization (EN1990) [41], lognormal or Weibull distributions have usually been used for material and structural resistance parameters and to model uncertainties. However, the hazard function of the lognormal distribution decreases with increasing life, violating the observed physical deterioration of fiber reinforced concrete under fatigue loading [42]. Consequently, the two parameter Weibull distribution was applied to the achieved fatigue data aiming to estimate fatigue life according to distinct probabilities of failure. The cumulative distribution function (C.D.F.) for the Weibull distribution may be expressed according to Equation 4.5.

$$F_n(x) = 1 - e^{\left(\frac{x}{u}\right)^{\alpha}} \tag{4.5}$$

Where x is the specific value of the random variable N (number of cycles until failure), α is expressed as the Weibull shape parameter and u is described as the scale parameter [42, 43].

The graphical method was employed to estimate the parameters of the distribution α and u. Equation 4.6 brings the survivorship function *LR(x)* of the two parameter Weibull distribution [24, 42, 43].

$$L_R(x) = e^{\left(-\frac{x}{u}\right)^{\alpha}} \tag{4.6}$$

It is possible apply the logarithm twice on both sides of Equation 4.6, resulting on Equation 4.7.

$$\ln\,(\ln\,(\frac{1}{L_R(x)})) = \alpha\,\ln(x) - \alpha\ln\,(u) \tag{4.7}$$

In this way, Equation 4.7 describes a linear relationship between $ln(ln(L_R(x)))$ and $ln(x)$. The fatigue-life can be expressed in terms of each load level S arranging them in ascending order of cycles until reaching failure (N) the empirical survivorship function, then, is obtained for each fatigue life data according to Equation 4.8.

$$L_R = 1 - \frac{i}{k+1} \tag{4.8}$$

In which i denotes the failure order number and k corresponds the total number of specimens tested for each load level S. Figure 4.6(a) brings the plotted relationship for the studied load levels (S = 70%, 80% and 90%). The two main parameters of the Weibull distribution can be achieved through the linear regression. The linear regression and the coefficient of determination (R^2) are displayed in Figure 4.6(a). Table 4.5 brings an overview the obtained parameters.

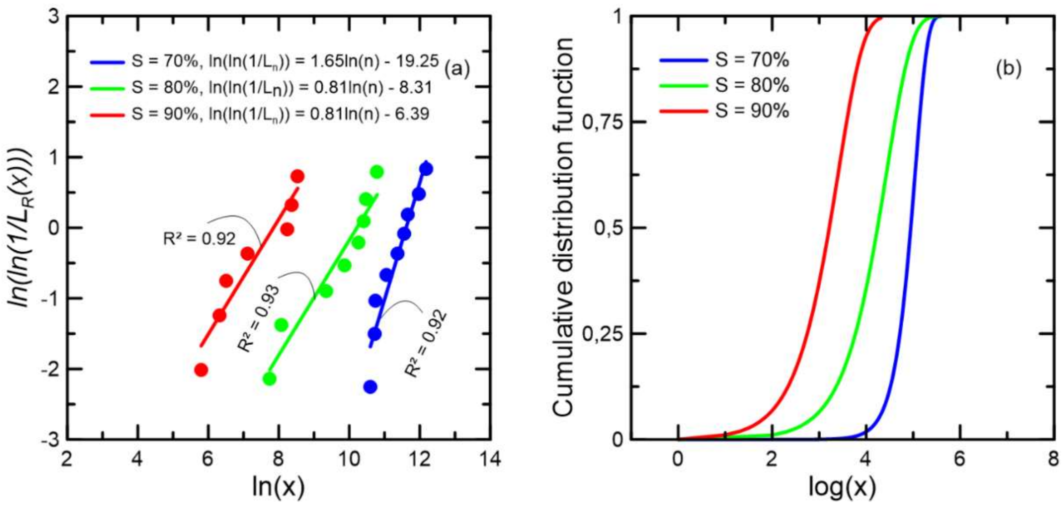

Figure 4.6 - Weibull distribution (pre-cracked FRC) for the studied load levels (70%, 80% and 90%): (a) Representation of the fatigue results in Gumbel distribution including the model parameters and (b) Weibull cdfs of lifetimes for the (a) results

4.5.2.3. Goodness-of-fit test (Kolmogorov-Smirnov)

In order to validate the achieved two parameter Weibull distribution for the studied load levels (70%, 80% and 90%), Kolmogorov-Smirnov test was carried out on the fatigue life data and is described on Equation 4.9. For more information on the Kolmogorov-Smirnov test, refer to Oh [46].

$$D_n = \max\left[abs\left(F^*(x_i) - F_n(x_i)\right)\right] \tag{4.9}$$

$F^*(x_i)$ is described as the observed cumulative histogram and $F_N(x_i)$ is associated to the Hypothesized cumulative distribution function, which is the two parameter Weibull function for this present research (Equation 4.5). The critical value D_c is obtained through the Kolmogorov-Smirnov table for a 5% significance level. As shown in table 4.5, $D_c > D_n$ for all studied load levels. Therefore, all developed models passed the test are considered acceptable.

4.5.2.4. Fatigue life through two parameter Weibull distribution

Figure 4.6(b) shows the steel fiber self-consolidating concrete C.D.F. curve as function of the cycles until failure for each load level. Since the achieved data follows the two-parameter Weibull distribution, this probabilistic approach can be used to estimate the fatigue lives (number of cycles until failure, *N*) in accordance to the failure probabilities P_f. As the chance of survival (L_R) is equal to $1-P_f$, it is possible to rearrange Equation 4.7, giving Equation 4.10.

$$\ln(\mathrm{N}) = \frac{\ln\left(\ln\left(\frac{1}{1-P_f}\right)\right) + \alpha\ln(u)}{\alpha} \tag{4.10}$$

Using the obtained parameters of the two parameter Weibull distribution, it is possible to express the fatigue life in terms of a particular P_f.

Figure 4.7 brings the S-N-P_f curves for a failure probability of 5%, 50% and 95%. The experimental data seems to be encompassed between the S-N-P_f curves for 5% and 95% of failure probability. When it comes to a P_f of 50%, the fatigue curve comes closer to the mean Wöhler curve. The use of a curve based on probability of failure of 5% seems more appropriate when addressing the application of the composite in terms of structural design. Moreover, the fatigue life curves will be key for the development of the present methodology.

For the load levels 0.80 and 0.90, shape parameter reveled to be inferior to 1 ($\alpha < 1$), which is associated to a decreasing hazard function with increasing cycles. Although the applied goodness-of-fit test showed that the Weibull distribution is valid, it violates the expected fatigue behavior. Hence, $\alpha = 1$ can be assumed [47] and the value of scale parameter (*u*) was recalculated accordingly. Figure 4.7 already brings the S-N-P_f with the modified values of α and *u*. The obtained and the final adopted values are shown in table 4.5.

Although past research [42, 43, 46, 47] also achieved shape parameter inferior to 1 ($\alpha < 1$), more recent models already brought new methods that can overcome those inconsistencies [22-24]. As shown by Castillo *et al.* [22], a three parameter Weibull distribution seems to be more adequate to predict the fatigue life.

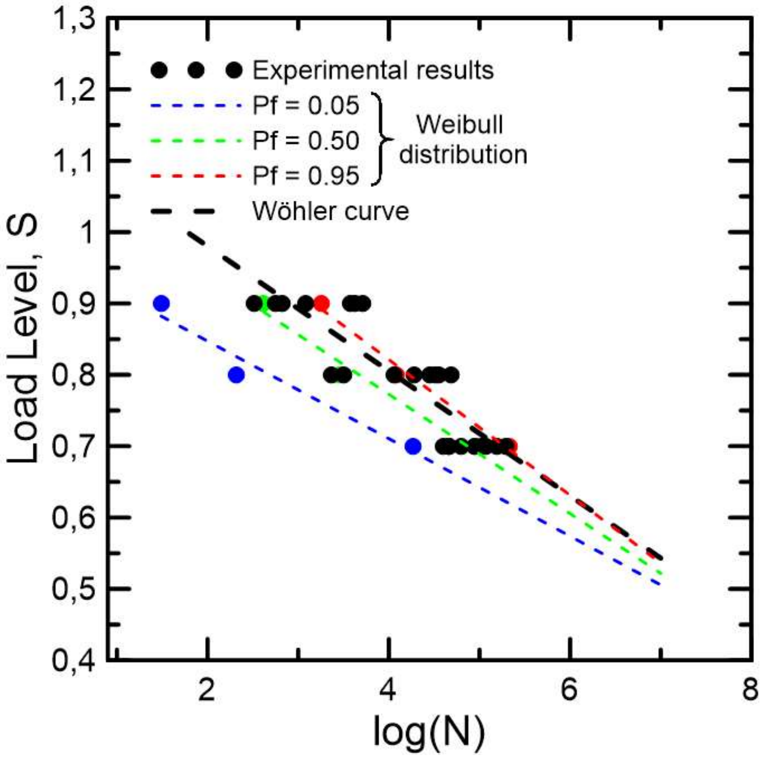

Figure 4.7 - Fatigue life of pre-cracked steel fiber reinforced concrete through two parameter Weibull distribution

4.5.2.5. Three parameter Weibull distribution

The cumulative distribution function (C.D.F.) for the three parameter Weibull distribution may be expressed according to Equation 4.11.

$$F(x;\lambda;u;\alpha) = 1 - \exp\left(-\left(\frac{x-\lambda}{u}\right)^{\alpha}\right) \tag{4.11}$$

Where *F(x,λ;u;α)* represents the probability of the event $X<x$ and u, α and λ are the scale, location (minimum possible value of the random variable *X*) and shape parameters, respectively.

Based on the C.D.F in Equation 4.11, it is possible to apply the probability density function (P.D.F) shown in Equation 4.12.

$$p(x;\lambda;u;\alpha) = \frac{\alpha}{u}\left(\frac{x-\lambda}{u}\right)^{\alpha-1} \exp\left(-\left(\frac{x-\lambda}{u}\right)^{\alpha}\right) \tag{4.12}$$

For more information on the applied functions, refer to Castillo et al [22].

In order to evaluate all load levels in a unified S-N field, the experimental data in normalized through the parameter *V*, which is described in Equation 4.13.

$$x = V = (\ln(N) - B)(\ln(S) - C) \tag{4.13}$$

Where *N* and *S* are the correspondent experimental data for all studied load levels, *B* is the threshold value of lifetime *N* and *C* is the endurance limit of *S*. Using the parameter *V*, the final cumulative density function is obtained in Equation 4.14, which was used determine the three parameter Weibull distribution for present research

$$F(N,S) = 1 - \exp\left(-\left(\frac{(\ln(N) - B)(\ln(S) - C) - \lambda}{u}\right)^{\alpha}\right) \tag{4.14}$$

As described by Castillo *et al.* [22], the first step achieve three parameter Weibull distribution is by determining the values of *B* and *C*. The threshold value *B* is described by a vertical asymptote, which is associated to the minimum limit of fatigue lifetime for the correspondent studied material. According to the present experimental data, the lowest value of fatigue life reported was 329. Therefore, the value of *B* must be lower than *ln(329)* and the value of *ln(1) = 0* was the best to fit the experimental research.

The value of C is associated to the endurance limit of the evaluated cement composite. Previous research has tried to estimate the endurance limit the fiber reinforced concrete [16, 21, 25-28] and reached endurance limit of around *S = 50%.*

In general, the endurance limit is determined experimentally by the load level S which allows the specimen to reach 2,000,000 cycles without reaching failure. The best fit according to the present experimental data, the load $S = 40\%$, resulting the value of $C = ln(0.40) = -0.91$.

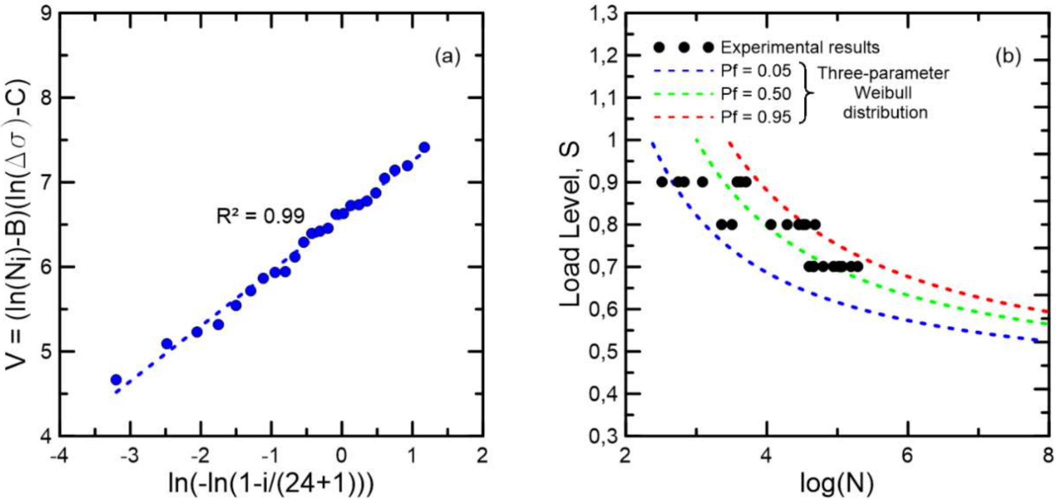

Figure 4.8 - Development of the three parameter Weibull distribution: (a) relation between the variable V as a function of the normalized survivorship function and (b) fatigue life of pre-cracked steel fiber reinforced concrete through three parameter Weibull distribution

In order to verify the fitting capacity, the values *B* and *C*, the parameter *V* is plotted in accordance as a function of the empirical survivorship function (L_R). Figure 4.8(a) brings the parameter *V* for the present experimental data using the estimated values of *B* and *C*. The strong linear relationship ($R^2 = 0.99$) of *V* guarantees that the Weibull law assumption is reasonable [22].

Thereafter, the maximum likelihood estimation (MLE) approach is applied to verify the Weibull distribution parameters [48]. The MLE function at the Matlab software was used to make the present estimation according to the current experimental data. Equation 4.15 brings the obtained cumulative density function with the values for u, α and λ. Figure 4.8(b) brings the achieved three parameter curves for 5%, 50% and 95% of failure probabilities.

$$F(N,S) = 1 - \exp\left(-\left(\frac{(\ln(N))(\ln(S) + 0.91) - 0.21}{6.35}\right)^{10.35}\right) \qquad (4.15)$$

The three parameter Weibull distribution revealed to be the most adequate to verify the failure probability along the fatigue life for the pre-cracked steel fiber reinforced concrete. The equations proposed by Castillo et al [22] depend on an estimation of the material endurance limit. For this present research, the endurance limit of $S = 40\%$ was applied. More studies on the correct estimation of the endurance limit for fiber reinforced concrete are necessary aiming to confirm the value of $S = 40\%$. The use of three parameters achieved a shape parameter α of 10.35, which is higher than 1 (α > 1). The value of α > 1 confirms a failure rate that increases with time, which adequate for the present fatigue analysis [22].

4.5.3. Evolution of crack mouth opening displacement (CMOD)

Figure 4.9(a) brings the evolution of the maximum CMOD over the cycles, according with the maximum fatigue loading: 90%, 80% and 70% of the $P_{0.50mm}$. All evaluated specimens achieved failure before reaching the fatigue limit of 1,000,000 cycles. Figure 4.9(b) shows the crack opening increase in terms of *n/N*, described as the relative load cycle number. The CMOD evolution for all studied load levels present a similar three stage of failure progression [26]. First, there is a stable increase of crack opening at a decreasing rate CMOD evolution (stage I). Thereafter, the second stage (stage II) corresponds to slow and gradually increase of damage, resulting in an approximately linear CMOD per cycle regime. As explained by Stephen *et al.* [26], fiber bridging mitigates crack propagation and restricts fatigue damage. The third and final stage III of CMOD evolution occurs right before failure, with a rapid increase of crack opening and drastic decrease in stiffness due to uncontrolled propagation [10, 11]. Figure 4.10(a) presents a characteristic CMOD x *n/N* curve divided into the three main stages and brings, in Figure 4.10(b), the correspondent CMOD x Force curve. As shown in Figure 4.9(b), stage II is ranged between the values of 0.90 and 0.10 of *n/N*. At this phase, the dCMOD/dn (slope of the CMOD-n relationship) is almost constant and corresponds to the crack opening displacement ratio before reaching stage III, beyond which the CMOD rate starts increasing until achieving failure. The ratio dCMOD/dn was calculated according to $CMOD_{0.10}$ and $CMOD_{0.90}$, which are represented by the crack opening at $n/N = 0.10$ and $n/N = 0.90$, respectively. Equation 4.16 describes the how the dCMOD/dn was calculated for all studied specimens. Table 4.4 summarizes the number of cycles until failure and dCMOD/dn of all studied specimens.

$$\frac{dCMOD}{dn} = \frac{CMOD_{0.90} - CMOD_{0.10}}{\left(\frac{n}{N_{0.90}} - \frac{n}{N_{0.10}}\right) N} = \frac{CMOD_{0.90} - CMOD_{0.10}}{(0.90 - 0.10)N} = \frac{CMOD_{0.90} - CMOD_{0.10}}{0.80N} \tag{4.16}$$

where N is the number of cycles until reaching failure of each specimen.

According to the estimated rates of crack opening over the cycles, the following mean values of dCMOD/dn were achieved for the following load levels 90%, 80% and 70% of the $P_{0.50mm}$, respectively: 5.3×10^{-4},4.4×10^{-5}, 3.6×10^{-6} mm/cycle. At higher fatigue loads, a faster increase in CMOD in second stage of cracking is generally attributed to the higher energy imposed on the specimen within a short duration of time, which leads to higher damage in the fracture process zone [25, 28].

In order to better understand the damage evolution in the fracture process zone (FPZ), Vicente *et al.* [48] evaluated the internal microstructure of fiber-reinforced concrete after fatigue tests through computed tomography scanning. The authors could visualize the failure mechanisms in areas surrounding the crack and, in general, fiber breakage and fiber anchorage failure were the two main ones observed. While fiber rupture depends only on its properties, anchorage failure is related to fiber, matrix and interface fiber-matrix influences. According to CT-scan images, overall, over 80% of failure are due to debonding, while 20% is associated due to fiber breakage.

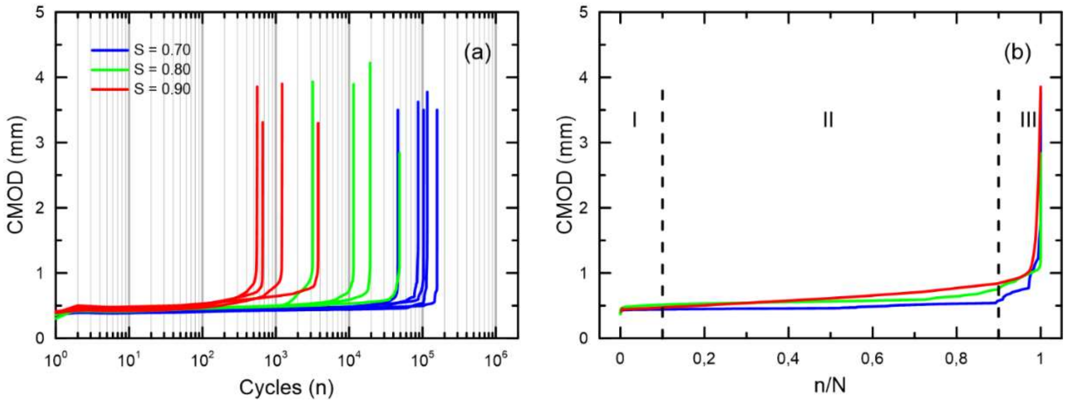

Figure 4.9 - CMOD evolution of all studied load level (90%, 80% and 70% of the $P_{0.50mm}$) in accordance with (a) number cycles (n) and (b) referred load cycle number (n/N).

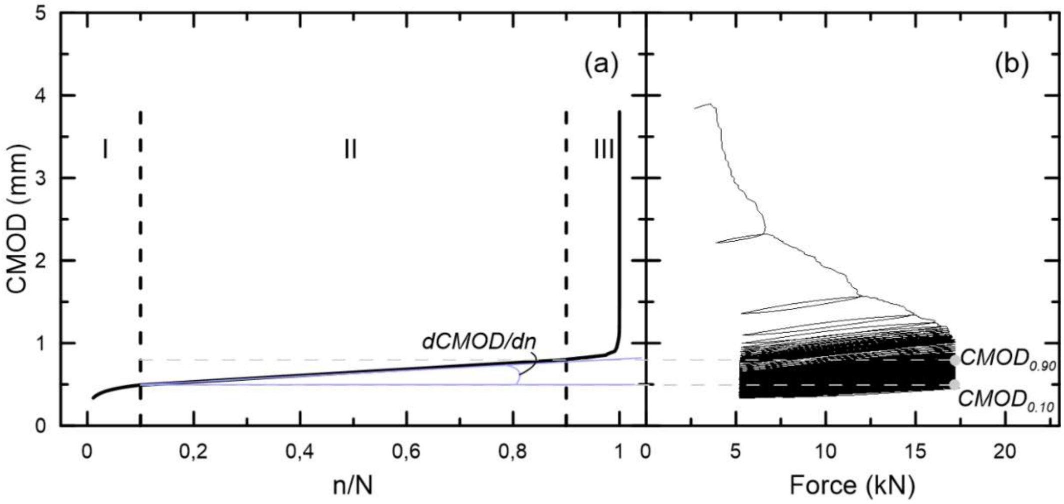

Figure 4.10 - Comparison between typical (a) cyclic creep curve and (b) CMOD per load curves.

The evaluation of CMOD evolution is key for better understanding the fatigue failure of fiber reinforced concrete. Results of the current work for crack opening along the cycles exhibited the same three stage of failure progression presented on past research [24-28] and an increase on the CMOD evolution rate for higher fatigue loads. Present research also presents an attempt to estimate the CMOD evolution rate through Equation 4.16, enhancing the analysis on crack increase under the evaluated load levels. Although only a few papers bring a better understanding on the fiber failure when under fatigue loads [29, 49], fiber rupture and pull-out were the main observed mechanisms of failure. The crack opening increase over the cycles will serve as a base to the development of stiffness degradation and energy growth models.

4.5.4. Mechanical degradation under fatigue loading: stiffness decay and energy release

Figure 4.11 illustrates the mechanical degradation of the studied steel fiber reinforced self-consolidating concrete C40 when under fatigue loading for $S = 70\%$. Figure 4.11(a) brings the pre-crack applied until reaching 0.50 mm of CMOD and Figure 4.11(b) show the hysteresis loops throughout the fatigue test. Stiffness (*k*) is determined as the slope of each hysteresis loop of the fatigue test, whereas the dissipated energy (*ER*) in the damaged zone, in turn, is computed by the summation of the areas enclosed by each unloading-loading cycle.

Figure 4.12(a) brings the stiffness variation along the cycles and reveals a progressive stiffness decay until reaching the material failure [19, 50-53]. The stiffness decline in concrete during flexural fatigue follows a similar phase division observed in Figure 4.10(a), associated with crack opening development along the fatigue life of the specimen. The S-shaped curve is characterized by an initial deacceleration stage followed by an almost linear second phase. The last stage of stiffness decrease reveals a sharp decrease until reaching the material collapse [10].

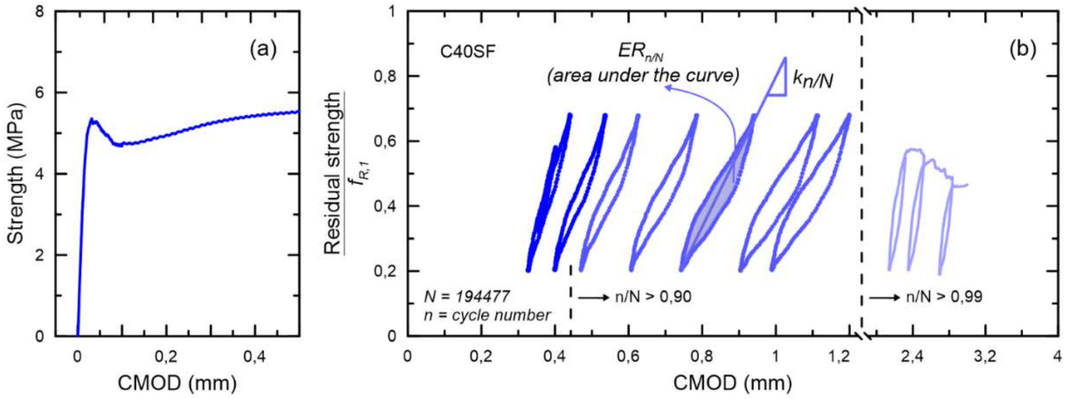

Figure 4.12 - Fatigue test on the FRC composite C40SF: (a) specimen pre-crack until reaching 0.50 mm of CMOD and (b) material degradation throughout the fatigue loading

Figure 4.12(b) shows the dissipated energy along *n/N* and presents a distinct trend throughout the fatigue life. The dissipated energy begins with an almost linear increase until reaching, approximately $n/N = 0.80$, followed by a sharp rise that precedes the material failure. Kolloru *et al.* [10] correlates energy dissipation with crack propagation: crack evolves throughout the cycles in a stable manner if the energy release growth rate is smaller than the crack resistance. Crack propagation becomes sharp right after the energy release growth rate overcomes crack resistance [54].

Figures 4.12(a) and 4.12(b) present both stiffness and energy release in terms of fiber volume fraction of the studied composites (C20SF, C40SF and C60SF). It is possible to verify on both illustrations a direct association between both mechanical parameters and the amount of fibers on the cracked concrete section. Therefore, Figures 4.13(a) and 4.13(b) bring the correlation between initial stiffness and initial energy release (ER_0) and the residual strength at 0.50 mm of CMOD ($f_{r,1}$). Equations 4.17 and 4.18 show both linear tendencies for both cases, respectively. The values of $k_{n/N=0}$ and $ER_{n/N=0}$ were associated to the cycle (n) equals to 100, due to system accommodations that usually occur within the first cycles of the fatigue test.

$$k_0 = 11.32 f_{R,1} + 13.32; R^2 = 0.98 \tag{4.17}$$

$$ER_0 = 0.022 f_{R,1} + 0.0071; R^2 = 0.86 \tag{4.18}$$

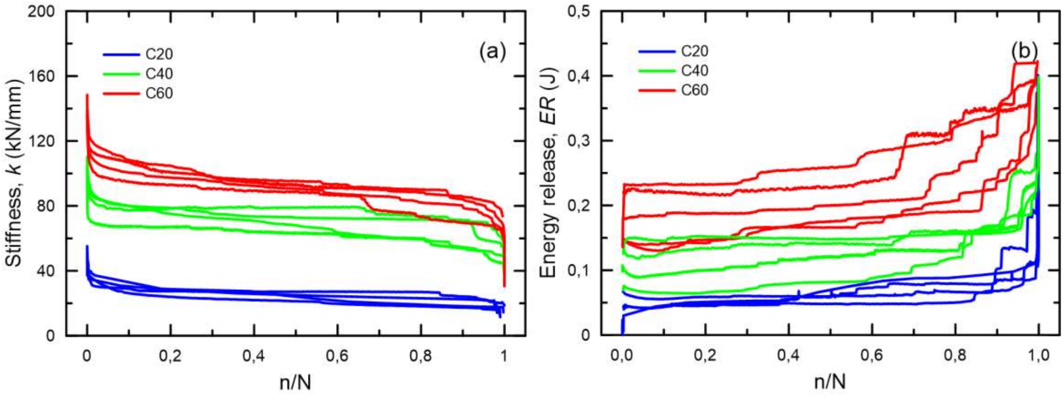

Figure 4.12 - Mechanical deterioration of steel fiber reinforced self-consolidating concrete under distinct load levels (70%, 80% and 90%): (a) stiffness decay and (b) energy release across n/N.

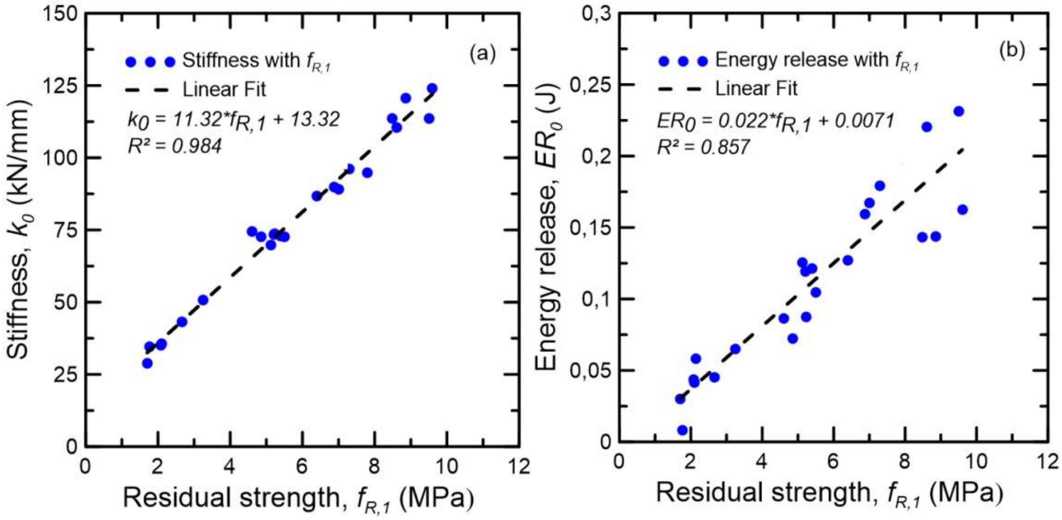

Figure 4.13 - Linear correlation between (a) initial stiffness and (b) initial energy release with residual strength $f_{R,1}$

There is a strong linear correlation between the studied mechanical parameters and $f_{R,1}$, specially for initial stiffness (k_0). Therefore, it is possible to estimate both initial parameters carrying only the static flexural bending test according to EN 14651 [32] and evaluating the residual strength at 0.50 mm of CMOD. This a key step for the development of the current model for damage evolution and energy release growth rate across the cycles. The linear correlation presented at Equations 17 and 18 will serve as input parameters for the degradation prevision methodology explained on the next sections.

4.5.5. Damage evolution and energy release growth rate models

The stiffness deterioration can be assessed through the damage ratio (D), as shown in Equation 4.19. The value of $k_{n/N\,=\,0}$ was associated to the stiffness relative to cycle (n) equal to 100. Figure 4.14 displays damage evolution in terms of *n/N*.

$$\mathrm{D} = 1 - \frac{k\frac{n}{N}}{k_0} \tag{4.19}$$

After damage localization due to FRC pre-crack, the continuous damage accumulation controls the stress-strain behavior on the cracked damaged zone [55]. As observed on Figure 4.14(a), the internal propagation of damage leads to a gradual increase of D until it reaches around 30%, after which a sharp growth of damage is observed before achieving material failure [55, 56]. The condition of reaching 30% of damage ratio may serve a criterion for predicting material failure under fatigue (critical value of D).

Evaluating Figure 4.13(a), the damage curves present very similar values across the useful life of the studied composite, regardless of the applied load level. Therefore, it is possible to determine a unified curve which represents the damage evolution in terms of n/N. Figure 4.14(b) presents the proposed damage model curve in this work. The fitting curve was implemented with the application of the OriginPro software and a Levenberg Marquadt iteration algorithm [57]. Equation 4.20 brings the obtained model for damage evolution with a coefficient of determination (R^2) of 0.97.

$$\mathrm{D} = -5.844 * \ln\left(-0.0450 * \ln\left(\frac{\mathrm{n}}{\mathrm{N}}\right)\right); R^2 = 0.97 \tag{4.20}$$

Different damage models have already proposed in the past for concrete [19, 20, 52, 53, 58]. The nonlinear damage rule by Shah [53], for instance, is based on cubic polynomial model and evaluates damage as a function of *n/N*. Grzyboski *et al.* [54], in turn, proposes another nonlinear model, divided in two distinct loading ranges and defined by the upper stress level S_{max}. Although both equations are greatly mentioned for damage analysis in concrete, they do not properly represent the fatigue deterioration in bending of pre-cracked FRC prisms. As shown in Figure

4.14(b), the proposed model is able to represent the damage evolution on the three main phases of the behavior.

The energy release growth rate (*ΔER*) was measured to assess the energy dissipation variation along the cycles and is described by Equation 4.21.

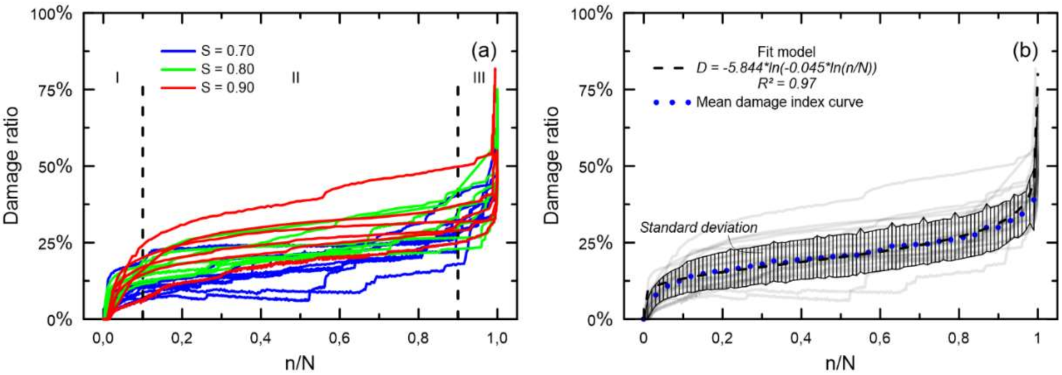

Figure 4.14 - Damage evolution: (a) experimental results and (b) mean points and damage model in terms of *n/N*. the vertical bars represents the standard deviations.

$$\Delta \mathrm{ER} = \frac{ER_{\frac{n}{N}}}{ER_{\frac{n}{N}=0}} - 1 \tag{4.21}$$

The variation of energy release presents a distinct behavior in relation to damage evolution. First, ΔER present a linear behavior until reaching, approximately, n/N = 0.80. Subsequently, a sharp increase on the energy release growth rate takes place until reaching the fatigue failure. Figure 4.15(a) presents an overview of the experimentally-determined energy release growth rate in terms of the cycle ratio *n/N*. Similar to the damage evolution model, a unified model for energy release growth rate was proposed based on the mean results of the experimental assessment of energy dissipation, as shown in Figure 4.15(b).

The ΔER model was divided into two distinct stages. First, a linear curve estimates the rate of energy dissipation until *n/N = 0.80* (Equation 4.22a). Thereafter, an exponential equation is applied up to the end of the material fatigue life (Equation 4.22b). The fitting curves were implemented with the application of the OriginPro software and a Levenberg Marquadt iteration algorithm.

$$\Delta \mathrm{ER} = -0.029 + 0.59 * \left(\frac{\mathrm{n}}{\mathrm{N}}\right); \frac{\mathrm{n}}{\mathrm{N}} \leq 0.80; \mathrm{R}^2 = 0.98 \tag{4.22a}$$

$$\Delta \mathrm{ER} = -0.0029\mathrm{e}^{6.3\left(\frac{n}{N}\right)}; \frac{\mathrm{n}}{\mathrm{N}} > 0.80; \mathrm{R}^2 = 0.99 \tag{4.22b}$$

Similar procedure was to study energy dissipation under fatigue loading was carried on by Germano *et al.* [28]. The authors proposed equation correlates cumulative dissipated energy with the number of cycles at failure. Similar equations were achieved for distinct fiber volume fractions, which is in accordance with the present methodologies. As shown by Germano *et al.* [28], steel fiber reinforced concrete shows definitely higher energy dissipation with respect to plain concrete.

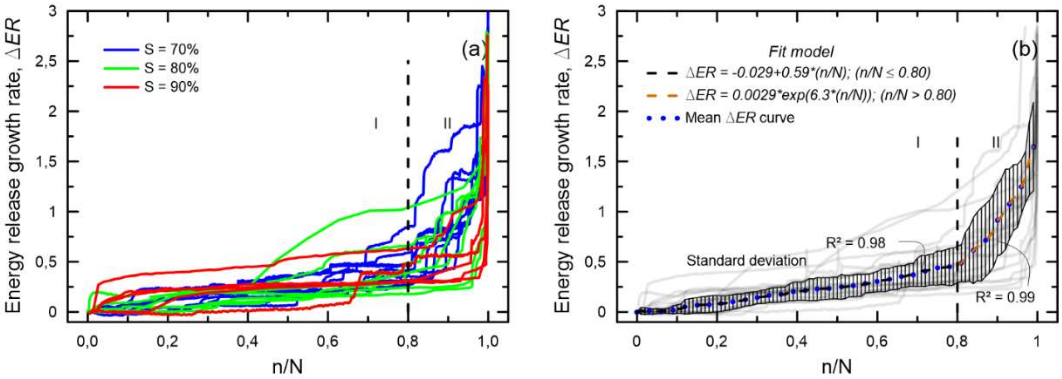

Figure 4.15 - Energy release growth rate along *n/N*: (a) experimental results for distinct load levels (70%, 80% and 90%) and (b) proposed model

4.6. Conclusions

The present study brings a comprehensive study on the mechanical degradation (stiffness decay and energy dissipation progression) and on fatigue life of steel fiber reinforced concrete subjected to fatigue loading. Initially, the experimental campaign addresses the influence of the addition of steel fibers on the composite fatigue life and evaluates the fatigue life of SFRC for distinct failure probabilities through Weibull distribution. At last, two models to estimate damage evolution and energy dissipation are proposed aiming to verify the material mechanical degradation through phenomenological equations. The following conclusions are achieved from the research:

- There is a positive influence on the fiber addition on fatigue life of the fiber reinforced composite. The inclusion higher fiber volume fractions on the concrete mixture are responsible on enhancing the fatigue life of the composite, especially when comparing with plain concrete. With the use of 60 kg/m³, the steel fiber reinforced composite is able to reach the proposed fatigue limit of 1,000,000 cycles without collapsing. During fatigue loading, crack mouth opening displacement permanently grows in relation to the number of cycles. For plain concrete, the specimen reaches collapse due to a lack of post-crack residual resistance. With the fiber inclusion, the reinforcement is responsible bridging the crack and enhancing the useful life of the composite after the matrix crack.

- The Wöhler relation and the two-parameter Weibull distribution presented key limitations when it comes to assess the fatigue life of pre-cracked FRC. The application of a three-parameter Weibull distribution, on the other hand, could successfully estimate fatigue life for distinct failure probabilities (5%, 50% and 95%). For the last studied model, there is a need to apply the endurance limit, which is a complex variable to evaluate experimentally. The cumulated distribution functions better fitted to the experimental fatigue results, when $S = 40\%$ of endurance limit was used.
- The CMOD evolution for all studied load levels presents a similar three stage failure progression. First, there is a stable increase in crack opening at a decreasing rate of CMOD evolution. Thereafter, a slow and gradually increase of CMOD takes place, entailing an approximate a linear CMOD per cycle regime. Finally, the last stage occurs right before collapse, with a rapid increase of crack opening and drastic decrease in material stiffness. The load level influences significantly the rate of crack opening over the cycles. At higher fatigue load levels, a faster increase in CMOD, during the second stage of failure progression, is attributed to the higher energy imposed on the specimens within a short time duration.
- The proposed methodology for estimating mechanical degradation (stiffness decay and energy release evolution) of steel fiber reinforced concrete is oriented on the initial measured stiffness and energy release of the composite. The mechanical parameters at the initial relative life cycle (n/N = 0) present a strong linear correlation the residual strength at 0.50 mm of CMOD ($f_{R,1}$). Hence, the presented linear relations allow to estimate the initial stiffness and energy release of the composite before the initializing the fatigue material degradation.
- Using the fatigue experimental results, two novel empirical correlations are proposed to estimate damage evolution and energy release growth rate throughout the relative life cycles (n/N). Both equations have as input variables fatigue life until reaching failure (N) and the respective initial mechanical parameters (k_0 and ER_0), which were already estimated through

the Weibull distribution and the residual flexural strength at 0.50 mm of CMOD. Hence, by following the proposed methodology and applying the present equations is possible the have the mechanical degradation (stiffness decay and energy release evolution) along the fatigue life without carrying an extensive experimental campaign.

4.7. References

1 CONFORTI, A. TIBERTI, G. PLIZZARI, G. CARATELLI, A. MEDA, A. Precast tunnel segments reinforced by macro-synthetic fibers. **Tunnelling and Underground Space Technology**, vol. 63, p. 1-11, 2017.

2 LIAO, L. DE LA FUENTE, A. CAVALARO, S. AGUADO, A. Design procedure and experimental study on fibre reinforced concrete segmental rings for vertical shafts. **Materials and Design**, vol. 92, p. 590-601, 2016.

3 BELLETTI, B. CERIONI, R. MEDA, A. PLIZZARI, G. Design aspects on steel fiber-reinforced concrete pavements. **Journal of Materials in Civil Engineering**, vol. 20, p. 599-607, 2008.

4 SRITHARAN, S. SCHMITZ, G. **Design of tall wind turbine towers utilizing UHPC**. In: RILEM-fib-AFGC International Symposium on Ultra-High Performance Fibre-Reinforced Concrete, 2013.

5 HOLMEN, J. Fatigue design evaluation of offshore concrete structures. **Matériaux et Construction** (1984), vol. 17, p. 39-42, 1984.

6 AGLAN, H. FIGUEROA, J. Damage-evolution approach to fatigue cracking in pavements. **Journal of Engineering Mechanics**, vol. 119, p. 1243-1259, 1993.

7 SUBRAMANIAM, K. GOLDSTEIN, G. POPOVICS, J. SHAH, S. fatigue response of concrete subjected to biaxial fatigue in the compression-tension region. **ACI Materials Journal**, vol. 96, p. 663-669, 1999.

8 GÖRANSSON, F. NORDENMARK, A. **Fatigue assessment of concrete foundations for wind power plants**. MSc dissertation, 142 p. Göteborg, Sweden: Chalmers University of Technology, 2011.

9 GAO, L. HSU, T. Fatigue of concrete under uniaxial compression cyclic loading. **ACI Materials**, vol. 95, p. 575-581, 1998.

10 SUBRAMANIAM, K. O'NEIL, E. POPOVICS, J. SHAH, S. Crack propagaton in flexural fatigue of concrete. **Journal of Engineering Mechanics**, vol. 126, p. 891-898, 2000.

11 GAEDICKE, C. ROESLER, J. SHAH, S. Fatigue crack growth prediction in concrete slabs. International **Journal of Fatigue** (2009), vol. 31, p. 1309-1317, 2009

12 CACHIM, P. **Experimental and numerical analysis of the behavior of structural concrete under fatigue loading with application to concrete pavements**. Ph.D. thesis, Faculty of Engineering, University of Porto, 1998

13 NAAMAN, A. HAMMOUD, H. Fatigue characteristics of high performance fiber-reinforced concrete. **Cement Concrete Composites**, vol. 20, p. 353-363, 1998.

14 BANJARA, N. RAMANJANEYULU, K. Experimental investigations and numerical simulations on the flexure fatigue behavior of plain and fiber-reinforced concrete. **Journal of Materials in Civil Engineering** (2018), vol. 30.

15 CHANG, D. CHAI, W. Flexural fracture and fatigue behavior of steel-fiber-reinforced concrete structures. **Nuclear Engineering and Design** (1995), vol. 156, p. 201-207, 1995.

16 LEE, M. BARR, B. An overview of the fatigue behavior of plain and fibre reinforced concrete. **Cement Concrete Composites**, vol. 26, p. 299-305, 2004.

17 HSU, T. Fatigue of plain concrete. **ACI Journal**, vol. 78, p. 292-304, 1981.

18 MEDEIROS, A. ZHANG, X. RUIZ, G. YU, R. VELASCO, M. Effect of the loading frequency on the compressive fatigue behavior of plain and fiber reinforced concrete. **International Journal of Fatigue**, vol. 70, p. 342-350, 2015.

19 BAKTHEER, A. HEGGER, J. CHUDOBA, R. Enhanced assessment rule for concrete fatigue under compression considering the nonlinear effect of loading sequence. International **Journal of Fatigue**, vol. 126, p. 130-142, 2019.

20 BAKTHEER, A. CHUDOBA, R. Experimental and theoretical evidence for the load sequence effect in the compression fatigue behavior of concrete. **Materials and Structures**, vol. 54, p. 82, 2021.

21 SINGH, S. KAUSHIK, S. Fatigue strength of steel fibre reinforced concrete in flexure. **Cement & Concrete Composites**, vol. 25, p. 779-786, 2003.

22 CASTILLO, E. CANTELI, A. **A unified statistical methodology for modeling fatigue damage**. 1st ed. Springer, 2009.

23 CANTELI, A. CASTILLO, E. BLASÓN, S. A methodology for phenomenological analysis of cumulative damage processes. Application to fatigue and fracture phenomena. **International Journal of Fatigue** (2021), vol. 150, 2021.

24 DE LA ROSA, A. RUIZ, G. CASTILLO, E. MORENO, R. Calculation of dynamic in concentrated cementitious suspensions: probabilistic approximation and Bayesian analysis. **Materials**, vol. 14, 2021.

25 CARLESSO, D. DE LA FUENTE, A. CAVALARO, S. Fatigue of cracked high performance fiber reinforced concrete subjected to bending. **Construction and Building Materials**, vol. 220, p. 444-455, 2019.

26 STEPHEN, S. GETTU, R. Fatigue fracture of fibre reinforced concrete in flexure. **Materials and Structures**, vol. 53, p. 56, 2020.

27 CARLESSO, D. CAVALARO, S. DE LA FUENTE, A. Flexural fatigue of pre-cracked plastic fibre reinforced concrete: experimental study and numerical modeling. **Cement and Concrete Composites** (2021), vol. 115, 2021.

28 GERMANO, F. TIBERTI, G. PLIZZARI, G. Post-peak fatigue performance of steel fiber reinforced concrete under flexure. **Materials and Structures**, vol. 49, p. 4229-4245, 2016.

29 FATAAR, H. COMBRINCK, R. BOSHOFF, W. An experimental study on the fatigue failure of steel fibre reinforced concrete at a single fibre level. **Construction and Building Materials**, vol. 299, 2021.

30 FATAAR, H. COMBRINCK, R. NOSHOFF, W. **An experimental study on the flwxural fatigue behavior of pre-cracked steel fibre reinforced**

concrete. In: Fibre Reinforced Concrete: Improvements and Innovations II, BEFIB 2021, RILEM Bookseries, vol. 36, 2021.

31 CARLESSO, D. DE LA FUENTE, A. CAVALARO, S. **Fatigue of cracked steel fibre reinforced cocnrete subjected to bending**. In: Fibre Reinforced Concrete: Improvements and Innovations II. BEFIB 2021. RILEM Bookseries, 36, 2021.

32 EUROPEAN COMMITTEE FOR STANDARDIZATION. **EN 14651**. Test method for metallic fibre concrete – Measuring the flexural tensile strength (limit of proportionality (LOP), residual), 2005.

33 CARDOSO, D. PEREIRA, G. SILVA, F. SILVA, J. PEREIRA, E. Influence of steel fibers on the flexural behaviour of RC beams with low reinforcing ratios: Analytical and experimental investigation. **Composite Structures**, 222, 2019.

34 RAMBO, D. SILVA, F. TOLEDO, R. Mechanical behavior of hybrid steel-fiber self-consolidating concrete: Materials and structural aspects. **Materials and Design**, vol. 54, p. 32-42, 2014.

35 AMERICAN SOCIETY FOR TESTING AND MATERIALS. **ASTM C1611**: Standard test method for slump flow of self-consolidating concrete, 2005.

36 EUROPEAN FEDERATION OF NATIONAL ASSOCIATIONS REPRESENTING FOR CONCRETE. **EFNARC**. The European guidelines for self-compacting concrete: specification, production and use, 2005.

37 INTERNATIONAL FEDERATION FOR STRUCTURAL CONCRETE. **CEB-FIB**. International Recommendations for the Design and Construction of Concrete Structures, 2010.

38 SCHIJVE, J. **Fatigue of Structures and Materials**. Second ed., Springer, 2009.

39 DOWLING, N. **Mechanical Behavior of Materials**. Fourth ed., Pearson, 2013.

40 RAMAKRISHNAN, V. WU, G. HOSALLI, G. Flexural fatigue strength, endurance limit, and impact strength of fiber reinforced concrete. **Transportation Research Record Journal**, vol. 1226, p. 17-24, 1984.

41 MCCALL, J. Probability of fatigue failure of plain concrete. Journal of the **American Concrete Institute**, vol. 30, p. 233-244, 1958.

42 SINGH, S. SINGH, B. KAUSHIK, S. Probability of fatigue failure of steel fibrous concrete. **Magazine of Concrete Research**, vol. 57, p. 65-72, 2005.

43 SINGH, S. SHARMA, U. Flexural fatigue strength of steel fibrous concrete beams. **Advances in Structural Engineering**, vol. 10, p. 197-207, 2007.

44 EUROPEAN COMMITTEE FOR STANDARDIZATION. **EN 1990**. Basis of Structural Design, 2005.

45 FREUDENTHAL, A. GUMBEL, E. **On the statistical interpretation of fatigue tests**. Proceedings of the Royal Society A: Mathematical, Physical and Engineering Sciences, vol. 216, p. 309-332, 1953

46 OH, B. Fatigue-life distributions of concrete for various stress levels. **ACI Materials Journal**, vol. 88, p. 122-128, 1991.

47 SINGH, S. KAUSHIK, S. Flexural fatigue life distributions and failure probability of steel fibrous concrete. **ACI Materials Journal**, vol. 97, p. 658-667, 2000.

48 YANG, F. REN, H. HU, Z. Maximum likelihood estimation for three-parameter Weibull distribution using evolutionary strategy. **Mathematical Problems in Engineering**, 2019, doi.org/10.1155/2019/6281781.

49 VICENTE, M. MÍNGUEZ, J. GONZÁLEZ, D. Computed tomography scanning of the internal microstructure, crack mechanisms, and structural behavior of fiber-reinforced concrete under static and cyclic bending tests. International **Journal of Fatigue**, vol. 121, p. 9-19, 2019.

50 BOULEKBACHE, B. HAMRAT, M. CHEMROUK, M. AMZIANE, S. Flexural behavior of steel fiber-reinforced concrete under cyclic loading. **Construction and Building Materials**, vol. 126, p. 253-262, 2016.

51 SHAN, Z. YU, Z. LI, X. XIE, Y. Damage quantification in concrete under fatigue loading using acoustic emission. **Journal of Sensors**, 2019.

52 LEI, L. XINGANG, S. YUNHUA, C. LEFAN, W. XIANGCHENG, Y. A new fatigue damage model for pavement concrete beams bearing multi-level bending loads. **Journal Pone**, 2021

53 SHAH, S. Predictions of cumulative damage for concrete and reinforced concrete. **Matériaux et Construction Journal** (1984), vol. 17, p. 65-68.

54 SHAH, S. CHANDRA, S. Determination of fracture parameters (K_{IC} and $CTOD_C$) of plain concrete using three-point tests. **Materials and Structures Journal** (1990), vol. 23, p. 457-460, 1990.

55 MU, B. KOLLURU, V. SHAH, S. Failure mechanism of concrete under fatigue compressive load. **Journal of Materials in Civil Engineering,** vol. 16, p. 566-572, 2004.

56 GYLLTOFT, K. A fracture mechanics model for fatigue in concrete. **Matériaux et Construction**, vol. 17, p. 55-58, 1984.

57 BARD, Y. **Nonlinear parameter estimation**. Academic Press, 1973

58 GRZYBOWSKI, M. MEYER, C. Damage accumulation in concrete with and without fiber reinforcement. **ACI Materials Journal**, vol. 90, p. 594-604, 1993.

5 The influence of steel fibers on the bond-slip behavior between rebars and concrete: experimental and analytical investigation

Chapter 5 brings a broad analysis on the influence of steel fibers on quasi-static and fatigue rebar pull out loading. The analysis covers the impact of fiber addition on diverse mechanical parameters, such as peak bond strength, stiffness and bond degradation under fatigue. A model previously developed for single fiber pull out in the literature was modified in order to study the bond response through analytical equations. The fiber reinforcement is responsible for providing post-crack resistance to the composite, raising the confinement around the interface and significantly increasing the peak bond strength. Moreover, by enhancing the bond strength, the addition of steel fibers could successfully increase fatigue life of cyclic pull out tests. Finally, the proposed model for rebar pull out from steel fiber reinforced concrete matrices successfully fitted the bond-slip behavior observed the experimental data. The model divided the bond-slip response in three distinct stages: elastic, nonlinear and dynamic.

This section was partly made at the Arizona State University under supervision of Barzin Mobasher.

Published article: December 10th, 2023 – *Construction and Building Materials Journal,* *doi.org/10.1016/j.conbuildmat.2023.134357*.

Notations			
AR	Aspect ratio	$P_{1b,max}$	Maximum model bond force at stage 1
A_m	Mobilized concrete area	$P_{b,max}$	Maximum experimental bond force
A_R	Rebar area	P_{upp}	Upper applied pull-out force
d	Debonded length	P_{low}	Lower applied pull-out force
δ_R	Model rebar elongation	P_d	Model debonded force at stage 2
δ_m	Model matrix shortening	$P_{2b,max}$	Model bonded force at stage 2
δ_0	Initial slip	ϕ_R	Rebar diameter
$\delta_{n/N}$	Slip at referred cycle number n/N	ϕ_m	External concrete ring diameter
δ_{peak}	Slip at bond strength	E_R	Rebar young modulus
ε_R	Model rebar deformation	E_m	Matrix young modulus
ε_m	Model matrix deformation	τ	Shear stress
f_c	Concrete compressive strength	τ_b	Bond shear stress
F	Tensile force on the rebar	$\tau_{b,max}$	Monotonic bond strength
K_b	Bond stiffness	τ_{max}	Model elastic peak shear strength
κ	Model linear slope	τ_{frc}	Model frictional shear strength
L	Embedment length	τ_{dyn}	Model dynamic shear strength
λ	Fiber factor	T_{peak}	Toughness up to peak strength
M	Matrix	T_{4mm}	Toughness up to 4 mm slip
λ	Fiber factor	s	Model slip
n	Cycle number	S	Fatigue load level
N	Number of cycles before failure	V_f	Fiber volume fraction
n/N	Normalized cycle number		

5.1. Introduction

Bond between rebars and concrete plays a major role in RC members design aiming the analysis of the structural mechanical behavior [1-3]. Serviceability and safety conditions demand continuous improvement of the rebar-concrete bond similarly to what is applied to control concrete cracking under service conditions [4]. Especially under complex loading conditions and harsh environments, bond performance and its degradation along structural life become a key factor for accurate design.

In general, the interaction of steel reinforcing bars with concrete mainly consists of three major components: friction, chemical adhesion and mechanical interlock [5, 6]. While friction and adhesion are dominant for smooth bars, mechanical interlock becomes the major resisting mechanism for ribbed bars. Previous studies have already extensively verified that the three mentioned components are influenced by innumerous factors, such as concrete cover, rebar diameter and matrix mechanical properties [7-10]. Meanwhile, with the development of fiber application in concrete structures, it has also been verified that the addition of the fiber reinforcement is an effective way of improving rebar bond performance of concrete members [11-16].

Assessment of the bond between concrete and rebar by pull out experiments has been carried out through very distinct standards and references. In general, a pull out test consists of pulling a rebar out through a tension force in a static loading rate from a previously cast cementitious specimen. Both applied force and relative displacement between rebar and concrete (bond-slip) are continuously recorded and measured. Distinct test parameters, such as concrete specimen dimensions, bond length and loading rate, are suggested in the literature [2, 11, 17, 18]. RILEM [19] and ASTM A944-22 [20] recommendations are some of the main followed references that bring recommendations on the pull out test. The bond between rebars and concrete can also be assessed through beam specimens. In order to evaluate the bond resistance for each splice, one rebar is extended bond free inside the beam and the bond free length is secured by placing the reinforcement inside PVC tubes [11, 21]. After the matrix reaches its cracking tensile resistance, the bond around the splice length begins to control the overall mechanical behavior. The assessment of the bond through structural tests was evaluated by past works of Haraji *et al.* [21], Wu *et al.* [22] and Al-Salloum *et al.* [23]

Several research works [24-27] have attempted to formulate equations to represent the bond between the reinforcing bars and concrete. In general, the proposed empirical formulas include the effects of the concrete cover, the cylinder compressive strength, rebar diameter and the development length. A rebar bond model for plain concrete, including stress-slip curve and maximum bond stress, has already been presented in Model Code 2010 [4], summarizing all previous studies in this subject. While bond stress is calculated through bond force in relation to contact area at rebar-concrete interface, bond slip is defined as the displacement of the rebar relative to the surrounding concrete. However, as explained by Chu *et al.* [28], the lack of information about bond stiffness does not enable one to verify crack width analysis in reinforced concrete structures.

Bond strength is defined as the maximum recorded bond stress along the bond-slip curve and is the main parameters used on the determination of bond-slip models in the literature [14-16]. Past works in the literature have already proven the beneficial effects on the fiber addition on the increase on the bond strength between fiber reinforced concrete and the rebar. The fiber reinforcement can successfully enhance confinement on the rebar during its pull out from the specimen [10-13].

When it comes to the study of fiber reinforced concrete (FRC) influence on the bond models, distinct empirical equations have already been proposed. Haraji *et al.* [29], for instance, modified an earlier bond model to account the steel fiber influence by using the post-crack resistance of the fiber composite. Subsequently, Chao [30] proposed that the peak bond strength can be evaluated through a linear equation based on the concrete compressive strength and the post-cracking resistance due to fiber addition. More recently, Chao [31] suggested that the effect of fiber addition may be assessed as a function of the fiber factor ($V_f\,x\,AR$), where V_f is the fiber volume fraction and AR is the fiber aspect ratio. More recently, Yoo *et al.* [32] pointed out that the recommended equations stablished in the Model Code [4] are inappropriate for modelling the bond behavior of ultra-high performance concrete (UHPC), proposing a correction factor on the bond strength equation.

A second step on the analysis of the bond degradation takes place during the long-term service life, which can often result in deterioration of structural performance, such as anchorage failure and crack propagation. Therefore, the study of the fatigue bond behavior for assessing the long-term mechanical properties of reinforced concrete structures is key when it comes for accurate design. Previous works have already carried out incipient tests to verify the slip evolution at fatigue tests [33-37] and pull out failure has been observed in the majority of the cases. The development of relative slip appears in three stages in accordance with the increase of fatigue cycles. First, initial slip increase rate slows down progressively and, then, remains almost constant in the second stage [38-41]. In the third stage, the slip sharply increases before reaching the complete rebar pull out from the concrete specimen.

Overall, the existing studies of the influence of steel fibers on bond behavior under quasi-static and fatigue loading have not yet been refined and the present models may not agree with each other. Therefore, the present research brings an extensive discussion about the effect of fiber reinforcement on the rebar-concrete bond strength and on the fatigue degradation through pull out tests. A high strength self-consolidating concrete with the addition of 20 kg/m^3, 40 kg/m^3, 60 kg/m^3 and 80 kg/m^3 of steel fibers was selected for the experimental program. The analytical model for steel fiber pull out previously developed by Naaman *et al.* [42] and Sueki *et al.* [43] is, subsequently, modified in this paper and used to investigate the bond mechanism for rebar pull out from concrete matrices. The adapted model is then applied for the achieved experimental results and for other studies in the literature [6, 28, 44, 45, 46], including the rebar pull out from a UHPC matrix. The present study aims to better refine the main influence of steel fibers on the main bond-slip parameters (bond strength, stiffness and toughness), propose a novel analytical methodology for rebar pull out and bring a better understanding of the bond degradation under fatigue.

5.2. Experimental program

5.2.1. Materials

A self-consolidating concrete matrix was used to evaluate bond between steel rebar and concrete bond mechanism. In terms of mineral addition, fly ash, silica fume and silica mesh 325 (ground quartz) were added to the mix composition. Two classes of particle size of river sand were used: the first one ranged from 0.15 mm to 4.8 mm (S1) and the second from 0.15 to 0.85 mm (S2). The coarse aggregate had maximum diameter of 9.5 mm. When it comes to the cementitious materials, Brazilian CPII-F 32 (ASTM Cement type IL - Portland-Limestone Cement [47]) was used. The following admixtures were added: superplasticizer MasterFlenium 51 and the viscosity modifying admixture MasterMatrix VMA 358. For a water/cement ratio of 0.50, the concrete matrix reached 50 ± 2 MPa after 28 days. The design of the matrix was made according to the compressible packing model (CPM), proposed by de Larrard [48]. More information on the material development can assessed by Rambo *et al.* [49, 50]. The flowability of the fresh composition was characterized through ASTM C1611 [51] standard, reaching a value of 710 mm of concrete spread. Table 5.1 shows the studied mix composition.

Table 5.1 – Mix composition of self-consolidating concrete matrix

Constituent	Matrix
Coarse aggregate	492
Sand (S1) (kg/m^3)	827
Sand (S2) (kg/m^3)	100
Silica Mesh 325 (kg/m^3)	70
Cement (kg/m^3)	360
Fly Ash (kg/m^3)	168
Silica Fume (kg/m^3)	45
Water (kg/m^3)	164
Superplasticizer (%)	5.50
Viscosity modifying admixture (%)	0.75

**Sand (S2): Sand (S1) with diameter less than 0.85 mm*

One type of hooked-end steel fiber was used in this research. The steel fiber reinforcement presents 35 mm length, 45 of aspect ratio and 1225 MPa of wire direct tension strength. Table 5.2 summarizes the properties for the studied steel fibers. Four distinct fiber volume fractions were analyzed: 0.25% (20 kg/m^3), 0.50% (40 kg/m^3), 0.75% (60 kg/m^3) and 1.0% (80 kg/m^3). The fiber factor is defined as the fiber aspect ratio times the fiber volume fraction ($\lambda = AR \times V_f$). Since 45 was the aspect ratio of the applied fiber, the following fiber factors were analyzed in this study: 0.11, 0.22, 0.33, 0.44. The cementitious composites were, then, named accordingly to their fiber factors: C0.11SF, C0.22SF, C0.33SF and C0.44SF. The composition without fiber addition is represented by C0SF.

The steel fiber reinforced concrete (SFRC) post-peak flexural resistance was determined through pre-notched beam tests in accordance with EN 14651 [52] standard and taken from previous work carried by Monteiro *et al.* [53, 54]. Table 5.3 summarizes the post-crack stress parameters for the four SFRC studied compositions. The values of $f_{R,i}$ are defined as the flexural residual stresses with i = 1,2,3 and 4, respectively, for Crack Mouth Opening Displacements (CMOD) values of 0.50, 1.50, 2.50 and 3.50 mm.

A 6.3 mm diameter steel bar was used in this research program. A nominal 500 MPa yield strength was reported by the manufacturer. The deformed steel bars have transverse ribs.

Table 5.2 – Steel fiber properties

Properties	SF 
Type	Hooked-end
Length (mm)	35
Diameter (mm)	0.75
Aspect Ratio	45
Tension strength (MPa)	1225

5.2.2.Concrete mixing procedure

The concrete was produced with a 100 L concrete mixer. First, both coarse aggregate and sand were blended together with 70% of the water for 1 minute. Thereafter, mineral materials (silica fume, silica flour and fly ash) were added and mixed with the aggregate for another minute. Next, the cement is added and blended for 1 minute. The 30% remaining water, the viscosity modifying admixture and superplasticizer are added inside the mixer and blended with the rest of the materials for 10 minutes. The final step consists on the addition of the steel fiber reinforcement and an extra mixing procedure for more 5 minutes before casting the molds. The specimens were cured in air for 28 days with an average temperature and humidity, respectively, of 22ºC and 55%.

Table 5.3 – Post-peak parameters for monotonic three-point bending tests in accordance with EN 14651 [41] standard. Standard deviation values presented in parentheses.

Mix	f_{lop} MPa	$f_{R,1}$ MPa	$f_{R,2}$ MPa	$f_{R,3}$ MPa	$f_{R,4}$ MPa
C0.11SF	5.59	3.31	2.76	1.66	1.23
	(0.21)	(3.31)	(2.76)	(1.66)	(1.23)
C0.22SF	6.38	7.07	6.01	3.78	2.75
	(0.56)	(1.00)	(0.82)	(0.33)	(0.22)
C0.33SF	6.37	7.88	6.95	4.87	3.82
	(0.75)	(2.09)	(1.89)	(1.80)	(1.26)
C0.44SF	6.39	9.16	6.25	4.4	3.34
	(0.35)	(0.68)	(1.48)	(1.49)	(1.35)

5.2.3. Test program

5.2.3.1. Quasi-static pull out tests

To characterize the interface between steel rebars and concrete, pull out tests were performed using a setup adapted from RILEM recommendations [19]. All quasi-static and fatigue tests were performed in a universal testing machine MTS 311 model with a capacity of 1000 kN. The typical specimen for the pull out test is shown in Figure 5.1. Concrete specimens presented 150 mm side cubic form with a single deformed rebar embedded along the axle wire of mold and a PVC tube was applied to adjust the bond length. A bond length of 60 mm (ten times the rebar diameter) was used for all tests.

Figure 5.2 brings an overview of the complete test setup applied for the pull out tests. The specimens were positioned at the bottom of a metallic cage, which was anchored on the superior machine grip. The specimen rebar was then anchored on the inferior grip, before starting the pull out test. Two 10 mm LVDTs were used for this experiment. The first one recorded the displacement between the cage and the specimen throughout the test. The second LVDT was attached to the rebar and measured the slip between it and the concrete specimen. The quasi-static tests were performed under 0.50 mm/min machine displacement control rate until reaching 10 mm slip. A total of four specimens was tested for each mix composition analyzed in this research.

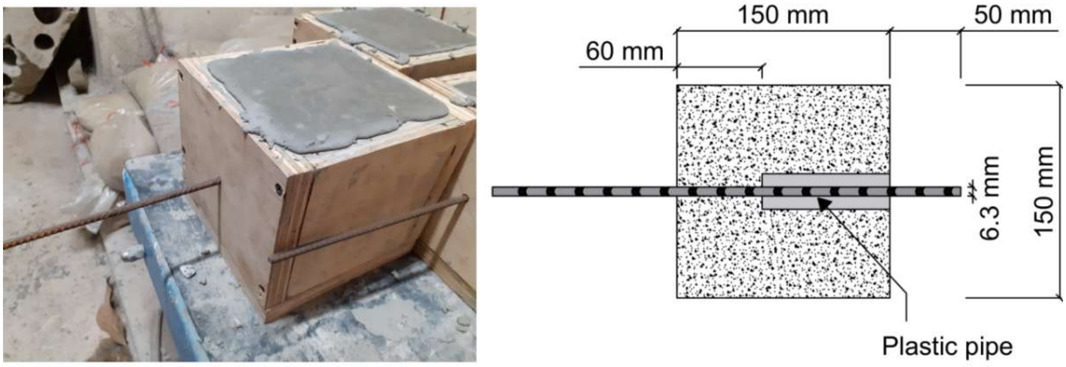

(a) (b)

Figure 5.1 - Pull out specimen details: (a) specimen molding and (b) dimensions.

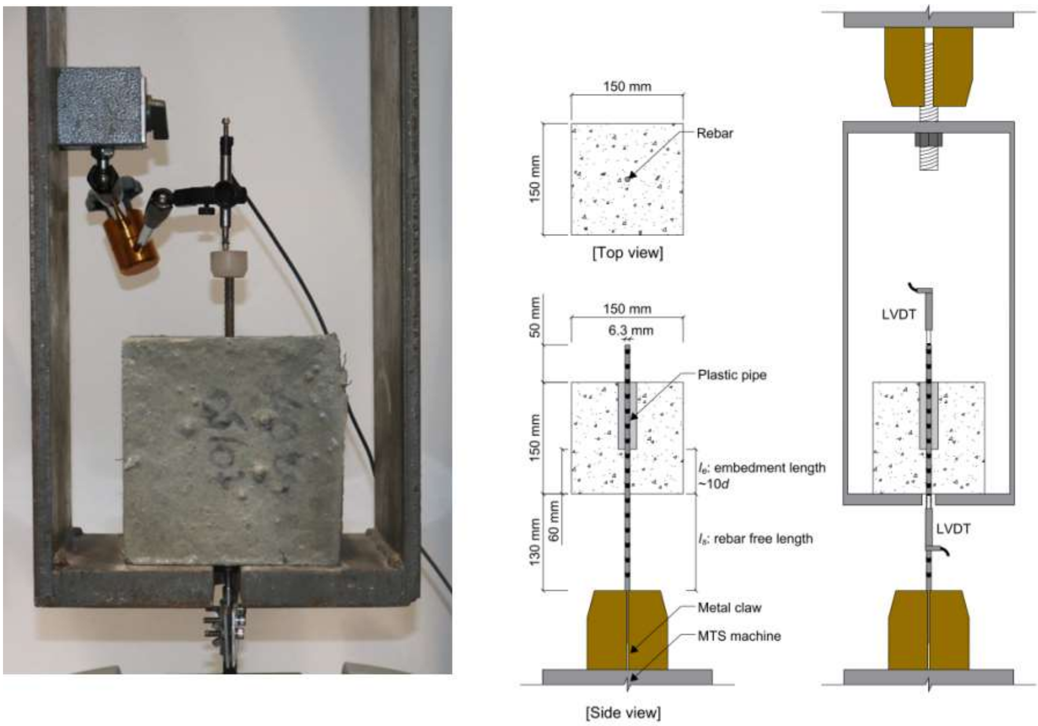

(a) (b)

Figure 5.2 - Pull out test setup: (a) test photo and (b) test illustration.

5.2.3.2. Fatigue pull out tests

The pull out fatigue tests experimental procedure was illustrated in figure 5.3. After achieving the monotonic bond strength ($\tau_{b,max}$), the corresponding minimum and maximum bond force under fatigue loading could be determined. The minimum bond force (P_{low}) was set as 30% of the maximum bond force (P_{upp}), resulting in a force ratio of 0.30 ($R = P_{low}/P_{upp} = 0.30$). During the loading process, the pull out forces were first loaded until reaching P_{upp}. Thereafter, the specimens were cycled between P_{upp} and P_{low} in a sinusoidal form. Three distinct load levels ($S = \%P_{b,max}$) were applied in this research: 50%, 80% and 90%. The load level is defined as the ratio between the bond strength and the maximum stress applied on the fatigue test. All tests were carried on at a 6 Hz frequency. The test was terminated when the studied specimen either reached failure or 1,000,000 cycles (run-out), which is in accordance with previous research works on fatigue in cementitious composites [55-57].

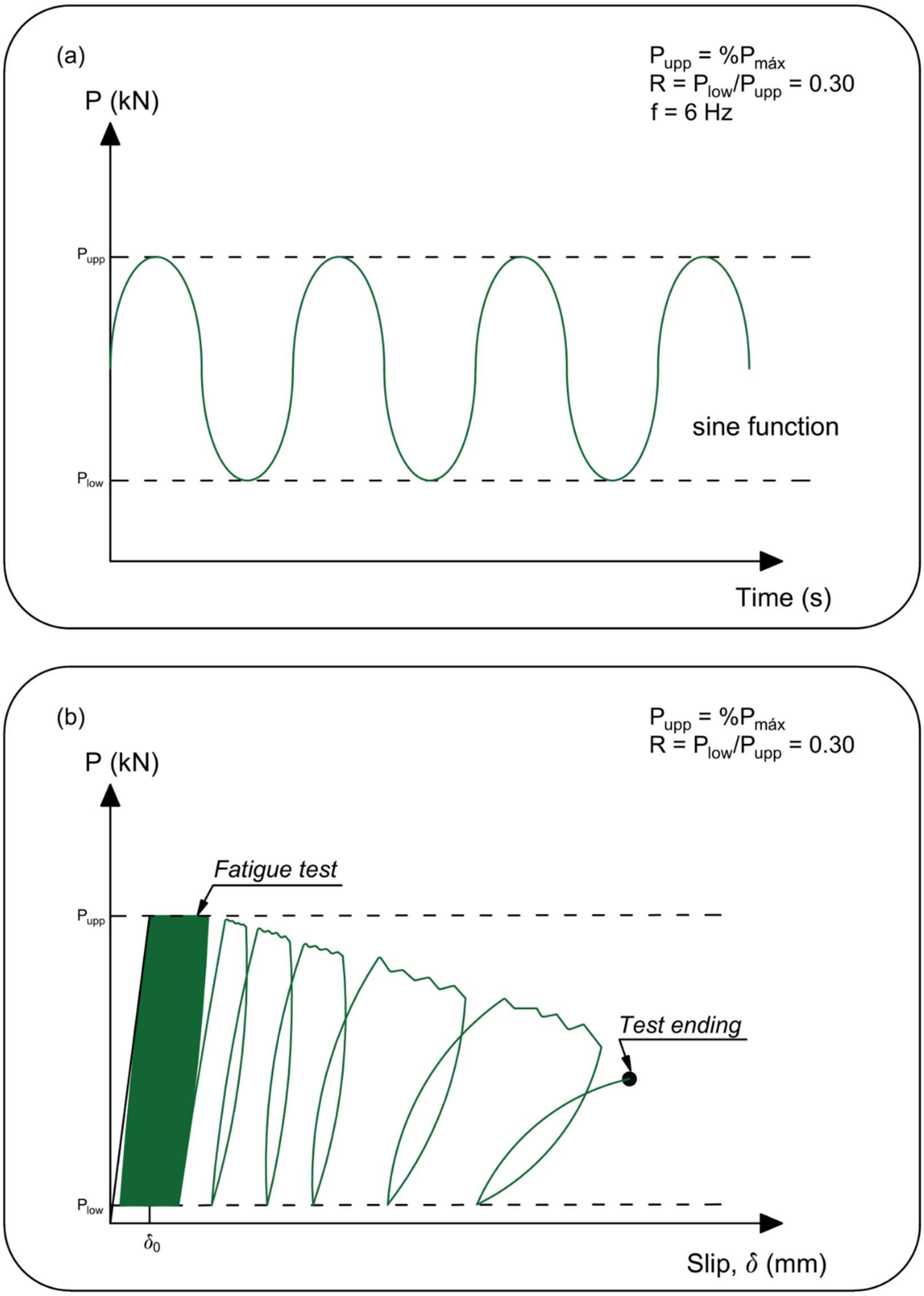

Figure 5.3 - Pull out fatigue test experimental procedure: (a) sinusoidal cyclic loading in 6 Hz of frequency and (b) loading variation in relation slip evolution.

5.3. Analytical model

The applied analytical model was originally developed by Naaman *et al.* [42] for steel fiber pull out from cementitious matrices and, subsequently, modified for the pull out-slip response of fabrics from cement pastes by Sueki *et al.* [43]. Figure 5.4(a) shows a typical pull out-slip response obtained by pulling the rebar from a concrete matrix. The extension of the proposed model from fibers to rebars in possible since the same shear mechanisms take place along the both interfaces. In general, the interaction of rebars/fibers with concrete mainly consists of three major components: friction, chemical adhesion and mechanical interlock. While friction and adhesion are dominant for smooth pieces, mechanical interlock becomes the major resisting mechanism when ribs or hooks are present.

The curve is divided into three major zones based on distinct stages of shear distribution along the rebar. At first (stage I), a perfect bond with linear behavior is assumed on the rebar-concrete interface. Stage II is characterized for the constant frictional stress (τ_{frc}) along the debonded zone in addition to a shear lag model terminating with the maximum bond strength value (τ_{max}). As debonding propagates, the stiffness of the load-slip curve decreases until the entire embedment length is debonded. Stage III is linked to the dynamic slide of the rebar from the matrix. After a smooth decay from the frictional shear strength (τ_{frc}) until to the final dynamic shear stress (τ_{dyn}), stage III if governed solely by a constant dynamic shear stress (τ_{dyn}). The dynamic stage is associated to the rigid body motion of the rebar inside the concrete matrix until it is completed pulled out. The mechanisms of force distribution, shear stress and resulting derivations for each stage are detailed in the next sections.

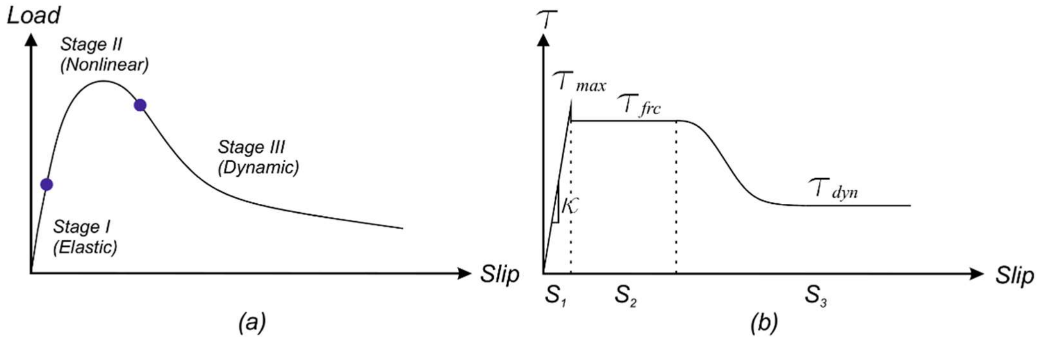

Figure 5.4 - Bond-slip behavior for rebar pull out from concrete matrix: (a) global load-slip response and (b) local shear strength distribution along the slip.

5.3.1. Rebar pull out equations

In order to guarantee static equilibrium, the tensile forces on the rebar (*F*) need to be fully transferred to the matrix (*M*) through the interface and along the embedment length. This relationship is expressed in equation 5.1.

$$\frac{dF}{dx} = -\frac{dM}{dx} = \pi\phi_R\tau \tag{5.1}$$

Where τ represents the shear stresses at the interface and $\pi\phi_R$ is the equivalent circumference of the rebar. For small loads, the local shear stress behaves in a linear elastic manner as a function of slip with slope κ, calculated from the shear strength curve, as shown in Figure 5.4(b). The slip s (equation 5.2) is verified by the elongation of the rebar (δ_r) subtracted by the shortening of the matrix (δ_m).

$$\tau = \kappa s = \kappa(\delta_R - \delta_m) = \kappa\int_0^L [\varepsilon_R(x) - \varepsilon_m(x)]dx \tag{5.2}$$

Where $\varepsilon_R = F/E_RA_R$, $\varepsilon_m = -F/E_mA_m$, A is the cross section area and E is young modulus for each studied material. Subscripts 'R' and 'm' correspond to the rebar and matrix, respectively. The mobilized concrete area during pull out is key to achieve the correct bond-slip response. The present model assumes the pull out failure, during which small hollow circular concrete area is engaged during slip. Figure 5.5 illustrates the areas for the used model. The external concrete ring diameter (ϕ_m) was evaluated as a factor of the rebar diameter of around 1.2 ($\phi_m = 1.20*\phi_R$). By substituting eq. 5.2 in eq. 5.1 and taking the derivative with respect to x, it is possible to yield the differential equation for the rebar pull out force through equation 5.3.

$$\frac{d^2F}{dx^2} - \beta^2F = 0 \tag{5.3}$$

Where $\beta^2 = \pi\phi_R\kappa Q$ and $Q = (1/A_RE_R) + (1/A_mE_m)$. The general solution of the second differential equation has the form showed in equation 5.4.

$$F(x) = C_1e^{\beta x} + C_2e^{-\beta x} \tag{5.4}$$

By applying the force boundary conditions ($F(0) = 0$ and $F(L) = P$), in equation 5.4 and taking a derivative with respect to x, the shear distribution in equations 5.5 and 5.6 are achieved. L is defined as the embedment length of the rebar in the concrete matrix.

$$F(x) = \frac{Psinh(\beta x)}{sinh(\beta L)} \tag{5.5}$$

$$\tau(x) = \frac{P\beta cosh(\beta x)}{\pi \phi_R sinh(\beta L)} \tag{5.6}$$

5.3.2.Bond-slip behavior in elastic stage (I)

While the shear stress at the interface is less than the maximum shear strength (τ_{max}), rebar and matrix are fully bonded ($P_1 < P_{1b,max}$). Figure 5.6(a) illustrates the elastic condition, when the shear stresses reach the elastic peak strength (τ_{max}). The slip at the end of the rebar can be verified through equation 5.7. When the maximum strength (τ_{max}) is achieved at $x = L$, the maximum load is calculated by equation 5.8 and the elastic stage reaches its end.

$$S(L)_1 = \int_0^L \left[\frac{F(x)}{A_R E_R} + \frac{F(x)}{A_m E_m}\right] dx = \frac{P1Q}{\beta \sinh{(\beta L)}}[\cosh(\beta L) - 1] \tag{5.7}$$

$$P_{1b,max} = \frac{\tau_{max} \phi_R \pi}{\beta} \tanh{(\beta L)} \tag{5.8}$$

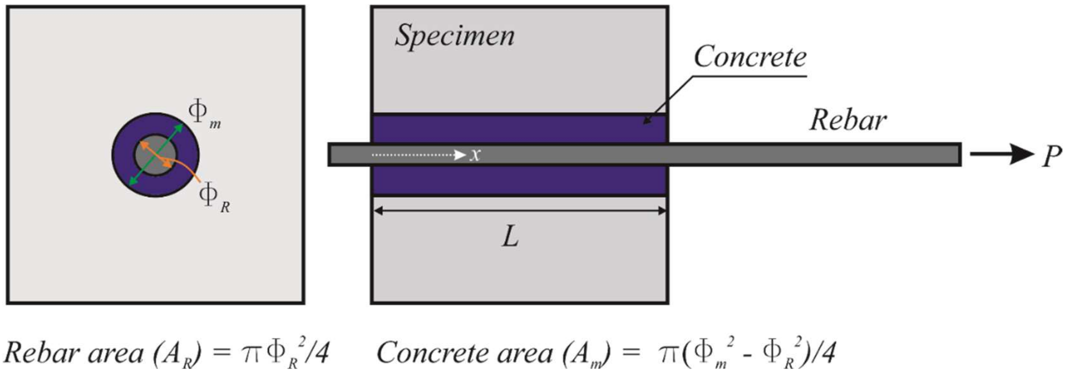

Figure 5.5 - Pull out model geometrical properties.

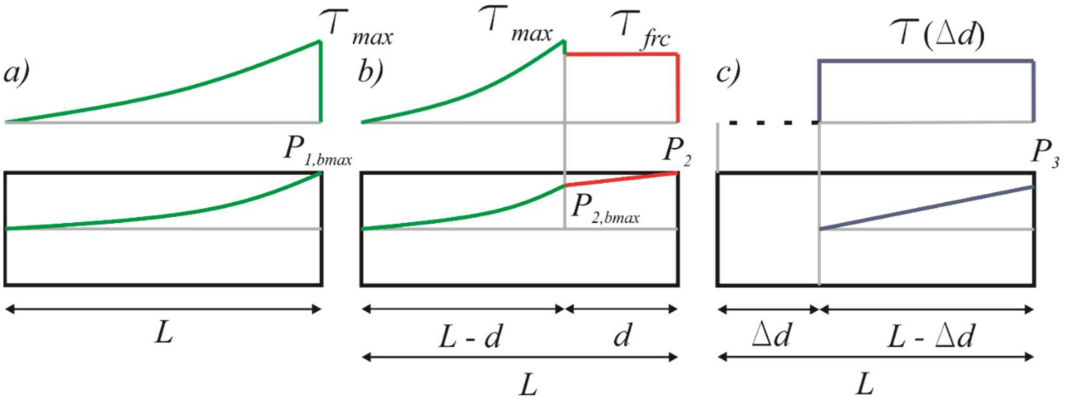

Figure 5.6 - Shear stress and force distribution along the rebar: (a) stage I (elastic behavior), (b) stage II (nonlinear behavior) and (c) dynamic response with incremental sliding.

5.3.3. Bond-slip behavior in nonlinear stage (II)

When shear stress reaches the maximum shear strength (τ_{max}), the nonlinear stage takes place. Stage (II) is associated with debonding for a length of d as displayed in Figure 5.6(b). While the two materials are still perfectly bonded on the left portion ($L - d$), debonding progresses for a length of d on the right. The shear distribution is governed by a constant frictional stress (τ_{frc}) along the debonded zone in addition to a shear lag model terminating with the maximum bond strength value (τ_{max}). The model stage (II) algorithm is based on incrementally increasing the debonded length (d) and, consequently, calculating the applied force from the shear stress distribution. The pull out load (P_2) at stage (II) is assessed by the sum of the bonded zone ($P_{2b,max}$) and debonded zone (P_d), as shown in equation 5.9.

$$P_2 = P_d + P_{2b,max} = \tau_{frc}\pi\phi_R d + \frac{\tau_{max}\pi\phi}{\beta}\tanh\left(\beta(L-d)\right) \tag{5.9}$$

The force boundary conditions are modified for stage (II) with $F(0) = 0$, $F(L - d) = P_{2b,max}$.and $F(L) = P2$, according to the bonded and debonded zones. Applying these boundary conditions on equation 5.4), it is possible to achieve force distribution in bonded (eq. 5.10) and debonded zones (eq. 5.11).

$$F_b(x) = \frac{P_{2b,max}\sinh(\beta x)}{\sinh\left(\beta(L-d)\right)}; 0 \leq x \leq L-d \tag{5.10}$$

$$F_d(x) = P_{2b,max} + \tau_{frc}\pi\phi_R(x - L - d); L-d \leq x \leq L \tag{5.11}$$

The slip at the end of rebar is assessed by applying the same procedure in stage (I), but dividing in two separate regions: bonded and debonded zones (eqs. 5.12 and 5.13).

$$S(L)_2 = \int_0^{L-d} \left[\frac{F(x)}{A_R E_R} + \frac{F(x)}{A_m E_m}\right] dx + \int_{L-d}^{L} \left[\frac{F(x)}{A_R E_R} + \frac{F(x)}{A_m E_m}\right] dx \tag{5.12}$$

$$S(L)_2 = \frac{P_{2b,max} Q}{\beta} \frac{\left[\cosh\big(\beta(L-d)\big) - 1\right]}{\sinh\big(\beta(L-d)\big)} + \frac{1}{2} Qd(\tau_{frc} \pi \phi_R d + 2P_{2b,max}) \tag{5.13}$$

5.3.4. Bond-slip behavior in dynamic stage (III)

Stage (III) is characterized by the dynamic response, which is associated with the rebar sliding ($\Delta_d > 0$) after complete debonding. The shear stress smoothly decays from the frictional shear strength (τ_{frc}) until reaching the final dynamic shear stress (τ_{dyn}). The decay of shear stress during the dynamic stage is associated with the presence of the ribs along the rebar, which provides a mechanical interlock along the interface [58]. Thereafter, the pull out resistance is calculated by a constant dynamic shear strength (τ_{dyn}). The Gumbel distribution [59] function was empirically chosen to verify the dynamic shear stress variation as a function of the rebar sliding (Δ_d) and is presented in equations 5.14 and 5.15. Figure 5.6(c) illustrates the shear stress variation with slip.

$$\tau(\Delta d) = \left(\tau_{frc} - \tau_{dyn}\right) e^{-e^{(-z)} + 1 - z} + \tau_{dyn} \tag{5.14}$$

$$z = \frac{\Delta d}{\alpha} \tag{5.15}$$

Where Δd is the sliding during the rigid body motion of the rebar along the interface and $\alpha = 0.10\phi_R$ is the constant adjust the shear stress decay from τ_{frc} to τ_{dyn}. During the rigid body motion stage, the embedment length reduces to ($L - \Delta d$) and the dynamic pullout force at the end of the rebar can be calculated using equation 5.16. From equilibrium, the force distribution can be calculated through equation 5.17 and the slip is evaluated as shown in equation 5.18.

$$P_3 = \tau(\Delta d) \pi \phi_R (L - \Delta d) \tag{5.16}$$

$$F(x) = \tau(\Delta d) \pi \phi_R (L - \Delta d) + \tau(\Delta d) \pi \phi_R (x - L + \Delta d), 0 \leq x \leq L - \Delta d \tag{5.17}$$

$$S(L)_3 = \int_0^{L-\Delta d} \left[\frac{F(x)}{A_R E_R} + \frac{F(x)}{A_m E_m}\right] dx + S(L)_{2,last} + \Delta d =$$
$$\frac{\tau(\Delta d)\pi\phi_R Q}{2}(L - \Delta d)^2 + S(L)_{2,last} + \Delta d, \Delta d \geq 0 \tag{5.18}$$

The total slip at the end of the rebar measured in dynamic stage is calculated as the slip at the end of stage II added by the dynamic slip in stage III. In order to compare the measured experimental slip with the analytical model calculations, the sliding during the rigid body motion of the rebar along the interface (Δd) is also added to equation 5.18.

5.3.5. Pull out model application algorithm

The rebar pull out from a concrete matrix can be simulated through the equations in the previous described sections and in accordance with the following summarized steps:

a) Compute mean and standard deviation of the pull out experiment for each slip level in order to achieve a representative curve;
b) In the elastic stage I, a pull out load P_1 is assumed and the slip $s(L)_1$ is evaluated in equation 5.7. The value of P_1 is increased until reaching the $P1b_{,max}$, which determines the conclusion of the first stage;
c) At stage II, the debonded length 'd' is incrementally imposed and the values of P_2 and slip $s(L)_2$ are recorded through equations 5.9 and 5.13, respectively. Stage II reaches its end when the slip $s(L)_2$ is computed;
d) In final stage III, the shear stress is computed as a function of the value of rebar sliding along the interface ($\tau(\Delta d)$) with equation 5.14. The calculated force-slip response is evaluated with equations 5.16-5.18.

The described model was applied for a several experimental pull out tests, including the results obtained from the current and previous researches, namely, Huang *et al.* [44], Chu *et al.* [28], Varona *et al.* [6] and Li *et al.* [45]. The simulations encompass distinct rebar diameters, embedment lengths, concrete resistances and fiber factors. The rebar pull out results from the ultra-high performance concrete studied by Liang *et al.* [46] was also analyzed.

5.4. Discussion and analysis

5.4.1. Bond under quasi-static pull out tests

5.4.1.1. Bond strength and slip at peak

Figure 5.7 brings the mean bond-slip curves obtained from the pull out tests for all studied fiber reinforced concrete composites. The results show the influence of the addition of 20, 40, 60 and 80 kg/m³ of steel fiber addition on the bond behavior. The bond stresses were calculated in accordance to equation 5.19, which relates the pull out force along the test with the interfacial area between rebar and concrete. Table 5.4 summarizes all estimated parameters obtained from the carried out quasi-static pull out tests. The obtained results for peak rebar tensile strength are identified as σ_{peak}.

$$\tau_b = \frac{P}{\pi \phi_R L} \tag{5.19}$$

Where *P* is the measured pull out force along the test, ϕ_R is the rebar diameter (ϕ_R = *6.3* mm) and *L* is the embedment length ($L \approx 10d =$ 60 mm).

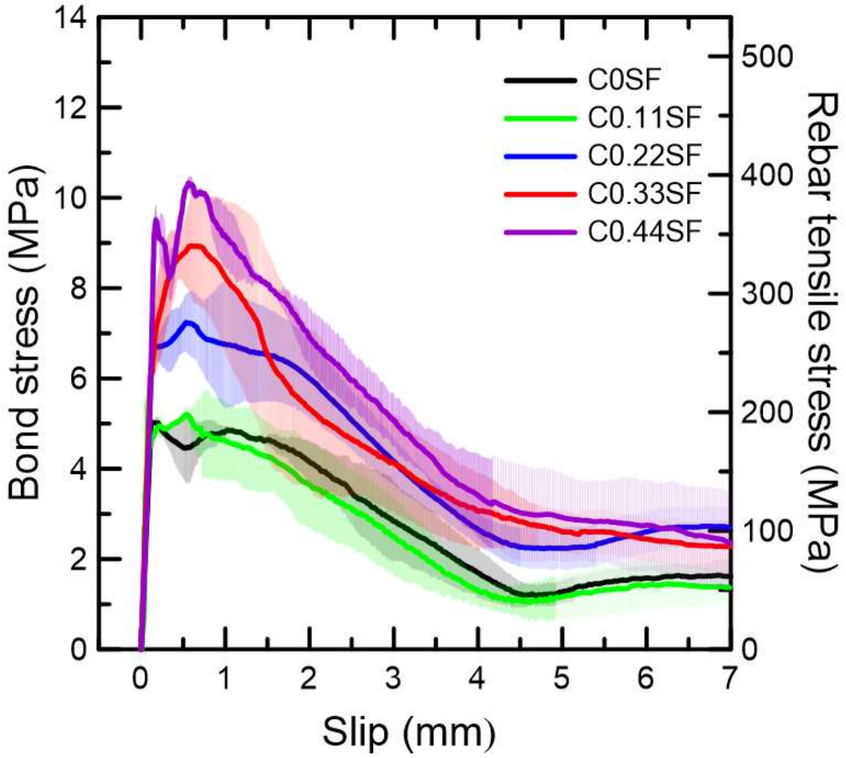

Figure 5.7 - Mean bond slip curves for studied plain and steel fiber reinforced concrete specimens.

Figure 5.8 presents the evolution of the bond strength ($\tau_{b,max}$) with respect to the fiber factor (λ) whereas a plot of $\tau_{b,max}$ *vs* the flexural residual strength ($f_{R,1}$) obtained in pre-notched bending tests is presented in Figure 5.8b. Equations 5.20 and (21) allows the determination of the regression models for the obtained experimental results for bond strength. Linear regressions were applied to estimate the bond strength. High values of coefficient of determination (R^2) were obtained for both regressions.

$$\tau_{b,max}(MPa) = 11.8\lambda + 4.8(MPa), R^2 = 0.94 \qquad (5.20)$$

$$\tau_{b,max}(MPa) = 20.3f_{R,1}(MPa) + 0.9(MPa), R^2 = 0.93 \qquad (5.21)$$

Although the increase of bond strength is evident with the increase of the fiber factor, the confinement potential may become less efficient for higher fiber dosages. As shown in table 5.4, for C0.44SF composition, the rebar peak stress was around 350 MPa, which is closer to the rebar yielding strength. Past experiments by Li *et al.* [7] have verified the rebar rupture when the adherence strength exceeded the rebar yielding stress. Therefore, the linear regression is only reliable assuming that the yielding is not achieved during the rebar pullout.

Table 5.4 - Mean results of obtained from the pull out tests. Standard deviations are presented in parentheses.

Composition	$P_{b,max}$ kN	$\tau_{b,max}$ MPa	σ_{max} MPa	δ_{peak} mm	K_b MPa/mm	T_{peak} kN-mm	$T_{4.0mm}$ kN-mm
C0SF	6.32 (0.26)	5.32 (0.22)	202.80 (8.39)	0.1 (0.02)	41.7 (2.5)	1.8 (0.36	17.5 (1.8)
C0.11SF	6.29 (0.30)	5.30 (0.25)	201.80 (9.59)	0.57 (0.01)	53.2 (3.2)	3.1 (0.5)	18.0 (4.2)
C0.22SF	8.80 (1.42)	7.41 (1.20)	282.30 (45.52)	0.58 (0.19)	54.0 (5.1)	4.1 (1.0)	25.6 (3.0)
C0.33SF	10.80 (2.31)	9.10 (1.95)	346.61 (74.13)	0.62 (0.23)	55.4 (7.3)	4.9 (0.7)	28.0 (3.6)
C0.44SF	11.94 (0.58)	10.05 (0.49)	382.70 (19.13)	0.59 (0.20)	57.0 (4.2)	5.3 (0.6)	31.5 (2.1)

Equation 5.23 brings, in turn, another proposal to estimate the bond strength in terms of fiber reinforced concrete post-crack residual strength. In general, the calculation of FRC structures is based on the obtained mechanical properties achieved from three-point bending tests [4, 60, 61]. Therefore, a similar relation

can be applied for the bond strength. Through a linear regression, bond strength could be successfully estimated in accordance with $f_{R,1}$. More experimental results should be carried out to verify if the proposed regression model can be used for distinct fiber types.

Since the use of fibers enhances the bond confinement after concrete crack along the rebar pull out, a significant increase on the slip at bond strength (δ_{peak}) is observed. While C0SF achieved a mean value of 0.10 mm of slip, SFRC specimens fluctuated around 0.50 mm and 0.60 mm (table 5.4). The fiber reinforcement is responsible for providing the post-crack resistance of the composite [62, 63], resulting in a significant raise of the bond strength after the composite reaches its matrix failure. Consequently, the fiber action to contain crack opening promotes a hardening behavior during the rebar pull out tests from SFRC specimens.

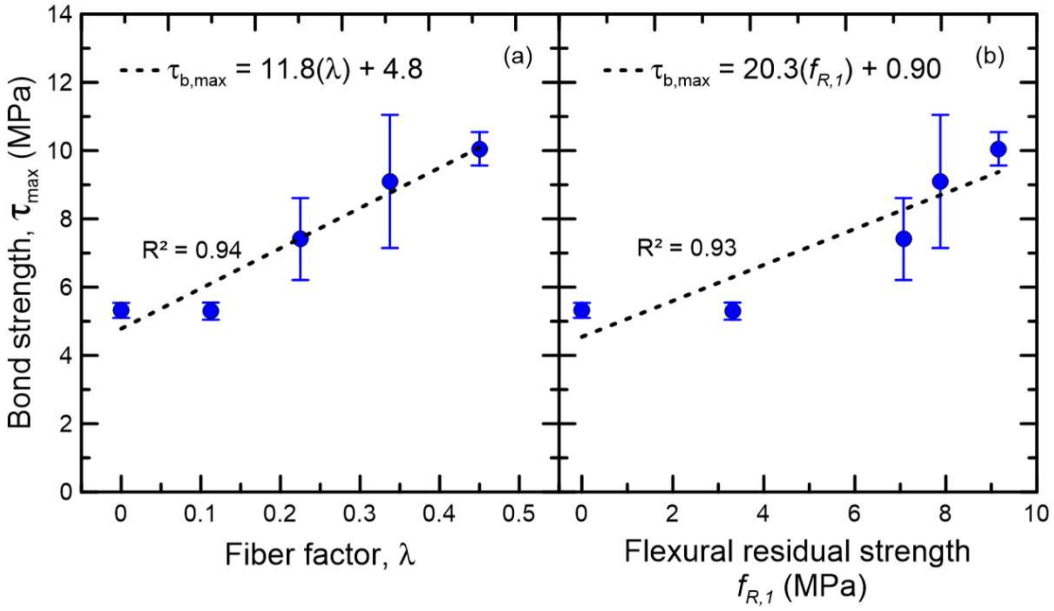

Figure 5.8 - Proposed regression models for bond strength in accordance with (a) the fiber fraction (λ) and (b) flexural residual strength ($f_{R,1}$).

5.4.1.2. Bond stiffness

Figure 5.9 brings an illustrative bond stress-slip curve with the main studied parameters for the carried pull out tests. As shown before by Chu *et al.* [25], the bond stiffness (K_b) can be evaluated through the secant gradient, which was calculated as half of peak bond stress divided by slip also at half of peak bond strength. The mean stiffness results are summarized in table 5.4.

There is a significant increase in stiffness when fibers are added in the pull out specimens in relation to plain concrete of around 30%. Therefore, not only the fiber confinement can provide an increase in bond strength, but also enhance the bond stiffness. Figure 5.10 brings the evolution of stiffness in terms of the added fiber dosages. The obtained regression model for stiffness was computed using equation 5.22. As described by the proposed equation, a major increase in stiffness is observed from plain concrete to the first fiber factors. However, different to what is observed on the bond strength variation, the increase in stiffness is not as prominent. After reaching 0.11 of fiber factor a very slow rate of stiffness increase is observed. Therefore, the confinement provided by the fiber addition is responsible not only to enhance the bond strength, but also significantly impacts the bond stiffness. The bond stiffness evaluation is key when it comes to further crack width analysis [25].

$$K_b(\frac{MPa}{mm}) = 41.7 + 17.6(\lambda)^{0.21}, R^2 = 0.99 \tag{5.22}$$

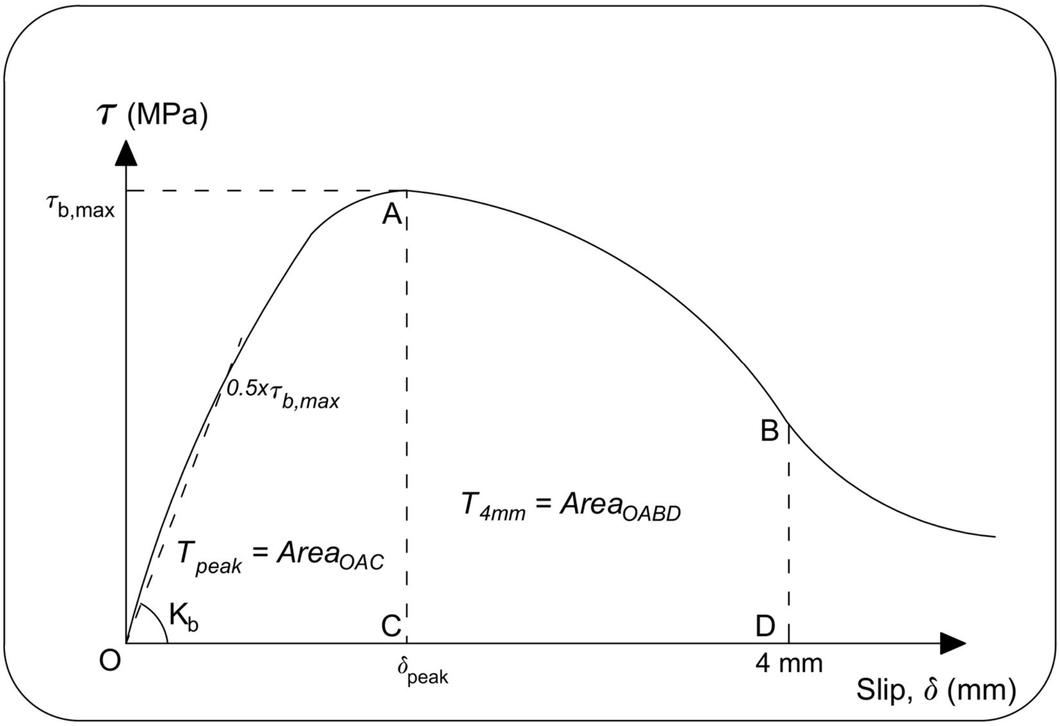

Figure 5.9 - Typical bond stress-slip curve illustrating the studied bond parameters.

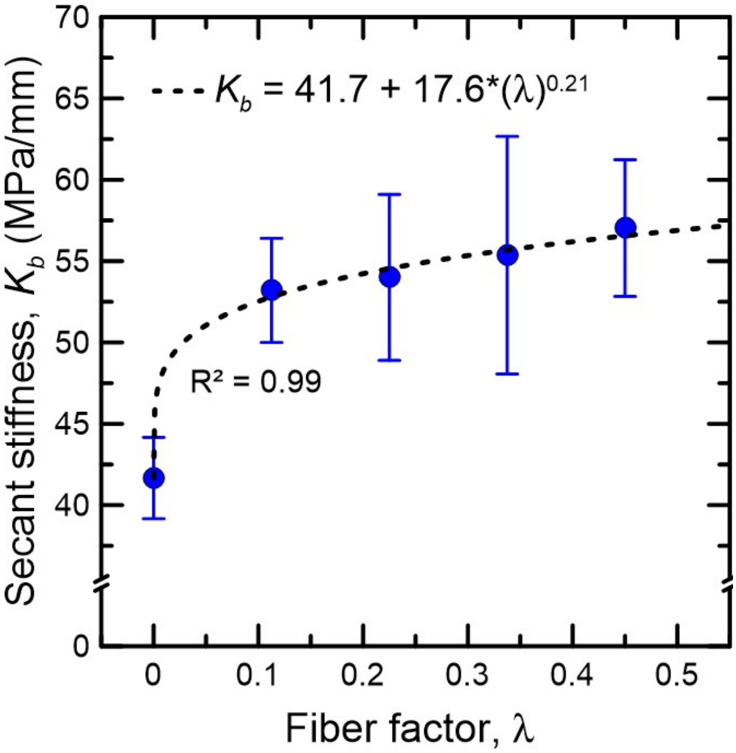

Figure 5.10 - Secant stiffness (K_b) in terms of fiber factor (λ).

5.4.1.3. Bond toughness

The bond toughness up to peak strength (T_{peak}) and bond toughness up to 4 mm slip (T_{4mm}) are plotted in terms of fiber factor in figure 5.11. The bond toughness is analyzed through literature [49, 50] as the total energy dissipated during the bond slip. As shown in figure 5.9, while T_{peak} was defined as the area under the force-slip curve up to peak bond force, T_{4mm} was calculated as the area under the force-slip curve until reaching 4 mm slip. After 4 mm slip, a major drop on the bond resistance has already taken place and the bond-slip behavior is governed by only a constant residual level.

As displayed on the achieved experimental results, the significant increase on both T_{4mm} and T_{peak} can attributed to the increase on bond strength and ductility due to fiber addition on concrete composition. The obtained linear regressions are consistent with previous experimental equations for toughness obtained by Garcia *et al.* [12] and Chu *et al.* *[*25]. Both present best-fit curves plotted in figure 5.11 displayed very high R² values, confirming the fiber influence on governing bond toughness. The linear regression can be analyzed in equations 5.23 and 5.24.

$$T_{peak}(kNmm) = 7.87\lambda + 2.06, R^2 = 0.97 \tag{5.23}$$

$$T_{4mm}(kNmm) = 33.78\lambda + 16.5, R^2 = 0.94 \qquad (5.24)$$

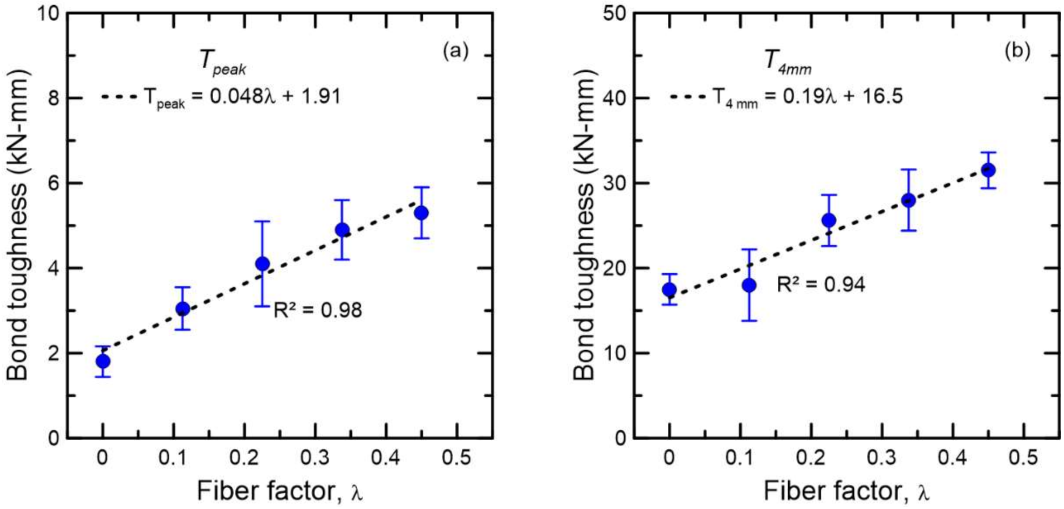

Figure 5.11 - Bond toughness regression models for (a) T_{peak} and (b) T_{4mm}.

5.4.1.4. Failure mode

Three distinct failure modes are commonly observed in literature when pull out tests are carried out: pull-out failure, concrete splitting with pull out failure and cone failure [10, 44, 45, 46]. The observed failure mode depends directly on the material and geometrical properties of the conducted mechanical tests. Rebar fracture can also be detected, when the bond strength inside the matrix surpasses the rebar tensile strength. While concrete splitting is characterized by the appearance of radial microcraks on the surface of the specimen, cone failure can be verified when the complete matrix specimen is mobilized and major cracks take place along the embedment length. Along the present research program, no splitting crack were observed during rebar pull out. Figure 5.12 displays the observed failure mode for all studied specimens.

Figure 5.12 – Observed pull out failure after the mechanical test

5.4.2. Analytical model

The pull out model previously developed by Naaman *et al.* [39] and Sueki *et al.* [40] was applied to distinct rebar pull out experimental results in the present paper. Table 5.5 summarizes all the geometrical and material parameters used to fit the applied model on the experimental data points. While Figure 5.12 brings the model implementation on the present research data, Figures 5.13 and 5.14 present the fitting to all collected experimental data from literature [6, 25, 41, 42, 43]. The experimental data encompasses different rebar diameters (ϕ_R = 6.3, 12, 20 mm), compressive concrete strengths (*fc* = 25, 50 and 83 MPa), embedment lengths (*L* = 2ϕ, 3ϕ, 4ϕ and 10ϕ) and steel fiber factors (λ = 0 – 1.6). The model was also applied to Liang *et al.* [43] experiments, which were based on rebar pull out tests from UHPC matrices with 150 MPa concrete strength and the addition of three fiber factors (0.65, 1.3 and 1.95).

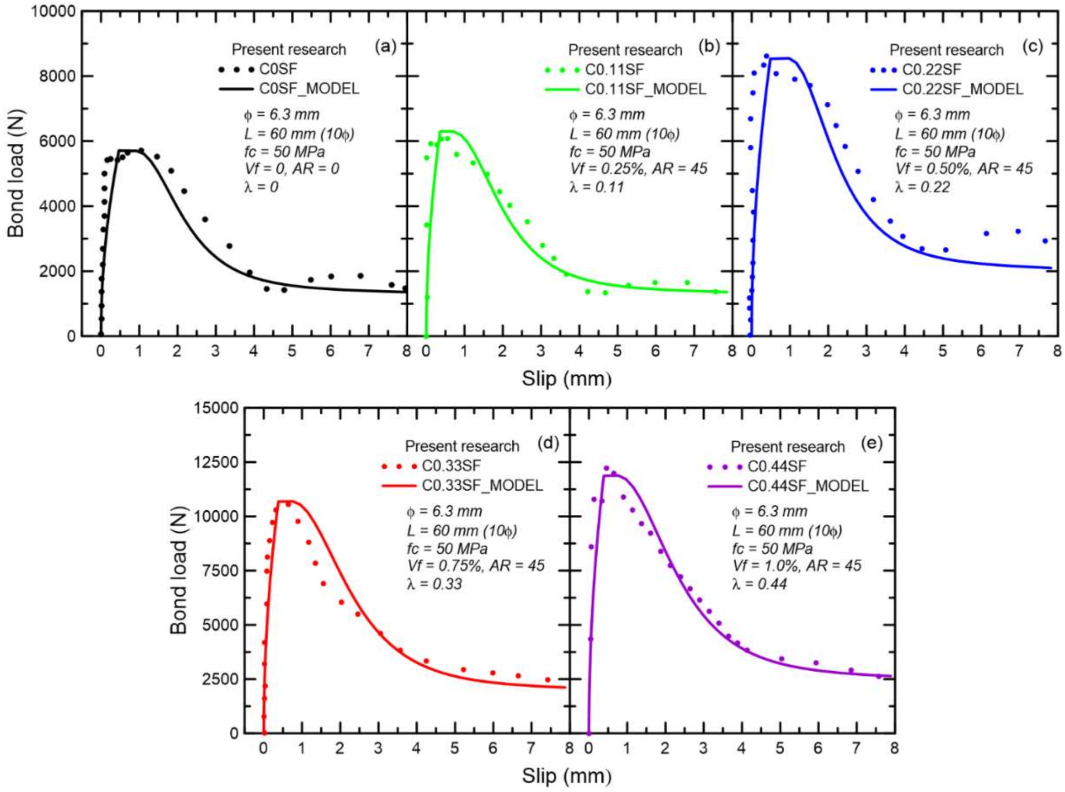

Figure 5.12 - Model application for the experimental results achieved in present research in terms of the following fiber factors (λ): (a) 0.11, (b) 0.22, (c) 0.33, (d) 0.44 and (e) 0.55.

The model successfully fit the bond-slip behavior observed from rebar pull out experimental data. For all studied cases, the maximum elastic shear strength (τ_{max}) was assumed to be equivalent to the frictional shear strength (τ_{frc}) in order to achieve the best possible fit for the slip at peak of the rebar pull out response. Due to this assumption, the maximum reached elastic bond force is significantly lower in relation to the peak bond strength after the completion of the frictional stage. The adopted smooth decay of shear stress from τ_{frc} until reaching τ_{dyn} with a Gumbel function also represented well the dynamic stage observed from the experimental data.

The major limitations of the 2-D model are associated to the pull out stiffness estimation. The fiber addition on the concrete matrix has positive influence on the stiffness due to confinement, as observed in the present study and also in the work of Chu *et al.* [25]. However, the stiffness achieved in the model is evaluated by the interaction between cross section rebar and the FRC matrix properties (Young modulus and area). Consequently, the FRC post-crack response plays no influence on the observed pull out stiffness. The nonlinear stage is, then, adjusted based on the mobilized concrete area along, which reached optimal results when the outer concrete annulus diameter (ϕ_m) was evaluated around 1.2 times the rebar diameter ($\phi_m = 1.20\phi_R$).

The developed model assumes that the rebar is slowly pulled out from the concrete matrix with a small hollow circular concrete area is engaged during slip. Radial microcracks can emerge on the surface of the specimen during the slip when the greater values of bond strength are observed. However, when small microcracks are observed, the pull out failure is still dominant, since the interface degradation during debonding is major failure mechanism occurring on the pull out test. The model could not be validated when cone failure is observed and the complete concrete specimen is mobilized during slip, since the presented analytical equations only account the hollow circular concrete area around the rebar.

Another key aspect observed on the pull out response is linked to the concrete cover around the rebar, as shown in past studies [7, 9, 12]. The adapted 2-D model, on the other hand, does not present a major influence on the increase of bond strength when enhancing the mobilized concrete area (A_m). The variation on the pull out bond strength due to cover could only be assessed by modifying the value of frictional shear stress in order to achieve a better fitting. Other observed aspects along the interface (mechanical interlock, cracking behavior) may only be correctly incorporated with a 3-D model [61, 62].

Equations 5.25 and 5.26 bring the achieved empirical equation that estimates peak bond strength in accordance to the four model studied parameters (ϕ_R, L, fc, λ). Therefore, the regression analysis was carried on in accordance with four constants (a, b, c, d). The comparison between the regression strength with the experimental values can be analyzed in figure 5.15. The proposed empirical equation could successfully estimate the peak bond strength for distinct conditions, including the fiber influence. The regression analysis can be used as input on the analytical model in order obtain the complete bond-slip response.

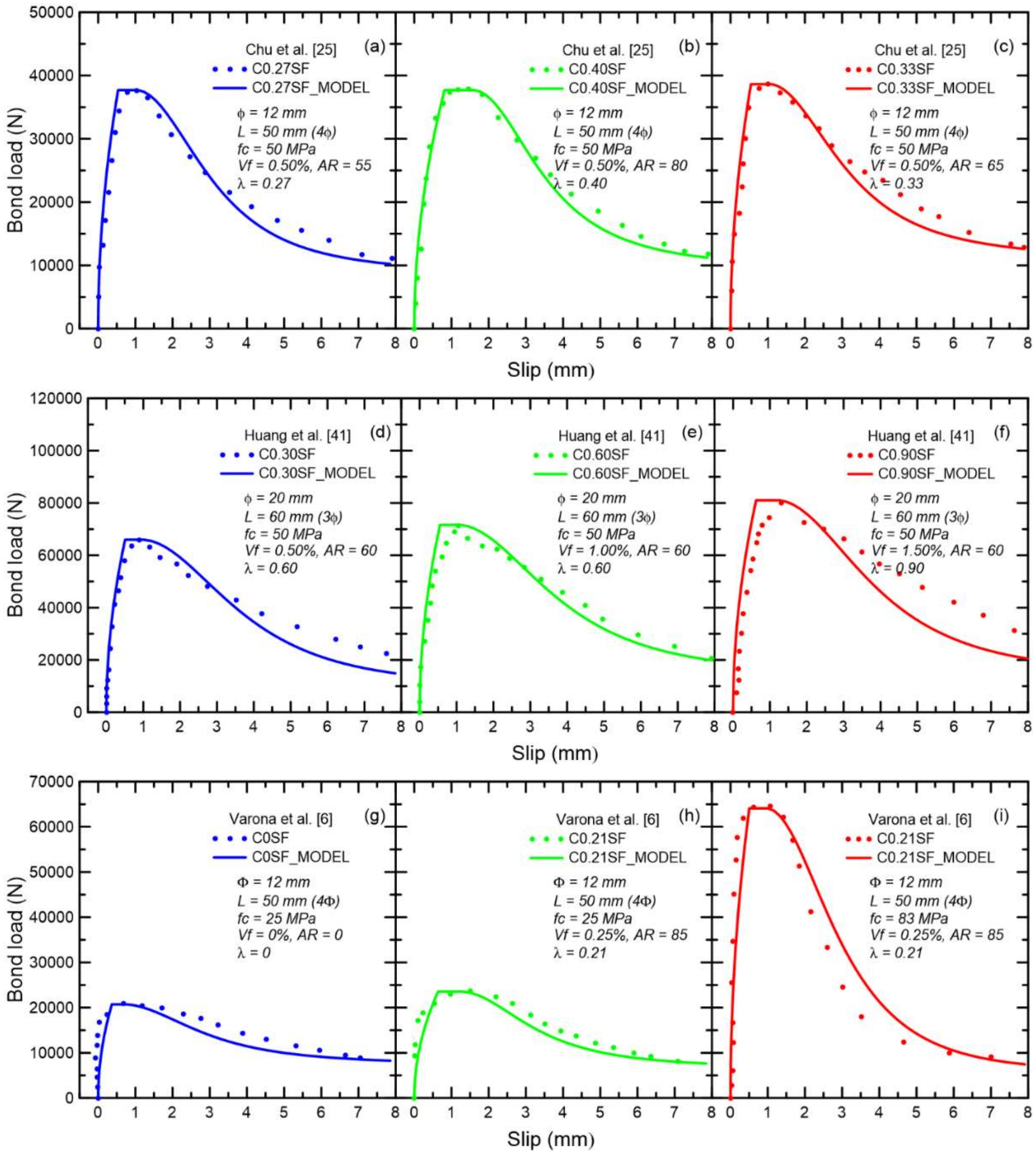

Figure 5.13 - Model application for pull out experimental data carried on by (a-c) Chu *et al.* [25], (d-f) Huang *et al.* [41] and (g-i) Varona *et al.* [6].

$$\tau_{regression} = f_c\left(a + b\frac{\phi_R}{L} + c\lambda + d\phi_R\right) \tag{5.25}$$

$$\tau_{regression} = f_c\left(0.025 + 3.97\frac{\phi_R}{L} + 0.12\lambda - 0.05\phi_R\right), R^2 = 0.90 \tag{5.26}$$

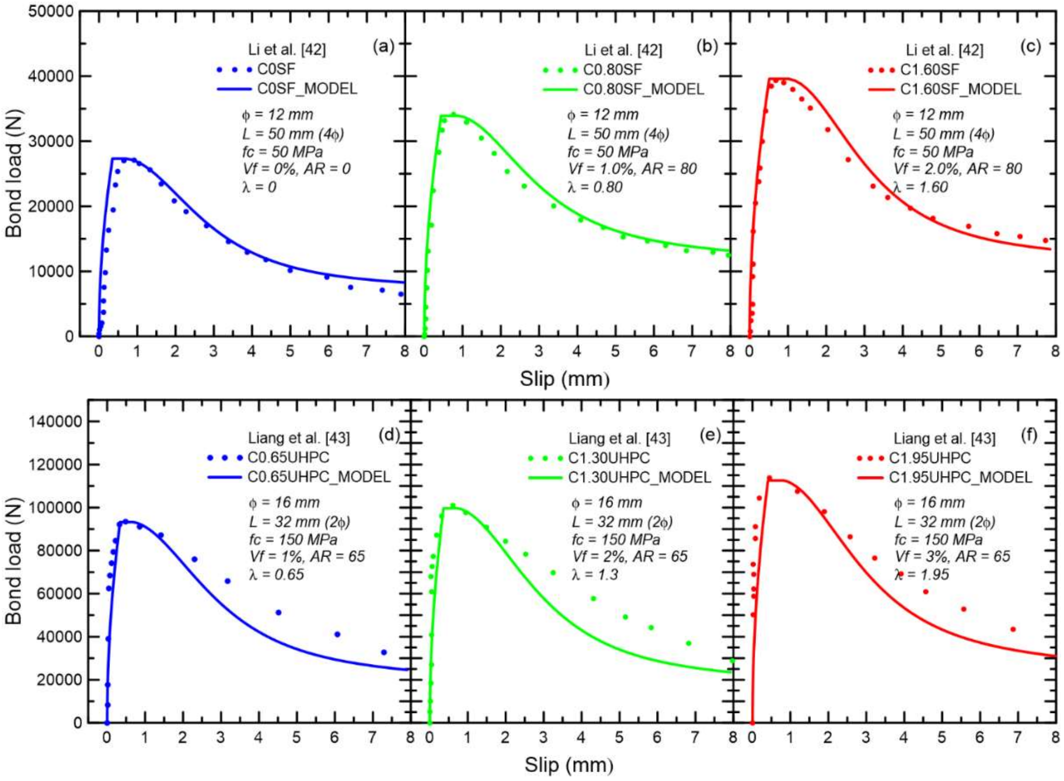

Figure 5.14 - Model application for pull out experimental data carried on by (a-c) Li *et al.* [42] and (d-f) Liang *et al.* [43].

Some of the main proposed equations to estimate the bond strength in the literature usually also enclose concrete cover as one the studied terms [9, 10, 11]. Garcia-Taengua *et al.* [12] verified statistically the influence of all possible variables on the bond strength and reached similar equation form as proposed in this work, including the effect of the concrete cover. However, the used analytical model does not verify the impact of the cover on the bond strength. Therefore, equation 5.28 cannot add this variable in this present study and is one the main limitations for a 2D model. Garcia-Taengua *et al.* [12] proposes a square exponent for diameter at their equations (Φ^2). On other hand, a lower R^2 (around 0.78) was reached by the authors in relation to the displayed results.

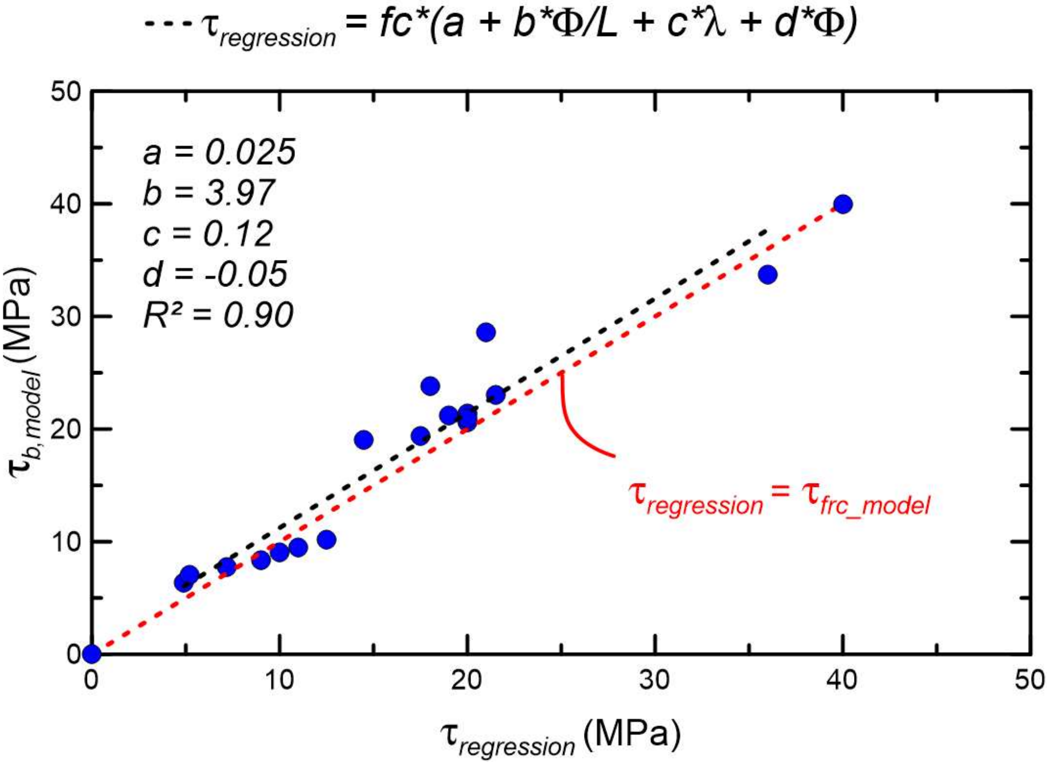

Figure 5.15 - Comparison between the shear stress used on the analytical model with the shear stress from the empirical formulation.

Table 5.5 - All used geometrical and material parameters used to fit the proposed model on the experimental results.

Author	ϕ	*AR*	V_f	λ	f_c	A_f	A_m	E_f	E_m	L	τ_{max}	τ_{frc}	τ_{dyn}
	mm	-	%	-	MPa	mm²	mm²	GPa	GPa	mm	MPa	MPa	MPa
Present research	6.3	-	0	0	50	31	19	200	33	10Φ (60)	4.9	4.9	1.1
Present research	6.3	45	0.25	0.113	50	31	19	200	33	10Φ (60)	5.2	5.2	1.1
Present research	6.3	45	0.5	0.225	50	31	19	200	33	10Φ (60)	7.2	7.2	2
Present research	6.3	45	0.75	0.338	50	31	19	200	33	10Φ (60)	9.0	9.0	2
Present research	6.3	45	1	0.45	50	31	19	200	33	10Φ (60)	10.0	10.0	2.5
Chu *et al.* [28]	12	55	0.5	0.275	50	113	40	200	33	4Φ (50)	20.0	20.0	6
Chu *et al.* [28]	12	80	0.5	0.4	50	113	40	200	33	4Φ (50)	20.0	20.0	6.5
Chu *et al.* [28]	12	65	0.5	0.325	50	113	40	200	33	4Φ (50)	20.0	20.0	7.5
Huang *et al.* [44]	20	60	0.5	0.3	50	314	138	200	33.2	3Φ (60)	17.5	17.5	3.5
Huang *et al.* [44]	20	60	1	0.6	50	314	138	200	33.2	3Φ (60)	19.0	19	5
Huang *et al.* [44]	20	60	1.5	0.9	50	314	138	200	33.2	3Φ (60)	21.5	21.5	5
Varona *et al.* [6]	12	0	0	0	25	113	40	200	23.5	4Φ (50)	11.0	11.0	5
Varona *et al.* [6]	12	85	0.25	0.213	25	113	40	200	23.5	4Φ (50)	12.5	12.5	4.5
Varona *et al.* [6]	12	85	0.25	0.213	83	113	40	200	42.8	4Φ (50)	36.0	36	6
Li *et al.* [45]	12	0	0	0	50	113	40	200	33.2	4Φ (50)	14.5	14.5	5
Li *et al.* [45]	12	80	1	0.8	50	113	40	200	33.2	4Φ (50)	18.0	18	8
Li *et al.* [45]	12	80	2	1.6	50	113	40	200	33.2	4Φ (50)	21.0	21	8
Liang *et al.* [46]*	16	65	1	0.65	150	201	88	200	57.6	2Φ (32)	58.0	58	19
Liang *et al.* [46]*	16	65	2	1.3	150	201	88	200	57.6	2Φ (32)	62.0	62	18
Liang *et al.* [46]*	16	65	3	1.95	150	201	88	200	57.6	2Φ (32)	70.0	70	24

**Liang et al. [34] carried on pull out tests from UHPC matrixes*

ϕ = *rebar diameter*

AR = fiber aspect ratio

V_f = *fiber volume fraction*

λ = *fiber factor*

f_c = *concrete compressive strength*

A_f = *rebar section area*

A_m = *concrete section area*

E_f = *rebar moudulus*

E_m = *concrete modulus*

L = *embedment length*

5.4.3. Bond under fatigue pull out tests

5.4.3.1. Influence of fibers on slip evolution under pull out fatigue loading

Figure 5.17 presents the experimental results for the slip evolution with respect to the recorded number of cycles along the pull out fatigue tests. C0SF composition was tested for three different load levels (*S*): 50%, 80% and 90%. The load level (*S*) was defined as a percentage of the maximum recorded bond force presented on table 5.4. Table 5.6 summarizes the obtained experimental results from the fatigue tests.

As observed in figure 5.17(a) and 5.17(c), the increase on the applied load level (*S*) is responsible for enhancing the slip evolution rate along the fatigue cycles, resulting on a drastic decrease on the number of cycles before failure (*N*). While the specimens under S = 50% of fatigue loading reached 1,000,000 cycles, for 90% of load level the fatigue pull out test ended after 813 cycles. The achieved experimental results are in accordance with those reported by Rehm *et al.* [66], who verified that the application of a load level higher than 65% will result in a failure prior to one million cycles.

Figure 5.17(b) shows the results for slip evolution for C0SF and C40SF under the same load range (1.50 kN < P < 5.0 kN). The addition of 40 kg/m^3 of fibers is responsible for substantially enhancing the fatigue life of the specimen under the analyzed fatigue loading. As previously shown on the bond-slip quasi-static results in figure 5.7, the fiber reinforcement enhances the maximum bond strength reaching a peak of 10 MPa when using 80 kg/m^3 of steel fibers. Therefore, the increase in bond strength allows the cementitious composite to reach 1,000,000 cycles under higher fatigue load levels. Since the slip evolution is proportional to the bond strength and the applied load levels, these two parameters will be key for the development of empirical models. The proposed models for slip evolution are presented in the next section.

Table 5.6 - Slip evolution under fatigue pull out loading experimental parameters. Standard deviation presented in parentheses.

Composition	*Quasi-static pull out*			*Fatigue pull out*		
	$P_{b,max}$ (kN)	$\tau_{b,max}$ (MPa)	K_b (MPa/mm)	*S (= %Pb,max)* -	$\delta_{0,exp}$ (mm)	*N* Cycles until failure/run-out
C0SF	6.32 (0.26)	5.32 (0.22)	41.7 (2.5)	50%	0.045	500,000**
C0SF	6.32 (0.26)	5.32 (0.22)	41.7 (2.5)	50%	0.055	1,000,000*
C0SF	6.32 (0.26)	5.32 (0.22)	41.7 (2.5)	50%	0.054	1,000,000*
C0SF	6.32 (0.26)	5.32 (0.22)	41.7 (2.5)	80%	0.090	272,100
C0SF	6.32 (0.26)	5.32 (0.22)	41.7 (2.5)	90%	0.098	813
C0.22SF	8.8 (1.42)	7.41 (1.2)	54 (5.1)	50%	0.05	1,000,000*
C0.22SF	8.8 (1.42)	7.41 (1.2)	54 (5.1)	50%	0.058	1,000,000*

**Run-out*
***Test stopped before reaching 1,000,000 cycles*

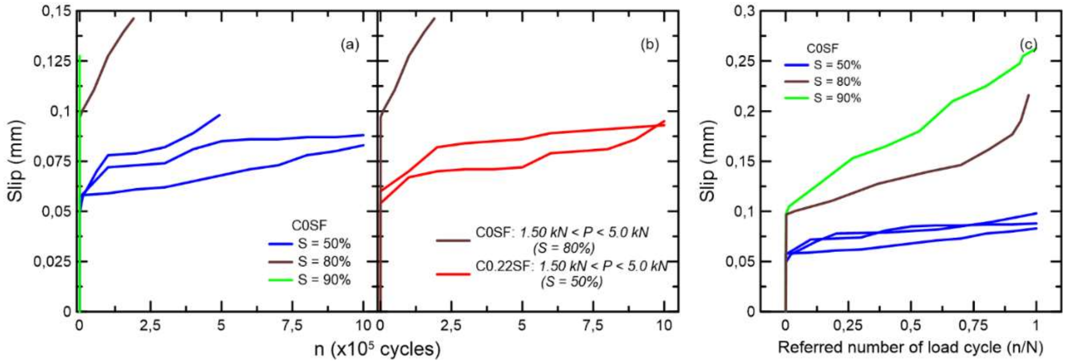

Figure 5.17 - Slip evolution under fatigue pull out loading for plain and steel fiber reinforced concrete specimens: (a) results for plain concrete under distinct load levels (S), (b) slip increase for C0SF and C0.22SF under the same load range (1.50 kN < P < 5.0 kN) and (c) fatigue results for C0SF in accordance to the referred number load cycle (n/N).

5.4.3.2. Model development for slip increase under fatigue pull out loading

The slip evolution along the fatigue cycles present a similar behavior for all studied load level conditions. The curves start from an initial slip value and rises through a power law, which is similar to what has been observed previously in the literature by Rehm *et al.* [66] and Lindorf *et al.* [39]. The initial slip (δ_0) is estimated empirically through the value of the slip at the peak bond strength (δ_{peak}), which can be achieved through the quasi-static pull out tests and the applied fatigue load level (S). The initial slip depends primarily on the quasi-static pull out behavior before reaching the peak bond strength ($\tau_{b,max}$). The proposed initial slip equation was calculated based on the present results (equation 5.27) and on the research by Rehm *et al.* [66] (equation 5.28).

Since the initial slip is majorly governed by the quasi-static bond behavior, it is expected to achieve distinct equations for δ_0 for each experimental program. As already stated by Lindorf *et al.* [39], a major error is expected when estimating the results for the initial slip due to intrinsic deviation observed from the quasi-static pull out tests. Its empirical relation will depend on the rebar and matrix materials and geometrical properties. Therefore, the initial slip needs to be analyzed independently for experimental series. In the current paper, equation 5.28 was applied to describe the slip evolution for the Lindorf *et al.* [39] fatigue behavior, since the quasi-static response is not available. Figure 5.18 brings an overall description of the applied pull out fatigue model in this paper.

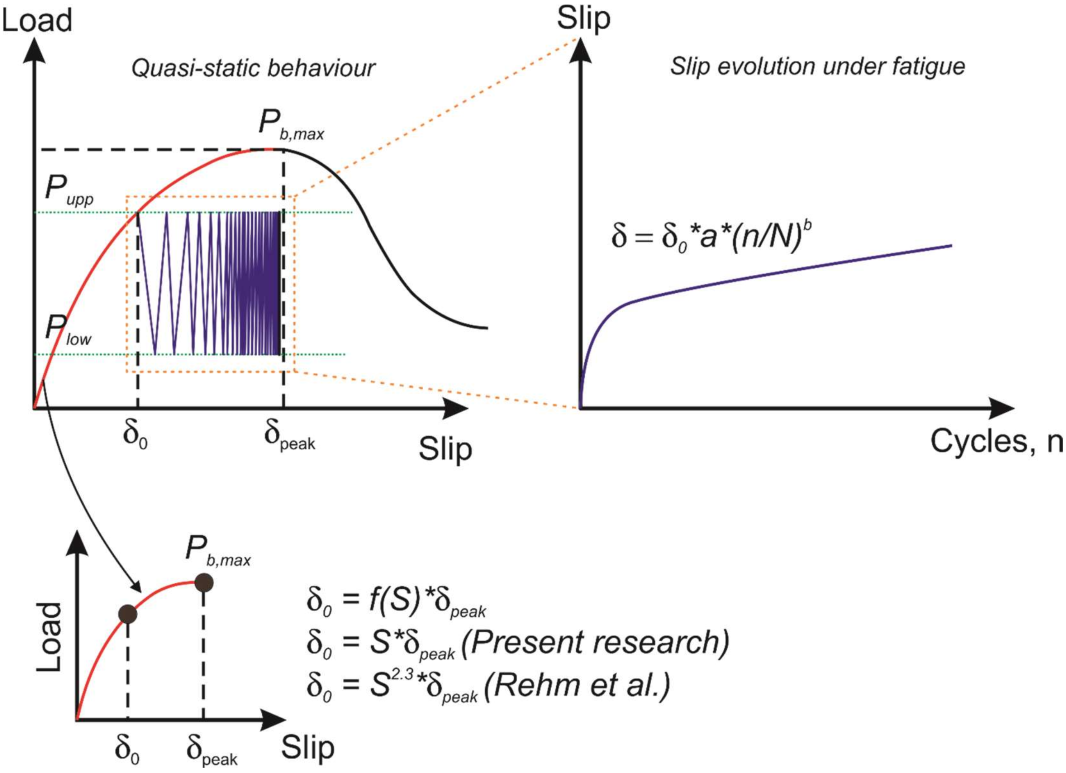

Figure 5.18 - Overall description of the proposed model for fatigue pull out

The proposed slip evolution law in the present research can be analyzed in equation 29. Both 'a' and 'b' empirical parameters were correlated with the applied load level (*S*), as shown in equation (5.30) and (5.31). The main goal of the proposed correlation is having as input the main studied fatigue parameters, which are already used to study the concrete fatigue behavior in flexural or compression cyclic loading [53, 55]. Moreover, the slip evolution is evaluated in terms of the referred cycle number *n/N*. In order to achieve the slip evolution in terms of the loading cycles (*n*), the number of cycles before failure (*N*) or '*run-out*' needs to be provided as an input.

$$\delta_0 = S * \delta_{peak} \tag{5.27}$$

$$\delta_0 = \delta_{peak} * S^{2.3} \tag{5.28}$$

$$\delta\left(\frac{n}{N}\right) = \delta_0 * a\left(\frac{n}{N}\right)^b \tag{5.29}$$

$$a = 3.75 * S^{0.65} \tag{5.30}$$

$$b = 0.226 * S^{2.43} \tag{5.31}$$

Where δ_0 is the initial slip, δ_{peak} is the recorded slip the peak bond strength from the quasi-static test, S is the fatigue load lelvel, a and b are adimensional empirical, $\delta_{n/N}$ is the slip at the normalized load cycle *n/N* and *N* is the number of cycles before failure or *run-out*.

Figures 5.19 and 5.20 bring the application of the present model on the present experimental results and on the fatigue behavior observed by Lindorf *et al.* [39] and Rehm *et al.* [66]. Table 5.7 summarizes all the achieved empirical parameters for the studied curves. It possible to verify that the proposed equations could successfully describe the overall behavior of the slip evolution along the cycles. Since the used empirical equation (5.28), derived from Rehm *et al.* [66], was used for the analysis of Lindorf *et al.* [39] fatigue response, a deviation for $S = 0.50$ can be verified. Therefore, the initial slip response from the quasi-static behavior is key to achieve more precise results for the model. Due to lack of more results in the literature, the proposed model could only have as an input the fatigue load level. Future research can bring the more information on the influence of the force ratio of 0.30 ($R = P_{low}/P_{upp}$) on the model and on the general fatigue behavior.

Table 5.7 – Slip evolution model parameters used for each author in this research

Author	*Input*		*Model parameters*		
	S	δ_{peak}	δ_0	*a*	*b*
	-	*(mm)*	*(mm)*	-	-
Present Research	0.50	0.07	0.04	2.39	0.04
Present Research	0.80	0.07	0.06	3.24	0.13
Present Research	0.90	0.07	0.06	3.50	0.17
Lindorf *et al.* [39]	0.52	0.40	0.09	2.45	0.05
Lindorf *et al.* [39]	0.69	0.40	0.17	2.95	0.09
Rehm *et al.* [66]	0.40	0.30	0.04	2.07	0.02
Rehm *et al.* [66]	0.50	0.30	0.06	2.39	0.04
Rehm *et al.* [66]	0.65	0.30	0.11	2.83	0.08
Rehm *et al.* [66]	0.77	0.30	0.16	3.16	0.12

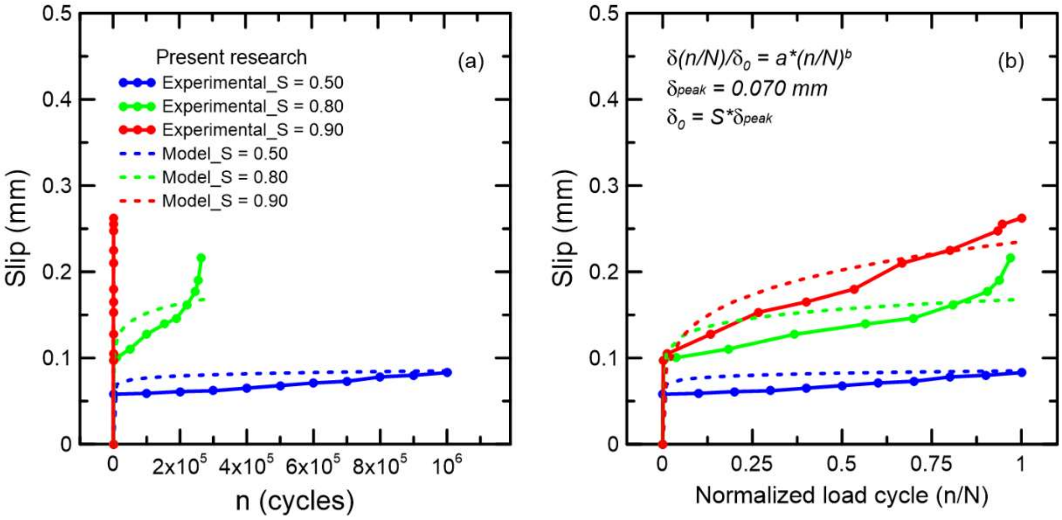

Figure 5.19 - Application slip evolution model for plain concrete under distinct load levels (*S*): results for slip per cycles and (b) slip per normalized load cycle.

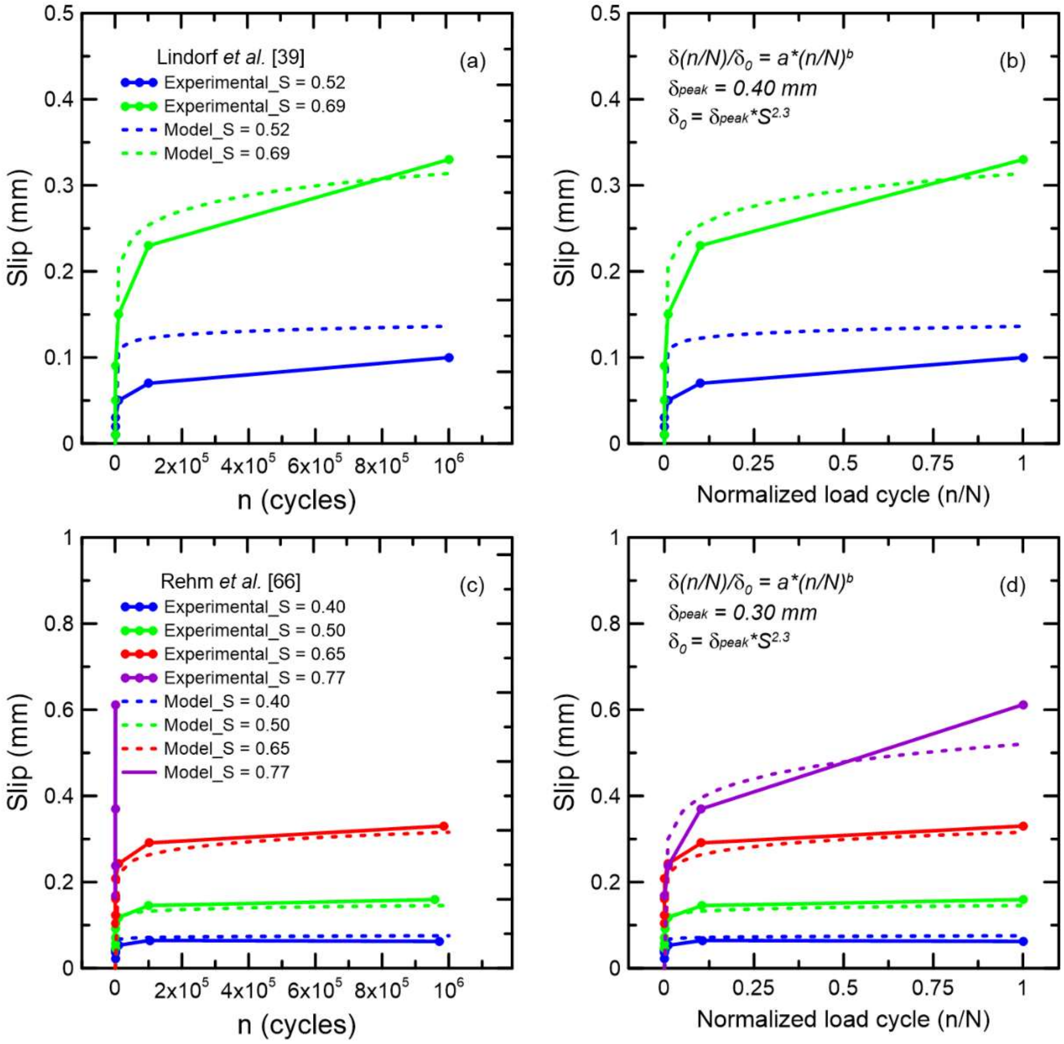

Figure 5.20 - Application slip evolution model for plain concrete under distinct load levels (*S*) for (a) and (b) Lindorf *et al.* [39] in (a) and (b) and for Rehm *et al.* [66] in (c) and (d).

The present research on the pull out fatigue degradation tries to bring an initial step on the influence of fibers on the cyclic behavior and to propose more recent equations to describe slip evolution along the fatigue cycles. There is still a major lack of experimental information to apply the proposed models and verify its validation. Moreover, the present model needs as an input the number of cycles before failure, which could be achieved through Wöhler curves. However, there is not enough experimental data in the literature to reach empirical S-N curves of fatigue pull out. Future research on the topic should bring a broader experimental program to assess the discussed issues.

5.5. Conclusions

The present research brings a broad analysis on the influence of steel fibers on quasi-static and fatigue rebar pull out loading. The analysis covers the impact of fiber addition on diverse mechanical parameters, such as peak bond strength, stiffness and toughness. Moreover, a model previously applied for single fiber pull out in the literature was modified in order to study the bond response through analytical equations. The model was used not only on the present experiments, but also on data collected from the literature to validate the proposed methodology. Finally, the present study also brings an analysis on the bond degradation under fatigue loading. A novel empirical equation was proposed to evaluate slip evolution under cyclic pull out loading. The following main conclusions can be derived from the present paper:

- The main pull out mechanical parameters are enhanced by the addition of steel fibers on the concrete mix. The fiber reinforcement is responsible for providing post-crack resistance to the composite, raising the confinement around the interface and peak bond strength. Both bond stiffness and toughness also report a significant increase as a function of the added fiber fraction. The covered pull out mechanical parameters were empirically correlated in order to be estimated based on the fiber factor.
- The proposed model for rebar pull out from steel fiber reinforced concrete matrices successfully fitted the bond-slip behavior observed the experimental data. The model divided the bond-slip response in three distinct stages: elastic (I), nonlinear (II) and dynamic (III). The bond-slip curve is assessed by correctly inputting the rebar and concrete geometrical and material properties, as well as projected shear strength distribution. The model achieved adequate results when distinct rebar diameters, concrete strengths, fiber fractions and embedment lengths were analyzed.
- When it comes to the fatigue pull out response, a novel empirical equation was proposed to verify the slip evolution under distinct fatigue load levels. The initial slip was evaluated in terms of the quasi-static mechanical properties and the slip increase along the cycles were estimated based on a power law. The equation was, finally, calibrated in accordance with tested load levels, based on the achieved experimental data.

- The addition of steel fibers successfully enhanced the fatigue response in relation to plain concrete. For the same applied fatigue maximum load value, pull out from SFRC could achieve 1,000,000 cycles, while the specimen without fiber reinforcement could only reach around 10^3 cycles. The fiber reinforcement is, therefore, responsible for enhancing the bond strength and improving the fatigue life under the same maximum load level.

5.6. References

1 FANG, C. LUNDGREN, K. PLOS, M. GYLLTOFT, K. Bond behavior of corroded reinforcing steel bars in concrete. **Cement and Concrete Research**, vol. 36, p. 1931-1938, 2006.

2 DANCYGIER, A. KATZ, A. WEXLER, U. Bond between deformed reinforcement and normal and high-strength concrete with and without fibers. **Materials and Structures**, vol. 43, p. 839-856, 2010.

3 ZHANG, X. WU, X. ZHANG, X. WANG, L. TANG, Y. QIU, F. Bond behaviors of pre- and post-yiled deformed rebar embedded in ultra-high performance concrete. **Construction and Building Materials**, vol. 341, 2022.

4 INTERNATIONAL FEDERATION FOR STRUCTURAL CONCRETE. **CEB-FIB**. International Recommendations for the Design and Construction of Concrete Structures, 2010.

5 KIM, S. YUN, H. evaluation of the bond behavior of steel reinforcing bars in recycled fine aggregate concrete. **Cement & Concrete Composites**, vol. 46, p. 8-18, 2014.

6 VARONA, F. BAEZA, F. BRU, D. IVORRA, S. Evolution of the bond strength between reinforcing steel and fibre reinforced concrete after high temperature exposure. **Construction and Building Materials**, vol. 176, p. 359-370, 2018.

7 LI, X. ZHANG, J. LIU, J. CAO, W. Bond behavior of spiral ribbed ultra-high strength steel rebar embedded in plain and steel fiber reinforced high-strength concrete. **KSCE Journal of Civil Engineering**, vol. 23, p. 4417-4430, 2019.

8 CAI, J. PAN, J. TAN, J. LI, X. Bond behaviours of deformed steel rebars in engineered cementitious composites (ECC) and concrete. **Construction and Building Materials** (2020), vol. 252, 2020.

9 DIAB, A. ELYAMANY, H. HUSSEIN, M. ASHY, H. Bond behavior and assessment of design ultimate bond stress of normal and high strength concrete. **Alexandria Engineering Journal**, vol. 53, p. 355-371, 2014.

10 YOO, D. SHIN, H. Bond performance of steel rebar embedded in 80-180 MPa ultra-high strength concrete. **Cement and Concrete Composites**, vol. 93, p. 206-217, 2018.

11 HARAJI, M. HAMAD, B. KARAM, K. Bond-slip response of reinforcing bars embedded in plain and fiber concrete. **Journal of Materials in Civil Engineering**, vol. 14, p. 503-511, 2002.

12 GARCIA-TAENGUA, E. MARTÍ-VARGAS, J. SERNA, P. Bond of reinforcing bars to steel fiber reinforced concrete. **Construction and Building Materials**, vol. 105, p. 275-284, 2016.

13 HAMEED, R. TURATSINZE, A. DUPRAT, F. SELLIER, A. Bond stress-slip behavior of steel reinforcing bar embedded in hybrid fiber reinforced concrete. **KSCE Journal of Civil Engineering** (2013), vol. 17, p. 1700-1707, 2013.

14 HOU, L. ZHOU, B. GUO, S.ZHUANG, N. CHEN, D. Bond-slip behavior between pre-corroded rebar and steel fiber reinforced concrete. **Construction and Building Materials**, vol. 182, p. 637-645, 2018.

15 MAJAIN, N. RAHMAN, A. ADNAN, A. MOHAMED, R. Bond behavior of deformed steel bars in steel fibre high-strength self-compacting concrete. **Construction and Building Materials**, vol. 318, 2022.

16 NZAMBI, A. OLIVEIRA, D. OLIVEIRA, A. PICANÇO, M. **Pull-out tests of ribbed steel reinforcing bars embedded in concrete with steel fibres**. Proceedings of the Institution of Civil Engineers – Structures and Buildings, vol. 174, p. 181-189. 2021.

17 QASEM, A. SALLAM, Y. ELDIEN, H. AHANGARN, B. Bond-slip behavior between ultra-high-performance concrete and carbon fiber reinforced polymer bars using a pull-out test and numerical modelling. **Construction and Building Materials** (2020), vol. 260, 2020.

18 AMERICAN SOCIETY FOR TESTING AND MATERIALS. **ASTM 1081**. Standard test method for evaluating bond of seven-wire steel prestressing strand, 2013.

19 INTERNATIONAL UNION OF LABORATORIES AND EXPERTS IN CONSTRUCTION MATERIALS, SYSTEMS AND STRUCTURES. **RILEM**. Technical Recommendations for the testing and use of construction materials, 1994.

20 AMERICAN SOCIETY FOR TESTING AND MATERIALS. **ASTM A944-22**. Standard test method for comparing bond strength of steel reinforcing bars to concrete using beam-end specimens, 2022.

21 HARAJI, M. SALLOUKH, K. Effect of fibers on development/splice strength reinforcing bars in tension. **ACI Materials Journal**: 94, 314-324, 1997.

22 HUNG, C. YUEN, T. HUANG, C. YEN, C. Tension splices in UHPC beams: influence of rebar size, steel fibers, splice length and coarse aggregate**. Journal of Building Engineering** (2022): 55, 2022.

23 Al-Salloum, Y. Alaoud, L. Elsanadedy, H. Albidah, A. Almousallam, T. Abbas, H. Bond performance of GFRP bar-splicing in reinforced concrete beams. **Journal of Composites for Construction**, 2, 2022.

24 DARWIN, D. MCCABE, S. IDUN, E. SCHOENEKASE, S. Development length criteria: Bars not confined by transverse reinforcement. **ACI Structural Journal**, vol. 89, p. 709-720, 1992.

25 ORANGUN, C. JIRSA, I. BREEN, J. A re-evaluation of test data on development length and splices. **ACI Journal**, vol. 74, p. 114-122, 1977.

26 HADI, M. Bond of high strength concrete with high strength steel. **The Open Civil Engineering Journal**, vol. 2, p. 143-147.

27 ESFAHANI, M. RANGAN, B. Bond between normal strength and high-strength concrete (HSC) and reinforcing bars in splices in beams. **ACI Structural Journal**, vol. 95, p. 272-280, 1998.

28 CHU, S. KWAN, A. A new bond model for reinforcing bars in steel fibre reinforced concrete. **Cement and Concrete Composites**, vol. 104, 2019.

29 HARAJI, M. HOUT, M. JALKH, W. Local bond stress-slip behavior of reinforcing bars embedded in plain and fiber concrete. **ACI Materials**, vol. 92, p. 343-353, 1995

30 CHAO, S. **Bond characterization of reinforcing bars and prestressing strands in high performance fiber reinforced cementitious composites under monotonic and cyclic loading**. University of Michigan, PhD dissertation, 2005.

31 CHAO, S. NAAMAN, A. PARRA-MONTESINOS, G. Bond behavior of reinforcing bars in tensile strain-hardening fiber-reinforced cement composites. **ACI Structures**, vol. 106, p. 897-907, 2009.

32 YOO, D. SHIN, H. YANG, J. YOON, Y. Material and bond properties of ultra-high performance fiber reinforced concrete with micro steel fibers. **Composites Part B Journal** (2014), vol. 58, p. 122-133, 2014.

33 BALAZS, G. Fatigue of bond. **ACI Materials Journal**, p. 620-629, 1991

34 OH, B. KIM, S. Realistic models for local bond stress-slip of reinforced concrete under repeated loading. **Journal of Structural Engineering**, vol. 133, p. 216-224, 2007.

35 AL-HAMMOUD, R. SOUDKI, K. TOPPER, T. Confinement effect on the bond behavior under static and repeated loading. **Construction and Building Materials**, vol. 40, p. 934-943, 2013.

36 AL-HAMMOUD, R. SOUDKI, K. TOPPER, T. Bond analysis of corroded reinforced concrete beams under monotonic and fatigue loads. **Cement and Concrete Composites**, vol. 32, p. 194-203, 2010.

37 LIN, H. ZHAO, Y. OZBOLT, J. HANS-WOLF, R. The bond behavior between concrete and corroded steel bar under repeated loading. **Engineering Structures Journal**, vol. 140, p. 390-405, 2017.

38 VELJKOVIC, A. CARVELLI, V. HAFFKE, M. PAHN, M. Effect of small concrete cover on the fatigue behavior of GFRP bars and concrete bond. **Journal of Composites for Construction**, vol. 23, 2019.

39 LINDORF, A. LEMNITZER, L. CURBACH, M. Experimental investigations on bond behavior of reinforced concrete under transverse tension and repeated loading. **Engineering Structures Journal**, p. 1469-1476, 2009.

40 ZHANG, W. ZHANG, Y. LI, H. GU, X. Experimental investigation of fatigue bond behavior between deformed steel bar and concrete. **Cement and Concrete Composites**, vol. 108, 2020.

41 VERDERAME, G. RICCI, P. DE CARLO, G. MANFREDI, G. Cyclic bond behavior of plain bars. Part I: experimental investigation. **Construction and building Materials**, vol. 23, p. 3499-3511, 2009.

42 NAAMAN, A. NAMUR, G. ALWAN, J. NAJM, H. Fiber pullout and bond slip. I: Analytical study. **Journal of Structural Engineering**, vol. 117, p. 2769-2790, 1991.

43 SUEKI, S. SORANAKOM, C. MOBASHER, B. PELED, A. Pullout-slip response of fabrics embedded in a cement paste matrix**. Journal of Materials in Civil Engineering**, vol. 19, p. 718-727, 2007.

44 HUANG, L. CHI, Y. XU, L. CHEN, P. ZHANG, A. Local bond performance of rebar embedded in steel-polypropylene hybrid fiber reinforced concrete under monotonic and cyclic loading. **Construction and Building Materials**, vol. 103, p. 77-92, 2016.

45 LI, L. CHEN, Z. OUYANG, Y. ZHU, J. CHU, S. KWAN, A. Synergistic effects of steel fibres and expansive agent on steel bar-concrete bond. **Cement and Concrete Composites**, vol. 104, 2019.

46 LIANG, R. HUANG, Y. XU, Z. Experimental and analytical investigation of bond behavior of deformed steel bar and ultra-high performance concrete. **Buildings**, vol. 12, p. 460, 2022.

47 AMERICAN SOCIETY FOR TESTING AND MATERIALS. **ASTM C595**. Standard specification for blended hydraulic cements, 2008.

48 DE LARRARD, F. **Concrete mixture proportioning: a scientific approach**. E&FN SPON, 1999.

49 RAMBO, D. SILVA, F. FILHO, R. Effect of steel fiber hybridization on the fracture behavior of self-consolidating concretes. **Cement & Concrete Composites**, vol. 54, p. 100-109, 2014.

50 RAMBO, D. SILVA, F. TOLEDO, R. Mechanical behavior of hybrid steel-fiber self-consolidating concrete: Materials and structural aspects. **Materials and Design**, vol. 54, p. 32-42, 2014.

51 AMERICAN SOCIETY FOR TESTING AND MATERIALS. **ASTM C1611**: Standard test method for slump flow of self-consolidating concrete, 2005.

52 EUROPEAN COMMITTEE FOR STANDARDIZATION. **EN 14651**. Test method for metallic fibre concrete – Measuring the flexural tensile strength (limit of proportionality (LOP), residual), 2005.

53 MONTEIRO, V. CARDOSO, D. SILVA, F. A novel methodology for estimating damage evolution and energy dissipation for steel fiber reinforced concrete under flexural fatigue loading. **International Journal of Fatigue**, vol. 166, 2023.

54 MONTEIRO, V. LIMA, L. SILVA, F. On the mechanical behavior of polypropylene, steel and gybrid fiber reinforced self-consolidating concrete. **Construction and Building Materials**, vol. 188, p. 280-291, 2018.

55 CARLESSO, D. FUENTE, A. CAVALARO, S. Fatigue of cracked high performance fiber reinforced concrete subjected to bending. **Construction and Building Materials**, vol. 220, p. 444-455, 2019.

56 CARLESSO, D. CAVALARO, S. DE LA FUENTE, A. Flexural fatigue of pre-cracked plastic fibre reinforced concrete: experimental study and numerical modeling. **Cement and Concrete composites**, vol. 115, 2021.

57 STEPHEN, S. GETTU, R. Fatigue fracture of fibre reinforced concrete in flexure. **Materials and Structures**, vol. 53, p. 56, 2020.

58 TAO, W. CHEN, C. JUN, H. TING, R. Effect of bolt rib spacing on load transfer mechanism. **International Journal of Mining Science and Technology**, vol. 27, p. 431-434, 2017.

59 KOTZ, S. NADARAJAH, S. **Extreme value distributions: Theory and Applications**. Imperial College Press, London, 2000.

60 AMERICAN CONCRETE INSTITUTE**. ACI 544.4R**. Guide to design with fiber-reinforced concrete, 2018.

61 TECHNICAL REPORT 34. **TR 34**. Concrete industrial ground floor: A guide to design and construction, 2018.

62 MOBASHER, B. **Mechanics of Fiber and Textile Reinforced Cement Composites**, 1st. ed, CRC Press, 2019.

63 PAJAK, M. PONIKIEWSKI, T. Flexural behavior of self-compacting concrete reinforced with different types of steel fibers. **Construction and Building Materials** (2013), vol. 47, p. 397-408, 2013.

64 ZHANG, N. WU, Y. GU, Q. HUANG, S. SUN, B. DU, R. CHANG, R. Refined three-dimensional simulation for ribbed bar pull-out tests based on an enhanced peridynamic model. **Engineering Structures**, vol. 278, 2023.

65 LIU, M. JIN, L. CHEN, F. ZHANG, R. DU, X. 3D meso-scale modelling of the bonding failure between corroded ribbed steel bar and concrete. **Engineering Structures**, vol. 256, 2022.

66 REHM, G. ELIGEHAUSEN, R. Bond of ribbed bars under high cycle repeated loads. **ACI Journal**, vol. 76, p. 297-310.

6 Closed-form solutions for flexural fatigue mechanical degradation of steel fiber reinforced concrete beams

Chapter 6 brings a novel methodology to estimate FRC mechanical degradation throughout closed-form solutions for FRC beams. The first step consisted on deriving the constitutive relations for tension and compression. While a quad-linear model was used for tension, an elastic perfectly plastic model was applied for compression. Thereafter, the moment-curvature was calculated using the proposed closed-form solution equations. Crack opening is, then, verified using the characteristic length, which allows to evaluate crack increase and stress intensity factor under quasi-static loading. After the composite quasi-static response completely characterized, the next step is to evaluate CMOD increase under fatigue loading with the proposed power law equation and the material S-N curve. The last step consisted to estimate the CMOD fatigue evolution and back-calculate the results with the analyzed closed-form solutions. The methodology was applied for three distinct concrete compositions in the literature and the results correctly fitted the observed CMOD evolution along the cycles.

This section was partly made at the Arizona State University under supervision of Barzin Mobasher supervision.

Published article: November 13th, 2023 – *Construction and Building Materials,* doi.org/10.1016/j.conbuildmat.2023.134200.

Notations			
A_1 - A_9	Coefficients in table 2	η	Normalized post-crack tensile modulus
a	Crack length	γ	Normalized compressive modulus
a_0	Notch height	ε	Strain
b	Section width	ε_c	Compressive strain
B_1 - B_6	Coefficients in table 2	ε_{cr}	First cracking strain
E	Elastic tensile modulus	ε_{cu}	Ultimate compressive strain
F	Force component	ε_{cy}	Compressive yield strain
h	Beam height	ε_t	Tensile strain
KI	Stress intensity factor	ε_{tu}	Ultimate tensile strain
k	Neutral axis depth ratio	λ	Normalized compressive strain
$\bar{k}$	Normalized axis depth ratio	λ_{cu}	Ultimate normalized compressive strain
L_p	Characteristic length	μ	Normalized post-cracked tensile stress
M	Moment	σ	Stress
M_{cr}	Moment at first cracking	σ_c	Compressive stress
$\bar{M}$	Normalized moment	σ_t	Tensile stress
y	Moment arm from force component	σ_{cr}	Cracking tensile stress
N	Number of cycles before failure	τ	Normalized post-crack tensile strain
n	Cycle number	ϑ	Empirical fatigue exponent
n/N	Normalized cycle number	ω	Normalized compressive yield strain
S	Load level	ϕ	Curvature
α	Crack length over height ratio	ϕ_{cr}	Cracking curvature
β	Normalized tensile strain	$\bar{\phi}$	Normalized curvature

6.1. Introduction

Steel fiber reinforced concrete (SFRC) structural members have been increasingly used in continuous cyclic loading applications, such as offshore platforms [1], concrete pavements [2] and wind tower rings [3-5]. Typically, the SFRC structures are submitted to fatigue loading especially due to wind or wave action, thermal variation, thermal oscillation and traffic loads. The cyclic loads throughout the structure life are responsible to lead crack initiation and propagation [6], which eventually can result in significant strength and stiffness decay [7].

To achieve a more comprehensive understanding of the fatigue mechanical degradation of fiber reinforced concrete (FRC), past research carried out experimental cyclic tests in the pre-peak regime based on unnotched [8, 9] or notched [10, 11] specimens. However, the published work in the last ten years have only dealt with the fatigue fracture of cementitious composites of pre-cracked specimens in flexure in accordance with the revised Model Code specifications [12]. The newest studies on FRC fatigue specially focused on the developing new S-N curves [13-16], applying Weibull models to predict fatigue life probabilistically [17-20], examining new equations to verify crack mouth opening displacement evolution [21-23] and proposing new models for damage propagation [24, 25].

In order to characterize the material performance under fatigue loading, several parameters should be carefully analyzed such as the maximum applied stress level [15-17], stress ratio [26], loading frequency [27, 28] and loading sequence [24, 25]. While Carlesso *et al.* [15] have already verified the influence of the stress level on the Wöhler curve analysis, Baktheer *et al.* [24] have shown how the loading sequence can significantly modify the damage evolution of concrete under fatigue loading. Medeiros *et al.* [27] and Saucedo *et al.* [28], in turn, could successfully insert the frequency variable on the failure probability of concrete under fatigue compression. More recently, a series of researchers [29, 30] have been trying to develop Bayesian mathematical methods to determine the fatigue life in concrete materials, but they still have not been properly applied to fiber reinforced concrete.

Along with the development of new methods and equations to study concrete fatigue response, recent research works have also brought formidable breakthrough in modelling the FRC material behavior through stress-strain relationships [31-36]. Among the first papers about the flexural response characterization is the work by Soranakom *et al.* [31], which proposes a closed-form solution for the moment-curvature response. The generalized fiber reinforced concrete is based on two intrinsic material parameters (elastic modulus and cracking tensile strain) and two normalized parameters (normalized post-peak tensile strength and compressive to tensile strength ratio). On one hand, the material compressive response is described with an elastic perfectly plastic behavior. On the other, the tensile stresses are analyzed through a linear relationship from the origin until the cracking strain and, then, remains constant by a fraction of the peak tensile strength.

The subsequent formulations to describe the constitutive relationships try to better refine the tensile FRC post-peak behavior [32, 33] and include the rebar reinforcement on the equations [34, 35]. Soranakom *et al.* [32], for instance, already proposes a tri-linear response for tensile stress-strain response, which could better fit the strain softening and strain hardening behaviors of cement based composites. Mobasher *et al.* [33] and Pleesudjai *et al.* [36], in turn, proposes a quad-linear model, which can correctly fit almost any type of fiber reinforced concrete response in terms of fiber fraction or type, including the improved performance of ultra-high performance concrete (UHPC) and textile reinforced concrete (TRC).

In general, the proposed design guidelines address the fiber contribution on the post-crack strength through flexural data obtained from beam tests such as three point bending tests by EN 14651 [37] and four point bending tests in accordance with ASTM C1609 [38]. The mentioned standards reach the tensile stress-strain relation from the load capacity at certain deflections or crack mouth opening displacements. However, present guidelines and analytical models still do not incorporate the effects of long-term and fatigue degradation along the time. The present equations on the Model Code [12], for instance, only account for empirical equations for deformation evolution under compression. When it comes to flexural fatigue, little can be found in the literature on how to incorporate the mechanical decay on the stress-strain models.

The present research brings a novel methodology to estimate FRC mechanical degradation throughout closed-form solutions for FRC beams. First, the constitutive equations for tension and compression are determined and moment-curvature responses are calculated using the proposed closed-form solutions developed by

Mobasher *et al.* [33], Pleesudjai *et al.* [39], Soranakom *et al.* [32] and Yao *et al.* [40]. The tension response is analyzed by a quad-linear model in this present research. The crack opening is, then, verified with the application of the characteristic length (L_p) as proposed by di Prisco *et al.* [41]. Thereafter, an empirical equation for crack mouth opening displacement evolution under flexural fatigue loading is proposed and validated with experimental published data. The CMOD evolution depends directly on the material *S-N* curve and the applied fatigue load level (*S*). Finally, with CMOD increase, it is possible to back-calculate deformation, tensile stress, residual flexural strength and the fracture parameters variations along the fatigue cycles based on the characterized closed-form solutions for FRC beams.

6.2. Model development

The current section presents all equations used to characterize the FRC constitutive relations, calculate the solutions for moment-curvature response, estimate the crack mouth opening displacement and other fracture parameters. Thereafter, the proposed methodology to estimate the fatigue mechanical degradation along the cycles is developed as a function of the material *S-N* curve and the CMOD increase by a power law. Finally, by the end of section 2, a workflow is presented bringing all steps to achieve the fatigue mechanical degradation along the cycles. The model was proposed for three-point bending tests (EN 14651 [37] standard) and was compared to presented data from Monteiro et [23], Carlesso *et al.* [19] and Stephen *et al.* [21] experimental results.

6.2.1. Closed-form solution for moment-curvature response

The first step to achieve the fiber reinforced concrete moment-curvature response is to define the material constitutive relations. Figure 6.1 brings the adopted composite uniaxial parametrized constitutive relation with a quad-linear tension model and a bi-linear compression model. The quad-linear relations are controlled by four stress-strain coordinates in tension (σ_{cr}, σ_1, σ_2, σ_3) and two coordinates in compression (σ_{cy}, σ_{cu}). Two intrinsic parameters are defined based on the material properties: the tensile modulus (*E*) and the first cracking tensile strain (ε_{cr}). When it comes to the dimensional parameters of geometry, the beam section is defined by its width (b), depth (h), notch height (a_0) and span (S). All subsequent variables are normalized with respect to the mentioned input parameters

The main independent variable for both tensile and compressive strains is attributed to the normalized tensile strain parameter (β), which is associated to the strain at the bottom of the cracked section. Hence, the strain increments are evaluated by a function of β and the first crack strain as shown in equation 6.1.

$$\varepsilon_t = \beta \varepsilon_{cr} \qquad (6.1)$$

Where ε_t is the tensile strain and ε_{cr} is the tensile cracking strain.

After reaching the cracking tensile strength of coordinates (ε_{cr}, σ_{cr}), the material stiffness is modified in accordance with the normalized post-crack tensile strength parameter η and is identified by the index i for each subsequent linear segment, as shown in figure 6.1(a). The residual stresses are evaluated by multiplying the peak tensile strength by the parameter μ_i, as shown in equation 6.2. The tensile response terminates at the ultimate strain $\varepsilon_{tu} = \beta_3 \varepsilon_{cr}$. The normalized post-crack tensile modulus (η) for the linear segments is directly obtained from the normalized stress and strain parameters in accordance with equation 6.3. Therefore, the strain-hardening or strain-softening response can be defined by the positive and negative values of the normalized variable η_1, respectively. The correlated strain for each stress σ_i is associated to the normalized tensile strain parameter τ_i. For the best understanding of the application of the parameters, refer to figure 6.1(a).

$$\sigma_i = \mu_i \sigma_{cr} = \mu_i \varepsilon_{cr} E \qquad (6.2)$$

$$\eta_1 = \frac{\mu_1 - 1}{\tau_1 - 1}, \eta_1 = \frac{\mu_2 - \mu_1}{\tau_2 - \tau_1}, \eta_3 = \frac{\mu_{tu} - \mu_2}{\beta_{tu} - \tau_2} \qquad (6.3)$$

When it comes to compression constitutive model, figure 6.1(b) presents an elastic-perfectly plastic behavior analyzed in accordance with equation 6.4, which multiplies the tensile modulus by the normalized compressive modulus parameter γ. The difference between compressive and tensile modulus can sometimes be neglected, since earlier models by Soranakom *et al.* [32] considered $\gamma = 1$. The plastic range initiates at strain $\varepsilon_{cy} = \omega \varepsilon_{cr}$ corresponding to yield stress $\sigma_{cy} = \gamma E \omega \varepsilon_{cr}$ and ends at $\varepsilon_{cu} = \lambda_{cu} \varepsilon_{cr}$. Using the mentioned definitions, it is possible to define the tension and compression FRC constitutive models through equations 6.4 and 6.5. Due to the linear strain distribution in figure 6.2, parameters λ and β can be expressed as shown in equation 6.6.

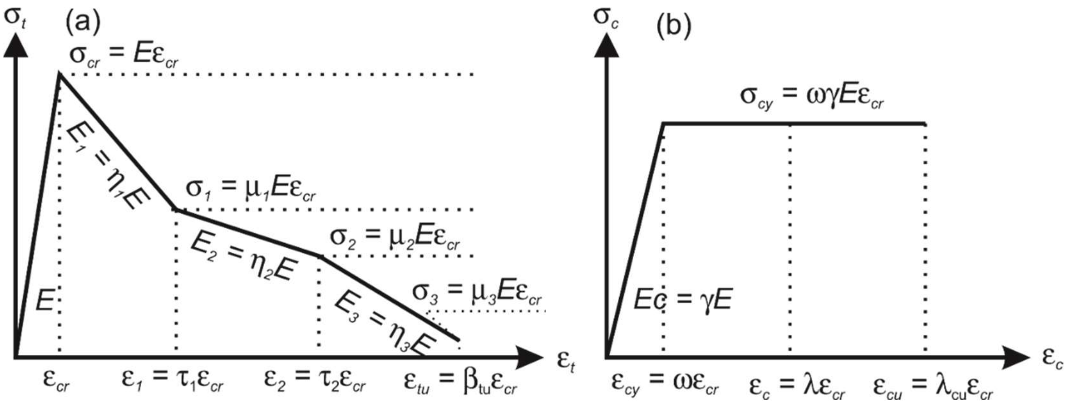

Figure 6.1 - Constitutive relations for FRC: (a) tensile and (b) compressive responses.

$$\frac{\sigma_t(\beta)}{E\varepsilon_{cr}} = \begin{cases} \beta & 0 \leq \beta \leq 1 \\ 1 + \eta_1(\beta - 1) & 1 \leq \beta \leq \beta_1 \\ 1 + \eta_1(\beta_1 - 1) + \eta_2(\beta_1 - \beta) & \beta_1 \leq \beta \leq \beta_2 \\ 1 + \eta_1(\beta_1 - 1) + \eta_2(\beta_2 - \beta_1) + \eta_3(\beta - \beta_2) & \beta_2 \leq \beta \leq \beta_3 \end{cases} \tag{6.4}$$

$$\frac{\sigma_c(\lambda)}{E\varepsilon_{cr}} = \begin{cases} \lambda\gamma & 0 \leq \lambda \leq \omega \\ \omega\gamma & \omega \leq \lambda \leq \lambda_{cu} \end{cases} \tag{6.5}$$

$$\lambda = \frac{\beta k}{1 - k} \tag{6.6}$$

Where k is the normalized neutral axis depth.

By assuming the Kichhoff hypothesis of the plane section remaining plane and ignoring shear deformations, the flexural failure is assumed to dominate the beam mechanical response. The constitutive model shown in figure 6.1 is applied to reach the stress distribution in accordance with the strains along the beam section. The integration of the linear stress function over the beam geometry brings as a result the internal force and moment distribution. The stress-strain block for all possible stages is described in figure 6.3. Given the distance from the bottom of the beam to the neutral axis as a function of the strain distribution ($y(\varepsilon)$), it is possible to achieve the net force through equations 6.7 to 6.9. A rectangular beam section is assumed in the present research. The neutral axis is calculated by solving the net force in equation 6.9 equal to zero. The moment can be analyzed by multiplying the moment arm with the total force, as displayed in equation 6.10. The corresponding curvature (ϕ) as a function of fiber bottom normalized strain (β) is expressed in equation 6.11. The final moment (M) and curvature (ϕ) can be analyzed through its normalized form multiplied by its critical value as shown in equations 6.12 and 6.13. The normalized parameters are identified by the addition of a dash over the variable ($\overline{M}, \overline{\phi}$).

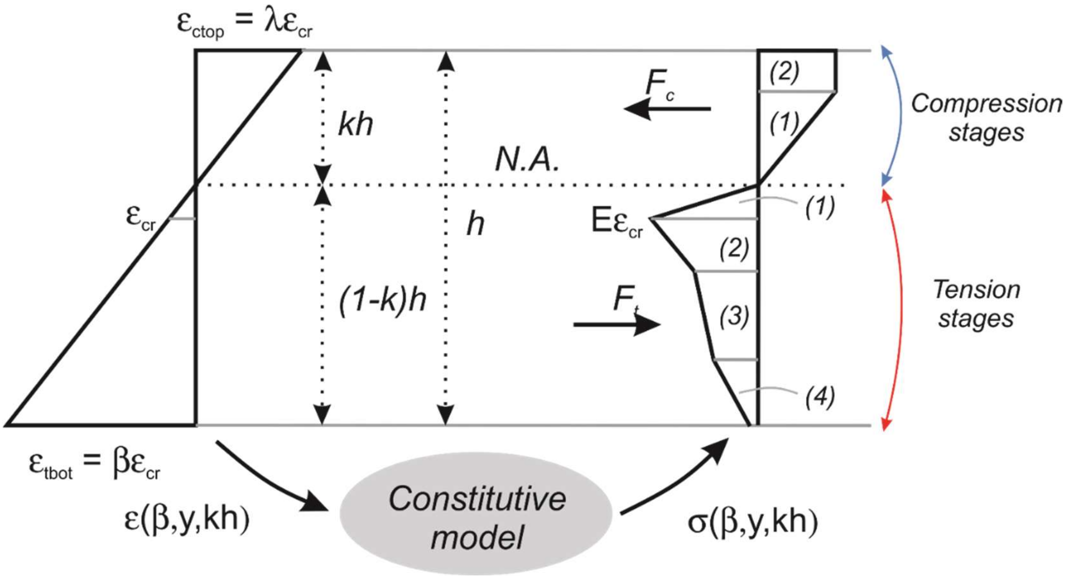

Figure 6.2 - Stress-strain distribution along the beam height.

The described approach brought previously is applied for each combination between tensile and compressive stress-strain block presented in figure 6.3. The potential stages can be divided into seven stages from zone 1.1 to 2.4. The first digit stands for compressive stress-strain response in accordance with the constitutive model. While zone 1.x means elastic compressive stress-strain behavior, zone 2.x is associated with perfectly plastic mechanical response. The second digit describes the tensile performance as described in figure 6.1. Zone 1.3, for instance, means elastic compressive strain with a 3rd post-cracking stage. Table 1 summarizes the identification of each quad-linear model. The complete solutions for the normalized neutral axis depth (k), normalized moment ($\overline{M}$) and normalized curvature ($\bar{\phi}$) are shown in table 2.

$$y(\varepsilon) = \frac{\varepsilon(1-k)h}{\beta\varepsilon_{cr}} \tag{6.7}$$

$$\frac{dy}{d\varepsilon} = \frac{(1-k)h}{\beta\varepsilon_{cr}} \tag{6.8}$$

$$\sum_0^h F = \int \sigma(\varepsilon)dA = b\int_0^h \sigma(y)dy = b\int_0^h \frac{\sigma(\varepsilon)(1-k)h}{\beta\varepsilon_{cr}}d\varepsilon \tag{6.9}$$

$$\sum_0^h M = \int F\bar{y} = b\int_0^\beta y(\varepsilon)\sigma(\varepsilon)\frac{(1-k)h}{\beta\varepsilon_{cr}}d\varepsilon = b\int_0^{\varepsilon_i} \sigma(\varepsilon)\varepsilon\left(\frac{(1-k)h}{\beta\varepsilon_{cr}}\right)^2 d\varepsilon \tag{6.10}$$

$$\phi = \frac{\beta\varepsilon_{cr}}{(1-k)h} \tag{6.11}$$

$$M_{cr} = \frac{\varepsilon_{cr} E b h^2}{6}; M = \bar{M} * M_{cr} \tag{6.12}$$

$$\phi_{cr} = \frac{2\varepsilon_{cr}}{h}; \phi = \bar{\phi} * \phi_{cr} \tag{6.13}$$

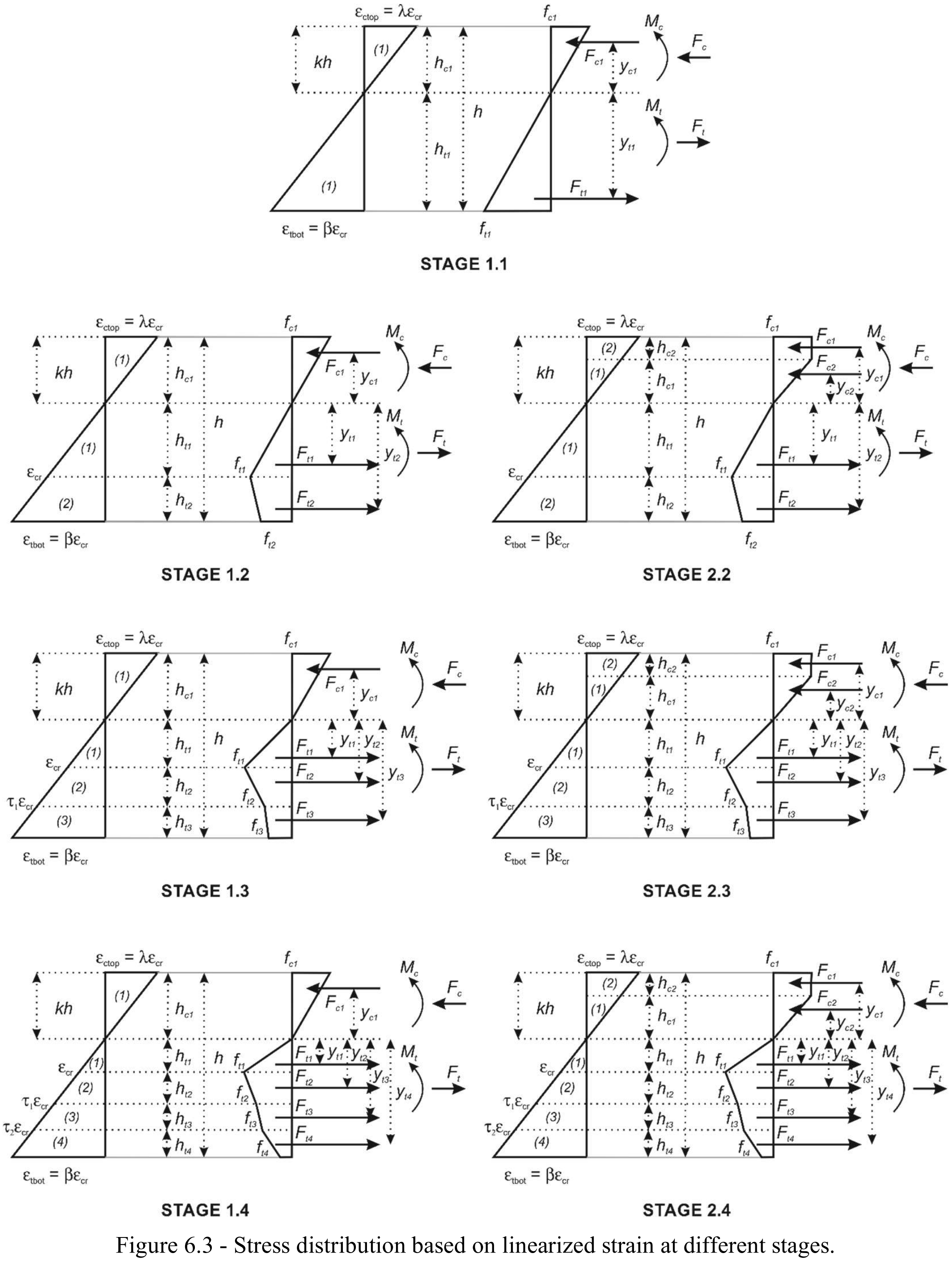

STAGE 1.1

STAGE 1.2

STAGE 2.2

STAGE 1.3

STAGE 2.3

STAGE 1.4

STAGE 2.4

Figure 6.3 - Stress distribution based on linearized strain at different stages.

Table 6.1 - Description of each stage for the quad-linear model

Stage	Tension	Normalized tension strain	Compression	Normalized compression strain
1.1	Elastic	$0 \leq \beta < 1$	Elastic	$0 \leq \lambda < \omega$
1.2	1st Post-cracking	$1 \leq \beta < \tau_1$	Elastic	$0 \leq \lambda < \omega$
1.3	2nd Post-cracking	$\tau_1 \leq \beta < \tau_2$	Elastic	$0 \leq \lambda < \omega$
1.4	3rd Post-cracking	$\tau_2 \leq \beta < \beta_{tu}$	Elastic	$0 \leq \lambda < \omega$
2.2	1st Post-cracking	$1 \leq \beta < \tau_1$	Plastic	$\omega \leq \lambda < \lambda_{cu}$
2.3	2nd Post-cracking	$\tau_1 \leq \beta < \tau_2$	Plastic	$\omega \leq \lambda < \lambda_{cu}$
2.4	3rd Post-cracking	$\tau_2 \leq \beta < \beta_{tu}$	Plastic	$\omega \leq \lambda < \lambda_{cu}$

6.2.2.Fracture parameter equations

The second step of the proposed methodology is to calculate the main fracture parameters in accordance with the constitutive relations of each material and its geometrical properties. The crack mouth opening displacement is the key parameter when it comes to the analysis the three-point bending tests in accordance with the EN 14651 [37] and the Model Code [12]. The fatigue degradation also depends fundamentally on the CMOD increase along the fatigue cycles, which will be explained in the next section.

In the present methodology, the CMOD was calculated using the characteristic length (L_p) as proposed initially by Hillerborg [42] and more recently analyzed by di Prisco *et al.* [41]. The basic concept is to propose a link between the constitutive relation (σ-ε) and fracture mechanics parameters governed by the stress-crack opening law (σ-$CMOD$). With the introduction of the characteristic length, it is possible to estimate crack opening following equation 6.14. When it comes to four-point bending test, the characteristic length can be assumed equal to the specimen loading span.

However, for three-point bending, no standard formula is still present in the literature [41, 43, 44]. The value L_p may also be modified empirically until the analytical curve correctly fits the experimental results. Past investigations by di Prisco *et al.* [41] and Massone *et al.* [43] verified good agreement between the measured CMOD and equation 6.14, when the characteristic length is equal to the beam height ($L_p/h = 1$). The recommended value for L_p is also present in the Model Code [12] and was adopted in this research. Figure 6.4 summarizes the use of characteristic length to estimate CMOD.

Table 6.2 - The complete solutions in accordance with the proposed constitutive model

Stg.	k	$\overline{M}$	$\overline{\phi}$
1.1	$k_{11} = \begin{cases} \frac{1}{2} \text{ for } \gamma = 1 \\ \frac{-1+\sqrt{\gamma}}{-1+\gamma} \text{ for } \gamma < 1 \text{ or } \gamma > 1 \end{cases}$	$\overline{M}_{11} = \frac{-2*\beta*(1+(\gamma-1)*k_{11}^3)}{(k_{11}-1)} + \frac{-2*\beta*(3*k_{11}^2-3*k_{11})}{(k_{11}-1)}$	$\overline{\phi}_{11} = \frac{\beta}{2(1-k_{11})}$
1.2	$k_{12} = \frac{A_1+\sqrt{A_2}}{A_1+\beta^2\gamma}$	$\overline{M}_{12} = \frac{(2\beta^3\gamma-B_1)k^3+3B_1k^2}{(1-k_{12})\beta^2} + \frac{-3B_1k+B_1}{(1-k_{12})\beta^2}$	$\overline{\phi}_{12} = \frac{\beta}{2(1-k_{12})}$
1.3	$k_{13} = \frac{A_3+\sqrt{A_4}}{A_3+\beta^2\gamma}$	$\overline{M}_{13} = \frac{(2\beta^3\gamma-B_2)k^3+3B_2k^2}{(1-k_{13})\beta^2} + \frac{-3B_2k+B_2}{(1-k_{13})\beta^2}$	$\overline{\phi}_{13} = \frac{\beta}{2(1-k_{13})}$
1.4	$k_{14} = \frac{A_5+\sqrt{A_6}}{A_5+\beta^2\gamma}$	$\overline{M}_{14} = \frac{(2\beta^3\gamma-B_3)k^3}{(1-k_{14})\beta^2} + \frac{3B_3k^2-3B_3k+B_3}{(1-k_{14})\beta^2}$	$\overline{\phi}_{14} = \frac{\beta}{2(1-k_{14})}$
2.2	$k_{22} = \frac{A_7}{A_7+2\beta\omega\gamma}$	$\overline{M}_{22} = \frac{B_4k^2-2B_4k+B_4}{\beta^2}$	$\overline{\phi}_{22} = \frac{\beta}{2(1-k_{22})}$
2.3	$k_{23} = \frac{A_8}{A_8+2\beta\omega\gamma}$	$\overline{M}_{23} = \frac{B_5k^2-2B_5k+B_5}{\beta^2}$	$\overline{\phi}_{23} = \frac{\beta}{2(1-k_{23})}$
2.4	$k_{24} = \frac{A_9}{A_9+2\beta\omega\gamma}$	$\overline{M}_{24} = \frac{B_6k^2-2B_6k+B_6}{\beta^2}$	$\overline{\phi}_{24} = \frac{\beta}{2(1-k_{24})}$

$A_1 = -\beta^2\eta_1 + 2\beta\eta_1 - 2\beta - \eta_1 + 1$

$A_2 = \beta^4\gamma\eta_1 - 2\beta^3\gamma\eta_1 + 2\beta^3\gamma + \beta^2\gamma\eta_1 - \beta^2\gamma$

$A_3 = -\beta^2\eta_2 - 2\beta\eta_1\tau_1 + 2\beta\eta_2\tau_1 + \eta_1\tau_1^2 - \eta_2\tau_1^2 + 2\beta\eta_1 - 2\beta - \eta_1 + 1$

$A_4 = \beta^4\gamma\eta_2 + 2\beta^3\gamma\eta_1\tau_1 - 2\beta^3\gamma\eta_2\tau_1 - \beta^2\gamma\eta_1\tau_1 + \beta^2\gamma\eta_2\tau_1^2 - 2\beta^3\gamma\eta_1 + 2\beta^3\gamma + \beta^2\gamma\eta_1 - \beta^2\gamma$

$A_5 = -\beta^2\eta_3 - 2\beta\eta_1\tau_1 + 2\beta\eta_2\tau_1 - 2\beta\eta_2\tau_2 + 2\beta\eta_3\tau_2 + \eta_1\tau_1^2 - \eta_2\tau_1^2 + \eta_3\tau_2^2 + 2\beta\eta_1 - 2\beta - \eta_1 + 1$

$A_6 = \beta^4\gamma\eta_3 + 2\beta^3\gamma\eta_1\tau_1 - 2\beta^3\gamma\eta_2\tau_1 + 2\beta^3\gamma\eta_2\tau_2 - 2\beta^3\gamma\eta_3\tau_2 - \beta^2\gamma\eta_1\tau_1 + \beta^2\gamma\eta_2\tau_1^2 - \beta^2\gamma\eta_2\tau_2^2$
$+\beta^2\gamma\eta_3\tau_2^2 - 2\beta^3\gamma\eta_1 + 2\beta^3\gamma + \beta^2\gamma\eta_1 - \beta^2\gamma$

$A_7 = \beta^2\eta_1 + \gamma\omega^2 - 2\beta\eta_1 + 2\beta + \eta_1 - 1$

$A_8 = \beta^2\eta_2 + 2\beta\eta_1\tau_1 + \gamma\omega^2 - 2\beta\eta_2\tau_1 - \eta_1\tau_1^2 - 2\beta\eta_1 + 2\beta + \eta_1 - 1$

$A_9 = \beta^2\eta_3 + 2\beta\eta_1\tau_1 - 2\beta\eta_2\tau_1 + 2\beta\eta_2\tau_2 - 2\beta\eta_3\tau_2 + \gamma\omega^2 - \eta_1\tau_1^2 + \eta_2\tau_1^2 - \eta_2\tau_2^2 + \eta_3\tau_2^2 - 2\beta\eta_1 + 2\beta + \eta_1 - 1$

$B_1 = 2\beta^3\eta_1 - 3\beta^2\eta_1 + 3\beta^2 + \eta_1 - 1$

$B_2 = 2\beta^3\eta_2 + 3\beta^2\eta_1\tau_1 - 3\beta^2\eta_2\tau_1 - \eta_1\tau_1^3 + \eta_2\tau_1^3 - 3\beta^2\eta_1 + 3\beta^2 + \eta_1 - 1$

$B_3 = 2\beta^3\eta_3 + 3\beta^2\eta_1\tau_1 - 3\beta^2\eta_2\tau_1 + 3\beta^2\eta_2\tau_2 - 3\beta^2\eta_3\tau_2 - \eta_1\tau_1^3 + \eta_2\tau_1^3 - \eta_2\tau_2^3 + \eta_3\tau_2^3 - 3\beta^2\eta_1 + 3\beta^2 + \eta_1 - 1$

$B_4 = 2\beta^3\eta_1 + 3\beta^2\gamma\omega - \gamma\omega^3 - 3\beta^2\eta_1 + 3\beta^2 + \eta_1 - 1$

$B_5 = 2\beta^3\eta_2 + 3\beta^2\eta_1\tau_1 - 3\beta^2\eta_2\tau_1 - \gamma\omega^3 - \eta_1\tau_1^3 - 3\beta^2\eta_1 + 3\beta^2 + \eta_1 - 1$

$B_5 = 2\beta^3\eta_3 + 3\beta^2\eta_1\tau_1 - 3\beta^2\eta_2\tau_1 + 3\beta^2\eta_2\tau_2 - 3\beta^2\eta_3\tau_2 - \gamma\omega^3 - \eta_1\tau_1^3 + \eta_2\tau_1^3 - \eta_2\tau_2^3 + \eta_3\tau_2^3 - 3\beta^2\eta_1 + 3\beta^2 + \eta_1 - 1$

The next fracture parameters to be estimated through analytical equations are crack length (*a*) and the stress intensity factor (*KI*). Both parameters already present well described formulations in the available literature [45-49]. Equations 6.15-6.17 brings the proposed equations for both crack length and *KI*, respectively. Figure 6.4 summarizes all geometrical parameters used through equations 6.15-6.17. An iteration process needs to be conducted in order to estimate the crack length in equation 6.15.

$$CMOD = \beta \varepsilon_{cr} L_p \tag{6.14}$$

$$CMOD = \frac{6PSaV_1(\alpha)}{Eh^2b}, V_1(\alpha) = 0.76 - 2.28\alpha + 3.87\alpha^2 - 2.04\alpha^3 + \frac{0.66}{(1-\alpha)^2} \tag{6.15}$$

$$KI = \frac{3PS\sqrt{\pi a}F(\alpha)}{2h^2b}, F(\alpha) = \frac{\left(1.99 - \alpha(1-\alpha)(2.15 - 3.93\alpha + 2.7\alpha^2)\right)}{\pi^{1/4}(1+2\alpha)(1-\alpha)^{3/2}} \tag{6.16}$$

$$\alpha = \frac{a}{h} \tag{6.17}$$

Where β is the normalized tensile strain parameter, $\varepsilon_{cr} L_p$ is the cracking tensile strain, L_p is the characteristic length, *E* the tensile modulus, *P* is load calculated through the achieved moment from the closed-form solutions, *S* is loading span, *h* the beam height, *b* the beam width.

Table 6.4 - List of used parameters for the analysis of the quasi-static FRC response for each author

Authors	ε_{cr} (mm/mm)	μ_1 (-)	μ_2 (-)	β_{tu} (-)	η_1 (-)	η_2 (-)	η_3 (-)	ω (-)	λ_{cu} (-)	γ (-)	L_p (mm)
Monteiro *et al.* [23]	0.000095	3	80	280	0.36	0	-0.00135	20.6	500	0.85	150
Carlesso *et al.* [19]	0.0090	12	50	340	0.009	-0.003	-0.003	14.8	300	0.95	75
Stephen *et al.* [21]	0.000145	2	35	280	0.63	0.003	-0.00079	20.6	500	0.85	150

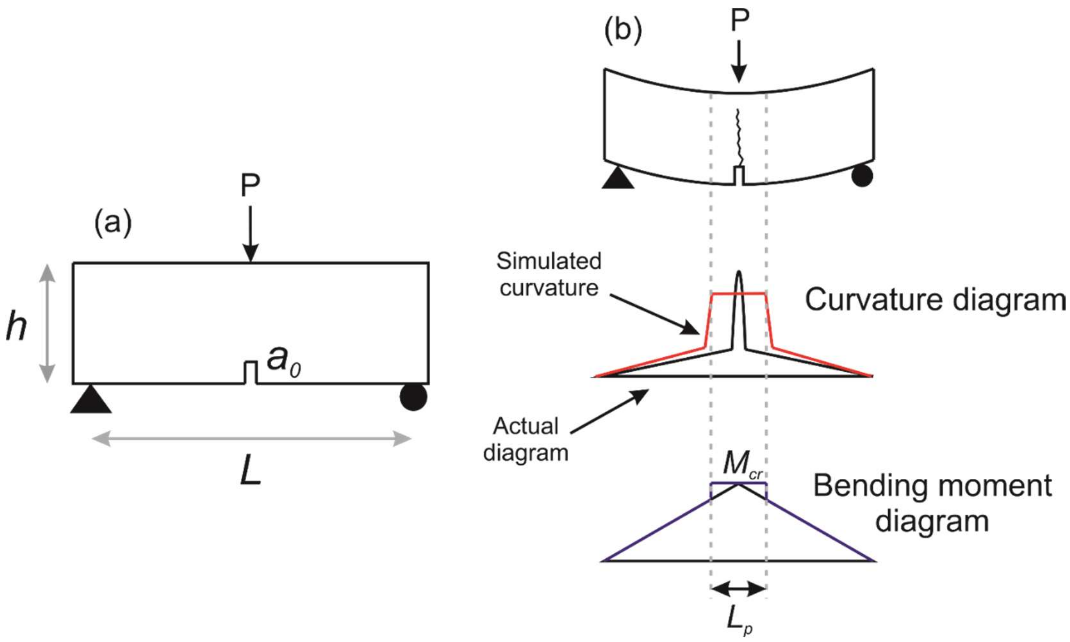

Figure 6.4 - Model geometrical parameters: (a) three-point bending test geometrical parameters and (b) application of the characteristic length (L_p) on the closed-form solution model.

6.2.3. Flexural fatigue degradation

The present model proposes an empirical equation to determine the CMOD evolution along the cycles. The equation is associated to the referred cycle number (n/N), the exponent ϑ and the initial CMOD ($CMOD_0$), similar to what has already been applied in past fatigue research works [50-52]. Equations 6.18-6.20 bring the CMOD evolution equation details. The residual CMOD was defined as 0.30 mm based on the past research of Smedt *et al.* [53], who studied the residual CMOD for distinct crack openings in FRC three-point bending tests. The authors verified that the residual crack opening was around 0.30 mm for distinct fractions and types of steel fiber reinforced concrete. Both ϑ and $CMOD_0$ are evaluated as a function of the applied load level (S) and the curve fitting was based on the available experimental data from Monteiro *et al.* [23], Carlesso *et al.* [19] and Stephen *et al.* [21]. The following sections bring the discussion about the fitting with the experimental output. Finally, the equation can estimate CMOD evolution along the material fatigue life depending on the load level.

The CMOD evolution has as an input the number of cycles before failure (N). The number of cycles can be achieved experimentally through an S-N curve, which correlates it with the applied load level (S). In general, S-N curves are determined in laboratories by applying cyclic constant loading amplitudes until reaching specimen failure [54, 55]. The *S-N* curves derive the mean fatigue life with significant standard deviations. More recent studies have already brought more precise probabilistic methods to reach the fatigue life, especially with the application of Weibull distributions [56-58]. However, when it comes to the analysis of the fatigue mechanical degradation, as proposed in this work, the mean fatigue life already brings a coherent result for the proposed model.

After estimating the CMOD evolution, it is possible to calculate the strain evolution along the cycles using equation 6.14 and the characteristic length (L_p) and the variation of the normalized strain value (β). Thereafter, by applying the variation of $\beta(n)$ as a function of the fatigue cycles on the closed-form solution, it is possible to back-calculate some of the main mechanical parameters and its degradation due to fatigue loading. The main purpose of this present model is to bring fatigue mechanical deterioration in terms of the main parameters used for FRC design, which generally are dependent on the mechanical response from the notched three-point bending tests [12, 59]. Figure 6.5 tries to summarize the complete proposed model workflow. The present research brings the evolution of crack length ($a(n)$), residual flexural stress ($f_R(n)$), tensile strain (ε_t) and curvature ($\phi(n)$).

$$CMOD(n) = CMOD_0 + \left(1 - \frac{n}{N}\right)^{\vartheta} - 1 \tag{6.18}$$

$$CMOD_0 = CMOD_{residual} + \frac{1}{5}S, CMOD_{residual} = 0.30\ mm \tag{6.19}$$

$$\vartheta = -\frac{1}{4}S^3 \tag{6.20}$$

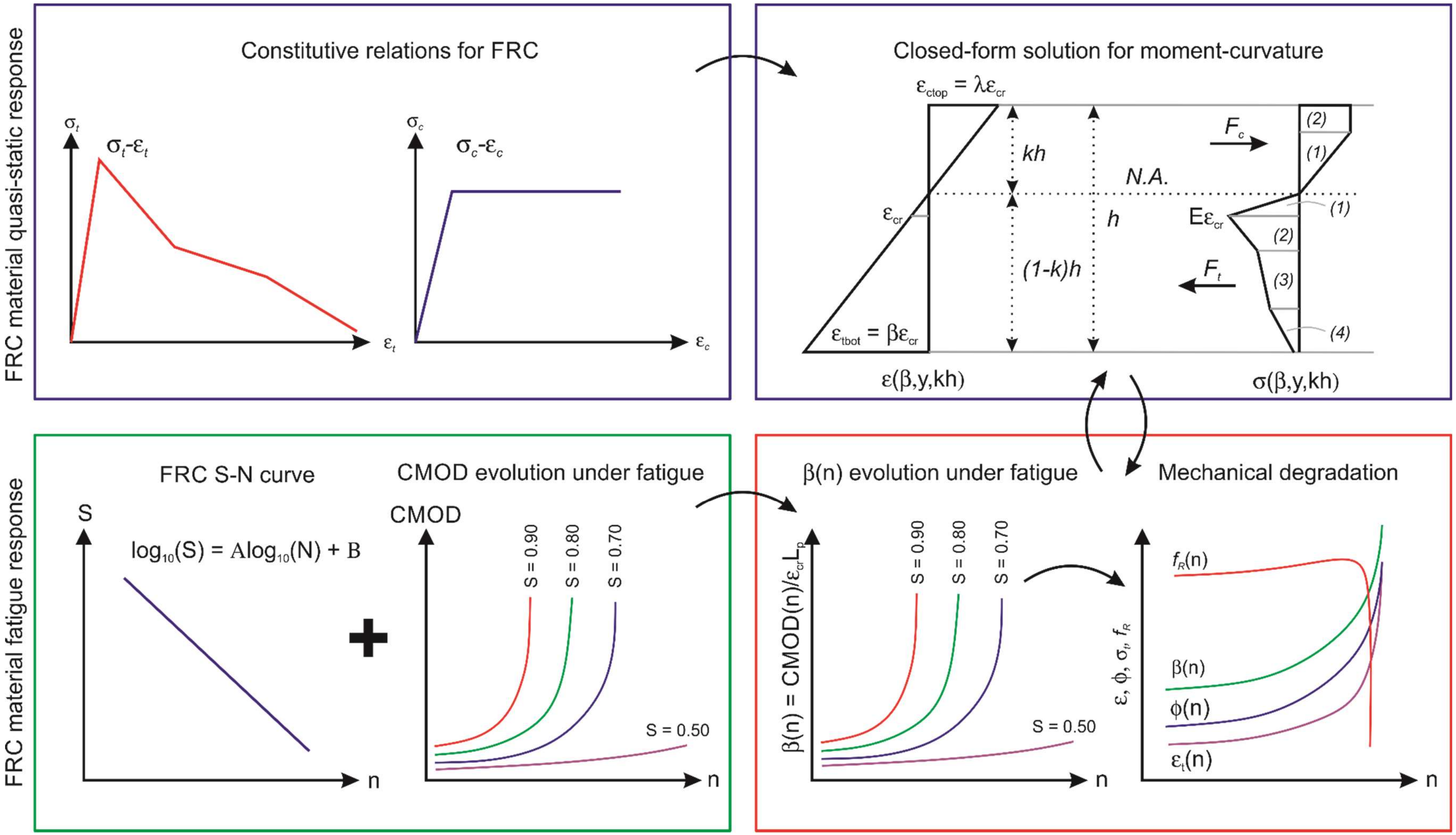

Figure 6.5 - Model workflow from defining the FRC quasi-static response until its mechanical degradation under flexural fatigue.

6.2.4. Discussion and analysis for the model application

6.2.4.1. Constitutive relations

Figure 6.6 brings the constitutive relations for all studied FRCs by Monteiro *et al.* [23], Carlesso *et al.* [19] and Stephen *et al.* [21]. The constitutive model was divided by tension and compression. The complete list of geometrical and applied normalized parameters for the constitutive model is shown in tables 3 and 4. For all studied materials a quad-linear tension response and an elastic perfectly plastic model was applied. The FRC models for Monteiro *et al.* [23] and Stephen *et al.* [21] show a typical stress-strain analysis for steel fiber reinforced concrete with a softening response after reaching a matrix crack strength. When it comes to the work of Carlesso *et al.* [19], it is possible to verify the hardening response for the studied UHPC. Based on the proposed constitutive relations, it is possible to calculate the quasi-static material curves, which are discussed in the next sections.

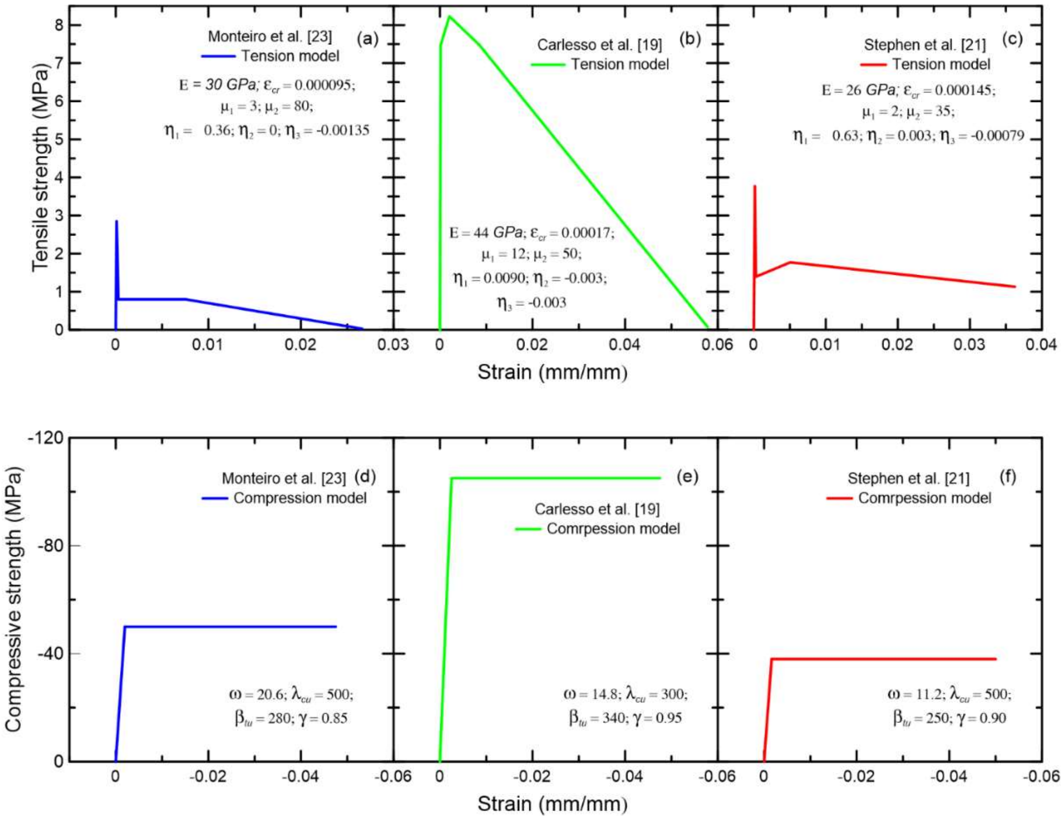

Figure 6.6 - Constitutive models for the different FRCs from Monteiro et al [23], Carlesso *et al.* [19] and Stephen *et al.* [21]: (a), (b) and (c) tension and (d), (e) and (f) compression models.

6.2.4.2. Quasi-static response

Figure 6.7 shows the moment-curvature response for all studied FRCs by Monteiro *et al.* [23], Carlesso *et al.* [19] and Stephen et l. [21]. The moment-curvature curves were calculated in accordance with the solutions for equations 6.9, 6.10 and 6.11 and table 6.2. With the M-ϕ result, it is possible to use equation 6.14 and calculate the load-CMOD response, since moment and curvature are reached as a function of load and strain, respectively. Figure 6.8 brings the load-CMOD curves by using the characteristic length and its comparison with the experimental data. Figure 6.8 shows a significant fit between analytical and experimental results, validating the proposed constitutive parameters for the analyzed fiber reinforced composite. For the present research the value of L_p was assumed to be equal to the beam height ($L_p = h$) as proposed in the literature [12, 41, 60, 61]. For the present proposed model, the analytical quasi-static response is validated through the load-CMOD, which guarantees that all steps applied until this section is in accordance with what is observed on the three-point bending experimental tests.

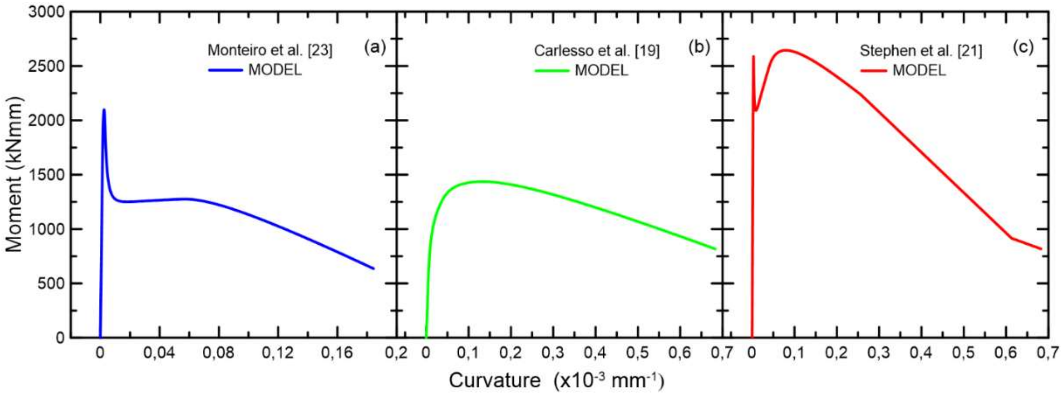

Figure 6.7 - Moment-curvature response for (a) Monteiro *et al.* [23], (b) Carlesso *et al.* [19] and (c) Stephen *et al.* [21] studied FRCs.

The application of a quad-linear tension constitutive model seemed to enhance the fitting capacity of the closed-form solution in relation to the observed experimental response of the beam tests. Past research works [31, 32 and 34] still used the three-linear models, which may not be adequate to estimate the complete mechanical FRC response in bending. This can be especially a concern when it comes to more special concrete mixtures such as UHPC and strain-hardening cementitious composites, which usually present significant stiffness variations along their strain range.

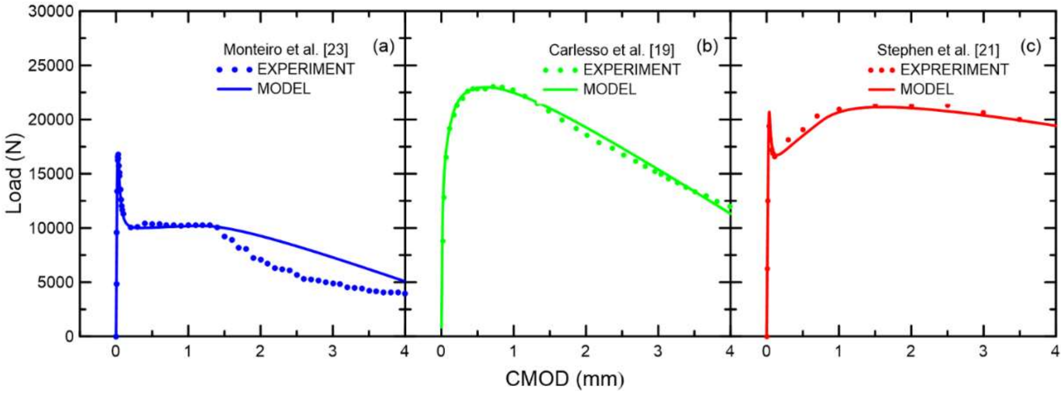

Figure 6.8 - Load-CMOD response for (a) Monteiro *et al.* [23], (b) Carlesso *et al.* [19] and (c) Stephen *et al.* [21].

Figure 6.9 brings the results for the fracture parameters (crack length and stress intensity factor) using the equations 6.15, 6.16 and 6.17 proposed Shah [45]. Past results presented by the work of Bhosale *et al.* [62] have already observed some disagreement between the equations proposed by Shah [45], especially when analyzing them for lower CMOD values under 0.50 mm. The applied equations in this model propose that crack length evolves very fast for the first values of CMOD. Bhosale *et al.* [62] verified experimentally with the use of digital image correlation a distinct correlation between CMOD and crack length. However, for the purpose of the present model, Shah [45] equations are still good enough when it comes to have an adequate analysis of the crack length evolution.

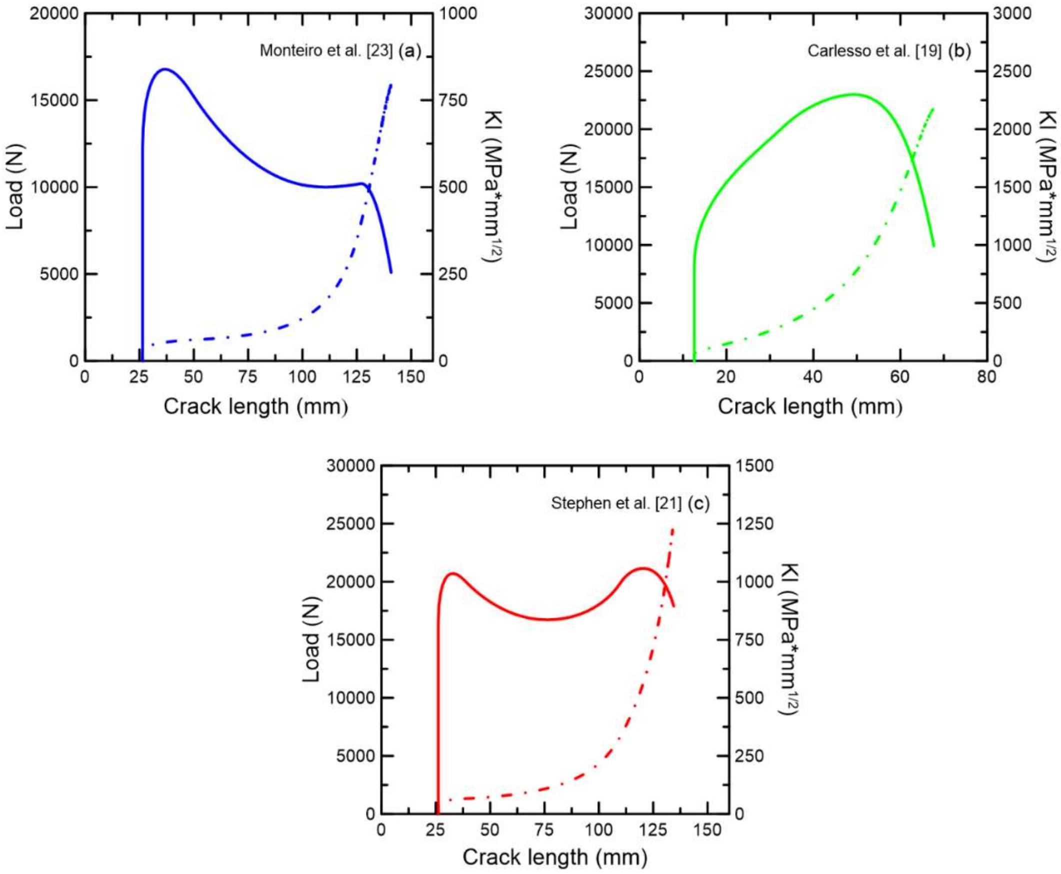

Figure 6.9 - Quasi-static response for the fracture parameters crack length and stress intensity factor for (a) Monteiro *et al.* [23], Carlesso *et al.* [19] and (c) Stephen *et al.* [21].

6.2.4.3. CMOD evolution under fatigue flexural loading

After characterizing the quasi-static response of the FRCs, it already possible to verify the material mechanical degradation under flexural fatigue. The proposed empirical model at equation 6.18 for fatigue CMOD evolution needs as an input the *S-N* curves. The *S-N* experimental results for Monteiro *et al.* [23], Carlesso *et al.* [19] and Stephen *et al.* [21] are displayed in figure 6.10. The $log_{10}(S)$-$log_{10}(N)$ regressions are also presented at the graphics. The achieved regressions were used to estimate the number of cycles before failure for the proposed CMOD evolution equation.

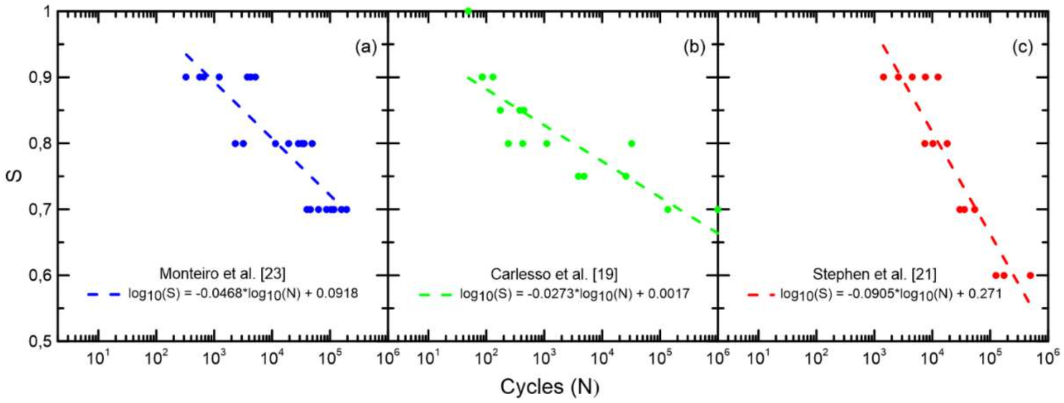

Figure 6.10 - S-N curves for the distinct studied FRCs under fatigue flexural by Monteiro *et al.* [23], Carlesso *et al.* [19] and (c) Stephen *et al.* [21].

The achieved fatigue CMOD evolution curves are displayed in figure 6.11. The obtained empirical curves are confronted with the experimental result for CMOD evolution obtained from the studied authors. It is possible to verify that the model adequately fits the experimental data. As already observed by different authors in the literature [7, 21, 23, 63], CMOD evolution presents distinct increasing rates depending on the applied load level. After an almost linear increase of CMOD, the degradation rate is sharply enhanced until reaching the complete material failure. As observed in figure 6.11, the proposed power law for CMOD evolution can correctly cover all observed degradation stages. The experimental *S-N* curve is, therefore, used to adjust the empirical model in terms of the number of cycles before failure. As expected, there is a major variation on the results for the number of cycles before failure for all studied load levels. However, the *N* value achieved from the empirical *S-N* curve can provide suitable results for the observed CMOD evolution. Probabilistic methods can be applied to achieve safer values of *N* in accordance with the desired failure probability [28-30].

Using the closed-form solution of the quasi-static response for FRC, it is possible to calculate the material pre-crack before applying the CMOD fatigue evolution model. Figure 6.12 summarizes the complete material response in terms of pre-cracking and being submitted to flexural fatigue loading. In accordance with the developed model, higher values of CMOD are observed when top load levels are applied. The results for S = 50% were also displayed, but the CMOD increase stopped at the fatigue testing limit of 10^6 cycles, since the studied authors observed test *run-out* at this load level. Past research [19, 21] also verified a more brittle failure when lower load levels were applied. Higher *S* failure may be associated to continuous fiber pullout along the crack, generating a more ductile response under fatigue loading. On the other hand, smaller load levels can be associated to the fiber rupture as shown by the works of Monteiro *et al.* [64], Fataar *et al.* [65] and Vicente *et al.* [66], who studied in detail the main mechanisms of fiber-matrix interface degradation under fatigue loading in steel FRC.

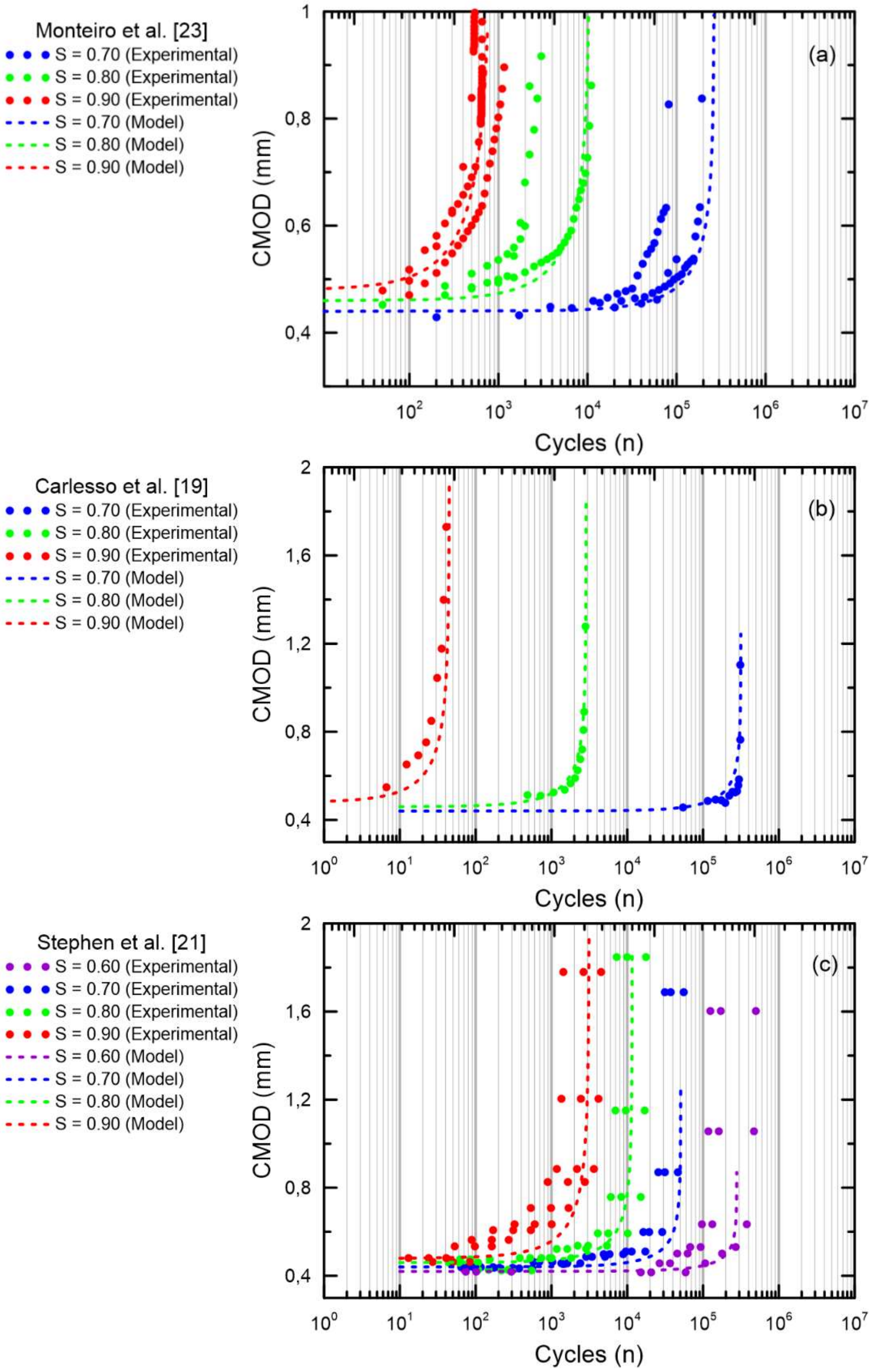

Figure 6.11 - CMOD evolution under flexural fatigue and the application of the proposed empirical model for (a) Monteiro *et al.* [23], (b) Carlesso *et al.* [19] and (c) Stephen *et al.* [21].

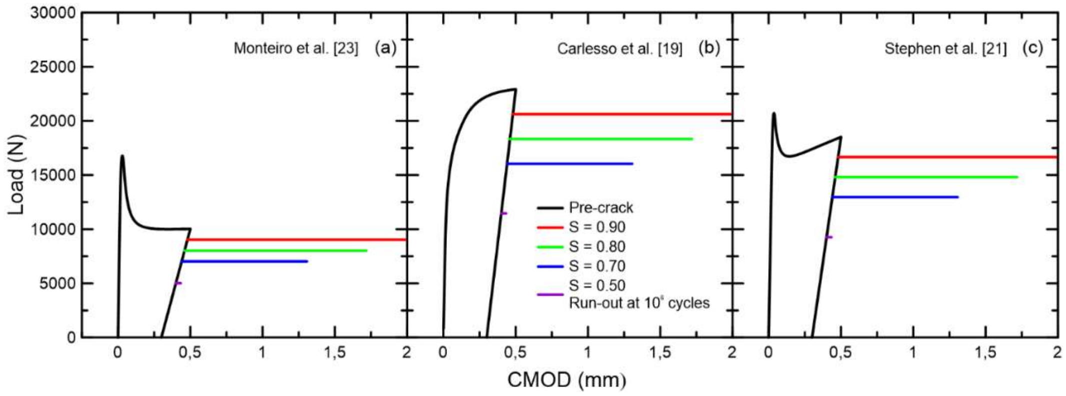

Figure 6.12 - Fatigue CMOD evolution after material pre-crack for the FRCs by (a) Monteiro *et al.* [23], Carlesso *et al.* [19] and Stephen *et al.* [21].

6.2.4.4. Mechanical degradation under fatigue flexural loading

After calculating the normalized strain parameter (β) based on the CMOD evolution under flexural fatigue loading, it is possible to use the closed-form solution to verify the mechanical degradation of the studied parameters in terms of the fatigue cycles. Figures 6.13, 6.14 and 6.15 bring the results of the fatigue degradation for the studied FRCs by Monteiro *et al.* [23], Carlesso *et al.* [19] and Stephen *et al.* [21]. All figures divide the analysis by the (a) crack length increase, (b) normalized strain parameter (β), (c) tensile strain, (d) curvature and (e) residual flexural stress. The model was applied by the following load levels: 0.50, 0.70, 0.80 and 0.90.

The evolution of crack length, tensile strain and curvature present very similar response to CMOD increase under fatigue loading, displaying, first, an almost linear increase and, subsequently, sharply enhancing the degradation rate until reaching the complete material failure. The increase rate is highly dependent on the load level as expected. Therefore, the proposed methodology can successfully bring the other mechanical variables degradation under flexural fatigue loading. Using the achieved results for curvature evolution under fatigue, it would be also possible to estimate the results for deflection evolution response along the cycles. The closed-form solutions for load-deflection response are explained in the research developed by Yao *et al.* [40] and Soranakom *et al.* [31].

When it comes to the analysis of the flexural residual strength variation under fatigue loading, a distinct response is verified. The residual stress follows the results achieved from the closed-form solutions shown in figures 6.7 and 6.8. For the studied FRCs, the post-crack region around 0.50 mm of CMOD does not present major variations in terms of residual strength. Since CMOD increases very slowly until reaching the material rupture, the flexural residual strength almost does not present significant changes when under fatigue degradation. Having Stephen *et al.* [21] constitutive model as an exception in this research, the stresses are almost constant along the fatigue life until reaching closer to the material rupture. However, if other constitutive models were studied with major decay around 0.50 mm of CMOD, the flexural residual stresses could display distinguished responses.

In accordance with the three studied authors, almost no mechanical degradation under flexural fatigue loading was verified under the load level of 0.50. It is important to remind that the achieved S-N curves presented test run-out at 1,000,000 cycles for $S = 0.50$. This means that the mechanical degradation could be observed if higher cycles were analyzed. In any case, the FRC beams under fatigue load up to the load level of 0.50 seem to present the most reliable mechanical response when thinking on future design applications of structural members.

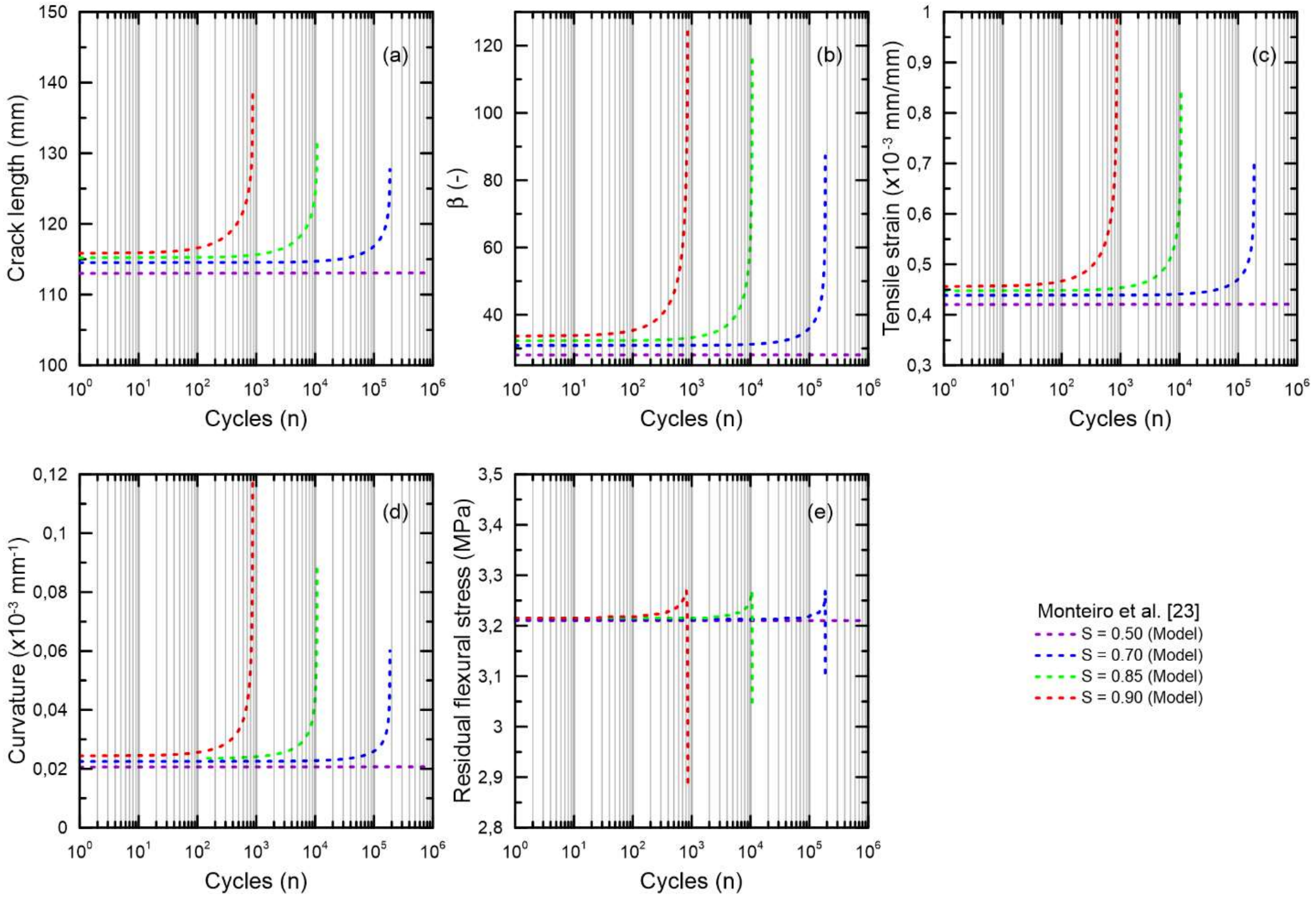

Figure 6.13 - FRC mechanical degradation under flexural fatigue in terms of (a) crack length increase, (b) normalized strain parameter (β), (c) tensile strain, (d) curvature and (e) residual flexural stress for Monteiro *et al.* [23].

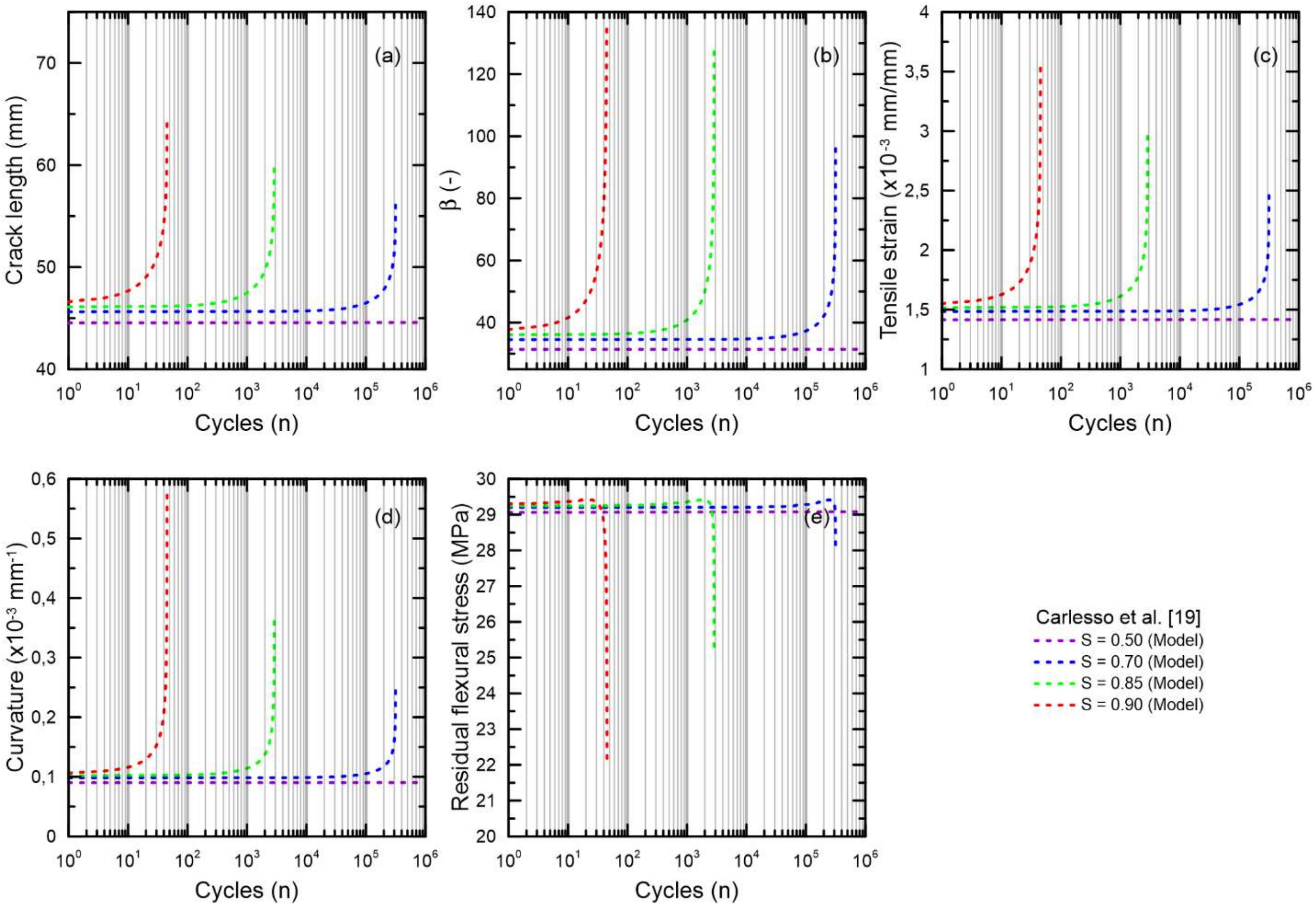

Figure 6.14 - FRC mechanical degradation under flexural fatigue in terms of (a) crack length increase, (b) normalized strain parameter (β), (c) tensile strain, (d) curvature and (e) residual flexural stress for Carlesso *et al.* [19].

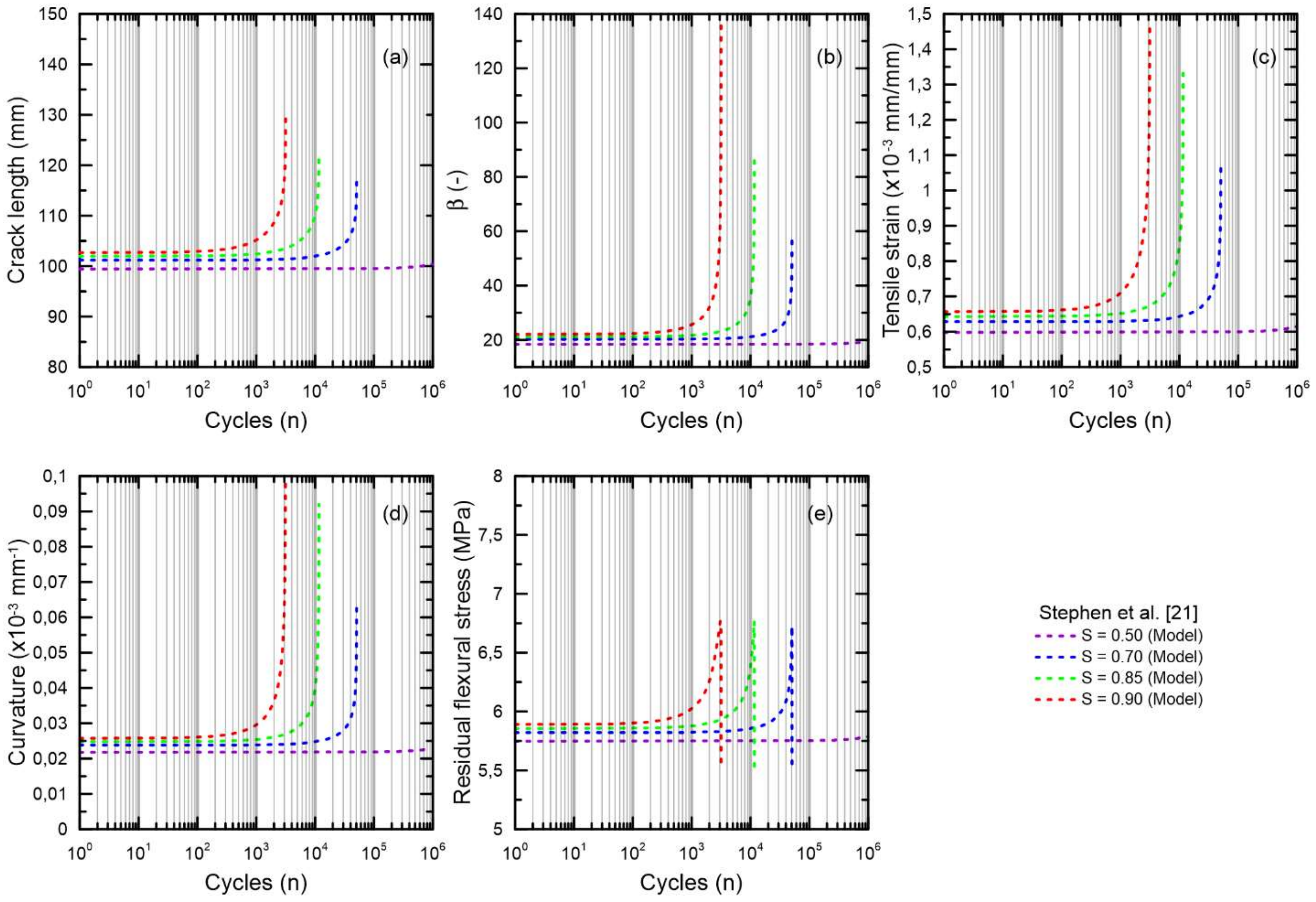

Figure 6.15 - FRC mechanical degradation under flexural fatigue in terms of (a) crack length increase, (b) normalized strain parameter (β), (c) tensile strain, (d) curvature and (e) residual flexural stress for Stephen *et al.* [21].

6.3. Conclusions

The present work brings a novel methodology to estimate FRC mechanical degradation throughout closed-form solutions for FRC beams. The first step consisted on deriving the constitutive relations for tension and compression for studied FRCs. While a quad-linear model was used for tension, an elastic perfectly plastic model was applied for compression. Thereafter, the moment-curvature was calculated using the proposed closed-form solution equations. Crack opening is, then, verified using the characteristic length, which allows to evaluate crack increase and stress intensity factor under quasi-static loading. With the composite quasi-static response completely characterized, the next step is to evaluated CMOD increase under fatigue with the proposed power law equation and the material *S-N* curve. Finally, any relevant mechanical parameters deterioration (curvature, strain, stress) can be estimated by using the CMOD fatigue evolution and back-calculating the results with the already analyzed closed-form solutions. The main conclusion can be derived from the present research:

- The quad-linear tension constitutive was successful to fit all studied FRC quasi-static responses, based on the applied closed-form solutions. The verified FRCs included 50 MPa steel fiber reinforced concrete and ultra-high performance concrete mixtures. The use of the characteristic length equal to the beam height also verified to be very accurate to estimate crack opening as a function of the tensile strains. With the correct calculation of CMOD, it was possible to reach the quasi-static characterization in terms of the fracture parameters.
- The proposed CMOD evolution under flexural fatigue loading correctly fitted the observed experimental data for the studied authors in this research. The power law equation is directly associated with the applied fatigue load level during the experiments and is modified accordingly. The instantaneous CMOD observed after the first fatigue cycle was calculated using previous experimental observations by past works and adjusted also in terms of the load level. CMOD evolution presents distinct increasing rates depending on the applied load level. After an almost linear increase of CMOD, the degradation rate is sharply enhanced until reaching the complete material failure.

- Based on the proposed CMOD evolution under flexural fatigue loading, it was possible to calculate the normalized strain parameter as a function of the load cycles. Since the strain parameters is directly linked to all other mechanical variables on the closed-form solution in the present model, the present research verified the fatigue degradation in terms the crack length increase, tensile strain, curvature and residual flexural stress. With the exception of the stress variation throughout the fatigue life, all other parameters presented very similar response in relation to CMOD variation with, first, an almost linear increase and, subsequently, sharply enhancing the degradation rate until reaching the complete material failure. When it comes to the flexural residual stresses, the post-crack region around 0.50 mm of CMOD does not present major variations in terms of strength. Since CMOD increases very slowly until reaching the material rupture, the flexural residual strength almost does not present significant changes when under fatigue degradation.

6.4. References

1 HOLMEN, J. Fatigue design evaluation of offshore concrete structures. **Maériaux et Construction**, vol. 17, p. 39-42, 1984.

2 BELLETTI, B. CERIONI, R. MEDA, A. PLIZZARI, G. Design aspects on steel fiber-reinforced concrete pavements. **Journal of Materials and Civil Engineering** (2008), vol. 20, p. 599-607, 2008.

3 DE LA LIAO, L. FUENTE, S. CAVALARO, S. AGUADO, A. Design procedure and experimental study on fibre reinforced concrete segmental rings for vertical shafts. **Material Design**, vol. 92, p. 590-601, 2016.

4 GÖRANSSON F, NORDENMARK A. **Fatigue assessment of concrete foundations for wind power plants**. MSc dissertation, 142 p. Göteborg, Sweden: Chalmers University of Technology, 2011.

5 SRITHARAN, S. SCHMITZ, G. **Design of tall wind turbine towers utilizing** UHPC. In: RILEM-fib-AFGC International Symposium of Ultra-High Performance Fibre-Reinforced Concrete, 2013.

6 AGLAN, H. FIGUEROA, J. Damage-evolution approach to fatigue cracking in pavements. **Journal of Engineering Mechanics**, vol. 119, p. 1243-1259, 1993.

7 SUBRAMANIAM, K. GOLDSTEIN, G. POPOVICS, J. SHAH, S. Fatigue response of concrete subjected to biaxial fatigue in the compression-tension region. **ACI Materials Journal**, vol. 96, p. 663-669, 1999.

8 CACHIM, P. **Experimental and numerical analysis of the behavior of structural concrete under fatigue loading with application to concrete pavements**. PhD thesis, Faculty of Engineering, University of Porto, 1998.

9 LEE, M. BARR, B. An overview of the fatigue behavior of plain and fibre reinforced concrete. **Cement Concrete Composites**, vol. 26, p. 299-305, 2004.

10 NAAMAN, A. HAMMOUD, H. Fatigue characteristics of high performance fiber-reinforced concrete. **Cement and Concrete Composites**, vol. 20, p. 353-363, 1998.

11 BANJARA, N. RAMANJANEYULU K. Experimental investigations and numerical simulations on the flexure fatigue behavior of plain and fiber-reinforced concrete. **Journal of Materials and Civil Engineering**, vol. 30, 2018.

12 CEB-FIB. The International Federation for Structural Concrete. FIB Model Code for Concrete Strucures (2010)

13 SINGH, S. KAUSHIK, S. Flexural fatigue life distribution and failure probability of steel fibrous concrete. **ACI Structural Journal**, vol. 97, p. 658-667, 2000.

14 BOULEKBACHE, B. HAMRAT, M. CHEMROUK, M. AMZIANE, S. Flexural behavior of steel fiber-reinforced concrete under cyclic loading. **Construction and Building Materials**, vol. 126, p. 253-262, 2016.

15 CARLESSO, D. CAVALARO, S. DE LA FUENTE, A. Flexural fatigue of pre-cracked plastic fibre reinforced concrete: experimental study and numerical modeling. **Cement and Concrete Composites**, vol. 115, 2021.

16 SINGH, S. KAUSHIK, S. Fatigue strength of steel fibre reinforced concrete in flexure. **Cement & Concrete Composites**, vol. 25, p. 779-786, 2003.

17 SINGH, S. SINGH, B. KAUSHIK, S. Probability of fatigue failure of steel fibrous concrete. **Magazine of Concrete Research**, vol. 57, p. 65-72, 2005.

18 SINGH, S. SHARMA, U. Flexural fatigue strength of steel fibrous concrete beams. **Advances in Structural Engineering**, vol. 10, p. 197-207, 2007.

19 CARLESSO, D. DE LA FUENTE, A. CAVALARO, S. Fatigue of cracked high performance fiber reinforced concrete subjected to bending. **Construction and Building Materials**, vol. 220, p. 444-455, 2019.

20 WU, W. HE, X. YI, Z. ZHU, Z. HE, J. WANG, W. ZHAO, C. Flexural fatigue behaviors of high-content hybrid fiber-polymer concrete. **Construction and Building Materials**, vol. 349, 2022.

21 STEPHEN, S. GETTU, R. Fatigue fracture of fibre reinforced concrete in flexure. **Materials and Structures**, vol. 53, p. 56, 2020.

22 GERMANO, F. TIBERTI, G. PLIZZARI, G. Post-peak fatigue performance of steel fiber reinforced concrete under flexure. **Materials and Structures**, vol. 49, p. 4229-4245, 2016.

23 MONTEIRO, V. CARDOSO, D. SILVA, F. A novel methodology for estimating damage evolution and energy dissipation for steel fiber reinforced concrete under flexural fatigue loading. **International Journal of Fatigue**, vol. 166, 2023.

24 BAKTHEER, A. BECKS, H. Fracture mechanics based interpretation of the load sequence effect in the flexural fatigue behavior of concrete using digital image correlation. **Construction and Building Materials**, vol. 307, 2021.

25 BAKTHEER, A. AHUILAR, M. CHUDOBA, R. Microplane fatigue model MS1 for plain concrete under compression with damage evolution driven by cumulative inelastic shear strain. **International journal of Plasticity** (2021), vol. 143, 2021.

26 HSU, T. Fatigue of plain concrete. **ACI Journal**, vol. 78, p. 292-304, 1981.

27 MEDEIROS, A. ZHANG, X. RUIZ, G. YU, R. VELASCO, M. Effect of the loading frequency on the compressive fatigue behavior of plain and fiber reinforced concrete. **International Journal of Fatigue**, vol. 70, p. 342-350, 2015.

28 SAUCEDO, L. YU, R. MEDEIROS, A. ZHANG, X. RUIZ, G. A probabilistic fatigue model on the initial distribution to consider frequency effect in plain and fiber reinforced concrete. **International Journal of Fatigue** (2013), vol. 48, p. 308-318, 2013.

29 CASTILLO, E. CANTELI, A. **A unified statistical methodology for modeling fatigue damage**, 1st ed. Springer, 2009.

30 CANTELI, A. CASTILLO, E. BLÁSON, S. A methodology for phenomenological analysis of cumulative damage process. Application to

fatigue and fracture phenomena. **International Journal of Fatigue**, vol. 150, 2021.

31 SORANAKOM, C. MOBASHER, B. Closed-form solutions for flexural response of fiber-reinforced concrete beams**. Journal of engineering Mechanics**, vol. 8, p. 933-941, 2007.

32 SORANAKOM, C. MOBASHER, B. Correlation of tensile and flexural responses of strain softening and strain hardening cement composites. **Cement & Concrete Composites**, vol. 30, p. 465-477, 2008.

33 MOBASHER, B. LI, A. YAO, Y. ARORA, A. NEITHALATH, N. Characterization of toughening mechanisms in UHPC through image correlation and inverse analysis of flexural results. **Cement and Concrete Composites**, vol. 122, 2021.

34 YAO, Y. BAKHSHI, M. NASRI, V. MOBASHER, B. Interactions diagrams for design of hybrid fiber-reinforced tunnel segments. **Materials and Structures**, vol. 51, p. 35, 2018.

35 MOBASHER, B. YAO, Y. SORANAKOM, C. Analytical solutions for flexural design of hybrid steel fiber reinforced concrete beams. **Engineering Structures**, vol. 100, p. 164-177, 2015.

36 PLEESUDJAI, C. MOBASHER, B. Analytical moment-curvature solutions for generalized textile-reinforced concrete sections. **Engineering Structures**, vol. 276, 2023.

37 EUROPEAN STANDARD. **EN 14651**: Test method for metallic concrete - Measuring the flexural tensile strength (limit of proportionality (LOP), residual), 2005.

38 AMERICAN SOCIETY FOR TESTING AND MATERIALS. **ASTM C1609**. Standard Test Method for Flexural Performance of Fiber-Reinforced Concrete (Using Beam With Third-Point Loading), 2019.

39 PLEESUDJAI, C. **Generalized modeling and experimental validation of flexural response in cement-based composites**. MSc. Thesis, Arizona State University (ASU), Arizona: United States of America, 2021.

40 YAO, Y. ASWANI, K. WANG, X. MOBASHER, B. Analytical displacement solutions for statistically determinate beams based on a tri-linear moment-curvature model. **Structural Concrete**, vol. 19, p. 1619-1632, 2018.

41 DI PRISCO, M. COLOMBO, M. DOZIO, D. Fibre-reinforced concrete in fib Model Code 2010: principles, models and test validation. **Structural Concrete,** vol. 13, p. 4, 2013.

42 HILLERBORG, A. MODEER, M. PETERSON, P. Analysis of crack formation and crack growth by means of fracture mechanics and finite elements. **Cement and Concrete Research**, vol. 6, p. 773-782, 1976.

43 MASSONE, L. NAZAR, F. Analytical and experimental evaluation of the use of fibers as partial reinforcement in shotcrete for tunnels in Chile. **Tunnelling and Underground Space Technology** (2018), vol. 77, p. 13-25, 2018.

44 DIAS-DA-COSTA, D. VALENÇA, J. CARMO, R. Curvature assessment of reinforced concrete beams using photogrammetric techniques. **Materials and Structures** (2013), vol. 47, p. 1745-1760, 2013.

45 SHAH, S. Determination of fracture parameters (KsIC and CTODc) of plain concrete using three-point bend tests. **Materials and Structures** (1990), vol. 23, p. 457-460, 1990.

46 ZHANG, P. WANG, C. GAO, Z. WANG, F. A review on fracture properties of steel fiber reinforced concrete. **Journal of Building Engineering,** vol. 67, 2023.

47 XU, S. REINHARDT, H. Determination of double-K criterion for crack propagation in quasi-brittle fracture, Part II: analytical evaluation and practical measuring methods for three-point bending notched beams. **International Journal of Fracture**, vol. 98, p. 151-177, 1999.

48 XU, S. REINHARDT, H. Determination of double-K criterion for crack propagation in quasi-brittle fracture, Part I: Experimental investigation of crack propagation. **International Journal of Fracture**, vol. 98, p. 111-149, 1999.

49 XU, S. REINHARDT, H. A simplified method for determining double-K fracture parameters for three-point bending tests. **International Journal of Fracture**, vol. 104, p. 181-209, 2000.

50 BAKTHEER, A. CHUDOBA, R. Experimental and theoretical evidence for the load sequence effect in the compressive fatigue behavior of concrete. **Materials and Structures**, vol. 54, 2021.

51 GRZYBOWSKI, M. MEYER, C. Damage accumulation in concrete with and without fiber reinforcement. **Materials Journal**, vol. 90, p. 594-604, 1993.

52 SHAH, S. Predictions of cumulative damage for concrete and reinforced concrete. **Matériaux et Construction**, vol. 17, p. 65–68, 1984.

53 SMEDT, M. VRIJDAGHS, R. VAN STEEN, C. VERSTRYNGE, E. VANDEWALLE, L. Damage analysis in steel fibre reinforced concrete under monotonic and cyclic bending by means of acoustic emission monitoring. **Cement and Concrete Composites**, vol. 114, 2020.

54 SCHIJVE, J. **Fatigue of Structures and Materials**. Second ed., Springer, 2009.

55 DOWLING, N. **Mechanical Behavior of Materials**. Fourth ed., Pearson, 2013.

56 CASTILLO, E. CANTELI, A. A compatible regression Weibull model for the description of the three-dimensional fatigue σ_m-N-R field as a basis cumulative damage approach. **International Journal of Fatigue**, vol. 155, 2022 doi.org/10.1016/j.ijfatigue.2021.106596.

57 CANTELI, A. CASTILLO, E. BLÁSON, S. A methodology for phenomenological analysis of cumulative damage processes. Application to fatigue and fracture phenomena. **International Journal of Fatigue**, vol. 150, 2021.

58 DE LA ROSA, A. RUIZ, G. CASTILLO, E. MORENO, R. Calculation of dynamic in concentrated cementitious suspensions: probabilistic approximation and Bayesian analysis. **Materials**, vol. 14, 2021.

59 TECHNICAL REPORT 34. **TR 34**. Concrete industrial ground floor: A guide to design and construction, 2018.

60 BARROS, J. CUNHA, V. RIBEIRO, A. ANTUNES, J. Post-cracking behavior of steel reinforced concrete. **Materials and Structures** (2005), vol. 38, p. 47-56.

61 BUTTIGNOL, T. FERNANDES, J. BITTENCOURT, T. SOUSA, J. Design of reinforced concrete beams with steel fibers in the ultimate limit state. **IBRACON Structures and Materials Journal**, vol. 5, p. 997-1024, 2018.

62 BHOSALE, A. PRAKASH, S. Crack propagation of synthetic vs. steel vs. hybrid fibre-reinforced concrete beams using digital image correlation technique. **International Journal of Concrete Structures and Materials**, vol. 14, p. 57, 2020.

63 GAEDICKE, C. ROESLER, J. SHAH, S. Fatigue crack growth prediction in concrete slabs. **International Journal of Fatigue**, vol. 31, p. 1309-1317, 2009.

64 MONTEIRO, V. CARDOSO, D. SILVA, F. Mechanisms of fiber-matrix interface degradation under fatigue loading in steel FRC. **Journal of Building Engineering**, vol. 68, 2023.

65 FATAAR, H. COMBRINCK, R. BOSHOFF, W. An experimental study on the fatigue failure of steel fibre reinforced concrete at a single fibre level. **Construction and Building Materials**, vol. 299, 2021.

66 VICENTE, M. MÍNGUEZ, J. GONZÁLEZ, D. Computed tomography scanning of the internal microstructure, crack mechanisms, and structural behavior of fiber-reinforced concrete under static and cyclic bending tests. **International Journal of Fatigue**, vol. 121, p. 9-19, 2019.

7 On the mechanical degradation of R/SFRC beams under flexural fatigue loading

Present research brings the analysis of the influence of steel fibers on the mechanical degradation of reinforced concrete beams under flexural fatigue loading. Current experimental work aims to emphasize the fiber capacity in mitigating the mechanical decay of the concrete structures in terms of rebar deformation, crack spacing and other mechanical parameters. The experimental campaign encompassed reinforced concrete beams with low reinforcing ratio of 0.35%. While two beams were produced with plain concrete, the other two were fabricated with the addition of 40 kg/m^3 of hooked-end steel fibers. The fatigue tests were load-controlled under a 6 Hz sinusoidal wave under distinct loading level ranges. When comparing the same loading range, steel fiber reinforced concrete structural beams reported much lower strain values along the fatigue test. The fibers showed a very effective capacity to redistribute the stresses in the traction zone and, consequently, reducing the measured strains on the longitudinal reinforcement. Similar mechanical deterioration was observed when it comes to the analysis of deflection and curvature evolution along the fatigue test. The rate of mechanical deterioration is linked to the applied stress levels. The growth of one main crack reveals that the fatigue rupture was controlled by the stress concentrations in the tensile rebars at the crack location.

The article was submitted to peer-review analysis for the Materials and Structures Journal.

7.1. Introduction

The design of reinforced steel fiber reinforced concrete (SFRC) structural members subjected to cyclic loading such as offshore structures [1], concrete pavements [2, 3], bridge girders [4] and wind towers [5] demand the consideration of the fatigue mechanical degradation analysis. In general, these structures are subjected to millions of stress cycles during their service life [6], due to wind or wave action, thermal variation and traffic loads. The continuous stress variations along the service life is responsible to lead to crack initiation and propagation, which eventually can result in significant strength and stiffness decay [7].

First experiments in the field focused primarily on the fatigue degradation of plain and fiber reinforced concrete under cyclic compression loading [8-12], bringing the first results in terms of Wöhler curves [13] for distinct matrix compositions. Moreover, first results divided the fatigue behavior into three major stages: (1) flaw initiation due to weak regions within concrete, (2) slow and almost linear growth of the inherent flaws until a critical crack size is reached and (3) development of an unstable macrocrack, leading to failure [14, 15]. As studied by Subramaniam *et al.* [7] and Gaedick *et al.* [16], the resistance to crack growth increases up to critical crack length at the peak load of the quasi-static response. Based on these first fatigue results, it was already possible to propose the first specifications and guidelines on the Model Code [17], which brings the first equations for strain evolution and damage analysis only for cyclic compression loading.

The next generation of mechanical tests verified the analysis of fiber reinforced concrete (FRC) flexural fatigue degradation in the pre-peak regime on unnotched [18, 19] or notched [20, 21] specimens. Overall, an increase in fatigue life was reported for higher fiber aspect ratio and content. The review of Lee *et al.* [22] summarizes the flexural fatigue results in unnotched specimens and Subramaniam *et al.* [7] proposed the first equations to verify crack evolution under fatigue loading. However, the study of the fatigue mechanical degradation evolved dramatically in the last ten years, since the FRC fatigue performance began to be studied in the post-peak regime in order to better evaluate the crack bridging of fibers after the formation of the fracture process zone [23, 24]. Moreover, since FRC structures are designed according to post-cracking mechanical parameters, more fatigue research on the post-peak regime is of great importance. As analyzed by Carlesso *et al.* [25] and Monteiro *et al.* [26], fatigue on pre-cracked FRC is assessed through notched beam specimens, which are, first, monotonically loaded until 0.50 mm of crack mouth opening displacement (CMOD) and, then, subjected to fatigue loading until a pre-defined test run-out or up to the material rupture.

Aiming the characterize the cementitious composite performance under fatigue loading, innumerous parameters must be evaluated, such as the stress ratio [27], maximum stress level [28-31], loading frequency [32, 33] and loading sequence [34, 35]. While Baktheer *et al.* [34] has already verified the influence of the loading sequence on the damage evolution, Carlesso *et al.* [24, 28] bring the development of S-N curves for both steel and polypropylene fiber reinforced concretes. Medeiros *et al.* [32] and Saucedo *et al.* [33] worked to insert the oscillation frequency on the failure probability equations and Weibull distributions. More recently, novel probabilistic methodologies were proposed by past authors to determine the concrete fatigue life [36-40].

Along with the execution of the flexural fatigue tests for FRC performance analysis, the development of new design codes, models and experimental programs to study the fiber influence in reinforced concrete structural members also verified a major breakthrough in the last years [41-45]. The enhancement of the load capacity and ductility depend directly on the fiber parameters such as shape, aspect ratio, bond strength and volume fraction [46, 47], which are responsible for promoting the structural service life conditions. Among the main examples of fiber reinforced concrete structures developed are SFRC elevated slabs and precast tunnel lining segments [48, 49]. Moreover, a series of closed-form solutions through parametric constitutive models have already been successfully implemented by Yao *et al.* [50] in order to derive the hybrid SFRC flexural load-deflection behavior.

When it comes to the fatigue degradation of reinforced concrete structural members, a wide range of tests have been carried on to verify the structural deterioration along the fatigue life [51-54]. The fatigue performance of RC members is linked to the constituent and the interaction between steel bars and concrete [53, 55]. The main causes to increase deflection and stiffness degradation subjected fatigue flexural loading are damage accumulation on rebars and concrete, as well as the bond degradation between them. While compressive stresses of concrete are redistributed along the fatigue cycles, the tensile reinforcement must sustain more stress in order to maintain equilibrium. The fatigue damage of the tensile rebar accumulates substantially, resulting in nucleation and propagation of the crack along the concrete section. Therefore, based on this phenomenon, the performance of RC beams may be improved if fibers are added to the mix in order to enhance the cementitious composite resistance in the traction zone [56, 57].

However, there is still a major gap in the literature and in the present design codes and guidelines when it comes to the study of the fatigue degradation of FRC structural members. The only works by Gao *et al.* [56] and Parvez *et al.* [57] bring an overall analysis of the fiber influence on the mechanical deterioration when subjected to flexural fatigue loading. Compared with non-fiber reinforced beam, the fatigue life increased at least 38% for a volume fraction of 0.50%. Moreover, owning to the bridging effect of steel fibers, the stress range on the tensile reinforcement decreased with the increase in steel fiber content, promoting the increase in fatigue life.

Therefore, the present research developed an experimental program with the aim to enhance the knowledge about the mechanical degradation of FRC structural members under flexural fatigue loading. A 50 MPa self-consolidating concrete matrix with the addition of 40 kg/m^3 of hooked-end steel fibers was selected for this work. The reinforced concrete beams were manufactured with two 6.3 mm longitudinal rebars, resulting in an overall reinforcing ratio of 0.35%. High-speed cameras were used for the digital image correlation (DIC) system to study the crack opening oscillation along the fatigue tests. The mechanical deterioration under fatigue loading was analyzed in terms of rebar and concrete strains evolution, curvature and deflection increase along the cycles, stiffness decay and crack opening variation. The fatigue life was also analyzed as function of the rebar stress variations This work pretends to bring more information about the impact of the use of steel fibers on RC beams under fatigue loading.

7.2. Experimental program

7.2.1. Mix composition and material characterization

Brazilian cement type CPII-F (ASTM Cement type IL - Portland-Limestone Cement [58]), fly ash and silica fume were added as the main cementitious materials. For this mix composition, two distinct classes of particle size of river sand were used: sand S1 ranged from 0.15 mm to 4.8 mm and the second S2 from 0.15 mm to 0.85 mm. Coarse aggregate of 9.5 mm maximum diameter, superplasticizer (MasterGlenium 51), silica flour and a viscosity modifying admixture (MasterMatrix VMA 358) also composed the overall concrete formulation. A final water/cement ratio of 0.50 was used in this research. A compressive strength of 50 ± 2 MPa was verified after 28 days.

More information on the development of the used self-consolidating concrete (SCC) is available at De Larrard [59] and Rambo *et al.* [60]. The complete mix content can be verified in table 7.1.

Table 7.1 – Mix composition of the self-consolidating concrete

Constituent	Matrix
Coarse aggregate	492
Sand (S1) (kg/m^3)	827
Sand (S2) (kg/m^3)	100
Silica Mesh 325 (kg/m^3)	70
Cement (kg/m^3)	360
Fly Ash (kg/m^3)	168
Silica Fume (kg/m^3)	45
Water (kg/m^3)	164
Superplasticizer (%)	5.50
Viscosity modifying admixture (%)	0.75

**Sand (S2): Sand (S1) with diameter less than 0.85 mm*

Steel fibers with hooked-end were used as reinforcement. The steel fiber presents a length (*L*) of 35 mm, diameter (*d*) of 0.75 mm, aspect ratio of 45 (*L/d*) and tensile strength of 1225 MPa. A mass fraction of 40 kg/m^3 was added to all R/SFRC beams. The beams were named accordingly to the steel fiber mass fractions: C0SF and C40SF. The summary of the steel fiber properties is presented in table 7.2.

Table 7.2 – Steel fiber properties

Properties	SF 
Type	Hooked-end
Length (mm)	35
Diameter (mm)	0.75
Aspect Ratio	45
Tensile strength (MPa)	1225

The fresh concrete was analyzed by their flow ability based on ASTM C1611 standard [61] and no evidence of segregation or bleeding was verified. The following values of concrete spread were achieved for plain concrete (C0SF) and C20SF: 710 and 690 mm. The self-consolidating concrete spread was performed by two average mass diameters.

The post-peak flexural strength of the preset SFRC composition was previously verified through EN 14651 [62] three-point bending test standard. As defined in the Model Code 2010 [17], $f_{R,i}$ is the flexural residual stress obtained from the three point bending test on notched specimens with i = 1,2,3 and 4, respectively for CMOD values of 0.5, 1.5, 2.5 and 3.5 mm. The stress f_{lop} corresponds to the flexural limit of proportionality. The overall mean values of post-peak results can be analyzed in table 7.3 for C40SF.

A 6.3 mm diameter steel bar was used in this research program. A nominal 500 MPa yield strength and a 210 GPa young modulus were reported by the manufacturer. The deformed steel bars have transverse ribs.

Table 7.3 - Post-peak parameters for monotonic three-point bending tests in accordance with EN 14651 [41] standard. Standard deviation values presented in parentheses.

Mix	f_{lop} MPa	$f_{R,1}$ MPa	$f_{R,2}$ MPa	$f_{R,3}$ MPa	$f_{R,4}$ MPa
C40SF	6.38 (0.56)	7.07 (1.00)	6.01 (0.82)	3.78 (0.33)	2.75 (0.22)

7.2.2. Mixing procedure

The complete mixing procedure can be divided in five main stages. The aggregates (river sands S1 and S2, coarse aggregate) are first added inside the mixer with 70% of the water and blended together for 1 minute. Mineral and cementitious materials (silica flour, fly ash and silica fume) are, then, mixed with the previous added materials for 1 minute. Afterwards, the cement is added and mixed for 1 minute. The superplasticizer, remaining water and viscosity modifying admixture are blended until the matrix reaches its self-consolidating state (around 10 minutes). Finally, the steel fibers are added to the concrete matrix and blended for more 5 minutes. All specimens were cured in air, at room temperature of 25 ºC for 28 days before testing.

7.2.3. Test program

7.2.3.1. Monotonic structural bending tests

For the structural test, a short beam was produced with 120 mm height, 150 mm width and 1200 mm length. The beams were reinforced with two steel bars with 6.3 mm in diameter and 6.3 mm stirrups with 12.5 cm spacing. The total steel area in the cross section corresponds to 0.35%. The beam geometry and reinforcement configuration can be seen in figure 7.1(a).

All structural tests were carried on a MTS servo-controlled hydraulic system with maximum capacity of 500 kN. The monotonic tests were controlled by the machine servo-hydraulic LVDT at a rate of 2 mm/min. The beams deflection was measured by three LVDTs, which were equally distributed along the loading span. The span between the loading rollers measured 370 mm and the support rollers presented a span of 1100 mm. The test setup illustration is presented in figure 1(b) and figure 7.2. The longitudinal rebars were instrumented with two 6 mm and 120 Ω strain gauges. A 50 mm length strain gauges were also positioned along the beam height of the specimen in order to measure the concrete strain. The details of the strain gauge location on the RC beams can be seen in figure 7.1(a).

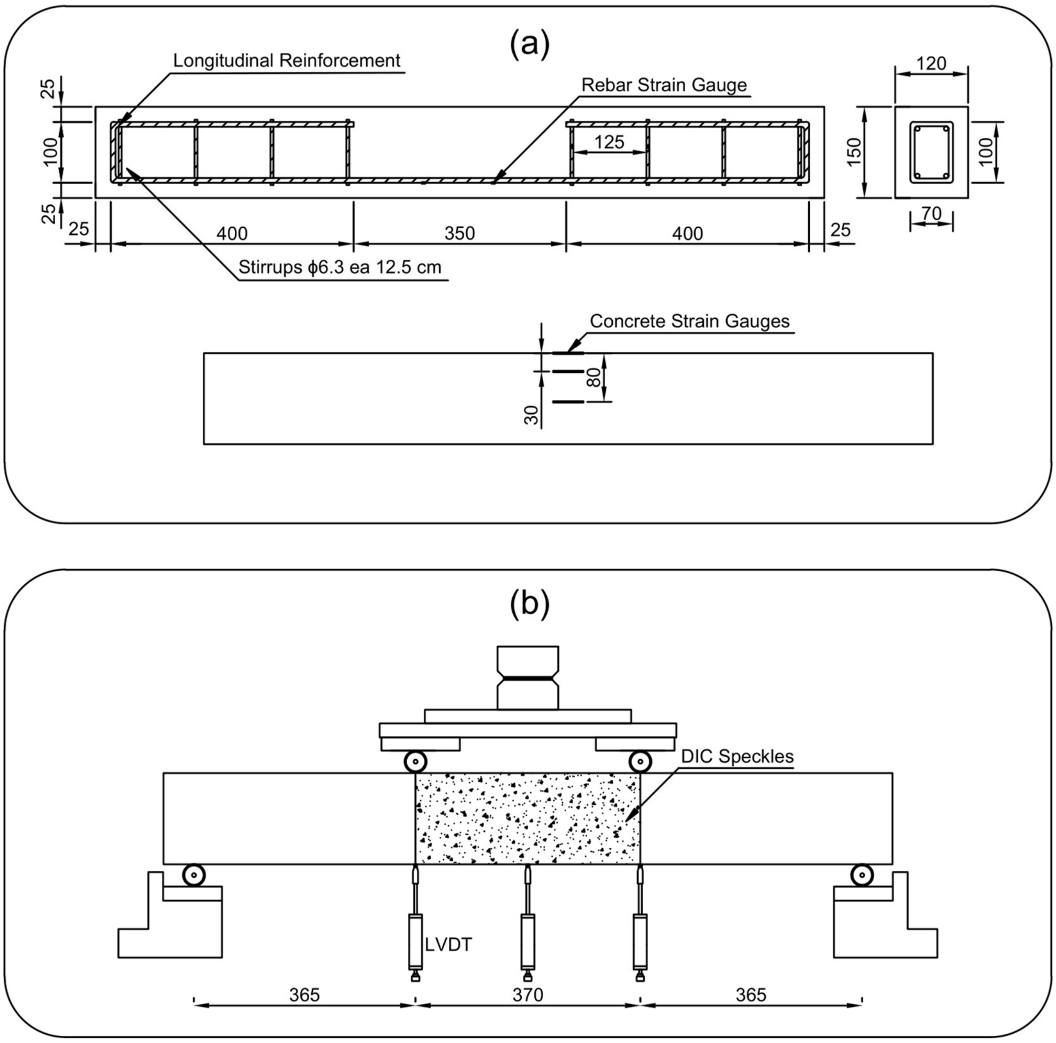

Figure 7.1 - Structural tests setup illustration: (a) beam reinforcement configuration and strain gauge positions and (b) tests setup with LVDTs disposal. Dimensions in mm.

7.2.3.2. Structural fatigue tests

The structural fatigue tests were carried out with the same beam geometry, testing machine, setup and instrumentation as described in the previous section. The fatigue tests were performed having as a reference the longitudinal rebar yield strain and strength, which was around 2400 µm/m and 500 MPa, respectively. Two load levels (S) were analyzed in this work ($\sigma_s{}^* = S \times \sigma_y$): 50% and 80%. While σ_y is the rebar yielding strength, $\sigma_s{}^*$ is the measured pre-crack rebar stress. The load level can be defined as the percentage of rebar yielding strength recorded through the strain gages attached on the steel bars, since the steel stress can be verified by multiplying the strain by the material modulus (210 GPa). The beams were first slowly pre-loaded at 0.10 mm/min rate until reaching the following pre-crack steel strain levels (ε_s*): 1900 μm/m ($S = 80\%$) and 1200 μm/m ($S = 50\%$). After reaching the pre-determined steel strain level, the pre-crack flexural load (P*) was recorded from the machine load cell and the beam was completely unloaded. Figure 7.3(a) illustrates the testing procedure carried on in this research.

Thereafter, the fatigue test starts off controlled by the actuator load cell. The beams were cycled between the maximum (P_{upp}) and minimum (P_{low}) forces in a sinusoidal form. The maximum load was set approximately equal to the force recorded during the pre-crack stage ($P_{upp} = P^*$) and the minimum force was defined as 30 % of P_{upp} ($P_{low} = 30\%P_{upp}$). All tests were carried on at 6 Hz frequency along the time, as illustrated in figure 7.3(b). The tests were terminated when the studied specimen either reached failure or 1,000,000 cycles (run-out), which is in accordance with previous works in fatigue cementitious composites [26, 28]. The complete test instrumentation (gauges, LVDT displacements, cycles number) was connected to a HBM data acquisition device, which stored the collected data at a 1024 points per second rate. The data was acquired every 30 minutes of test time for 30 seconds straight.

Figure 7.2 – Structural test setup photo.

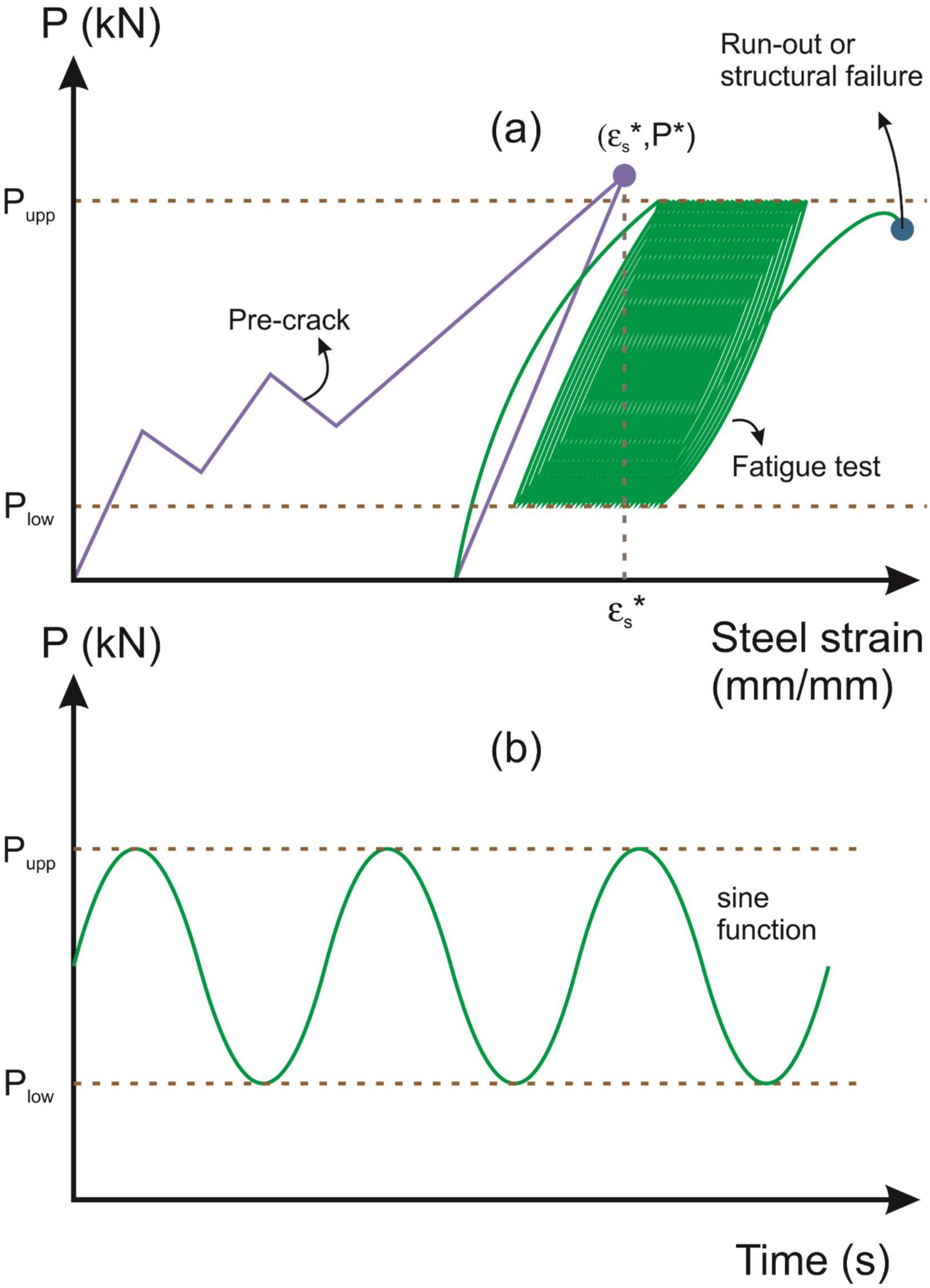

Figure 7.3 - Fatigue test program: (a) test stages (pre-crack and fatigue loading) and (b) loading oscillation based on a sine function.

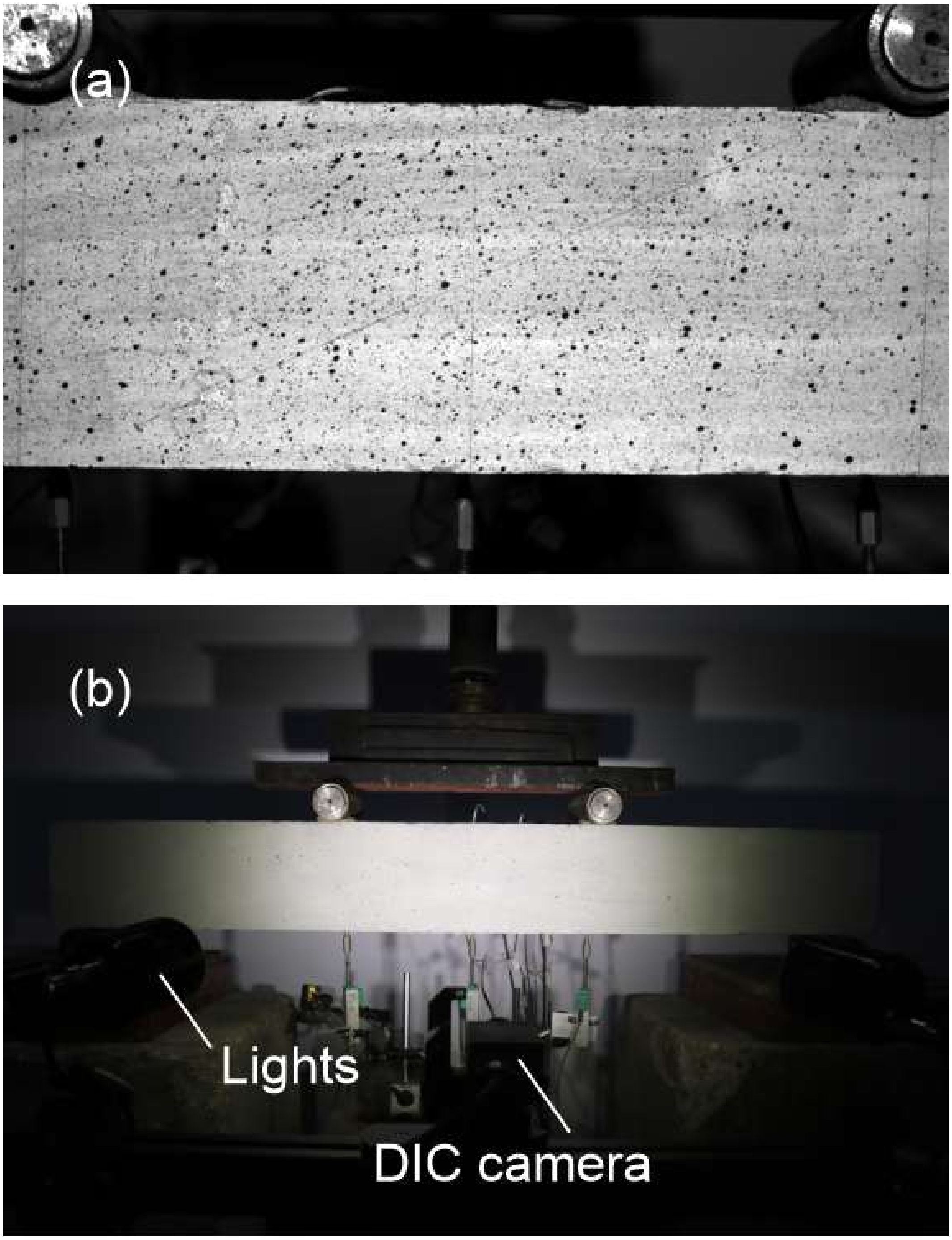

Figure 7.4 - Digital image correlation system: (a) spackle pattern on the beam surface and (b) camera and lights position.

7.2.3.3. Digital image system (DIC)

The cracking behavior was analyzed by digital image correlation (DIC), which allows to quantify full-filed deformations without physical contact [63]. The beams specimens' surface was, first, painted to create a speckle pattern with the use with a standardized paint roller. Figure 7.4(a) brings the applied spackle patterns in one of the tested beams. The system included one high speed camera, model FASTCAM Nova S12 12-bit monochrome 36-bit color with maximum 8GB of memory by Photron manufacturer. A 60 mm AF Micro-Nikkor lens was attached to the camera. The image acquisition was controlled by the Correlated Solution's Vic-Snap 9 software in a 1000 Hz capture frequency. Figure 7.4(b) brings the prepared DIC setup. The system was triggered in two distinct moments: 5 minutes and 24 hours (around cycle number 500,000) after the beginning of the cyclic test. The system captured 5000 frames for each trigger.

7.3. Discussion and analysis

7.3.1. Quasi-static mechanical response

Figure 7.5 shows the overall results from the quasi-static structural tests for both plain and steel fiber reinforced concretes. While figure 7.5(a) shows the force as a function of deflection response, figure 7.5(b) show the moment vs. curvature curves. The complete results for the quasi-static tests can be analyzed in table 7.4, which were divided in terms of the first matrix crack ($\varepsilon_{c,cr}$, $\varepsilon_{s,cr}$, ϕ_{cr}, P_{cr}, M_{cr}, δ_{cr}) and in terms of the yielding values ($\varepsilon_{c,y}$, $\varepsilon_{s,y}$, ϕ_y, P_y, M_y, δ_y). While deflections were verified by the mean values recorded by the three used LVDTs, the curvature was obtained by dividing the strains at the top and at the rebar by the vertical distance between them, as shown in equation 7.1. Both beams exhibited a typical behavior, characterized by a linear stage until matrix first crack. Thereafter, the cracked structure deflects up to rebar yielding strain, which presents a slightly post-ascendant post-yielding branch.

$$\emptyset(n) = \frac{\varepsilon_s(n) + |\varepsilon_s(n)|}{h_0} \tag{7.1}$$

Where ϕ is the curvature, ε_s is the rebar strain, ε_c is the top concrete strain, h_0 is the distance from beam top surface to rebar localization and n is the cycle number.

The addition of steel fibers positively affected the RC structures in all studied mechanical parameters. The R/SFRC beams showed improvements especially in the context of yielding strength, first crack load and rate of stiffness. Moreover, it is possible to observe that the maximum load levels are associated with significantly lower mid-span deflection. The decrease in deflections is associated with a lower rate of stiffness degradation with the fiber addition [46, 47, 64]. After the matrix rupture, steel fibers work to contain crack opening during the structure quasi-static loading, which helps to clarify the significant increase in stiffness after cracking and the rise in the yielding strength.

Table 7.4 - Overall results for structural beams under quasi-static flexural loading

Mix	$\varepsilon_{c,cr}$ µm/m	$\varepsilon_{s,cr}$ µm/m	δ_{cr} mm	ϕ_{cr} x1000/m	P_{cr} kN	M_{cr} kNm	$\varepsilon_{c,y}$ µm/m	$\varepsilon_{s,y}$ µm/m	δ_y mm	ϕ_y x1000/m	P_y kN	M_y kNm
C0SF	-140	134	0.42	2	12.1	2.1	712	2512	3.9	26.2	23	4
C40SF	-211	203	0.61	4.1	14.4	2.8	582	2489	4.5	27.6	31.1	5.5

‘cr’ = value at first matrix crack
‘y’ = value at rebar yielding
ε_c = *concrete strain*
ε_s = *rebar strain*
δ = *deflection*
ϕ = *curvature*
P = *load*
M = *moment*

Figures 7.5(c) and 7.5(d) show the cracking response of the structural beams with plain and steel fiber reinforced concretes, respectively. When it comes to crack formation along the beam deformation, RC structures presented cracks regularly spaced over the constant moment region. Moreover, after rebar yielding, the observed cracks keep growing equally until reaching the structural failure. On the other hand, R/SFRC beams exhibited close thin cracks formation and, after yielding, one major crack began to control the overall crack formation, which leaded to a non-uniform curvature distribution, similar to what was observed by Dancygier *et al.* for quasi-static tests [65]. The crack formation response helps to explain the overall mechanical behavior of the structural behavior of the studied beams and will be key to the analysis of structural fatigue tests in the next sections. The significant enhancement on the mechanical performance with fiber addition will also take place when verifying stiffness degradation and crack opening oscillation along the fatigue cycles.

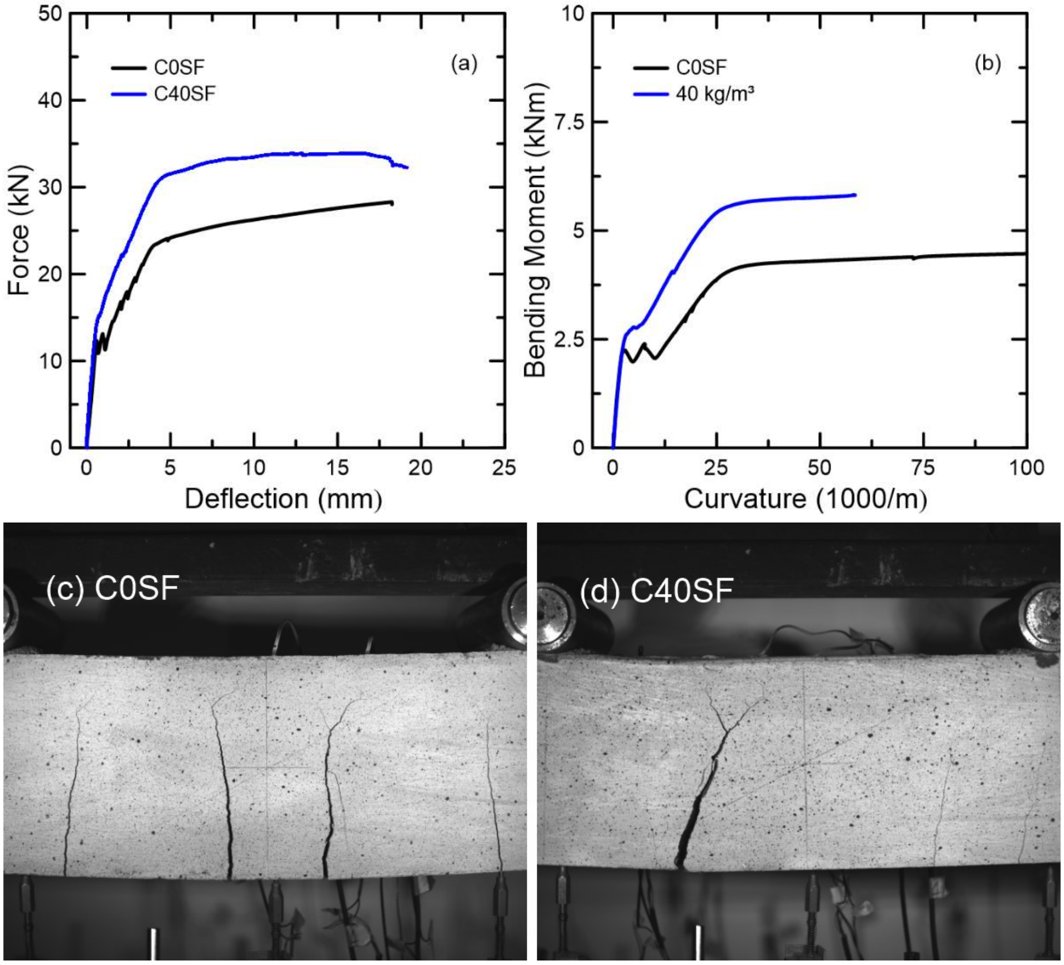

Figure 7.5 - Monotonic structural bending tests results: (a) force x deflection, (b) moment x curvature. Cracking response after rebar yielding for (c) C0SF and (d) C40SF.

7.3.2. Fatigue mechanical degradation

7.3.2.1. Rebar strain evolution

Figure 7.6 compares the longitudinal rebar reinforcement strain evolution for plain (C0SF) and steel fiber (C40SF) reinforced concretes. Both structural beams were subjected almost to the same loading range. While R/SFRC beam was pre-cracked until *S = 50%* of the yielding strain (~1200 μm/m), the reinforced concrete beam was pre-loaded up to *S = 80%* (~1900 μm/m). Figures 7.6(a) and 7.6(b) show the also the quasi-static curve in order to verify the monotonic pre-loading before the cycling phase. Each hysteresis cycle corresponds to a cycle number along the fatigue test. Although the beam shown in figure 7.6(a) reached failure after 935,022 cycles, the R/SFRC beam in figure 7.6(b) reached the test end (run-out) at 1,000,000 cycles. Table 7.5 summarizes all collected fatigue data.

The addition of steel fibers on the matrix composition promotes a significant influence on the rebar strain evolutions of RC structures. When comparing the same loading range, R/SFRC beams reported a significant lower strain value at the first strain cycle. While C0SF structures reported a rapid and higher strain increase along the fatigue life, C40SF beams presented a much more modest and slower strain evolution throughout the cycles. This can be attributed to the bridging effect of the steel fibers in the tensile region of the reinforced structure that are very effective in reducing the stress range of the tensile reinforcement. Therefore, it is possible to verify that the rise in the yielding strength by fiber addition observed on the quasi-static tests already indicated the potential gain in fatigue life and in reducing the steel strain evolution.

The strains of the tensile steel bar observed in the maximum fatigue load levels present similar trend. The strains increase rapidly in the initial stage, which constituted approximately 10% of the fatigue life, followed by a constant low growth rate. Figure 7.7 summarizes the overall strain evolution under distinct fatigue loading ranges for plain and steel fiber reinforced concrete beams. During almost a linear increase of strain through cyclic loading, the fatigue induced degradation of the beam was primarily caused by the tensile steel bar yielding after continuous damage accumulation along the cycles. The flexural failure of the beams was observed when the applied maximum fatigue load was around 80% of the rebar yielding strength ($S = 80\%$).

For the studied plain and steel fiber reinforced concrete beams, the strain evolution increased in a very similar rate when the same maximum loading level (S) was studied. As explained earlier, the fatigue load level (S) was defined as the ratio of the applied fatigue stress by the respective yielding strength of the longitudinal rebar ($\sigma_s{*} = S \ x \ \sigma_y$). Therefore, future models to verify rebar strain evolution under fatigue may be developed to calculate fatigue degradation of the other mechanical parameters.

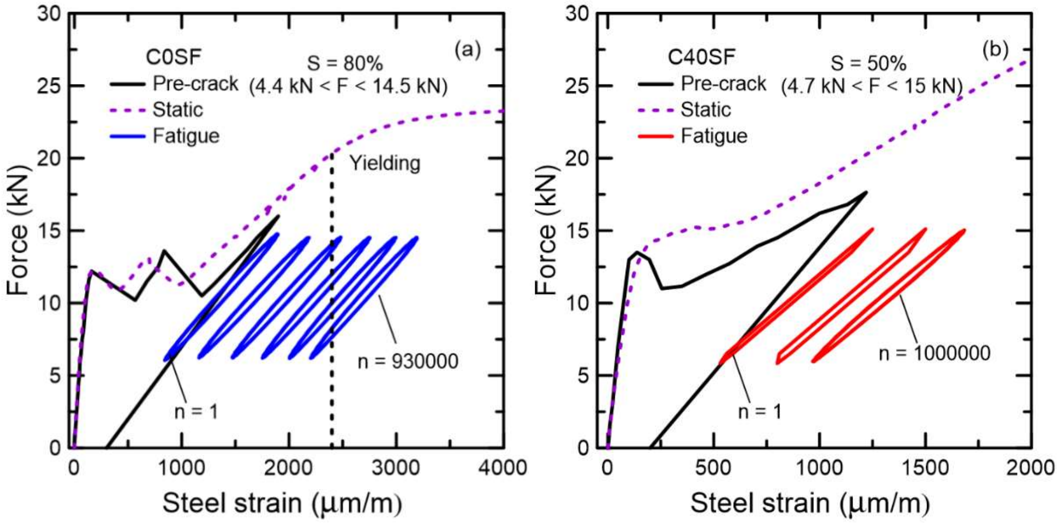

Figure 7.6 - Fatigue longitudinal rebar strain evolution, quasi-static and pre-crack results for (a) C0SF and (b) C40SF under the same fatigue loading range.

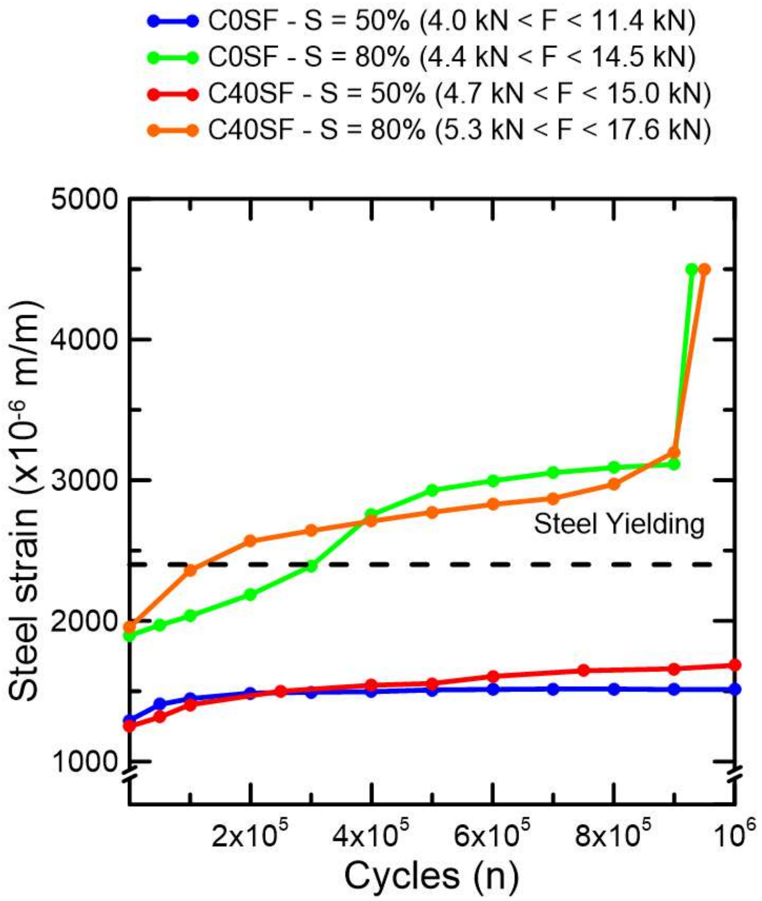

Figure 7.7 - Fatigue longitudinal rebar strain evolution under fatigue loading for C0SF and C40SF under distinct loading ranges.

Table 7.5 - Structural beam fatigue test results.

Mix	Pre-crack				Fatigue					
	S	ε_s*	σ_s*	P*	$\Delta\varepsilon_s$	$\Delta\sigma_s$	P_{upp}	P_{low}	*Cycles to failure*	*Failure mode*
	$\sigma^* = S \times \sigma_y$	µm/m	MPa	kN	µm/m	MPa	kN	kN	-	-
C0SF	50%	1200	252	11.4	680	140	11.4	4	1,000,000	Run-out
C0SF	80%	1900	400	14.5	1000	210	14.5	4.4	935,022	Steel yielding
C40SF	50%	1200	252	15	680	140	15	4.7	1,000,000	Run-out
C40SF	80%	1900	400	17.6	1000	210	17.6	5.3	955,000	Steel yielding

S = load level as percentage of rebar yielding strength

ε_s* *= pre-crack strain level recorded at the rebar*

σ_s* *= pre-crack stress level recorded at the rebar*

P = pre-crack flexural load*

$\Delta\varepsilon_s$ *= steel strain range*

$\Delta\sigma_s$ *= steel stress range*

P_{upp} *= maximum fatigue force*

P_{low} *= minimum fatigue force*

7.3.2.2. Deflection evolution

Figure 7.8 compares deflection evolution for plain (C0SF) and steel fiber (C40SF) reinforced concretes. Similar to the analysis carried on strain increase, the displayed results in figures 7.8(a) and 7.8(b) were subjected to approximately the same loading range to verify the fiber influence on the fatigue mechanical degradation. As expected by the results achieved on the rebar strains, steel fibers were very effective in reducing the deflection levels when analyzing the same force range. The steel fibers effectively contribute in enhancing the structure stiffness after concrete cracking, resulting in lower levels of deflection.

On the other hand, when comparing the C0SF and C40SF at the same steel yielding levels (*S = 50%* and *S = 80%*), the rate of deflection evolution under fatigue is not as comparable as the one observed in the previous section. Figure 7.9 shows the overall results for deflection evolution under the distinct steel yielding levels. The differences on the deflection values under the rebar stress levels can be attributed to differences on the structure flexural modulus. As shown on the analytical displacement solutions for statically determinate beams by Yao *et al.* [50], the deflections are dependent to a higher number of mechanical parameters such as the material modulus and the critical cracking moment. Moreover, for *S* =

50%, the R/SFRC are still subjected to higher loading ranges as shown in figure 7.9 and table 7.5, which also play a major influence on the displacement values.

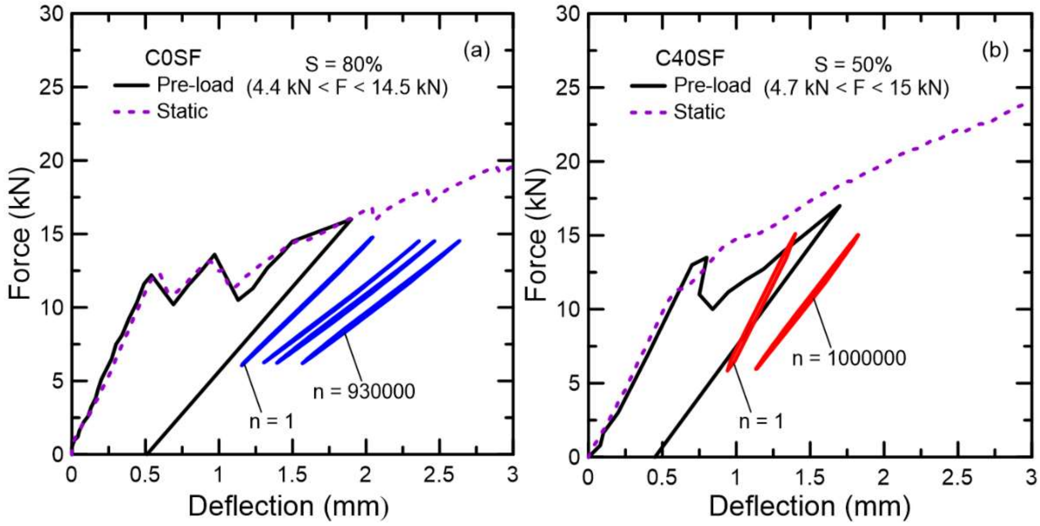

Figure 7.8 - Beam deflection evolution, quasi-static and pre-crack results for (a) C0SF and (b) C40SF under the same fatigue loading range.

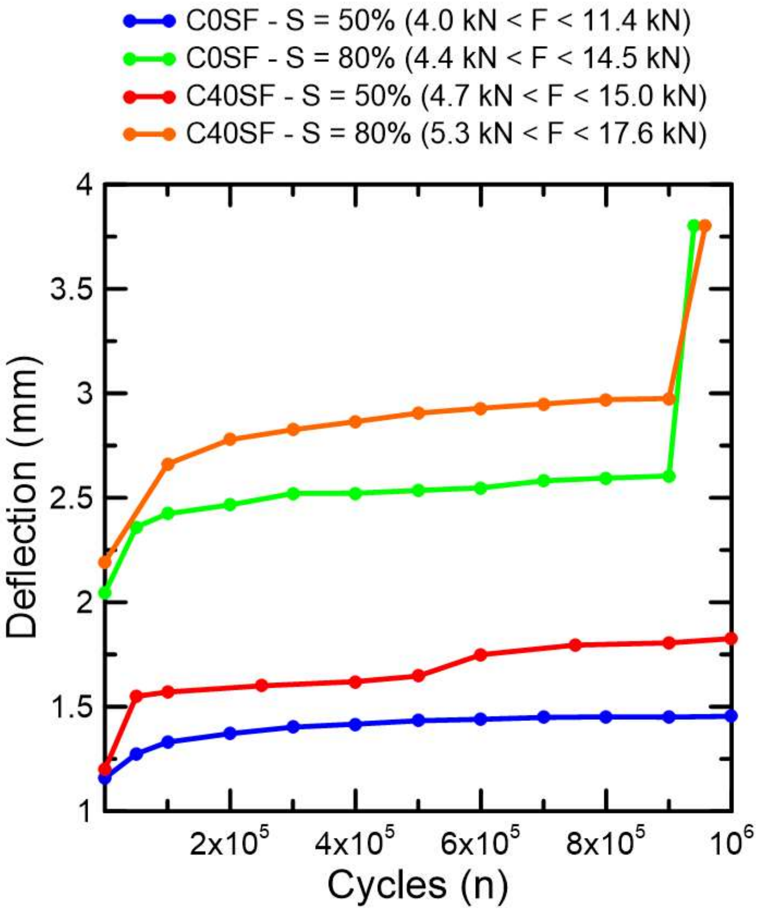

Figure 7.9 - Beam deflection evolution under fatigue loading for C0SF and C40SF under distinct loading ranges.

7.3.2.3. Curvature evolution

Figure 7.10(a) illustrates the employed methodology to verify the curvature evolution along the fatigue cycles. The curvature was calculated through equation 1. The curvature evolution was evaluated on the middle beam section, since the concrete gauges were situated exactly at the half of the beam span. The curvature was calculated for each fatigue loading cycle. Figures 7.10(b) and 7.10(c) compare the strain distributions along the beam section for C0SF and C40SF reinforced concrete beams under the same fatigue loading range. The addition of fibers significantly reduced the strain along the beam height. The use of fiber is especially effective in redistributing the strain in the traction zone and, consequently, reducing strains on the rebar. It is also possible to verify in figure 7.10(b) and 7.10(c) higher values of the neutral axis for SFRC/R beams, as defined in figure 7.10(a). The influence of fiber addition on the neutral axis, corroborates the idea of the fiber reinforcement capacity to contain crack propagation along the cracked section as observed in previous works [65-69].

Figure 7.11 summarizes all results for curvature evolution for C0SF and C40SF structural beams. The curvature increase along the fatigue cycles present very similar trend in relation to the rebar strain shown in figure 7.7, which indicates that the concrete deformation on the compressive region did not play a major role on the curvature increase. The resulting curvature is very dependent on the overall beam reinforcement design and the applied structural reinforcement ratio as shown in previous works [67, 70, 71]. Hence, a further analysis considering distinct reinforcement configurations could be carried on in a following fatigue experimental campaigns in structural members. Moreover, the influence of fiber addition definitely will bring distinct results depending on the rebar location along the beam section. The studied beam configuration was manufactured with very low reinforcement ratio aiming to maximize the fiber influence on the beam fatigue deterioration.

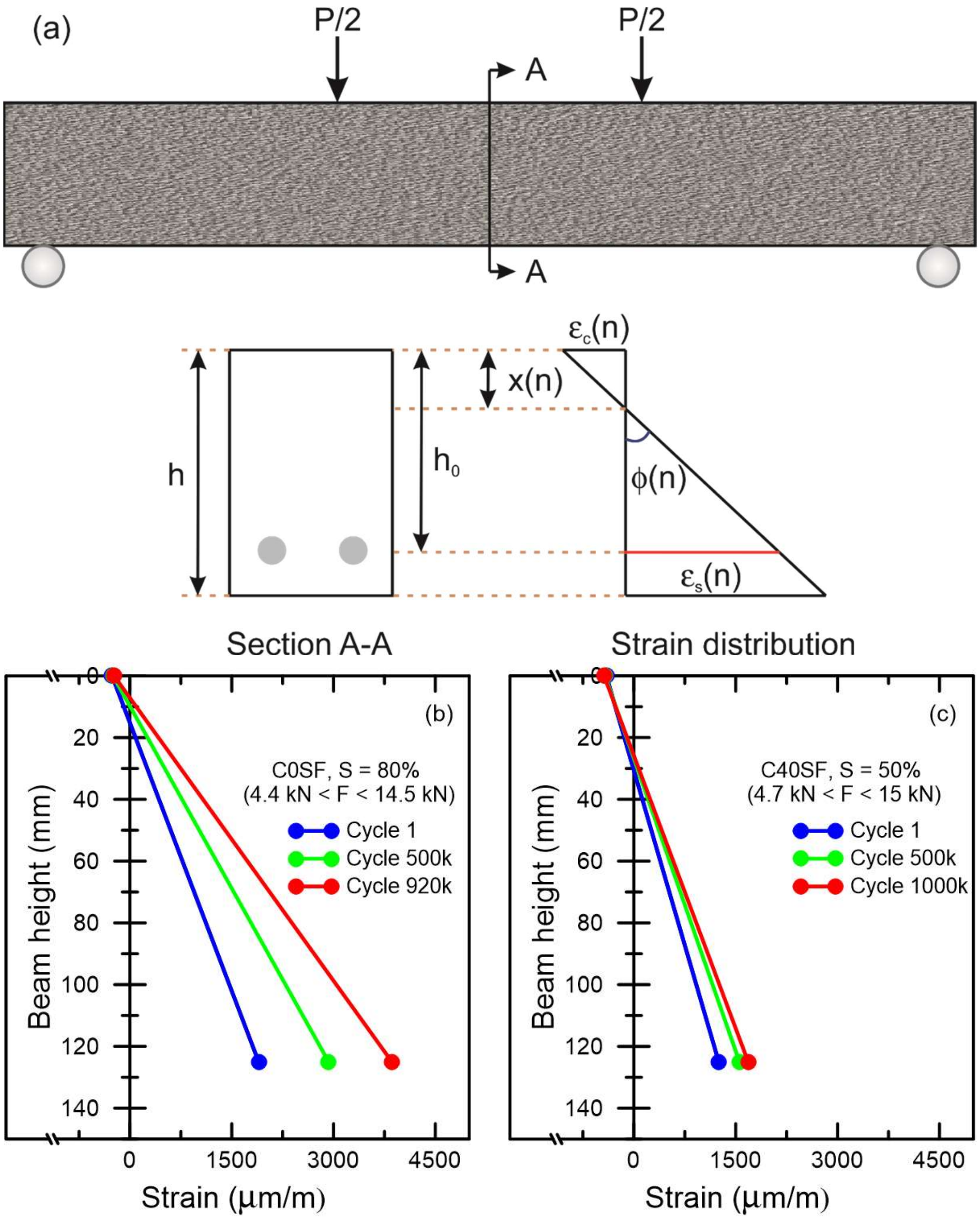

Figure 7.10 - Beam curvature evolution, quasi-static and pre-crack results for (a) C0SF and (b) C40SF under the same fatigue loading range.

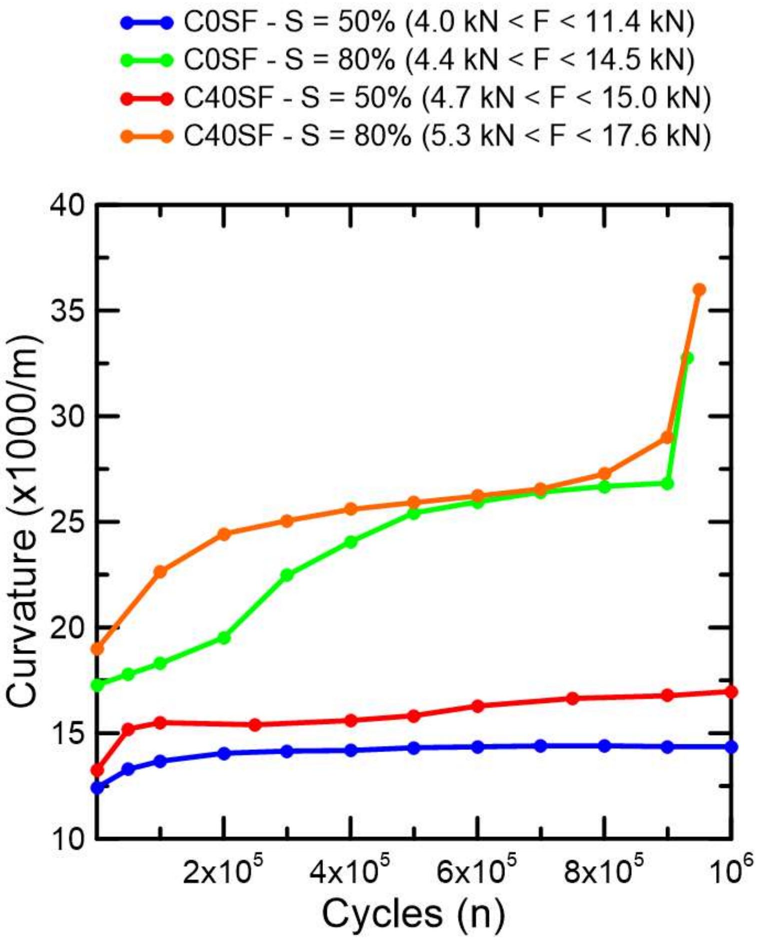

Figure 7.11 - Beam curvature evolution under fatigue loading for C0SF and C40SF under distinct loading ranges.

7.3.2.4. Stiffness degradation

Figure 7.12 illustrates the methodology for stiffness calculation in each fatigue hysteresis cycle along the time. For each cycle, the flexural stiffness was evaluated the ratio between the applied fatigue loading by the measured deflections on the LVDTs of the hysteresis cycle. The capacity of structural members to conserve its stiffness along the fatigue cycles is one of the main parameters to verify the mechanical degradation under fatigue loading and is a key factor when it comes to serviceability analysis. Moreover, the main published works in the literature [56, 57] about fatigue stiffness degradation of R/SFRC beams has still not brought this analysis.

Figure 7.13 brings the stiffness decay for C0SF and C20SF reinforced concrete beams under the fatigue loading for distinct testing conditions. When it comes to the analysis of stiffness in fatigue degradation, R/SFRC reported massive increase in stiffness when verifying the same fatigue loading range. While C0SF mix composition under *S = 80%* yielding stress level presented approximately 10 kN/mm along the fatigue life, C40SF in the same fatigue loading range resulted in almost 20 kN/mm. The capacity of increasing matrix post-crack stiffness has already been verified in the literature in quasi-static loading studies [46, 47, 72]. Based on the presented results, the same phenomena can be affirmed in cyclic loading. The increase in stiffness is directly linked to fiber capacity in crack control in cementitious composites in tension as also observed elsewhere [69, 70].

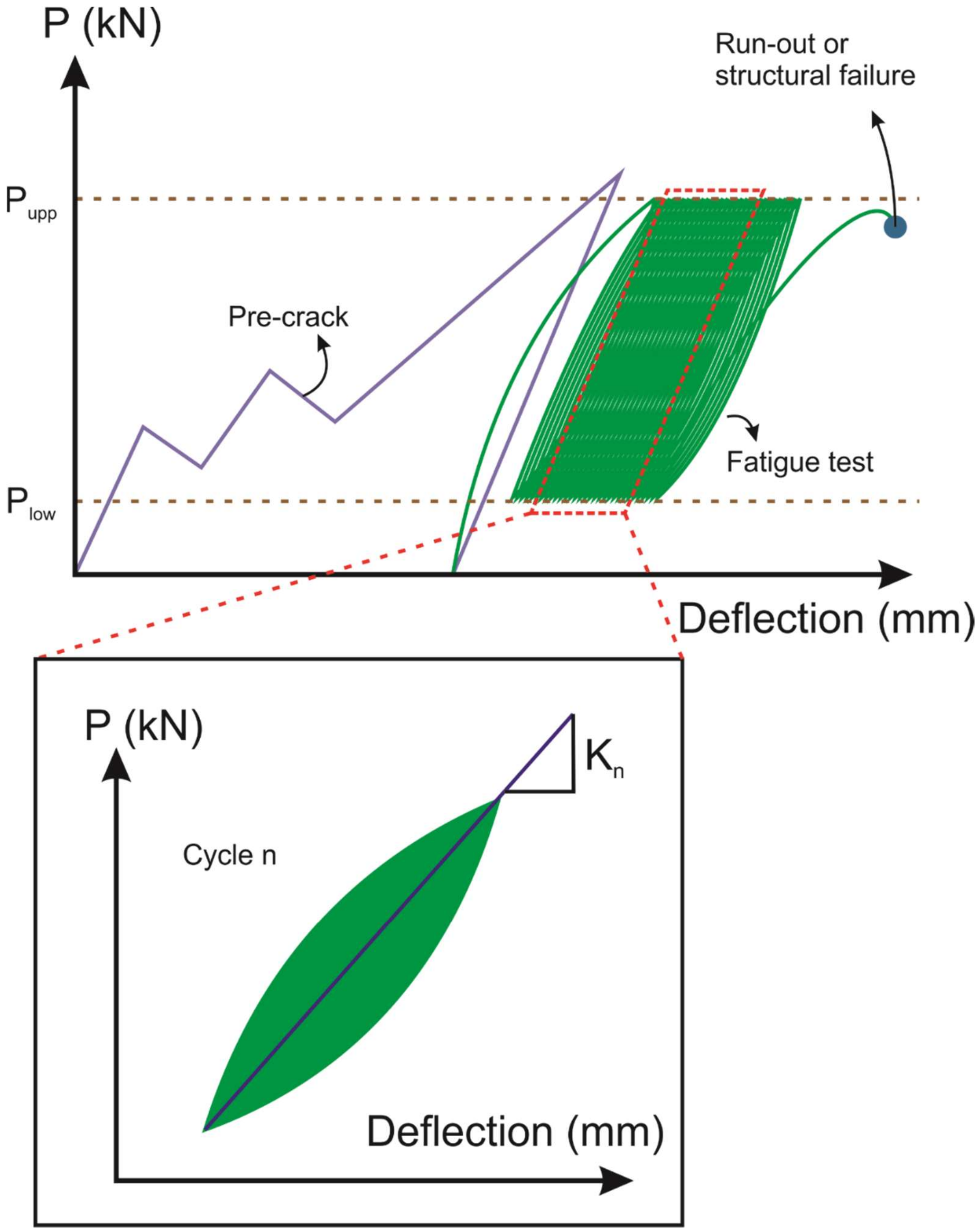

Figure 7.12 - Illustration for beam stiffness calculation for each cycle.

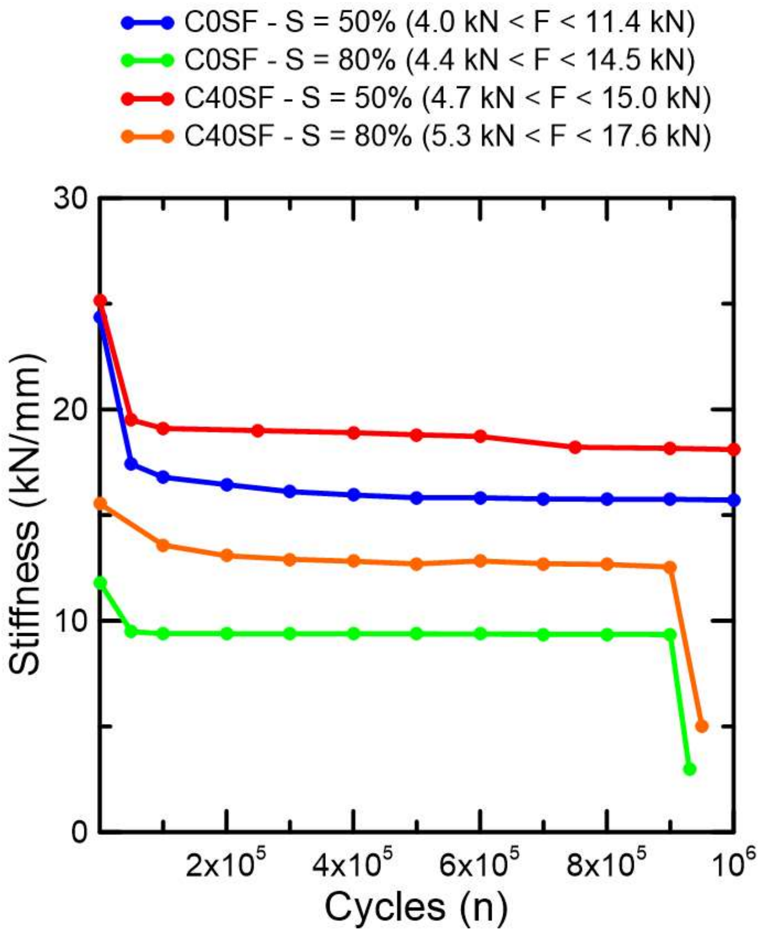

Figure 7.13 - Beam stiffness evolution under fatigue loading for C0SF and C40SF under distinct loading ranges.

7.3.3. Crack opening oscillation under fatigue loading

Figure 7.14(a) shows the analyzed DIC image from the C0SF reinforced concrete beam under fatigue loading at *S = 80%* yielding stress level. The value of 3.1 mm was the maximum crack opening recorded through the high speed cameras. Figure 7.15 shows the crack opening oscillation after 500,000 cycles of the fatigue test along 0.50 seconds span. Figure 7.14(b) displays the beam surface after rupture of the structure at the end of the fatigue tests. The same failure mode was observed for C0SF and C40SF beams under fatigue loading at *S = 80%* yielding stress level.

When comparing C0SF and C40SF under the same fatigue range in figure 7.15, the addition of fibers was very effective in reducing crack openings during the fatigue cycles. While RC beams reached a peak of around 0.30 mm of crack opening, R/SFRC structures presented a maximum value of approximately of 0.10 mm. It is already recognized that cracks provide easy access to chloride and other chemical agents in concrete, promoting the corrosion and the degradation of both the steel reinforcement and the cementitious matrix [73-75]. In accordance with the analyzed results, the fiber addition can be employed as an effective approach to promote the structure durability along the time. A diverse number of RC structures, such as offshore platforms, wind towers and bridge girders, is subjected to cyclic loading along their service life and is usually located in harsh environments. Hence, the addition of fibers on the concrete mix could bring great gains in terms of mechanical performance, but also in durability.

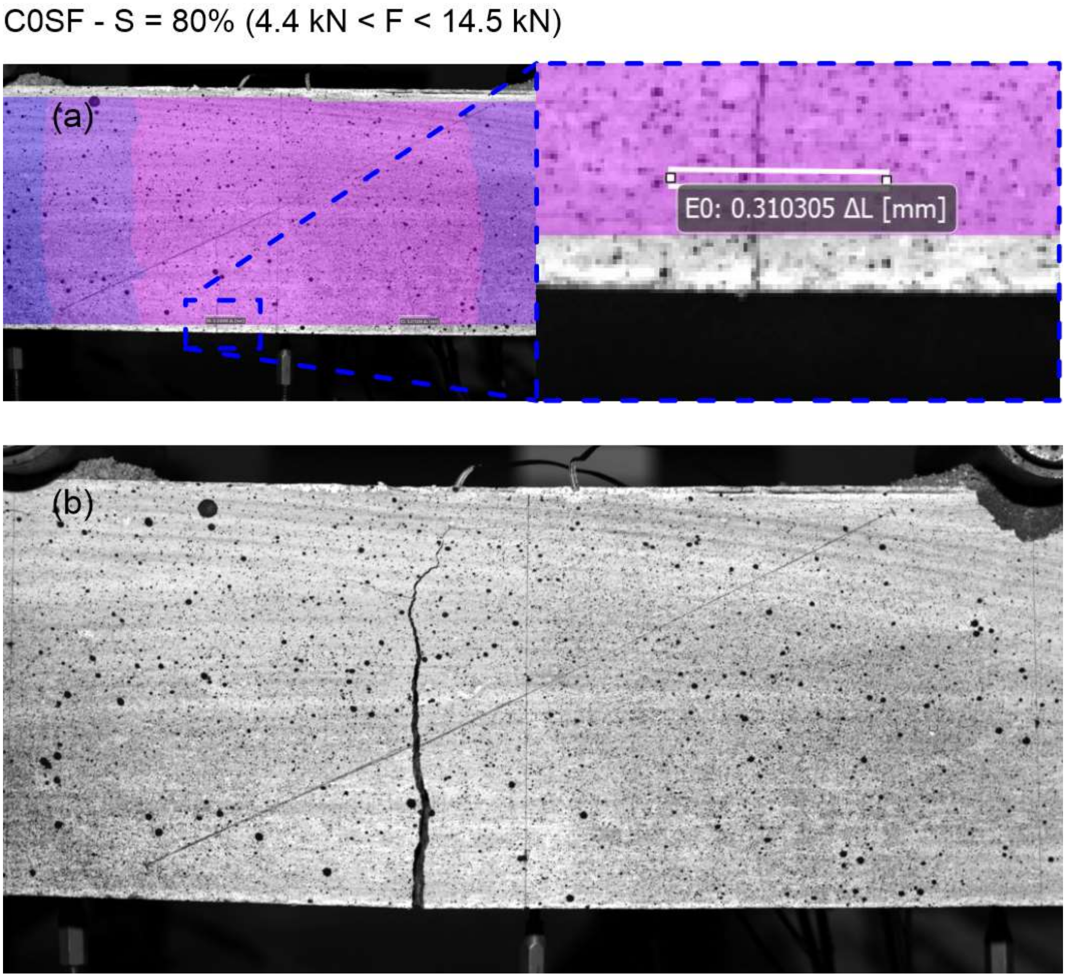
C0SF - S = 80% (4.4 kN < F < 14.5 kN)

Figure 7.14 - Application of the DIC analysis to verify the crack opening variation along the fatigue cycles during a 5 s time frame: (a) maximum observed crack opening during the load cycles at the cycle number 500,000 and (b) failure surface at the end the fatigue test.

Figure 7.14(b) shows a distinct failure mode of C0SF beams under fatigue when compared with the quasi-static failure shown in figure 7.5(a). While under quasi-static loading the RC beams multiple cracks are formed, only one major crack controls the failure mode in the fatigue tests. The growth of one major crack reveals that fatigue rupture is controlled by the stress concentrations of the tensile bars at the crack location of the beam. The fatigue damage is slowly accumulated at the rebar until it reaches its yielding strain and reaches failure along the fatigue cycles. Similar response was also reported by Gao *et al.* [56] during its experimental program.

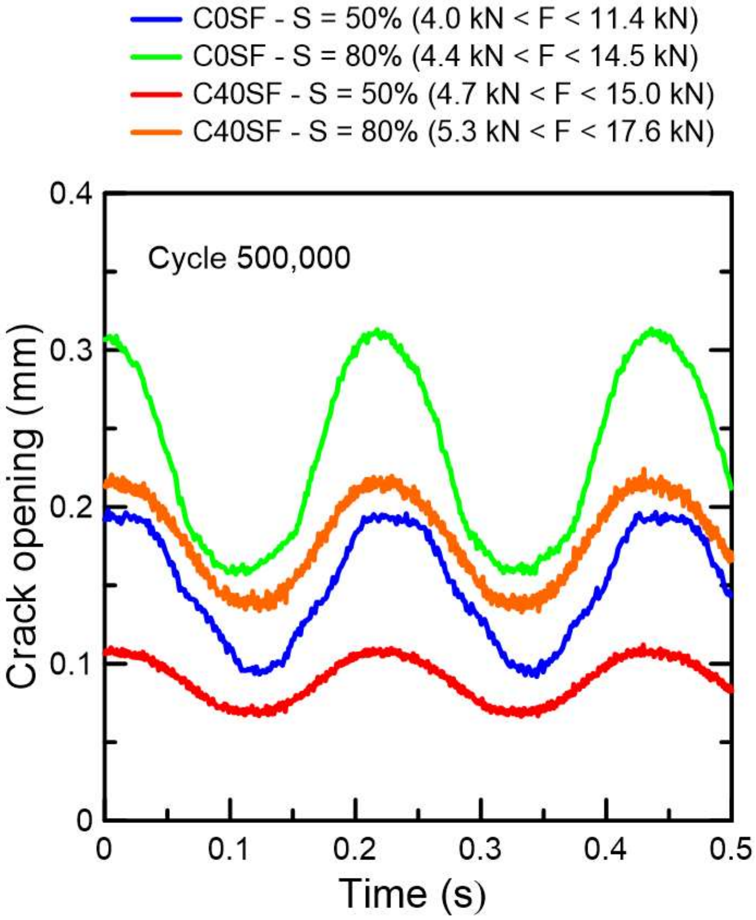

Figure 7.15 - Crack opening variation for the cycle number 500,000 C0SF and C40SF under distinct loading ranges.

7.3.4. Fatigue life of R/SFRC beams

Figure 7.16 brings the observed fatigue life of reinforced concrete beams under fatigue loading in terms of the measured rebar stress range. The plotted graph summarizes the results from Papakonstantinou *et al.* [55], Gao *et al.* [56], Parvez *et al.* [57] and the achieved results for present research. The dotted line responds for the proposed model code [17] equation for the rebar fatigue curve under tension. The details from plotted values in figure 7.16 can be analyzed in table 7.6. Both plain and steel fiber reinforced concrete structural beams are encompassed on the fatigue results in figure 7.16.

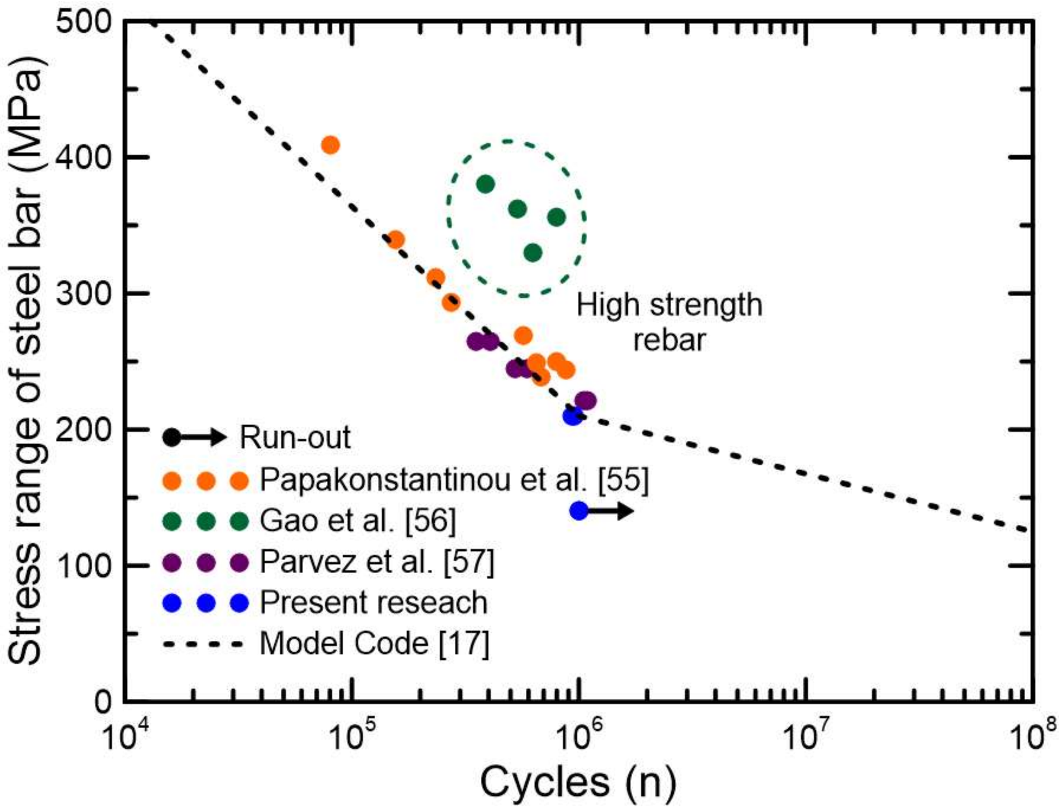

Figure 7.16 - Fatigue life of reinforced concrete beams under fatigue loading as a function of the rebar stress range.

It is possible to verify that the proposed equations for the rebar fatigue from the model code can successfully estimate the fatigue service life from the reinforced concrete structures. Therefore, the measured steel bar stress range from the reinforced concrete beams is responsible to control the overall fatigue behavior and service life of the structure. Moreover, as observed earlier in this work, the rebar strain evolution under fatigue loading is a key parameter for the analysis of the structure degradation and can be used to develop future analytical models in reinforced concrete structures. Since Gao *et al.* [56] studied a special high strength rebar, it did not fit the proposed model code equation for rebar fatigue life.

Table 7.6 - Collected fatigue life data for plain and steel fiber reinforced concrete structural beams under fatigue loading

Author	ϕ (mm)	σ_y (MPa)	V_f (%)	$\Delta\sigma_s$ (MPa)	P_{upp} (kN)	P_{low} (kN)	*Cycles to failure* -	*Failure mode* -
Papakonstantinou *et al.* [55]	12	427	0	249	40	3	650000	Steel yielding
Papakonstantinou *et al.* [55]	12	427	0	294	44	3	275000	Steel yielding
Papakonstantinou *et al.* [55]	12	427	0	339	53	3	155000	Steel yielding
Papakonstantinou *et al.* [55]	12	427	0	409	62	3	80000	Steel yielding
Papakonstantinou *et al.* [55]	12	427	0	239	45	3	685000	Steel yielding
Papakonstantinou *et al.* [55]	12	427	0	244	47	2	880000	Steel yielding
Papakonstantinou *et al.* [55]	12	427	0	250	49	4	800000	Steel yielding
Papakonstantinou *et al.* [55]	12	427	0	269	53	3	570000	Steel yielding
Papakonstantinou *et al.* [55]	12	427	0	312	58	3	235000	Steel yielding
Gao *et al.* [56]	12	585	0	380	107	17.9	387415	Steel yielding
Gao *et al.* [56]	12	585	0.5	362	111	18.5	533466	Steel yielding
Gao *et al.* [56]	12	585	1	356	117	19.6	799389	Steel yielding
Gao *et al.* [56]	12	585	1.5	330	122	20	625300	Steel yielding
Parvez *et al.* [57]	12	500	0	265	74	21	351530	Steel yielding
Parvez *et al.* [57]	12	500	0.4	245	74	21	591959	Steel yielding
Parvez *et al.* [57]	12	500	0.8	221	74	21	1092535	Steel yielding
Present research	6.3	500	0	140	11.4	4	1,000,000	Run-out
Present research	6.3	500	0	210	14.5	4.4	935,022	Steel yielding
Present research	6.3	500	0.5	140	15	4.7	1,000,000	Run-out
Present research	6.3	500	0.5	210	17.6	5.3	955,000	Steel yielding

ϕ = *rebar diameter*
σ_y = *rebar yielding strength*
V_f = *fiber volume fraction*
$\Delta\sigma_s$ = *steel stress range*
P_{upp} = *maximum fatigue force*
P_{low} = *minimum fatigue force*

The addition fibers also modify significantly the fatigue life of RC beams, as shown in table 7.6. Based on the present results and the works of Gao *et al.* [56] and Parvez *et al.* [57], the R/SFRC beams were responsible for reducing the measured rebar strains, promoting a significant increase in the structural fatigue life. At the same flexural loading range, the addition of fibers reduced from 210 MPa to 140 MPa the measured rebar stress range in this work. The stress redistribution in the traction zone of the concrete section, due to fiber bridging, entails the observed reduction on the steel strains and reduces the structure mechanical degradation rate along the time. Therefore, it is possible to verify that the addition of fibers is significantly effective in extending the overall structural service life under fatigue.

7.4. Conclusions

The present research brings an overall analysis of the fatigue mechanical degradation of RC structures under flexural fatigue loading. The main focus of the experimental program is to verify the potential gain in the mechanical performance of structural RC beams by the addition of steel fibers in reducing the mechanical deterioration of the structural members under cyclic loading. The structural degradation was evaluated in terms of rebar strain evolution, curvature increase along the cycles, stiffness degradation and deflection enhancement. A high speed camera was used to monitor crack opening oscillation after 500,000 fatigue cycles, which was key to evaluate the structure failure mode after the fatigue test. The fatigue life was also analyzed as function of the rebar stress variations. The following conclusion are achieved from the research:

- The addition of steel fibers on the matrix composition promotes a significant influence on the rebar strain evolution of RC structures. When comparing the same loading range, steel fiber reinforced concrete structural beams reported much lower strain values along the fatigue test. The fibers showed a very effective capacity to redistribute the stresses in the traction zone and, consequently, reducing the measured strains on the longitudinal reinforcement. Therefore, the rise in the yielding strength by fiber addition on the quasi-static tests can be used as a key parameter to evaluate the potential gain in the structural fatigue life and on the reduction of mechanical degradation of plain concrete beams.

- Similar mechanical deterioration was observed when it comes to the analysis of deflection and curvature evolution along the fatigue test. The rate of mechanical deterioration is linked to the applied stress levels. Moreover, the addition of fibers enables to the structural beam to reach higher load ranges, when compared with conventional RC structures. Due to the present analyzed beam geometry and rebar reinforcement, it was not possible to verify a major decay of concrete on the compressive stress zone. Both curvature and deflection were majorly controlled by the rebar strain evolution along the fatigue life due to the low reinforcement ratio. Future research can bring the influence of other rebar configuration along the beam on the fatigue response.
- The capacity of stiffness retention along the fatigue cycles was also studied in the present experimental program, since it is considered one of the main parameters to verify the mechanical degradation in RC structures. All evaluated beams reported an almost constant stiffness along all the cycles. The stiffness values were directly linked to the applied fatigue levels, since higher stresses are responsible for higher structural deterioration. Moreover, the use of fibers in the concrete mix promoted a significant increase in stiffness of the studied beams under flexural fatigue loading. The increase in stiffness is directly associated to the fiber capacity in controlling crack opening in cementitious composites under tension.
- The digital image correlation system successfully evaluated the crack opening oscillation around the cycle 500,000. It was possible to analyze the crack opening values along a 0.50 second span under a 6 Hz fatigue loading frequency. The lower values of crack opening when fibers were added to the mix support the observed enhancement in mechanical performance throughout the service life. The growth of one main crack reveals that the fatigue rupture was controlled by the stress concentrations in the tensile rebars at the crack location.

7.5. References

1 HOLMEN, J. Fatigue design evaluation of offshore concrete structures. **Matériaux et Construction**, vol. 17, p. 39-42, 1984.

2 BELLETTI, B. CERIONI, R. MEDA, A. PLIZZARI, G. Design aspects on steel fiber-reinforced concrete pavements. **Journal of Materials in Civil Engineering**, vol. 20, p. 599-607, 2008.

3 AGLAN, H. FIGUEROA, J. Damage-evolution approach to fatigue cracking in pavements. **Journal of Engineering Mechanics** (1993), vol. 119, p. 1243-1259, 1993.

4 TIAN, S. ZHANG, X. HU, W. Fatigue analysis of CFRP-reinforced concrete ribbed girder bridge deck slabs. **Polymers**, vol. 14, 2022.

5 SRITHARAN, S. SCHMITZ, G. **Design of tall wind turbine towers utilizing UHPC.** In: RILEM-fib-AFGC International Symposium on Ultra-High Performance Fibre-Reinforced Concrete, 2013.

6 GÖRANSSON, F. NORDENMARK, A. **Fatigue assessment of concrete foundations for wind power plants**. MSc dissertation, 142 p. Göteborg, Sweden: Chalmers University of Technology, 2011.

7 SUBRAMANIAM, K. O'NEIL, E. POPOVICS, J. SHAH, S. Crack propagation in flexural fatigue of concrete. **Journal of Engineering Mechanics**, vol. 126, p. 891-898, 2000

8 SUBRAMANIAM, K. GOLDSTEIN, G. POPOVICS, J. SHAH, S. Fatigue response of concrete subjected to biaxial fatigue in the compression-tension region. **ACI Materials Journal**, vol. 96, p. 663-669, 1999.

9 ZANUY, C. DE LA FUENTE, P. ALBAJAR, L. Effect of fatigue degradation of the compression of concrete in reinforced concrete sections. **Engineering Structures**, vol. 29, p. 2908-2920, 2007.

10 MU, B. SUBRAMANIAM, K. SHAH, S. failure mechanism of concrete under fatigue compressive load. **Journal of Materials in Civil Engineering** (2004), vol. 16, 2004.

11 OH, B. Fatigue-life distributions of concrete for various stress levels. **ACI Materials Journal**, vol. 88, p. 122-128, 1991.

12 SUBRAMANIAM, K. POPOVICS, J. SHAH, S. Fatigue fracture of concrete subjected to biaxial stresses in the tensile C-T region. **Journal of Engineering Mechanics**, vol. 128, p. 668-676, 2002.

13 CHUI, K. XU, L. LI, L. CHI, Y. Mechanical performance of steel-polypropylene hybrid fiber reinforced concrete subject to uniaxial constant-amplitude cyclic compression: fatigue behavior and unified fatigue equation. **Composite Structures**, vol. 311, 2023.

14 GAO, L. HSU, T. Fatigue of concrete under uniaxial compression cyclic loading. **ACI Materials**, vol. 95, p. 575-581, 1998.

15 CUI, K. XU, L. LI, X. HU, X. HUANG, L. DENG, F. CHI, Y. Fatigue life analysis of polypropylene fiber reinforced concrete under axial constant-

amplitude cyclic compression. **Journal of Cleaner Production**, vol. 319, 2021.

16 GAEDICKE, C. ROESLER, J. SHAH, S. Fatigue crack growth prediction in concrete slabs. **International Journal of Fatigue,** vol. 31, p. 1309-1317, 2009.

17 INTERNATIONAL FEDERATION FOR STRUCTURAL CONCRETE. **CEB-FIB**. International Recommendations for the Design and Construction of Concrete Structures, 2010.

18 CACHIM, P. **Experimental and numerical analysis of the behavior of structural concrete under fatigue loading with application to concrete pavements**. Ph.D. thesis, Faculty of Engineering, University of Porto, 1998

19 NAAMAN, A. HAMMOUD, H. Fatigue characteristics of high performance fiber-reinforced concrete. **Cement Concrete Composites** (1998), vol. 20, p. 353-363, 1998.

20 BANJARA, N. RAMANJANEYULU, K. Experimental investigations and numerical simulations on the flexure fatigue behavior of plain and fiber-reinforced concrete. **Journal of Materials in Civil Engineering** (2018), vol. 30, 2018.

21 CHANG, D. CHAI, W. Flexural fracture and fatigue behavior of steel-fiber-reinforced concrete structures. **Nuclear Engineering and Design**, vol. 156, p. 201-207, 1995.

22 LEE, M. BARR, B. An overview of the fatigue behavior of plain and fibre reinforced concrete. **Cement Concrete Composites** (2004), vol. 26, p. 299-305, 2004.

23 STEPHEN, S. GETTU, R. Fatigue fracture of fibre reinforced concrete in flexure. **Materials and Structures**, vol. 53, p. 56, 2020.

24 GERMANO, F. TIBERTI, G. PLIZZARI, G. Post-peak fatigue performance of steel fiber reinforced concrete under flexure. **Materials and Structures**, vol. 49, p. 4229-4245, 2016.

25 CARLESSO, D. DE LA FUENTE, A. CAVALARO, S. Fatigue of cracked high performance fiber reinforced concrete subjected to bending. **Construction and Building Materials** (2019), vol. 220, p. 444-455, 2019.

26 MONTEIRO, V. CARDOSO, D. SILVA, F. A novel methodology for estimating damage evolution and energy dissipation for steel fiber reinforced concrete under flexural fatigue loading. **International Journal of Fatigue**, vol. 166, 2023.

27 HSU, T. Fatigue of plain concrete. **ACI Journal**, vol. 78, p. 292-304, 1981.

28 CARLESSO, D. CAVALARO, S. DE LA FUENTE, A. Flexural fatigue of pre-cracked plastic fibre reinforced concrete: experimental study and numerical modeling. **Cement and Concrete Composites**, vol. 115, 2021.

29 SINGH, S. KAUSHIK, S. Fatigue strength of steel fibre reinforced concrete in flexure. **Cement & Concrete Composites** (2003), vol. 25, p. 779-786, 2003.

30 SINGH, S. SINGH, B. KAUSHIK, S. Probability of fatigue failure of steel fibrous concrete. **Magazine of Concrete Research**, vol. 57, p. 65-72, 2005.

31 SINGH, S. SHARMA, U. Flexural fatigue strength of steel fibrous concrete beams. **Advances in Structural Engineering**, vol. 10, p. 197-207, 2007.

32 MEDEIROS, A. ZHANG, X. RUIZ, G. YU, R. VELASCO, M. Effect of the loading frequency on the compressive fatigue behavior of plain and fiber reinforced concrete. **International Journal of Fatigue** (2015), vol. 70, p. 342-350, 2015.

33 SAUCEDO, L. YU, R. MEDEIROS, A. ZHANG, X. RUIZ, G. A probabilistic fatigue model on the initial distribution to consider frequency effect in plain and fiber reinforced concrete. **International Journal of Fatigue** (2013), vol. 48, p. 308-318, 2013.

34 BAKTHEER, A. BECKS, H. Fracture mechanics based interpretation of the load sequence effect in the flexural fatigue behavior of concrete using digital image correlation. **Construction and Building Materials**, vol. 307, 2021.

35 BAKTHEER, A. AHUILAR, M. CHUDOBA, R. Microplane fatigue model MS1 for plain concrete under compression with damage evolution driven by cumulative inelastic shear strain. **International journal of Plasticity** (2021), vol. 143, 2021.

36 CASTILLO, E. CANTELI, A. **A unified statistical methodology for modeling fatigue damage**, 1st ed. Springer, 2009.

37 BLASÓN, S. CANTELI, A. POVEDA, E. RUIZ, G. YU, R. CASTILLO, E. Damage evolution and probabilistic strain-lifetime assessment of plain and fiber-reinforced concrete under compressive fatigue loading: Dual and integral phenomenological model. **International Journal of Fatigue** (2022), vol. 158, 2022.

38 ORTEGA, J. RUIZ, G. POVEDA, E. GONZÁLEZ, D. TARIFA, M. ZHANG, X. YU, R. VICENTE, M. DE LA ROSA, A. GARIJO, L. Size effect on the compressive fatigue of fibre-reinforced concrete. **Construction and Building Materials**, vol. 322, 2022.

39 ORTEGA, J. RUIZ, G. YU, R. AFANADOR-GARCÍA, N. TARIFA, M. POVEDA, E. ZHANG, X. EVANGELISTA JR, F. Number of tests and corresponding error in concrete in fatigue. **International Journal of Fatigue**, vol. 116, 2018.

40 GONZÁLEZ, D. MENA, A. RUIZ, G. ORTEGA, J. POVEDA, E. MÍNGUEZ, J. DE LA ROSA, A. VICENTE, M. Size effect of steel fiber-reinforced concrete cylinders under compressive fatigue loading: influence of the mesostructure. **International Journal of fatigue**, vol. 167, 2023.

41 DI PRISCO, M. COLOMBO, M. DOZIO, D. Fibre-reinforced concrete in fib Model Code 2010: principles, models and test validation. Structural Concrete, vol. 14, p. 342-361, 2013.

42 VAN ZIJL, G. MBEWE, P. Flexural modelling of steel fibre-reinforced concrete beams with and without steel bars. **Engineering Structures**, vol. 53, p. 52-62, 2013.

43 TURK, K. BASSURUCU, M. An investigation on the effect of hybrid fiber reinforced on the flexural behavior of RC beams having different lad-spliced lengths. **Structural Concrete** (2022), p. 1-13, 2022.

44 MAHMOOD, S. Flexural performance of steel fibre reinforced concrete beams designed for moment redistribution. **Engineering Structures**, vol. 177, p. 695-706, 2018.

45 QASIM, M. LEE, C. ZHANG, Y. Flexural strengthening of reinforced concrete beams using hybrid fibre reinforced engineered cementitious composite. **Engineering Structures**, vol. 284, 2023.

46 MONTEIRO, V. LIMA, L. SILVA, F. On the mechanical behavior of polypropylene, steel and hybrid fiber reinforced self-consolidating concrete. **Construction and building Materials**, vol. 10, p. 280-291, 2018.

47 CARDOSO, D. PEREIRA, G. SILVA, F. SILVA, J. PEREIRA, E. Influence of steel fibers on the flexural behaviour of RC beams with low reinforcing ratios: Analytical and experimental investigation. **Composite Structures**, vol. 222, 2019.

48 MOBASHER, B. YAO, Y. SORANAKOM, C. Analytical solutions for flexural design of hybrid steel fiber reinforced concrete beams. **Engineering Structures**, vol. 100, p. 164-177, 2015.

49 BELLETI, B. CERIONI, R. MEDA, A. PLIZZARI, G. Design aspects on steel fiber-reinforced concrete pavements. **Journal of Materials in Civil Engineering**, vol. 20, 2008.

50 YAO, Y. ASWANI, K. WANG, X. MOBASHER, B. Analytical displacement solutions for statically determinate beams based on a trilinear moment-curvature model. **Structural Concrete**, vol. 19, p. 1619-1632, 2018

51 BISHARA, A. Some aspects of dynamic response of rectangular reinforced concrete beams. **ACI Special publication** (1982), vol. 75, p. 235-252, 1982.

52 ZANUY, C. FUENTE, P. ALBAJAR, L. Effect of fatigue degradation of the compression zone of concrete in reinforced concrete beams. **Engineering Structures**, vol. 29, p. 2908-2920, 2007.

53 MIRZAZADEH, M. NOEL, M. GREEN, M. Fatigue behavior of reinforced concrete beam with temperature differentials at room and low temperature. **Journal of Structural Engineering**, vol. 143, 2017.

54 BRESLER, B. BERTERO, V. Behavior of reinforced concrete under repeated load. Journal of the Structural Division, vol. 94, 1968

55 PAPAKONSTANTINOU, C. PETROU, M. HARRIES, K. Fatigue behavior of RC beams strengthened with GFRP sheets. **Journal of Composite Construction**, vol. 5, p. 246-253, 2001.

56 GAO, D. GU, Z. TANG, J. ZHANG, C. Fatigue performance and stress range modeling of SFRC beams with high-strength steel bars. **Engineering Structures**, vol. 216, 2020.

57 PARVEZ, A. FOSTER, S. Fatigue behavior of steel-fiber-reinforced concrete beams. **Journal of Structural Engineering** (2015), vol. 141, 2015.

58 AMERICAN SOCIETY FOR TESTING AND MATERIALS. **ASTM C595:** Standard specification for blended hydraulic cements, 2008.

59 DE LARRARD, F. **Concrete mixture proportioning: a scientific approach**. E&FN SPON, 1999.

60 RAMBO, D. SILVA, F. FILHO, R. Effect of steel fiber hybridization on the fracture behavior of self-consolidating concretes. **Cement & Concrete Composites**, vol. 54, p. 100-109, 2014.

61 AMERICAN SOCIETY FOR TESTING AND MATERIALS. **ASTM C1611**: Standard test method for slump flow of self-consolidating concrete, 2005.

62 EUROPEAN STANDARD. **EN 14651**: Test method for metallic concrete - Measuring the flexural tensile strength (limit of proportionality (LOP), residual), 2005.

63 BRUCK, H. MCNEILL, S. SUTTON, M. PETERS, W. Digital image correlation using Newton-Raphson method of partial differential correction. **Experimental Mechanics**, vol. 29, p. 261-267, 1989.

64 GRIMALDI, A. OLIVITO, R. RINALDI, Z. **Behaviour of R.C. beams reinforced With FRC material: analytical – Experimental evaluation**. In: 6th International RILEM Symposium on Fibre-Reinforced Concretes, 2004.

65 DANCYGIER, A. BERKOVER, E. Cracking localization and reduced ductility in fiber-reinfroced concrete beams with low reinforcement ratios. **Engineering Structures**, vol. 111, p. 411-424, 2016.

67 BHOSALE, A. PRAKASH, S. Crack propagation analysis of synthetic vs. steel vs. hybrid fibre-reinforced concrete using beams using digital image correlation technique. **International Journal of Concrete Structures and Materials**, vol. 14, p. 57, 2020.

68 ZHANG, J. LI, V. Simulation of crack propagation in fiber-reinforced concrete by fracture mechanics. **Cement and Concrete Research**, vol. 34, p. 333-339, 2004.

69 JENQ, Y. SHAH, S. Crack propagation in fiber-reinforced concrete. **Journal of Structural Engineering**, vol. 112, 1986.

70 YAO, Y. MOBASHER, B. WANG, J. XU, Q. Analytical approach for the design of flexural elements made of reinforced ultra-high performance concrete. **Structural Concrete** (2020), vol. 22, p. 298-317, 2020.

71 VOLPATTI, G. MARTÍNEZ, J. DIAZ, J. ZAMPINI, D. Advanced closed-form moment-curvature formulation for fiber-reinforced concrete members. **Composite Structures** (2022), vol. 279, 2022.

72 SMEDT, M. VRIJDAGHS, R. STEEN, C. VERSRYNGE, E. VANDEWALLE, L. Damage analysis in steel fibre reinforced concrete under monotonic and cyclic bending by means of acoustic emission monitoring. **Cement and Concrete Composites**, vol. 114, 2020.

73 POURSAEE, A. HANSSON, C. The influence of longitudinal cracks on the corrosion protection afforded reinforcing steel in high performance concrete. **Cement and Concrete Research**, vol. 38, p. 1098-1105, 2008.

74 SHAIKH, F. Effect of cracking on corrosion of steel in concrete. International **Journal of Concrete Structures and Materials**, vol. 12, p. 3, 2018.

75 SCOTT, A. ALEXANDER, M. The influence of binder type, cracking and cover on corrosion rates of steel in chloride-contaminated concrete. **Magazine of concrete Research**, vol. 59, p. 495-505, 2015.

8 Final conclusions

Along this present research, the fiber influence on the study of FRC degradation under fatigue was analyzed in fiber, material and structural levels. The work encompassed from the mechanisms of the fiber pull out failure until the analysis of R/SFRC beams under fatigue loading. Through the complete thesis, a series of empirical and analytical models were proposed aiming to enhance the comprehension of fiber reinforced concrete composites degradation characteristics in the literature.

In the material level, an extensive experimental program was carried on and novel fatigue life curves were proposed for the FRC literature. Moreover, the composite material fatigue life was studied in terms of distinct statistical methodologies, allowing to estimate the number of cycles before failure in terms of a survival probability. In order to better understand the flexural failure mode, the research also encompassed the fatigue response in the fiber level through cyclic pull out tests. For higher pull out load levels, the specimen presented a progressive fiber pull out along the time. On the other hand, for moderate load intensities, the wire rupture takes place near the hook.

Based on the achieved experimental results, a novel methodology to evaluate the mechanical degradation under fatigue was proposed using the current closed-form solutions for fiber reinforced concrete beams. The closed-form equations were attached to the S-N curves and CMOD evolution estimations. Therefore, using the CMOD increase along cycles, it was possible to evaluate analytically the degradation of the FRC beam in terms of other mechanical parameters, such as curvature, tensile strain and residual flexural stress.

Finally, the addition of steel fibers significantly enhanced the capacity of the reinforced concrete structure to withstand the fatigue cycles. The addition of steel fibers on the matrix composition promotes a significant influence on the rebar strain evolutions of RC structures. This can be attributed to the bridging effect of the steel fibers in the tensile region of the reinforced structure that are very effective in reducing the stress range of the tensile reinforcement. Moreover, the addition of fibers plays an important role when it comes to the bond of the rebar on the concrete matrix. Present research also verified the degradation of the rebar-concrete interface when under fatigue pull out. The increase in bond strength with the fiber reinforcement is responsible for enhancing the bond response under fatigue loading, which helps to understand the structural behavior observed in the concrete beams.

The main research contribution of this PhD thesis relies on a deeper analysis on the fatigue degradation of FRC, encompassing from the fiber level until the structural application and the proposal of new analytical models. The use of fibers revealed immense potential in reducing the mechanical degradation of concrete material and structural members, which is key when it comes to successfully enhancing the useful life of the RC structures under fatigue loading. Finally, the addition of the fiber reinforcement on the concrete mix are be responsible for mitigating the damage evolution along the cycles and extending the useful years of the reinforced concrete under flexural fatigue. This PhD thesis is just the kick-start of a series of other works supported by Furnas, which will carry on the development of cementitious composites when under fatigue loading.